DEVELOPMENT OF A HIGHLY RESILIENT GRAPHENE NANOPLATELET RESIN/ADHESIVE

by

Babak Ahmadi Moghadam

Submitted for partial fulfillment of requirements for the degree of Doctor of Philosophy

Dalhousie University

Halifax, Nova Scotia

February 2015

I lovingly dedicate this thesis to my wife, Mahdiyeh

who supported me in each step of the way

Table of Contents

LIST OF TABLES

LIST OF FIGURES

ABSTRACT

Fiber-reinforced polymer composites (FRPs) are extensively utilized in many industries due to their remarkable mechanical properties, corrosion resistance and light-weight attributes. Notwithstanding, FRP laminates are critically susceptible to delaminations, which are often initiated due to invisible interlaminar cracks. Delaminations in turn weaken the overall strength and stiffness of FRPs, thus degrading their longevity and in-service reliability. Delamination phenomenon, which is one of the most common failure modes in FRP structures, is considered as a matrix dominant failure, because it is governed by matrix's fracture toughness and the fiber/matrix interface bond strength.

The recent emergence of carbon nano-particles (CNPs), such as carbon nanotubes (CNTs) and graphene nanoplatelets (GNPs), have, however, enabled the engineers and scientists to develop a new generation of multi-functional modifiers for FRP composites. As a result, new breeds of FRPs, with remarkable mechanical, electrical and thermal properties have been generated in the recent years. However, the endeavor has not been without significant challenges; indeed, the production cost of CNPs, coupled with the effort (cost) associated with uniform dispersion of CNPs in resins, have been some of the major challenges encountered in the fabrication of CNP nanocomposites.

In the first section of this thesis, therefore, the details of an integrated and systematic investigation into the influence of processing parameters on the multi-functional performances of GNP/epoxy nanocomposites are presented. The obtained results led to the establishment of an optimized method for dispersing GNPs in epoxy resins, as a function of the configuration and geometry of the GNPs. In addition, a design diagram has been developed by which one could design GNP-reinforced composites, for a given application, in an effective manner.

In the second part, the details of efforts expended in studying the fracture and toughening mechanisms of GNP-nanocomposites, and the assessment of their interlaminar fracture toughness (IFT) of FRPs formed by the GNP-reinforced resins, are presented. As another contribution to the field, the performance of a GNP-reinforced epoxy was further enhanced by functionalizing the GNPs with a silane agent. Moreover, to the best of author's knowledge, for the first time, the fracture mechanics of GNP-reinforced epoxy under pure modes I and II fracture are assessed qualitatively and quantitatively, using the micro-structural analysis technique. Furthermore, in response to the lack of a comprehensive test method for evaluating the mode III IFT of FRPs reinforced by GNPs, a new torsion-based test method has been developed and proposed. It will be shown that the fracture toughnesses of both GNP nanocomposites and mode-I IFT of the FRPs formed by the GNP-reinforced resin were significantly enhanced, while it will be demonstrated that inclusion of GNPs in the resin produced much less enhancement when the nanocomposite become subjected to mode-II and -III fracture in comparison to the mode-I fracture.

Finally, the mechanical response of the developed resilient GNP-reinforced epoxy adhesive is evaluated under various strain rates subject to both tensile and compressive loading schemes. Empirical models were also developed and proposed based on the performed experiments. The models enable one to predict the stiffness of such nanocomposites, under different stain rates, based on the weight content of GNPs.

LIST OF ABBREVIATIONS AND SYMBOLS

FRP	Fiber- reinforced polymer
NP	Nanoparticle
NDP	Nano-diamond particle
CNT	Carbon nanotube
CNF	Carbon nano fiber
GNP	Graphene nanoplatelet
PVAc	Poly vinyl acetate
CTE	Coefficient of thermal expansion
ABJ	Adhesively bonded joint
wt%	weight content
SLJ	Single lap jont
FE-SEM	Field emission scanning electron microscopy
GNPRE	GNP-nanocomposite reinforced epoxy specimens
EPT	Electrical percolation threshold
IPD	Interparticle distance model
AFM	Atomic force microscope
SIF	Stress intensity factor

SENB	Single edge notch beam
PMMA	Poly methyl methacrylate
MTS	Maximum tangential stress criterion
3DMTS	3D maximum tangential stress criterion
MVG	Mean value of the total energy release rate
MVK	Mean value of stress intensity factor
ASTM	American Society of Testing Materials
UG	unmodified GNP
G-Si	Silane modified GNP
GO	Graphene oxide
G-NH_2	Amino- functionalized GNP
TGA	Thermo-gravimetric analysis
FTIR	Fourier transform infrared spectroscopy
XRD	X-ray diffraction
VARTM	Vacuum assistant resin-transfer molding
DCB	Double cantilever beam
ILFT	Interlaminar fracture toughness
ECT	Edge-crack torsion specimen

CERR	Critical energy release rate
E_C	young's modulus of the composites
l_f	Length of reinforcement
d_f	Average diameter of reinforcement
E_f	Elastic modulus of reinforcement
E_m	Elastic modulus of reinforcement
V_f	Reinforcement volume fraction
$K_{eff,}$	Effective fracture toughness of nanocomposite
G_{IC}	Mode I critical energy release rate
G_{IIc}	Mode II critical energy release rate
G_{IIIC}	Mode III critical energy release rate
D	Average diameter of graphene nanoplatelet
t	Graphene nanoplatelet thickness
EI	Flexural stiffness
D_i	Inner diameter of carbon nanotube
D_o	Outer diameter of carbon nanotube
T_g	Glass transition temperature
α_m	Matrix linear CTE

k_f	Bulk moduli of nano filler
k_m	Bulk moduli of marix
γ_f	Bulk thermal expansions of nano filler (Chow model)
γ_m	Bulk thermal expansions of matrix (Chow model)
μ	Shear Modulus
ρ	Graphenen nanoplatelet's characteristic ratio
K_{IC}	Mode I fracture toughness
P_{max}	Maximum load
B	Single- edge- notch bend specimen thickness
W	Single- edge- notch bend specimen width
a	Initial crack length
$f\left(\frac{a}{w}\right)$	Mode I geometry factor
K_{IIC}	Mode II fracture toughness
F	Magnitude of load
$f'\left(\frac{a}{w}\right)$	Mode II geometry factor
r_p	Plastic zone radius
σ_y	Yield strength
S	The length of support span in three-point bend fixture

υ	Poisson's ratio
γ_f	Kink angle
I_D	The intensity of the D-band in Raman signal
I_G	The intensity of the G-band in Raman signal
C	Compliance (i.e., crosshead displacement over the load)
σ_y^p	Absolute value of the yield stress under hydrostatic pressure
σ_y^0	Yield stress under zero hydro static pressure
α_p	Sensitivity coefficient
σ_i	Stress components
σ_y^{ref}	Yield strength evaluated under a static loading rate
$\dot{\varepsilon}_p^{eff}$	Effective plastic strain rate
$\dot{\varepsilon}_0$	Reference strain rate
T	Absolute temperature
k	Boltzmann's constant in Richeton's model
V_{eff}	Effective activation volume
ΔH_{eff}	Effective activation energy
E^{ref}	Young's modulus at strain rate of $\dot{\varepsilon}_0$

ACKNOWLEDGMENTS

I would like to express my deepest gratitude to Professor Farid Taheri for his continuous support, encouragement, and professional attitude, which helped me in stage of my research and enabled me to complete this dissertation.

I wish to extend my appreciation to all of my committee members; Prof. Hani Naguib Prof. Stephen Corbin and Dr. Zoheir Farhat for their helpful technical comments on my thesis.

I am very thankful to the skillful technicians of our department, Mr. Brian Kennedy, Mr. Mr. Blair Nickerson and Mr. Jesse Keane for their assistance and technical support throughout my experimental works.

The financial support of the Natural Sciences and Engineering Council of Canada (NSERC) through the Collaborative Research and Training Experience (CREATE) program is gratefully acknowledged

Chapter 1: Introduction

1.1 Fiber reinforced composites

A fiber-reinforced polymer (FRP), also known as fiber-reinforced plastic, is made of a polymer matrix, that could be thermoplastic or thermoset resin, reinforced with different type of fibers such as glass, carbon and aramid or a hybrid of these fibers. FRPs could also be categorized based on their resin types (e.g., epoxy, polyester and vinyl ester), and fiber configuration (chapped, short or long fibers) [1]. The main advantages of FRPs are their relatively large specific strength and stiffness, which combined with their low density, enables engineers to achieve significant weight reduction in their designs. In addition, superior fatigue response, corrosion resistance, higher flexibility in design, better damping, reduced flammability and lower radar signature, and in some cases, lower electrical and thermal conductivity are some of the positive attributes of FRPs that renders them as suitable engineering materials. As a result, they are broadly used in diverse industries like aerospace, automotive, marine, construction, and recently, in oil and gas industry [2].

FRPs are classified as orthotropic materials, a subcategory of anisotropic materials. Continuous fiber composites are normally laminated; that is, the individual layers of fibers or fabrics (plies or laminae), which could usually have different mechanical properties along the fibers, and normal to the fibers, are stacked at various angles to optimally achieve the required strength in the primary load direction(s). While FRPs have remarkable in-plane properties, they are weak in the directions that their matrix is subjected to load (e.g., through-the-thickness of a laminate). Therefore, in general, FRPs become vulnerable in the matrix dominated loading conditions.

High raw material costs and usually high fabrication and assembly costs, adverse effect of both temperature and moisture [3], inferior strength in the out of plane direction (and also in any other directions where the matrix is subject to the primary load), and susceptibility to impact are the main disadvantages of FRPs. Since FRPs are the combination of fibers and matrix, the flaws could exist either in fibers, in matrix or in the fiber/matric interface. As a result, FRPs are considered as complex systems, thus making the task of damage detection in structures made of FRPs, with the currently available techniques such as acoustic emission and ultrasonic, very challenging.

1.2 Delamination in FRP laminates

Due to the relatively weak interlaminar strengths of FRPs, delamination is one of the most common types of damage in laminated fiber-reinforced composites. Delamination can form any moment during the life of a FRP structure (i.e., starting from its manufacturing, transport, and in-service).

Pagano et al [4] showed that the technological causes of delamination could be grouped within two categories. The first category includes delamination due to section curvature, such as curved segments, and tubular, cylindrical and spherical configurations (e.g., pressurized containers). In all such cases, the normal and shear stresses at the interface of two adjacent piles can cause loss of adhesion and the initiation of an interlaminar crack. The abrupt changes in sections, such as ply drop-offs, unions between stiffeners and thin plates, free edges, and bolted joints are the second category that promote delaminations in FRPs.

Environmental effects such as temperature and moisture could also be added to these categories. The difference between the thermal coefficients of matrix and reinforcement

results in differential expansion/contractions between the piles during the curing process of a laminate. The residual stresses originated by this phenomenon could potentially become a source of delamination [5]. Similarly, the different expansion in the plies of a laminate due to moisture absorption can also cause delamination [6].

Delamination may also originate during the manufacturing stage due to the shrinkage of the matrix during the curing process, or due to the formation of resin-rich areas that result from poor practices when laying the piles [7, 8]. During the service of FRP structures, delamination may originate due to various circumstances, such as transversely concentrated loads created by a low-velocity impact event. Impact could also be considered as one of the most important sources of delamination in composite structures. Interlaminar cracks may originate from internal damage that could exist in the interface between adjacent plies. This could occur as a consequence of an impact caused by the drop of a tool during production, assembly, or maintenance of FRP structures, or due to impacts of objects, as well as ballistics.

According to Bolotin [7, 8], two types of delamination can be considered: internal delamination (Figure 1-1) and near-surface delamination (Figure 1-2). Internal delamination originates in the inner ply interfaces of the laminate and can be due to interaction of matrix cracks, and ply interfaces. The delamination originated by a transverse matrix crack in plies orthogonal to the compressive load is a common example of this type delamination.

Internal delamination adversely affects the stiffness of a composite structure, specifically when the applied loading subjects the part to compressive or flexural. If the

structure is subjected to a compressive loading condition, then its load-bearing capacity is influenced by existence of delaminations by a significant margin.

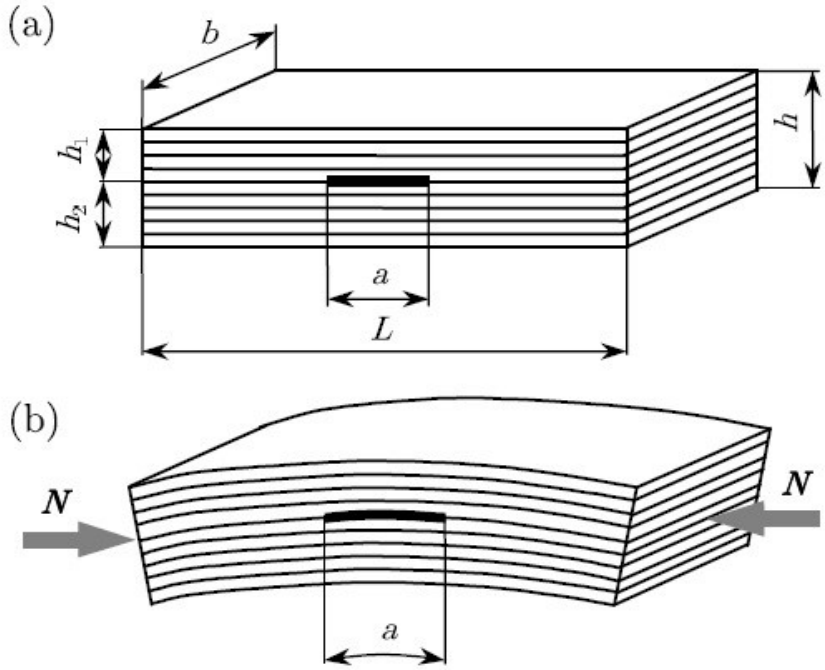

Figure 1-1. Internal delamination:(a) disposition across the laminate and (b) effect on the overall stability under a compressive loading state [7]

A near-surface delamination, as the name indicates, originates near the surface of the laminate and represents a more complex scenario than an internal delamination. In this case, the deformation of the delaminated part is less influenced by the deformation of the rest of the laminate.

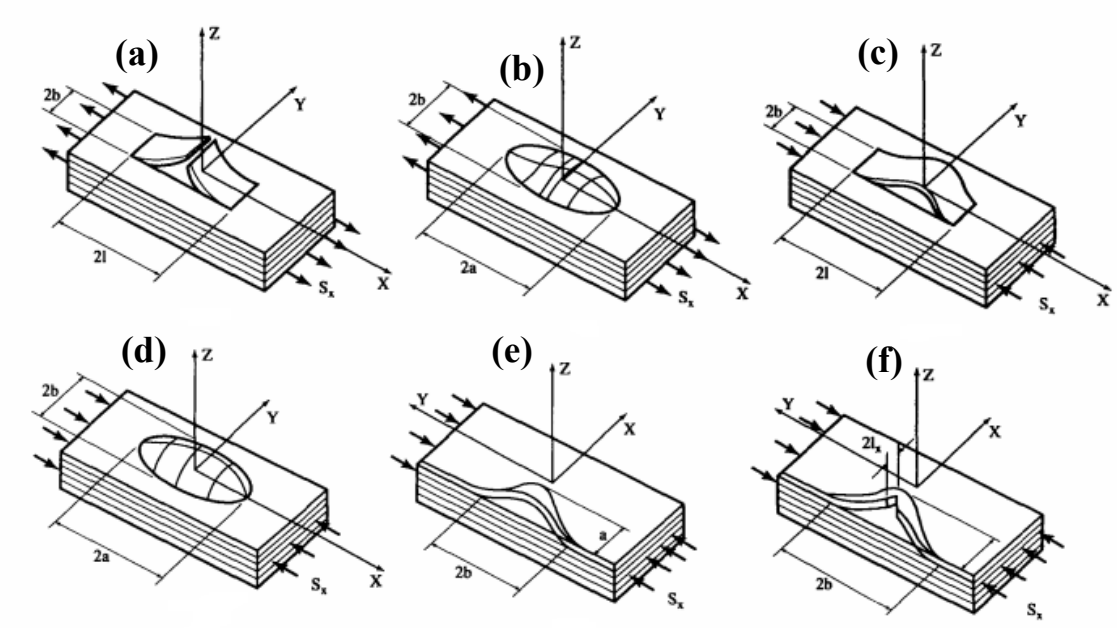

Figure 1-2. Near-surface delamination:(a) open delamination in tension; (b) closed delamination in tension (c) open buckled delamination; (d) closed buckled delamination; (e) edge buckled delamination and (f) edge buckled with secondary crack [7]

Delamination is often discussed in terms of interlaminar fracture toughness (energy release rate) in FRP composites. When a delamination develops, all three modes of fracture shown in Figure 1-3 become usually involved as a result of loading state and FRP's layup. Therefore, a complete understanding of fracture mechanics of FRPs is necessary in order to evaluate the delamination initiation and propagation in FRP composites.

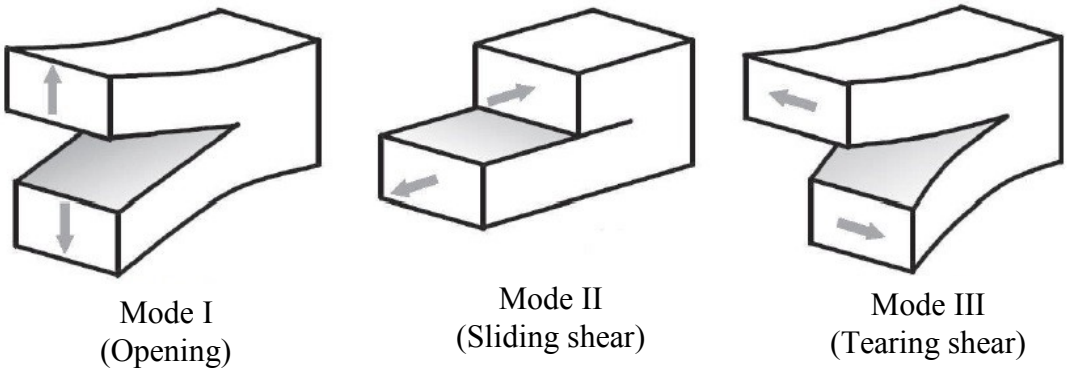

Figure 1-3. Different mode of fracture [9]

1.3 Carbon nano nanoparticles

A nanoparticle (NP) is defined as a particle with one of its dimensions being less than 100 nm [10]. In fact, a NP is considered as a bridge between material configuration in atomic and bulk scales. The key advantages of nano-size materials are as follows [11]: large specific surface area, high surface energy, reduced numbers of structural imperfections, and distinctively different physical properties from those of the same material in its bulk state. Unlike bulk materials, whose properties are fairly size independent, NPs exhibit size-dependency. This size-dependency is due to the significant increase in the ratio of the atoms on the surface of the particle to the total atoms forming the particle, as nanoparticle's dimensions approach zero.

The excellent capability of carbon NPs in ameliorating different properties of resins or matrices has persuaded researchers to perform extensive investigations into the behavior of carbon NP-reinforced polymers. As shown in Figure 1-4, there are three common configurations of carbon nanofillers, including zero dimensional or spherical particles, such as nano-diamond particles (NDP), one-dimensional or cylindrical fillers, such as

carbon nanotubes (CNTs) and carbon nanofibers (CNFs), and two-dimensional nanofillers such as graphene nanoplatelets (GNPs).

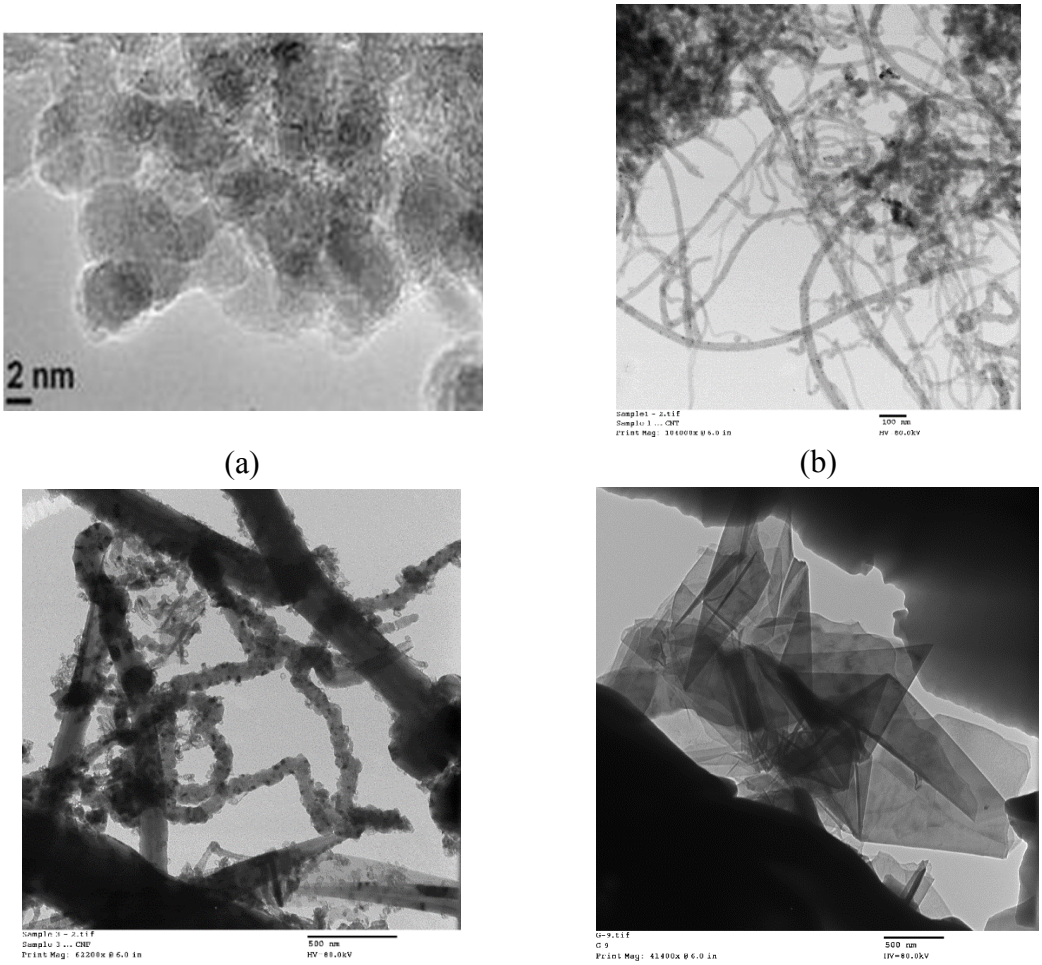

Figure 1-4. TEM micro-graphs of different configurations of carbon nanoparticles; (a) ND [12] (b) CNT, (c) CNF and (d) GNP

Carbon nanoparticles possess remarkable mechanical, electrical and thermal properties, which shows their potential for the modification of the conventional FRP mechanical, electrical and thermal properties. As an example, the elastic modulus of SWCNTs can be as high as 1 TPa and 60 GPa tensile ultimate strength. Moreover, they

can carry the highest electrical current density of any known materials (i.e., 109 A/cm^2), and their thermal conductivity is typically around 1750-5800 W/mK [13].

All these impressive features have encouraged the researchers to explore the reinforcing effect of nano materials when included in different polymer matrices. The main disadvantages of carbon nano materials are known to be: (a) the inconsistency in the quality of carbon NPs, especially in their mass-produced form, and (b) their relatively high cost.

1.4 Motivations and contributions

Developing a highly resilient adhesive using graphene nanoplatelets is the main aim of this research. Aforementioned statements revealed that resins such as epoxies play an important role in keeping fibers along the desired orientations, and transferring load from on fiber to another in FRP composites. As also stated, a failure mode such as a delamination, which is considered as a matrix dominated failure, usually initiates and grows within matrix or at the interface of matrix and fibers in FRP laminates. Therefore, improving the properties of the matrix would in turn lead into improvement in the response of FRPs.

Carbon nanoparticles, specifically carbon nanotubes (CNTs), because of their remarkable material properties (as will be discussed in detail in chapter 2), have been widely utilized to enhance the mechanical, electrical and thermal properties of adhesives. In this research, planar carbon nanoparticles, specifically graphene nanoplatelets (GNPs), are used to modify the material properties of epoxy resin/adhesive. Not only do GNPs offer positive multi-functional attributes to their host adhesives, but because of their simple production techniques and abundancy of graphitic sources in nature, they are also significantly less expensive than other carbon nanoparticles. Therefore, production cost of

GNP-based nanocomposites would be much less than those made with CNTs. Nonetheless, the production cost of GNP-nanocomposites could be further reduced by improving various features of the existing manufacturing techniques (see chapter 3 for more details).

It should, however, be noted that although GNPs could improve certain mechanical properties of adhesives, their potential agglomeration could cause the onset of a delamination in multi-scale laminated FRPs whose resins are reinforced by GNP. Therefore, a thorough understanding of the fracture mechanisms of both resins reinforced by GNPs, as well as FRPs formed by such reinforced resins would be necessary, which also forms a major objective of this research (see chapter 4- for more details)

In summary, the following statements describe the author's main contributions to the field of research:

- ✓ Optimization of the existing dispersion methods of GNPs in epoxy resins based on the structural features of GNPs, and production cost of nanocomposite.
- ✓ Evaluation of the effect of the synergy of CNTs and GNPs on the fracture toughness of GNP/epoxy resin nanocomposites.
- ✓ Establishment of modes I and II fracture and toughening mechanisms of the GNP-reinforced resin based on quantitative and qualitative assessment of fracture surfaces of GNP-based nanocomposites using scanning-electron and atomic-force microscopes.
- ✓ Introducing a new GNP functionalization methodology using a silane agent to improve the mechanical properties (i.e., stiffness and fracture toughness) of GNP-based nanocomposites.

- ✓ Evaluation of the interlaminar fracture toughness of an E-glass fiber-reinforced composite, with its resin reinforced with different types of GNPs (i.e., as-received and functionalized GNPs) under modes I, II and III fracture.
- ✓ Quantitative establishment of the influences of functionalized GNPs on the fracture mechanism of FRP composites filled with GNPs.
- ✓ Development of a semi-empirical micro-mechanical model for prediction of the stiffness of a GNP-based nanocomposites under various tensile and compressive strain rates.
- ✓ Development of a new procedure for the evaluation of mix-mode (I-III) fracture toughness of neat epoxy resins using the single-edge-notch beam.

1.5 Thesis layout

This thesis follows the "paper format" scheme, constituted relatively recently at Dalhousie University's Faculty of Graduate Studies. Therefore, it does not follow the conventional thesis format, but it presents an introductory section, followed by a collection of manuscripts that have either been published, accepted for publication or are under review in scholarly journals. In the end, a general conclusion section, followed by the recommended research works for future endeavors finalizes the thesis.

From the technical perspective, in order to accomplish the overall set goal of the doctoral project, which essentially involved the development of a highly resilient resin/adhesive, a systematic and extensive study has been conducted, whose details will be presented within a total of six chapters. As stated earlier, each chapter is, in fact, a manuscript, which is either published or accepted for publication (i.e., chapters 3-5, 7 and

8), or has been conditionally accepted for publication is peer-reviewed journals (i.e., chapter 6).

The collective tasks carried out within the project can also be categorized within three distinct phases. First, the details of an integrated investigation into the influence of processing parameters on the multi-functional performances of GNP/epoxy nanocomposites are detailed. In the second phase, details of the work conducted for characterizing the fracture and toughening mechanism in GNP nanocomposites and interlaminar fracture toughness assessment of FRPs reinforced by GNP are presented. Finally, the mechanical behavior of a GNP/epoxy adhesive is assessed under different strain rates. The following sections briefly describe the contents of each chapter of this thesis.

Chapter 1 (i.e., the current chapter) provides a brief introduction to FRP materials, the delamination phenomenon, and carbon nanoparticles. The thesis organization and the correlation among its chapters are also presented in this chapter.

Chapter 2 presents a summary of the literature review conducted throughout the course of the project. It should be noted that each manuscript (that forms a chapter), also provides detailed literature review for the particular topic that has been addressed within the chapter. Chapter 2 outlines the various techniques used for production of nanocomposites. A summary of the other researchers' relevant works that have investigated the influence of different types of carbon nanoparticles on the multi-functional performances of composite structures, and adhesively bonded joints is also presented in chapter 2. It should also be noted that some of the materials presented in chapter 2 are the specific contributions of the author, which could also be found in a co-authored manuscript,

entitled “Nano-enhanced Adhesives-A Critical Review”, published in the journal of Review of Adhesives and Adhesion.

Chapter 3 presents a detailed experimental approach for achieving an optimized GNP dispersion method in epoxy resins for developing a nanocomposite with significantly improved mechanical, electrical and thermal properties. The motivation for this work was the provision for processing a highly resilience adhesive, in a cost-effective manner, which would be used in the other phases of the investigations conducted by the author.

Chapter 4 details a comprehensive study conducted into characterization of the fracture response and toughening mechanism of the GNP-reinforced epoxy under both pure modes I and II fracture. A quantitative study was also performed to assess the roughness of the tested nanocomposites’ fracture surfaces with the aim of establishing a relation between the energy release rate of the nanocomposites and their fracture surface roughness. A combined toughening/pure mode-II fracture mechanism is also proposed based on the observed process-zone characteristic of the nanocomposites. Moreover, the applicability of linear fracture mechanic approach for assessing the response of GNP/epoxy nanocomposites is also investigated.

Chapter 5 outlines the details of an experimental framework used for the enhancement of performance of GNP reinforced epoxy nanocomposites by functionalizing GNPs with a silane agent. The main aim of the work described in this chapter was to obtain a more superior nanocomposite by achieving more even dispersion quality of the GNPs (by functionalization) in resin. The enhancement gained by the new functionalization method was confirmed by the standard chemical analysis. Furthermore, the gain in the

Mechanical properties of the nanocomposites processed with the functionalized GNPs was also compared against the gain obtained by the other functionalization methods.

Chapter 6 presents a detailed experimental study on the enhancement of the interlaminar strength of FRP structure using unmodified and modified GNPs. The interlaminar fracture toughness of FRP laminates were evaluated under pure mode I, II and III fracture. To assess the interlaminar fracture toughness in mode III, a new methodology was developed based on the twisting edge notch FRP specimens loaded by a torsion test machine.

Chapter 7 augments the worked describer in its previous chapter. It presents the details of a combined experimental and finite-element approach aimed at evaluating mix-mode I/III stress intensity factor of the epoxy resin using the single-edge-notch beam specimen. This specimen configuration is widely used for evaluating the plane strain mode I fracture toughness of plastic materials. Moreover, the procedure is equally applicable for assessing other polymeric resins, and is believed to be extendable for characterizing the fracture response of GNP-reinforced polymers.

Since FRP structures and adhesively bonded joints could be subject to different loading rates, thus gaining an insight into the response of nanoparticle reinforced epoxy adhesives under various loading rates is of paramount importance. The work presented in chapter 8 is a natural progression of the characterization effort. The chapter presents the details of the investigation targeting the effect of strain rate on the tensile and compressive response of GNP-reinforced epoxy composites. It also describes the methodology that lead into development of a semi-empirical model for assessing the response of GNP-reinforced epoxy nanocomposites under different strain rates as a function of their GNP content.

Finally, the last chapter is dedicated to summarizing the various segments of the studies presented in the earlier chapters, and the conclusions. The chapter also presents author's recommendations for the extension of this research work in the future.

1.6 References

[1] Ashbee KHG. Fundamental Principles of Fiber Reinforced Composites, Second Edition: Taylor & Francis; 1993.

[2] Taheri F. 18 - Advanced fiber-reinforced polymer (FRP) composites for the manufacture and rehabilitation of pipes and tanks in the oil and gas industry. In: Bai J, editor. Advanced Fibre-Reinforced Polymer (FRP) Composites for Structural Applications: Woodhead Publishing; 2013. p. 662-704.

[3] Eslami S, Taheri-Behrooz F, Taheri F. Long-term hygrothermal response of perforated GFRP plates with/without application of constant external loading. Polymer Composites. 2012;33:467-75.

[4] Pagano NJ, Schoeppner GA. 2.13 - Delamination of Polymer Matrix Composites: Problems and Assessment. In: Zweben AK, editor. Comprehensive Composite Materials. Oxford: Pergamon; 2000. p. 433-528.

[5] Tay TE, Shen F. Analysis of Delamination Growth in Laminated Composites with Consideration for Residual Thermal Stress Effects. Journal of Composite Materials. 2002;36:1299-320.

[6] Crasto AS, Kim RY. Hygrothermal influence on the free-edge delamination of composites under compressive loading1997.

[7] Bolotin VV. Delaminations in composite structures: Its origin, buckling, growth and stability. Composites Part B: Engineering. 1996;27:129-45.

[8] Bolotin VV. Mechanics of Delaminations in Laminate Composite Structures. Mechanics of Composite Materials. 2001;37:367-80.

[9] Anderson TL. Fracture Mechanics: Fundamentals and Applications, Third Edition: Taylor & Francis; 2005.

[10] Nanoparticle, http://en.wikipedia.org/wiki/Nanoparticle. 2014.

[11] Korotcenkov G. Chemical Sensors: Fundamentals of Sensing Materials Volume 2: Nanostructured Materials: Momentum Press; 2010.

[12] http://www.nanodiaproducts.com/diamond-products/suspensions/, suspension nano diamond. 2014.

[13] Kang I, Heung YY, Kim JH, Lee JW, Gollapudi R, Subramaniam S, et al. Introduction to carbon nanotube and nanofiber smart materials. Composites Part B: Engineering. 2006;37:382-94.

Chapter 2: Literature review

2.1 Introduction

This chapter aims at summarizing the recent advances made in the development of resilient adhesives reinforced with carbon nanopartciles (NPs). Different aspects of nano-reinforced adhesives, including various methods used for formulating and fabricating nanocomposites, their function and mechanism, as well as their advantages and disadvantaged are discussed. In addition, recent progresses made in improving the mechanical, electrical and thermal properties of adhesives reinforced by carbon NPs are also reviewed. It should be noted that most parts in this chapter have been taken from a manuscript which was coauthored by the author (with permission of the publisher), entitled: "*Nano-Enhanced Adhesives: A Critical Review*", published in the Review of Adhesives and Adhesion. The materials taken have been the specific contribution of the author in that manuscript.

2.2 Development of polymer-based nanocomposites

The first step in deployment of nanostructured materials is to devise a suitable strategy for their manufacturing process. Depending on the type of NPs, a number of production methods could be incorporated. For example, in selecting an effective and efficient dispersion technique, one should be concerned that the process would not damage NPs, and that the process would yield consistent results, and would be suitable for mass-production.

Perhaps the prime challenge in manufacturing of polymer-based nanocomposites is the attainment of a uniform dispersion of NPs in the polymer matrix. Due to the small dimensions and relatively large surface area of NPs, the intermolecular forces attract

individual particles to one another; as a result, they tend to form large clumps or agglomerations. In order to promote the efficiency of nanocomposites, it is vital to minimize the formation of such agglomerates and ensure a uniform dispersion of NPs. This task becomes more challenging as the volume content of NPs in a polymer increases, which, in turn, elevates the viscosity of the host polymer, thereby making it less workable. As an example, Figure 2-1 generated by Pinto et al. [1], reports the increase in the viscosity of poly vinyl acetate (PVAc), as a function of GNP content and shear rate.

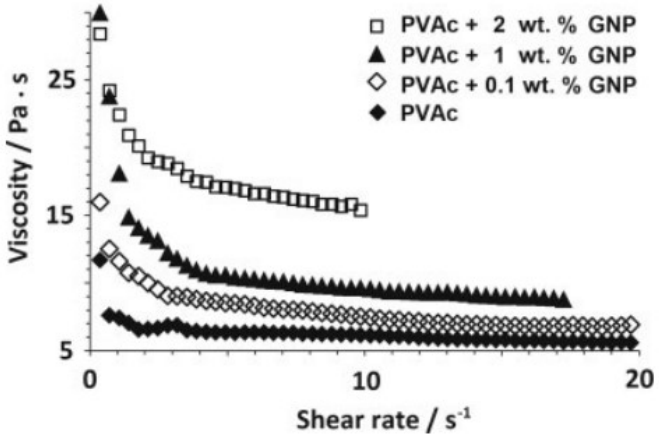

Figure 2-1. Brookfield viscosity GNP/PVAc as a function of shear rate [1]

An acceptable dispersion status can usually be achieved through two steps: (i) by distribution of NPs within the matrix, and (ii) by dispersion of NPs. A mechanical stirrer is usually used for distributing nanoparticles; however, depending on the selected method of dispersion, the distribution step may be avoided. For the second step (i.e. the dispersion), several methods have been developed. The selection of the most suitable method would depend on the type of NP, matrix and nanocomposite's application. The most commonly used techniques for dispersion of nanomaterials are briefly discussed.

2.2.1 Sonication

Sonication is the act of applying high-energy sound waves to disperse NPs in a matrix. For this purpose, usually ultrasonic frequencies greater than 20 kHz are employed, which is referred to as ultrasonication. Dispersion by ultrasonication is accomplished by the ultrasonic cavitation developed at the end of the probe, which generates high speed liquid jets with velocity as high as approximately 1000 km/h. The highly pressurized liquid is then forced between NPs agglomerates, thereby separating them from one another (see Figure 2-2). In addition, the NPs that are accelerated with the liquid jets may also crash into one another, resulting in a further dispersion [2].

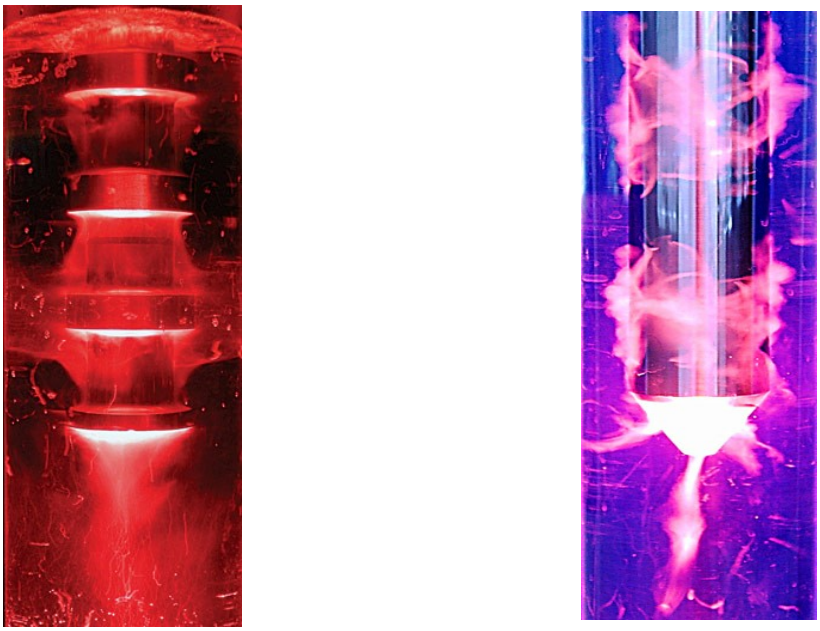

Figure 2-2. Cavitation phenomenon occurring during ultrasonication in two different shaped probe [2]

2.2.2 Three-roll milling (Calendering)

The three-roll mill machine (calender) exerts shear forces to the matrix through three adjacent rollers, with a tiny gap in between them. The rollers rotate in opposite directions at progressively increasing speeds to break down NPs agglomerations, thus dispersing them into the matrix. Figure 2-3 shows the schematic of calendering mechanism. The material is loaded between the feed- and center-rollers. Because of the narrow gaps between the rollers, essentially all the material would remain in the feed region. The mixture makes its way through the rollers, experiencing very large shear force magnitudes, which in turn, disperse NPs in the matrix. As the resin comes out the other side of the rollers, the material, which remains on the center roller (as a very thin layer), goes through the gap between the center roller and apron roller, experiencing even larger shear force resulting due to the higher rolling speed. The sharp knife-edge plate located immediately adjacent to the last roller collects the processed material from the apron roller. The three-roll milling process may be repeated for a number of cycles, until the material is perfectly dispersed. Calendering has proven to be a very effective means for dispersing different types of NPs, especially carbon-based NPs in resins [3].

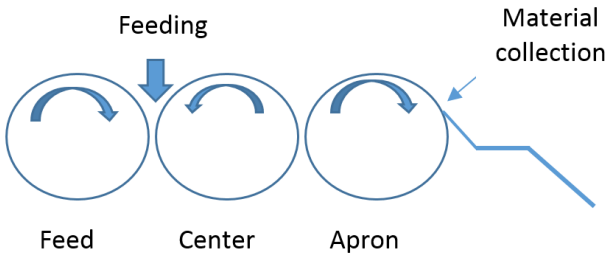

Figure 2-3. The schematic of calendering mechanism

2.2.3 High-shear mixing

A high-shear mixer, which has also been used for dispersing NPs within resins, consists of a driven vertical shaft, together with a high-shear disk type blade. The blade rotates at up to 5000 rpm, which creates a radial flow pattern within a stationary vessel. As shown in Figure 2-4, the rotating blade creates a vortex that pulls in the material within the vessel toward the blades sharp edges. The blades surfaces then mechanically tear apart the particles, thereby reducing their size, and at the same time dispersing them throughout the resin [4].

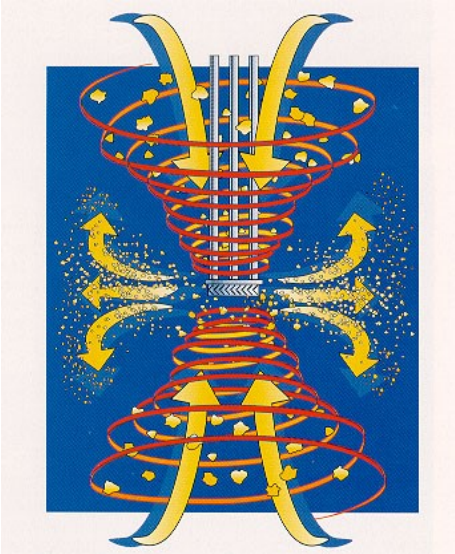

Figure 2-4. The vortex created by rotating blades [4]

2.3 Multi-functionality of carbon NP composites

2.3.1 Mechanical properties

Numerous researchers have reported enhancement in the stiffness of polymers by addition of carbon NPs to various resins [5, 6]. It is believed that the increase in stiffness

of polymers that include NPs is due to the constraint imposed on molecular mobility of the polymer chains. In fact, NPs that usually have much greater stiffness than their host polymers are nested within the spaces that exist among the polymer chains, thus reducing chains flexibility [7].

Considerable efforts have been expended by researchers with the aim of identifying or developing accurate and reliable models for predicting the stiffness of nanocomposites. The Halpin-Tsai model is one of the most commonly used models for predicting the Young's modulus of the composites. According to this model, the maximum attainable Young's modulus of a composite with uniform fiber distribution and perfect fiber/matrix bond is given by:

$$E_C = \left(\frac{3}{8} \frac{1+2(\lambda)\eta_l V_f}{1-\eta_l V_f} + \frac{5}{8} \frac{1+2\eta_T V_f}{1-\eta_T V_f} \right) E_m \qquad (2\text{-}1)$$

in which

$$\eta_l = \frac{E_f / E_m - 1}{E_f / E_m + 2(\lambda)}, \quad \eta_T = \frac{E_f / E_m - 1}{E_f / E_m + 2}, \quad \lambda = l_f / d_f \qquad (2\text{-}2)$$

where E_C is the Young's modulus of the composite, l_f, d_f and E_f are the length, average diameter and Young's modulus of the reinforcement, E_m is the Young's modulus of the matrix, and V_f is reinforcement volume content.

Figure 2-5 shows the accuracy of Halpin-Tsai's model against their experimental results for epoxy/CNT nanocomposites. As seen, there is a noticeable difference between the experimental and theoretically predicted results. This is mainly due to the underlying

assumptions used in developing the model (i.e., uniformity in distribution of reinforcement, perfect bond between matrix and reinforcement, and the absence of any void in the matrix). As a result, various researchers have proposed modifications to the model in order to improve its predictive accuracy when applied to nanocomposites.

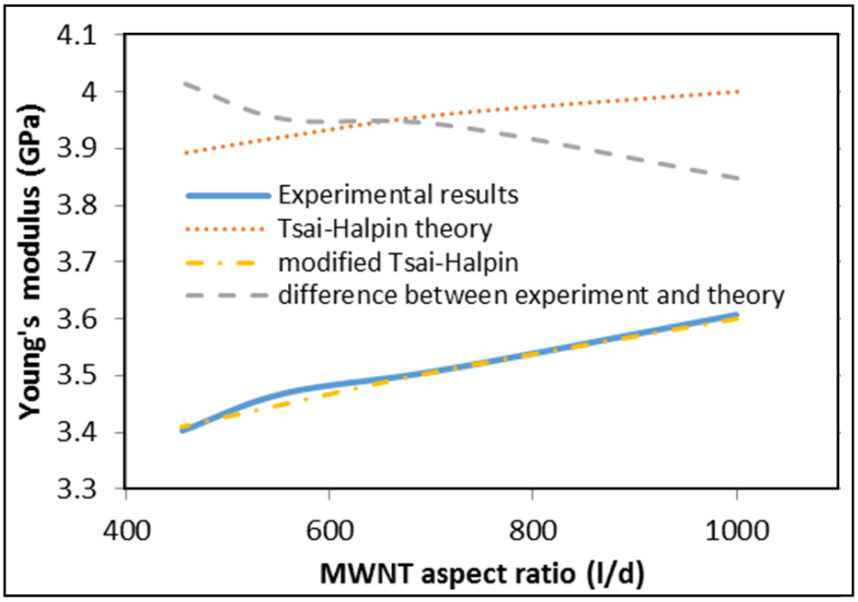

Figure 2-5. Comparison of the experimental results and theoretical predictions of the Young's modulus of MWNT reinforced nanocomposites [8]

In general, failure in FRPs is categorized as: (i) interfacial failure, in which a crack would initiate at the adhesive/fiber interface and subsequently propagates; (ii) cohesive failure, in which a crack would initiate and propagate within the matrix. Either of these two scenarios could occur, depending on the interfacial bond strength, fracture toughness of the adhesive, and presence of probable voids and microcracks within the adhesive. In the case of cohesive failure, the fracture toughness of adhesive is the key factor that governs the mechanical strength, in particular, if micro-cracks are present within the adhesive.

The use of NPs for enhancement of the fracture toughness of resin has been reported by several researchers [5, 9]. The effect of inclusion of different carbon-based NPs on the fracture toughness of an epoxy resin under different fracture mode was investigated. Figure 2-6 shows the experimental results obtained for pure epoxy and three types of nanocomposites. It is seen that the value of $K_{eff,}$ changes from mode-I to that of mode-II in the cases of both the neat epoxy and nano-diamond/epoxy nanocomposite. However, by adding the carbon nano fibers (CNF) and graphite oxide reinforcements, the maximum value of K_{eff} occurs under a mixed-mode state, and then as the fracture state transfers from the mixed-mode to the mode-II state, the enhancement of K_{eff} in nanocomposites reinforced with CNF and GNP decreases gradually [10].

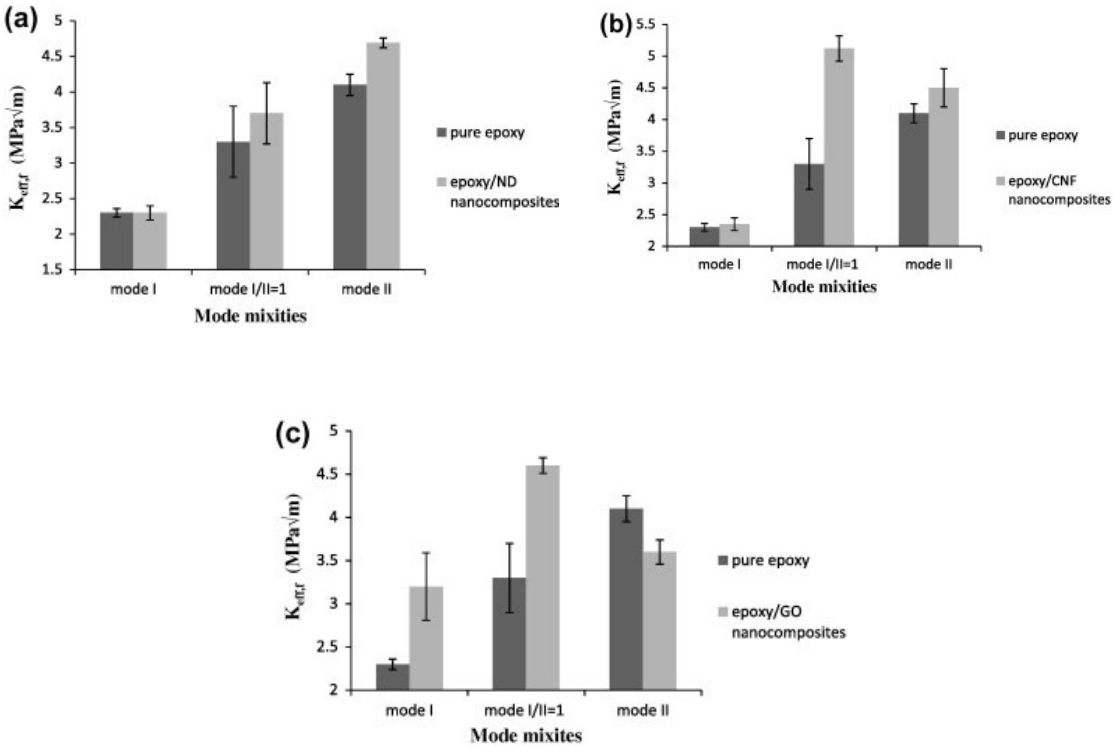

Figure 2-6. Effective fracture resistance, K_{eff} for pure epoxy and for nanocomposites reinforced with (a) ND, (b) CNF and (c) GO [11]

Burkholder et al. [12] investigated the effectiveness of CNTs as an epoxy adhesive additive for bonding steel to composite and composite to composite materials. The results, shown in Figure 2-7, revealed that the additions of CNTs to epoxy adhesive enhanced the fracture toughness of their adhesively bonded joints. However, higher contents of CNTs could decrease the properties by a significant margin (likely due to agglomeration).

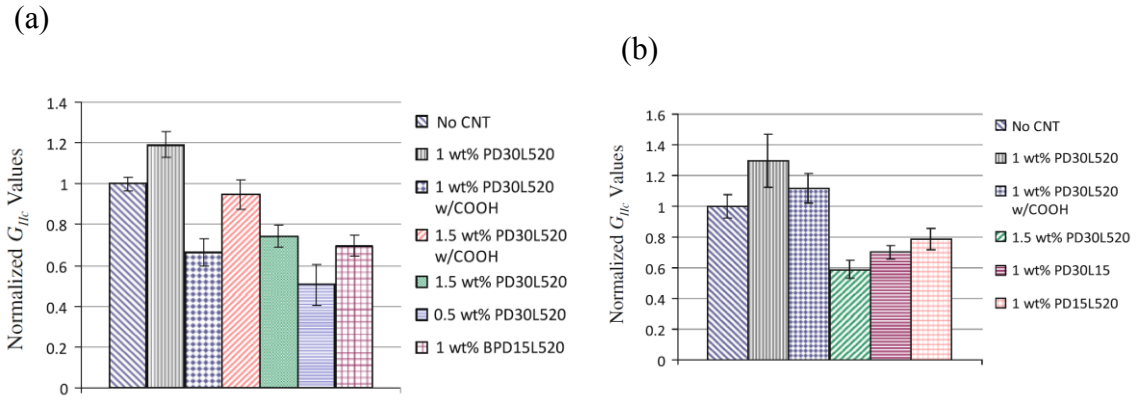

Figure 2-7. Normalized values of fracture energy, G_{IIc}, for (a) steel-composite and (b) composite-composite adhesive joints (the codes in the legend refer to various dimensions and functionality of CNT as described in reference) [12]

Two principal mechanisms that contribute to enhance the fracture toughness of polymers reinforced with NPs are: (i) crack deviation, and (ii) crack bridging. Either of these mechanisms may be dominant over the other one, depending on the geometry of NPs and loading states. For instance, in nanocomposites hosting CNTs of long cylindrical shapes, the main energy dissipating mechanism is the crack bridging. This is because CNTs have very small diameters compared to their lengths, and thus, the crack deviation might take a secondary role [7].

The crack deviation mechanism can be identified by investigation of the roughness of fracture surfaces of nanocomposites (i.e., the higher is the roughness of the fracture

surface, the more the crack would be deviated from its original plane). Figure 2-8 shows the increase in fracture surface roughness as a function of CNT wt% content. On the other hand, detection of crack bridging mechanism requires high magnification micrographs. The bridging mechanism plays an important role in improving the fracture toughness of composites. When a NP bridges two fracture surfaces, it may either fracture or pull out from one of the surfaces, depending on the embedded length, interfacial strength, angle to fracture surface and flexibility of the NP. A micrograph illustrating the bridging mechanism in CNT/epoxy adhesive is shown in Figure 2-9

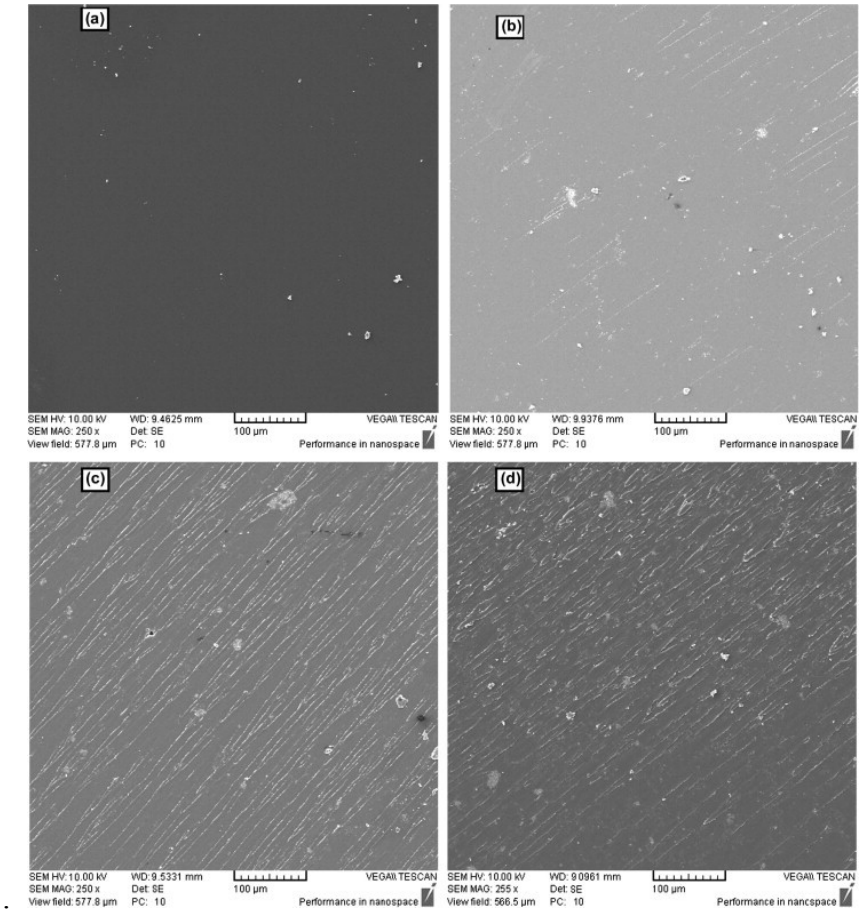

Figure 2-8. Mode-I fracture surfaces of (a) neat epoxy (b) 0.1 wt.% CNT/epoxy (c) 0.5 wt.% CNT/epoxy (d) 1 wt.% CNT/epoxy near the pre-crack tip. The direction of crack right to bottom left [13]

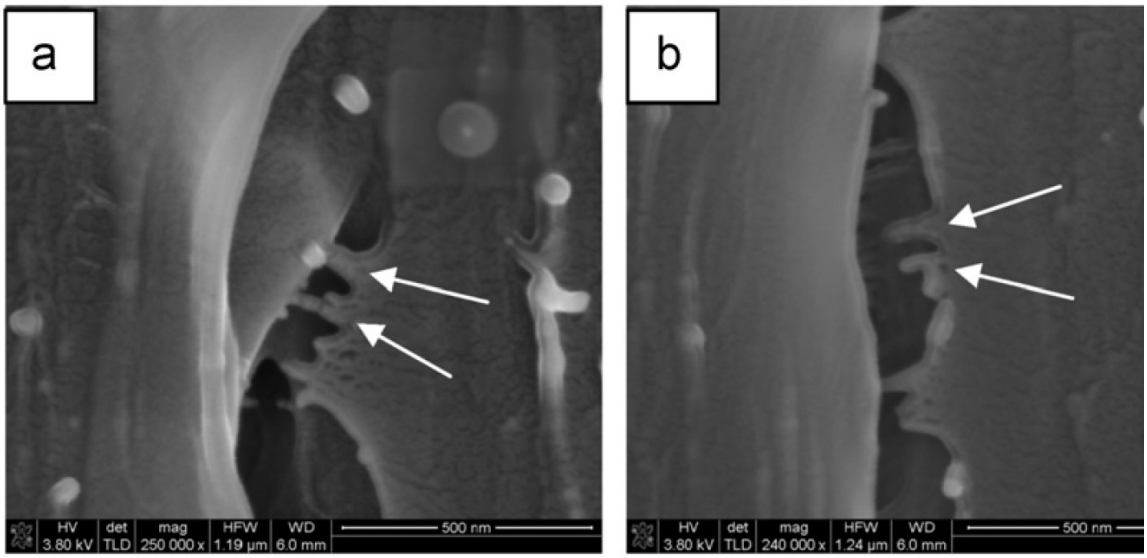

Figure 2-9. Micrographs showing the participation of CNTs, marked with white arrows, while bridging and (b) as being pulled-out [14]

2.3.2 Electrical properties

Common polymers used in structural application are not electrically conductive. In contrast, some types of NPs, especially carbon NPs, are superconductive. Therefore, addition of an appropriate amount of such NPs to polymers could significantly decrease their electrical resistance (also referred to as the "percolation threshold"). Generally, there are two different types of thresholds, namely: static and kinetic thresholds. The static percolation threshold refers to a situation when randomly distributed filler particles form the percolating paths. In the kinetic percolation, the particles are free to move, thereby forming a conducting network at much lower particle concentrations [15]. Different parameters, however, could affect the resulting electrical conductivity, including the fabrication method, matrix-wettability of filler, and filler dimensions. It is noteworthy to

mention that while an effective method of NP dispersion would result in better mechanical properties, it may lower nanocomposites' electrical conductivity [16].

The DC electrical conductivity of CNT/epoxy for different NP contents was measured by Ayotallahi et al. [8]. As seen in Figure 2-10, the resistivity decreases dramatically as the filler content approaches the value resulting into the electrical percolation threshold. Moreover, the conductive network of the CNTs is formed at approximately 0.25 wt%. Similar results were also reported by Yu et al. [17] and Wang et al. [18] for the surface electrical resistivity of epoxy adhesives.

Furthermore, several analytical and semi-empirical models have been proposed for predicting the electrical conductivity of nanocomposites. Some examples are the "exclude volume model" [19], Lu and Mai's model [20] and a recently proposed model based on the average inter-particle distance [21].

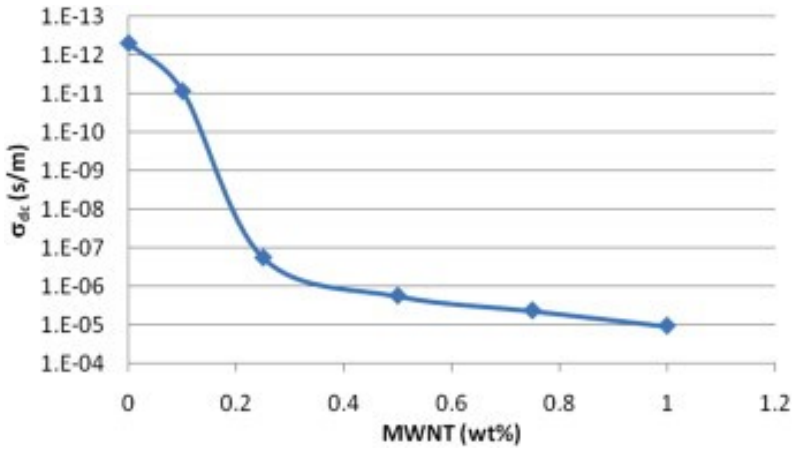

Figure 2-10. Electrical resistivity of epoxy/CNT nanocomposites [8]

Electrically conductive adhesives could have a variety of applications, including magnetic painting, circuit boards, damage sensing and solar cells [22, 23]. In addition to

the mentioned applications, the use of conductive adhesive for structural health monitoring purposes has recently attracted considerable attention. Lim et al. [24] used a conductive CNT modified adhesive (in addition to an acoustic emission sensor) to monitor the effect of adherend surface treatments on the failure mechanism of a single lap joint (SLJs). The results are shown in Figure 2-11. For their untreated adherend, the electrical resistance increased in a step-like manner, which represented the sudden failure of adhesive. A potential weak interaction between the steel and adhesive could result in a low overall shear strength of the ABJ, while the change in the resistance (i.e., the jumps in the electrical resistance) could signify the onset of a damage long before the specimen reaches its ultimate shear strength. On the other hand, in case of saline-treated adherend, the resistance increases gradually throughout the loading regime, which would indicate that a progressive damage event is occurring during the loading cycle, possibly due to presence of damage in the adhesive layer.

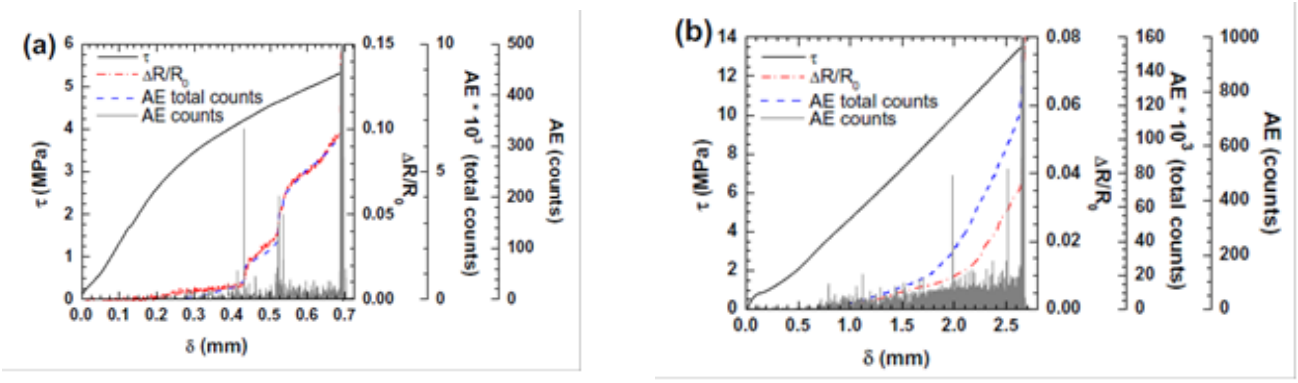

Figure 2-11. Mechanical, electrical and acoustic emission responses of (a) untreated specimens (b) saline-treated specimens (where τ is the shear stress and δ is the displacement)

2.3.3 Thermal properties

Inclusion of NPs in adhesives could also alter the thermal properties of adhesives, including their thermal conductivity and coefficient of thermal expansion (CTE). For instance, the thermal conductivity of CNTs at room temperature can be as high as 6600 W/m^oK. Therefore, the thermal conductivity of the host polymer reinforced with these NPs would be significantly altered. The main applications of thermally conductive adhesives are in heat sink bonding, potting/encapsulating sensors and in fabrication of power semiconductors.

2.4 Effect of carbon NPs on the performance of adhesively bonded joints

Essentially, two decades of research has been devoted toward developing NP-reinforced adhesives. Achieving higher mechanical properties for adhesively bonded joints (ABJs) has been the main objective of a majority of the studies conducted in this field. The increase in the mechanical strength for ABJs can be more accurately described as the increase in their peel and shear strengths. Several researchers have studied the effects of inclusion of different types of NPs on the shear and peel strengths of adhesives. Table 2-1 and Table 2-2 have been prepared to provide a summary of some of the most notable studies, and to compare their findings related to the enhancement of peel and shear strengths, respectively. As can be seen, a wide range of results has been reported in regard to the influence of NPs on the shear and peel strengths of adhesives. The reported results with an astonishing range from 75% improvement to 30% degradation in the properties. This enormous range stems from a large number of parameters that influence the final results, including the manufacturing-related factors, quality of NPs, particle size, and

functionality of the NPs, to mention a few. However, more consistent results could be expected by elimination of the undesirable perturbations.

Table 2-1. Influence of carbon NPs on the peel strength of the host adhesives

Adhesive	NPs	Adherends	NP wt%	Strength Increase (%)	Reference
PVAc	CNT	Glass/Steel	0.1	7.9	[18]
			0.3	26.3	
			1	5.3	
Epoxy	CNT	White iron	1	29	[25]

Table 2-2. Influence of carbon NPs on the shear strength of the host adhesives

Adhesive	NPs	Adherends	NP wt%	Strength Increase (%)	Reference
Epoxy	CNT	Copper	0.8	-19	[26]
Polyimide	MWNT	Steel	0.5	8	[27]
			1	23	
			1.5	4	
Epoxy	MWNT	Carbon/epoxy	1	24	[28]
			5	43	
PVAc	Graphene	Wood	0.75	36	[29]
			1.5	136	
			3	309	
PVAc	Graphene	Beech veneer	0.1	41	[1]
			0.15	52	
			0.3	49	
			0.5	38	
			1	15	
			2	8	
Epoxy	Carbon black	Glass/epoxy	0.5	17	[30]
			1	40	
			1.5	46	
			2	38	
			3	9	
Epoxy	Carbon black	Glass/epoxy composite,	0.5	14	[31]
			1	28	

			1.5	13	
			2	9	
			3	2	
Epoxy	CNF	Carbon fiber/epoxy	0.25	-3	[32]
			0.5	5	
			1	-6	

The durability of ABJs could be significantly reduced by environmental stresses arising from the moisture and difference in temperature. The absorbed fluids may plasticize and induce relaxation of adhesives, as well as degrading adhesive's mechanical properties; the latter is considered to be one of the primary causes of failure of ABJs [33].

The durability of a CNT reinforced epoxy adhesive bonded aluminum alloy joints utilizing the Boeing wedge test [34] (see Figure 2-12) subjected to humid conditions was studied by Yu et al [35]. The effects of the CNT content on the durability and failure mode of the joints were assessed as well in [35]. The wedge test creates a relatively high stress concentration at or near the interface, thus increasing joint's sensitivity to environmentally caused degradation. Therefore, the test is usually used to provide quantitative durability data for ABJs.

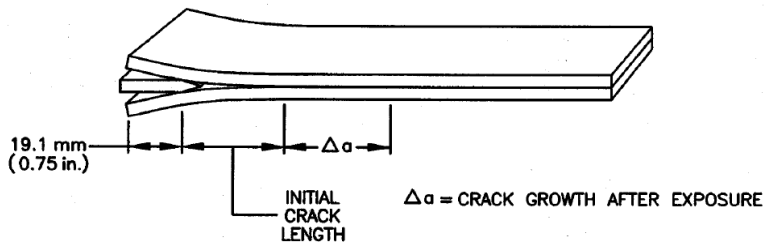

Figure 2-12. Configuration of the wedge-test specimen [34]

As shown in Figure 2-13, for the specimens bonded with CNT-reinforced epoxy, the initial crack length depended highly on the CNTs' weight fraction. The initial crack

length decreased when CNTs' weight fraction was increased from 0 to 1 wt%, but then it increased only slightly as the CNT weight fraction increased from 1 to 5 wt%. The initial crack length for the joint with epoxy filled with 0.5 wt% CNTs was 70.3% lower in comparison to that of the joint made with neat epoxy. However, the best results were obtained for the joint made with epoxy containing 1 w% CNTs; obviously, the addition of CNTs into the epoxy significantly improved the bond strength of the ABJs.

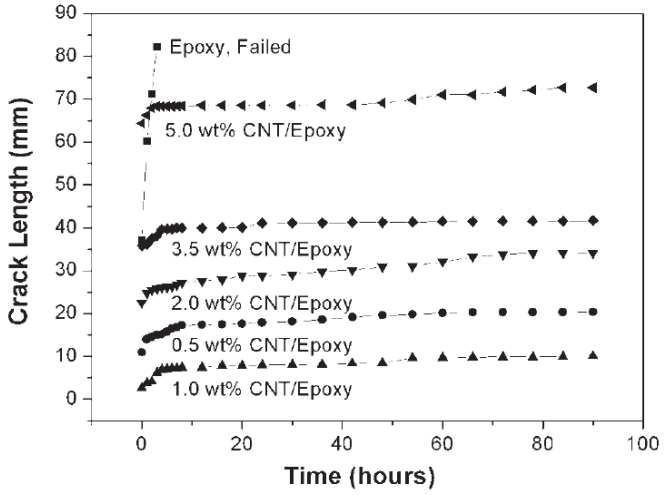

Figure 2-13. Crack propagation length of the CNT-reinforvced epoxy adhesive joints as a function of immersion time in 60 ^{o}C water [35]

Recently, the effects of different NPs and loading rates on the ultimate strength of adhesively bonded single lap joints (SLJs) have also been reported by Soltannia and Taheri [36]. The average ultimate shear strength of SLJs with graphite adherends was increased by as much as 32% (relative to the neat adhesive), when SLJs were subjected to a high loading rate. The observed increase in average was also quite significant (average of 26% improvement), when their SLJs were tested under the quasi-static loading rates.

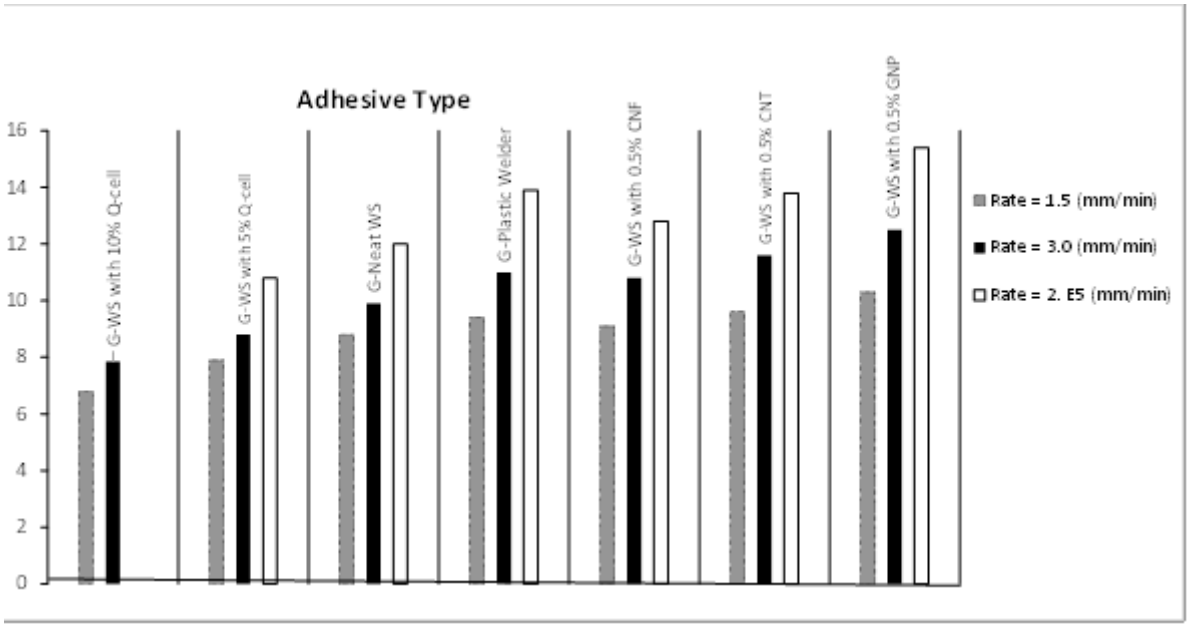

Figure 2-14. Effect of loading rate on nano-reinforced adhesively bonded single-lap joints with graphite/epoxy adherends [36]

A large volume of information related to the change in the stiffness, and the details in the response of an epoxy resin reinforced with various NPs, bonding both glass- and carbon-reinforced epoxy adherends have also been reported by Soltannia and Taheri [81].

2.5 References

[1] Pinto AM, Martins J, Moreira JA, Mendes AM, Magalhães FD. Dispersion of graphene nanoplatelets in poly(vinyl acetate) latex and effect on adhesive bond strength. Polymer International. 2013;62:928-35.

[2] Technology THU. Ultrasonic lab devices and industrial processors, www.hielscher.com Germany2014.

[3] Yasmin A, Abot JL, Daniel IM. Processing of clay/epoxy nanocomposites by shear mixing. Scripta Materialia. 2003;49:81-6.

[4] H. Charles Ross & Son Company, NY, High speed dispersers, http://www.pharmaceuticalonline.com 2014.

[5] Ayatollahi MR, Shadlou S, Shokrieh MM. Mixed mode brittle fracture in epoxy/multi-walled carbon nanotube nanocomposites. Engineering Fracture Mechanics. 2011;78:2620-32.

[6] Shokrieh MM, Kefayati AR, Chitsazzadeh M. Fabrication and mechanical properties of clay/epoxy nanocomposite and its polymer concrete. Materials & Design. 2012;40:443-52.

[7] Ayatollahi MR, Shokrieh MM, Shadlou S, Kefayati AR, Chitsazzadeh M. Mechanical and electrical properties of epoxy/multi-walled carbon nanotube/nanoclay nanocomposites. Iran Polym J. 2011;20:835-43.

[8] Ayatollahi MR, Shadlou S, Shokrieh MM, Chitsazzadeh M. Effect of multi-walled carbon nanotube aspect ratio on mechanical and electrical properties of epoxy-based nanocomposites. Polymer Testing. 2011;30:548-56.

[9] Benzaid R, Chevalier J, Saâdaoui M, Fantozzi G, Nawa M, Diaz LA, et al. Fracture toughness, strength and slow crack growth in a ceria stabilized zirconia–alumina nanocomposite for medical applications. Biomaterials. 2008;29:3636-41.

[10] Shadlou S, Ahmadi-Moghadam B, Taheri F. Nano-Enhanced Adhesives. Reviews of Adhesion and Adhesives. 2014;2:371-412.

[11] Shadlou S, Alishahi E, Ayatollahi M. Fracture behavior of epoxy nanocomposites reinforced with different carbon nano-reinforcements. Composite Structures. 2013;95:577-81.

[12] Burkholder GL, Kwon YW, Pollak RD. Effect of carbon nanotube reinforcement on fracture strength of composite adhesive joints. Journal of Materials Science. 2011;46:3370-7.

[13] Ayatollahi M, Shadlou S, Shokrieh M. Fracture toughness of epoxy/multi-walled carbon nanotube nano-composites under bending and shear loading conditions. Materials & Design. 2011;32:2115-24.

[14] Gude MR, Prolongo SG, Gómez-del Río T, Ureña A. Mode-I adhesive fracture energy of carbon fibre composite joints with nanoreinforced epoxy adhesives. International Journal of Adhesion and Adhesives. 2011;31:695-703.

[15] Bauhofer W, Kovacs JZ. A review and analysis of electrical percolation in carbon nanotube polymer composites. Composites Science and Technology. 2009;69:1486-98.

[16] Gojny FH, Wichmann MHG, Fiedler B, Kinloch IA, Bauhofer W, Windle AH, et al. Evaluation and identification of electrical and thermal conduction mechanisms in carbon nanotube/epoxy composites. Polymer. 2006;47:2036-45.

[17] Yu S, Tong MN, Critchlow G. Use of carbon nanotubes reinforced epoxy as adhesives to join aluminum plates. Materials & Design. 2010;31:S126-S9.

[18] Wang T, Lei CH, Dalton AB, Creton C, Lin Y, Fernando KAS, et al. Waterborne, Nanocomposite Pressure-Sensitive Adhesives with High Tack Energy, Optical Transparency, and Electrical Conductivity. Advanced Materials. 2006;18:2730-4.

[19] Celzard A, McRae E, Deleuze C, Dufort M, Furdin G, Marêché JF. Critical concentration in percolating systems containing a high-aspect-ratio filler. Physical Review B. 1996;53:6209-14.

[20] Lu C, Mai YW. Influence of aspect ratio on barrier properties of polymer-clay nanocomposites. Physical review letters. 2005;95:088303.

[21] Li J, Kim J-K. Percolation threshold of conducting polymer composites containing 3D randomly distributed graphite nanoplatelets. Composites Science and Technology. 2007;67:2114-20.

[22] Kim H, Miura Y, Macosko CW. Graphene/polyurethane nanocomposites for improved gas barrier and electrical conductivity. Chemistry of Materials. 2010;22:3441-50.

[23] Choudalakis G, Gotsis AD. Permeability of polymer/clay nanocomposites: A review. European Polymer Journal. 2009;45:967-84.

[24] Lim AS, Melrose ZR, Thostenson ET, Chou T-W. Damage sensing of adhesively-bonded hybrid composite/steel joints using carbon nanotubes. Composites Science and Technology. 2011;71:1183-9.

[25] Hedia HS, Allie L, Ganguli S, Aglan H. The influence of nanoadhesives on the tensile properties and Mode-I fracture toughness of bonded joints. Engineering Fracture Mechanics. 2006;73:1826-32.

[26] Li J, Lumpp JK. Electrical and mechanical characterization of carbon nanotube filled conductive adhesive. Aerospace Conference, 2006 IEEE: IEEE; 2006. p. 6 pp.

[27] Saeed MB, Zhan M-S. Adhesive strength of nano-size particles filled thermoplastic polyimides. Part-I: Multi-walled carbon nano-tubes (MWNT)–polyimide composite films. International Journal of Adhesion and Adhesives. 2007;27:306-18.

[28] Hsiao K-T, Alms J, Advani SG. Use of epoxy/multiwalled carbon nanotubes as adhesives to join graphite fibre reinforced polymer composites. Nanotechnology. 2003;14:791.

[29] Khan U, May P, Porwal H, Nawaz K, Coleman JN. Improved Adhesive Strength and Toughness of Polyvinyl Acetate Glue on Addition of Small Quantities of Graphene. ACS Applied Materials & Interfaces. 2013;5:1423-8.

[30] Park SW, Kim BC, Lee DG. Tensile Strength of Joints Bonded With a Nano-particle-Reinforced Adhesive. Journal of Adhesion Science and Technology. 2009;23:95-113.

[31] Park SW, Lee DG. Strength of Double Lap Joints Bonded With Carbon Black Reinforced Adhesive Under Cryogenic Environment. Journal of Adhesion Science and Technology. 2009;23:619-38.

[32] Prolongo SG, Gude MR, Sanchez J, Ureña A. Nanoreinforced Epoxy Adhesives for Aerospace Industry. The Journal of Adhesion. 2009;85:180-99.

[33] Davis GD. Durability of adhesive joints. Handbook of adhesive technology. 2003:273.

[34] ASTM-D3762-03. Standard Test Method for Adhesive-Bonded Surface Durability of Aluminum (Wedge Test). American Society for Testing and Materials: Philadelphia.2010.

[35] Yu S, Tong MN, Critchlow G. Wedge test of carbon-nanotube-reinforced epoxy adhesive joints. Journal of Applied Polymer Science. 2009;111:2957-62.

[36] Soltannia B, Taheri F. Static, Quasi-Static and High Loading Rate Effects on Graphene Nano-Reinforced Adhesively Bonded Single-Lap Joints. International Journal of Composite Materials. 2013;3:181-90.

Chapter 3: Effect of Processing Parameters on the Structure and Multi-Functional Performance of Epoxy/GNP Nanocomposites

B Ahmadi-Moghadam and F. Taheri

Published in the Journal of Materials Science, Volume 49, Issue 18, PP 6180-6190, 2014

3.1 Abstract

Graphene nanoplatelets (GNPs) are recently developed nanoparticles that are formed by stacks of short disk-like layers of graphite. They cost considerably less than their carbon nanotubes (CNTs) counterparts, and can be potentially used to generate multi-functional material systems. However, there are significant number of structural differences between GNPs and CNTs. It is therefore timely to review and optimize the current processing techniques used for generating GNP-nanocomposites. In this research, a scalable shear mixing approach (i.e., a three-roll mill) is utilized for achieving uniform dispersion of different fractions of GNPs in an epoxy resin. Then, the stiffness, electrical and thermal conductivity and linear coefficient of thermal expansion of the resulting nanocomposites were evaluated. The as-processed nanocomposites exhibited significant improvement in their thermal properties, but a moderate increase in stiffness. The electrical percolation threshold of the nanocomposite occurred at higher concentration of GNP than that predicted by the available micromechanical models. This is attributed to the change in size of GNPs, which occurs as a result of manufacturing process, as observed by scanning electron microscopy.

3.2 Introduction

Graphene nanoplatelets (GNP) are a class of 2D graphitic nanofillers, which are formed by stacks of graphite layers bonded to one another by weak Van der Waals forces [1]. In addition to possessing impressive mechanical and thermal properties as the classical

2D nanofillers such as nanoclays do, GNPs offer superior electrical properties. As a result, they are considered as distinctive nanofillers, since they can be utilized to improve the mechanical and electrical properties of polymers [2-4]. Furthermore, in contrast to carbon nanotubes (CNTs), whose production requires intricate manufacturing processes, thus making them relatively very costly [5, 6], highly pure GNPs can be derived from the available and plentiful sources of natural graphite, using the conventional methods [7, 8]. Accordingly, utilization of GNPs in various engineering applications could be rendered as more cost-effective than higher cost CNTs.

Several researches have experimentally assessed various beneficial effects of GNPs when added to various resins [9-13]. As a result, several theoretical and semi empirical models have been developed for predicting the elastic modulus and electrical conductivity of GNP-nanocomposites [14, 15]. The results have revealed that in a majority of cases, the elastic modulus of GNP-nanocomposites could be improved with addition of GNPs in resins, while however their ultimate strength and strain would be degraded [13]. It has also been demonstrated that the thermal conductivity of GNP-nanocomposites could be significantly increased, even when small amount of GNPs is included in resins [12, 16]. Moreover, it has been observed that the electrical resistivity of a GNP-nanocomposite would abruptly decrease when the concentration of GNP in the resin exceeds a specific value, referred to as the “electrical percolation threshold” [13, 15].

Dispersing GNPs in resin is the main challenge of processing a nanocomposite, because the optimum enhancement in the properties of a resin could be attained provided that the nanoparticles are uniformly dispersed within resin. Various dispersion techniques and processing, and their resultant effects on the properties of CNT-nanocomposite, have

been previously studied [17, 18]. The collective results have revealed that in general very large amounts of energy is required to uniformly disperse CNT particles in resins. This is due to the generation of large interaction forces amongst the CNTs, which should be overcome, in turn increasing the production cost, especially if one wants to engage in industrial scale applications.

When the processing of GNP-nanocomposites is concerned, one sees that most researchers have essentially adopted CNT related processing methods for preparation of GNP reinforced resins. Processes such as the high shear mixing [13], ultrasonication and three-roll mill calendering [16] are the commonly adopted methods. It should be note that GNPs and CNTs have several distinct inherent differences, including the interaction force among a GNP's stratified layers, geometry, and flexural stiffness. As a result, it is believed that the adoption of a dispersion method that is commonly used for production of CNT-nanocomposites to process GNP-nanocomposites could exhibit adverse effects on the properties of the GNP-nanocomposites. Therefore, a better understanding of the relationship between processing techniques and resulting GNP-nanocomposite properties is required for reducing the fabrication cost, thus facilitating industrial-scale manufacturing of such nanocomposites.

As mentioned earlier, calendering is the most promising method for dispersion of nanoparticles. One of the most critical parameters that controls the quality of resulting nanocomposite in this technique is the rollers' gap distance. To the best of authors' knowledge, the effect of processing on the GNP structure, and the resulting GNP-nanocomposite properties have not yet been explored. Moreover, our literature review revealed scarcity of research work in reference to the coefficient of thermal expansion

(CTE) of GNP-reinforced nanocomposites. The CTE of composite materials governs two important phenomena: (i) the magnitude of the thermal residual stresses that develops during fabrication of the polymer-based composite materials and (ii) those stresses that could be developed as a result of an applied thermal field onto the materials during their service. The CTE of neat epoxy is approximately $76x10^{-6}$ /^{o}C, while the CTE of E-glass fiber is around $5.1x10^{-6}$ /^{o}C. Thus, the magnitude of the resulting expansion and contraction of the resin would be greater than those of the fibers it is hosing during the heating and cooling cycles of the curing process (by roughly 14 times). This phenomenon would in turn create large magnitudes of residual stress.

In this study, the as-received commercially available GNPs were dispersed in an epoxy resin using a three-roll mill. The rollers' gap was set 20 μm, 40 μm and 60 μm in order to investigate gap distance effect on the nanocomposite properties. The elastic modulus, electrical resistivity, thermal conductivity and CTE of the resulting nanocomposites were assessed experimentally. The integrity of the various available models (i.e., Halpin-Tsai and others) for estimating the mechanical and electrical properties of such nanocomposites was also examined.

A comprehensive statistical study was also conducted on the influence of GNP size effect on the fracture surfaces of the nanocomposites using the scanning electron microscopy; this was done to further explore the effect of different preparation processes on the resulting GNP-nanocomposites.

It should be noted that in all part of this research (i.e., graphs and calculations), the volume fraction of the particles has been converted to percent weight. This is, because one could

easily weight nanoparticles, and that the weight percent provides more sense as opposed to the volume fraction of the particles.

3.3 Experimental Investigation

3.3.1 Materials

Araldite LY564 (Bisphenole-A epoxy resin) with density of 1.2 g/cm^3 was used with Aradure 2954 hardener (a cycloaliphatic polyamine hardener). This hot-cure and low viscosity epoxy system is available through the Huntsman (west Point, GA). The GNP nanoparticles with density of 2.0 g/cm^3 used in this research were obtained from XG Science (Lansing, MI), having an average thickness, t, of 7 *nm* and an average particle diameter, D, of 25 μm (see Figure 3-1a and b). As shown in Figure 3-1b, the GNP particles are assumed to be a disk-like geometry with diameter, D, and thickness, t in all the forthcoming micromechanical model discussions.

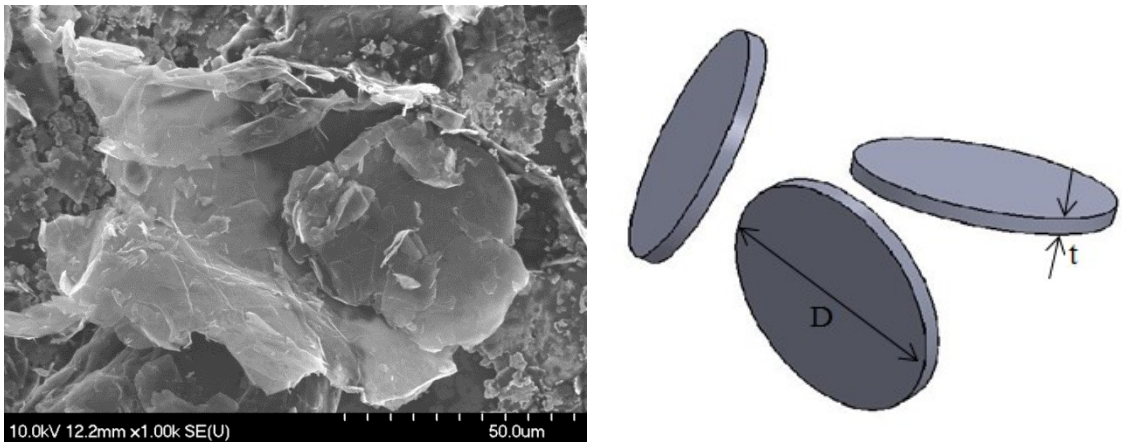

(a) (b)

Figure 3-1. X-GnP-25 (a) SEM image; (b) schematic of the idealized GNP

3.3.2 Specimens preparation

To fabricate the GNP-nanocomposite reinforced epoxy specimens (GNPRE), firstly, the appropriate amount of GNP were distributed into the resin using a mechanical

stirrer operated at 2000 rpm for 15 minutes. Then, the mixed GNP-resin slurry was further processed through a three-roll mill (Torrey Hill Technology, San Diego, CA). The rollers' rotating speeds were kept constant at 174, 84 and 31 rpm for the apron, middle and feed rollers, respectively. The dispersion of GNP was promoted with three different roller gap distances of 20, 40 and 60 μm, for the considered GNP weight percent in resin (i.e., 0.5, 1, 1.5 and 2 wt%).

The dispersion process was repeated seven times for each concentration of GNP. After the dispersion process, the appropriate amount of hardener was added to the resin and mixed using the mechanical stirrer set at 100 rpm for 10 minutes. The mixture was degassed in a chamber at -28 *in-Hg* for 30 minutes. Finally, the mixture was poured in the molds and cured at 100 ℃ for half an hour and then post-cured at 160 ℃ for 8 hours.

3.3.3 Test methods

Dog-bone shaped tensile coupons made from the neat resin and GNPRE with dimensions of specimen type V of ASTM D638 standard [19]. The specimens were subjected to tensile loading to evaluate the stiffness of each specimen. An Instron servo-hydraulic universal test machine (model 8500^{+}) with a 100 *kN* load cell was used to run the tests. A laser extensometer was used to measure the precise gauge length deformation of the specimens. The tests were conducted at a speed of 2 *mm/min*. At least five specimens were tested for each case.

To measure the electrical resistivity of GNPRE, rectangular specimens with dimension of 60 *mm* × 10 *mm* were cut from a 3 *mm* thick bar casted with the dimensions of 100 *mm* × 20 *mm*. The electrical resistivity of the neat epoxy and GNPRE specimens with less than 1 wt% GNP was measured through the thickness of specimens as

recommended by ASTM D257 [20]. For the remaining specimens, the electrical conductivity was assessed through the axial axes of the specimens as per ASTM D4496 [21].

The thermal conductivity of the GNPRE specimens was assessed using a physical property measurement system, PPMS (Quantum Design San Diego, CA). To fabricate the specimens required for evaluation of the thermal conductivity, the samples used to evaluate the electrical resistivity were cut into cuboid shaped specimens with 3 *mm* thickness and 5 to 7 mm^2 cross section. All the specimens were tested at 25 ℃ and 80 ℃ under steady sate condition (as described in [22]), in order to evaluate the thermal conductivity of GNPREs at room and elevated temperatures.

The CTE measurements of GNPRE were carried out using a differential dilatometer (DIL 420 PC, NETZSCH GmbH Burlington, MA), according to ASTM E228 [23]. Rectangular bar-shaped specimens, with approximate dimensions of 3 *mm* × 6 *mm* × 25 *mm,* were made from GNPREs having various GNP weight-contents. The end surfaces of each specimen were machined and polished to ensure the surfaces were parallel, so that they could be positioned precisely within the measurement probes of the instrument. The CTE was measured at 80 ℃ for all specimens.

3.4 Test results

3.4.1 Tensile modulus

Figure 3-2 shows the average values of the tensile elastic modulus of each group of GNPRE specimens. As expected, inclusion of GNPs in the resin improved resin's stiffness. The highest Young's modulus was obtained when the gap distance was set at 40 μm. The

GNPREs made by gap distances of 20 µm and 60 µm ranked second and third, respectively. As seen, while the stiffness of GNPREs were increased for the gap distances of 20 and 40 µm compared to that of the neat epoxy resin, the stiffness of GNPREs were degraded when the gap distance of 60 µm was used.

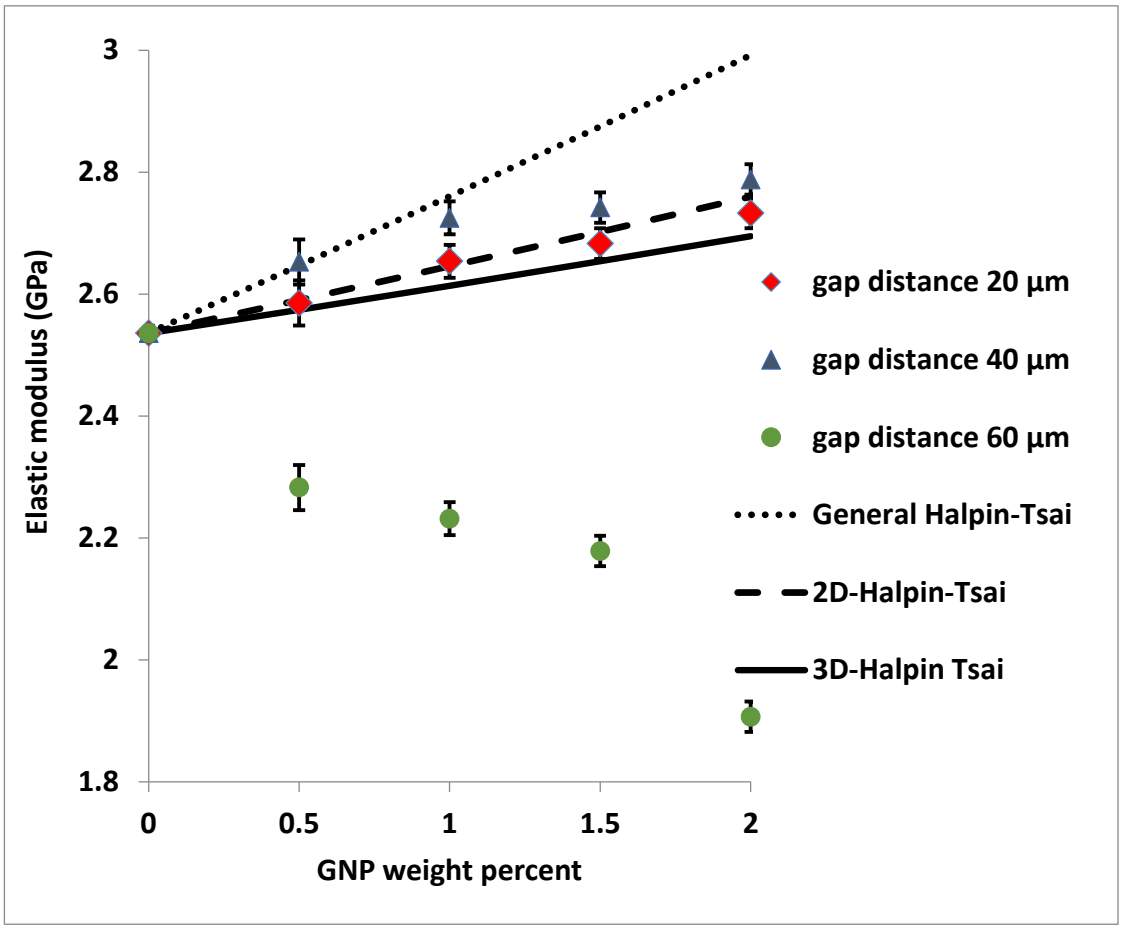

Figure 3-2. Variation in the elastic modulus of GNPRE as a function of roller gap distance and GNP content

Micromechanical models, such as the well-known modified Halpin-Tsai, have been utilized by several researchers for predicting the mechanical properties of nanocomposites (for more details see [13]). However, such models are idealistic models and do not consider factors like the agglomeration, non-perfect interfaces between GNPs and matrix, bending of GNP in the matrix, flaws in the GNP structure and presence of voids

in nanocomposites. The comparison of the values of the elastic modulus predicted by the modified Halpin-Tsai (both 2D and 3D versions) and those evaluated experimentally are illustrated in Figure 3-2. As can be seen, the general Halpin-Tsai model overestimates the elastic modulus of the GNPRE. This is because this model assumes that the GNP are perfectly aligned and uniformly dispersed. On the other hand, the values predicted by the modified Halpin-Tsai (which account for the 2D random orientation of fillers) better agree with the experimental results.

To further explore the influence of the roller gap distances on the properties of the GNPRE, the fracture surfaces of the GNPREs were examined using a field emission scanning electron microscope, FE-SEM, (Hitachi S-4700, Dallas, TX). The SEM micrographs of the GNPREs made by the gap distance of 60 μm, shown in Figure 3-3c evidence large agglomerations of GNPs on the fracture surfaces. On the other hand, an acceptable dispersion is seen in specimens prepared using roller gap distances of 20 μm and 40 μm (see Figure 3-3a and b). Examination of the results indicated that not only did the presence of agglomerations reduce the density of the effective interfacial areas between the GNPs and resin, but they also acted as equivalent flaw regions, in turn causing the reduction of GNPREs elastic modulus. Further examination of the experimental results obtained for the gap distance of 60 μm indicated that the applied shear force by the rollers was not sufficient to overcome the GNP flakes' interaction forces, as a result, facilitating agglomerates formation. This observation also corroborates with the well-known notion that more uniform dispersion could be obtained as a result of reduced rollers' gap distance. However, the decline in the values of the elastic modulus when the gap distance was

reduced from 40 μm to 20 μm indicates that dispersion is not the sole parameter that governs the mechanical properties of GNPRE.

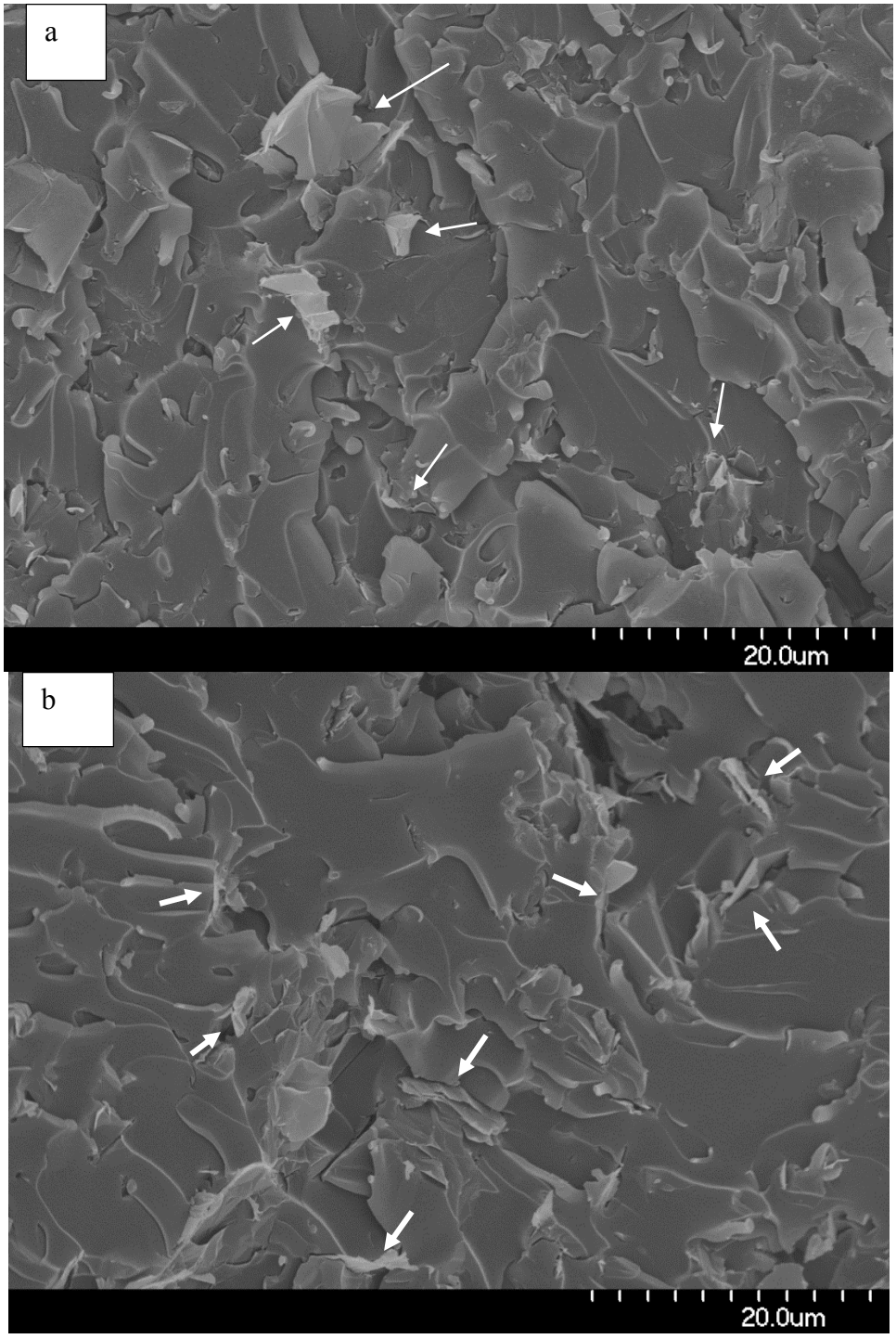

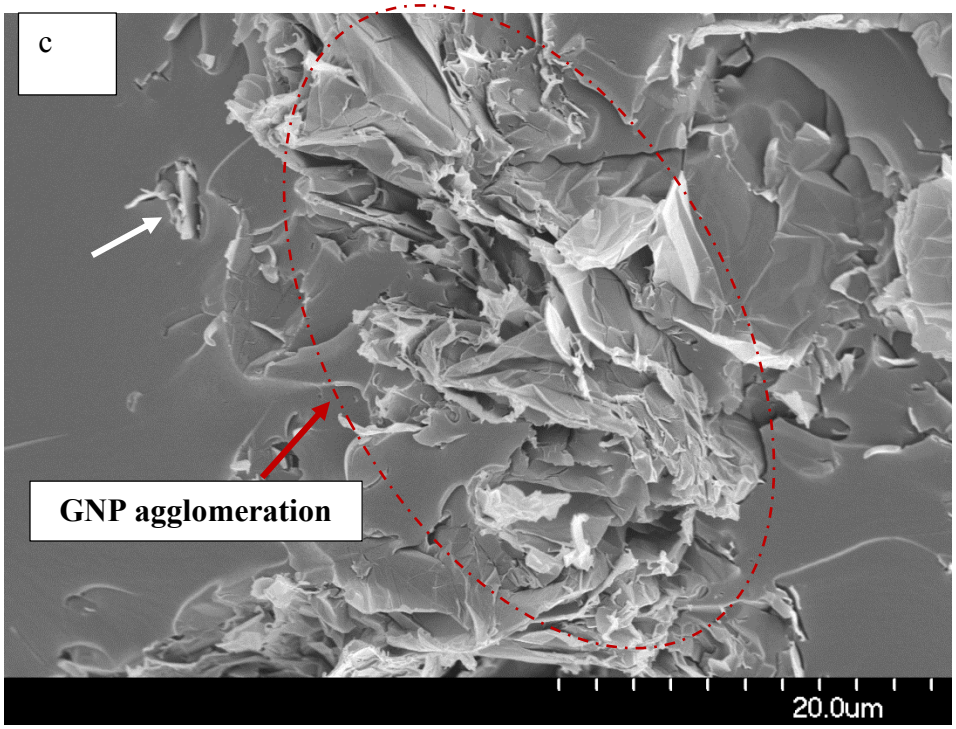

Figure 3-3. The existence of agglomerations on the fracture surface of GNPRE specimen with 2 wt% GNP content , processed by roller gap distances of (a) 20μm, (b) 40 μm and (c) 60 μm

Another parameter governing the stiffness of the GNPREs is believed to be the load transfer mechanism between the matrix and GNPs. This mechanism is partially governed by the interfacial strength created by the weak Van der Waals bond between GNPs and matrix. In addition, there would be the contribution of the so-called "mechanical lock" mechanism, created by the physical constraint of individual GNPs by the surrounding matrix [24]. The elastic modulus of GNPs is considerably larger than that of the commonly used polymers; thus, the presence of GNPs in a polymer reduces the inter-molecular mobility, leading to higher stiffness of GNPREs. As one would expect, therefore, the higher the load transfer is between GNPs and matrix, the higher would be the mechanical properties of the GNPRE.

Since the aspect ratio of GNPs (i.e., D/t) affects the mechanical interlock between the GNPs and the resin, an attempt was made to assess the GNP's characteristic length, D, using micrographs obtained using a SEM. Since it is difficult to measure the actual length of GNPs (even by using a SEM), a statistical study was performed on the SEM micrographs, by which the lengths of randomly selected individual GNPs bridging the fracture surfaces were measured. It should be noted the repeatability of an analysis depends on the number of samples being considered in the study. Therefore, to ensure that a sufficient number of GNPs were considered, the change in the average value of the collected data was calculated and monitored while accumulating new data. When the change in the average of the collected data from one reading to another reading corresponding to a new input did not vary noticeably (i.e., with a maximum difference less than 5%), then the number of the collected samples was considered adequate for addressing the repeatability issue.

It is recognized that the measured length of a bridged GNP on the fracture surfaces does not necessarily represent the real characteristic length of the GNP; nevertheless, the length is considered to be acceptable for a qualitative and comparative statistical study, so long as a sufficient number of individual GNPs is considered. These measured lengths will be referred to as the "bridging length" of the GNPs, hereafter.

In summary, in order to determine the influence of roller gap distance on the load transmission mechanisms between the GNPs and resin, the distribution of bridging lengths of GNPs was assessed in samples having different GNP contents. The results are illustrated in Figure 3-4, revealing that the effective lengths of bridged GNPs varied from less than 10 μm to more than 10 μm as a function of the increasing GNP weight content.

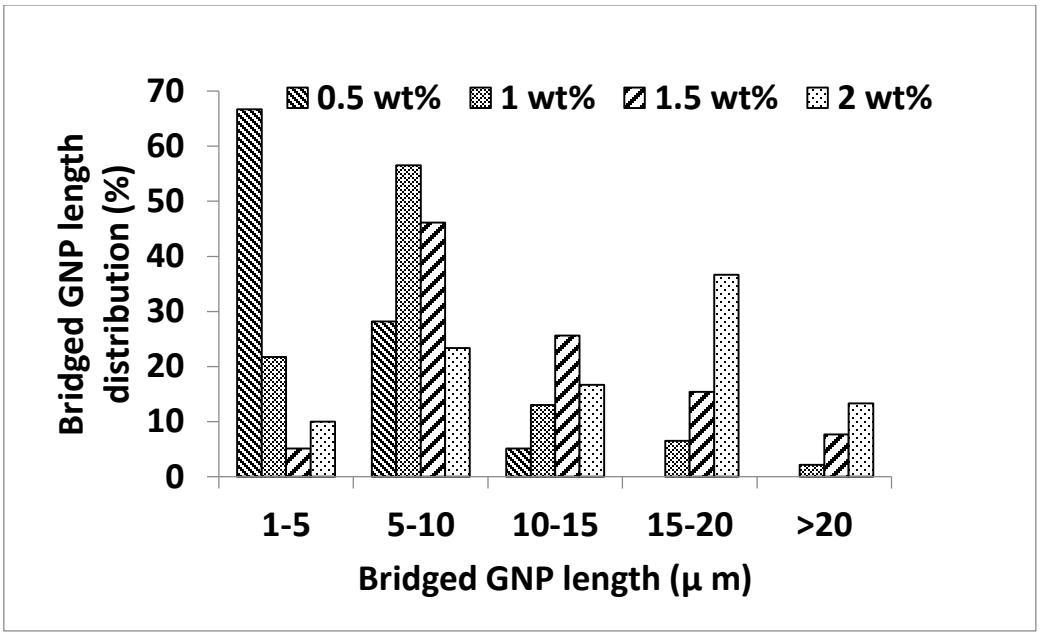

(a)

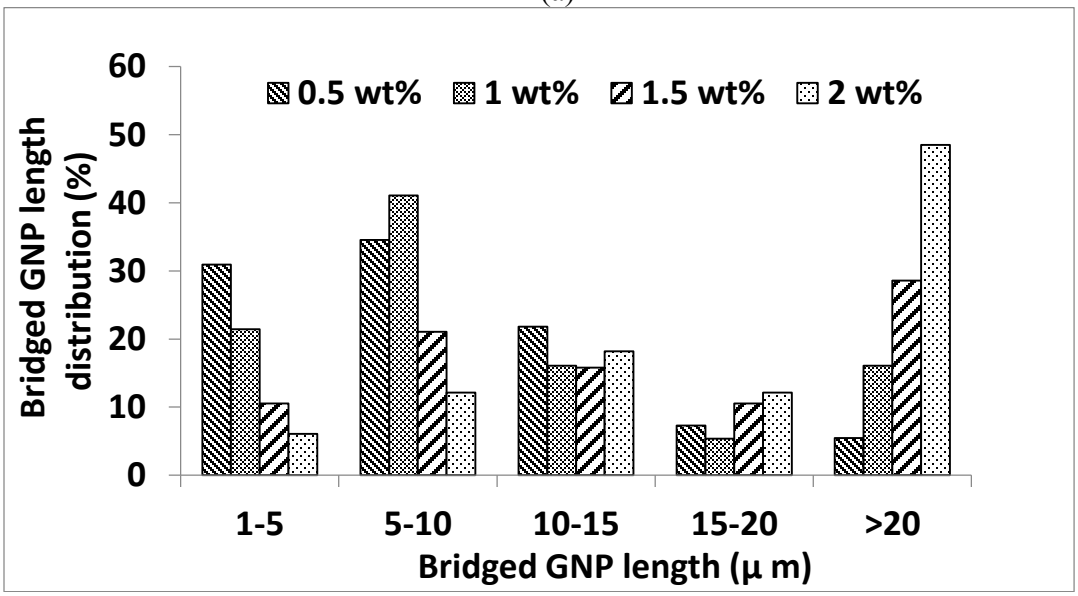

(b)

Figure 3-4. Distribution of GNP's bridged length in GNPREs with various GNP contents when the gap distances of (a) of 20 μm and (b) 40 μm were used.

It should be noted that a three-roll mill disperses GNPs in resin by applying a combined shear and normal forces to GNP agglomerates travelling through the rollers due to the variable speeds of the rollers. A careful study of SEM images of the specimens indicated that not only did the applied shear force in both the adopted gap distances

separated the GNP flakes (stratification), but it also fractured them, thus reducing their effective bridging lengths.

Considering the fact that all GNPRE specimens containing different GNP weight contents were produced using the same number of calendering cycles, the amount of energy applied to all the materials would therefore be constant within a selected gap distance. It is believed that observation of longer GNP bridging length in specimens with relatively high GNP contents would indicate that the calendering energy is mainly expended to separate the agglomerates. However, in specimens with relatively lower GNP contents, the energy would be consumed by fracturing of GNP nanoparticles. Assuming that there would be an optimum level of energy absorbed by each particle in a given nanocomposite, in order to obtain the acceptable dispersion without causing damage to the particles, the amount of energy could be controlled by reducing the cycles of calendering.

The examination of the fracture surfaces of GNPREs as illustrated in Figure 3-5 indicates an increasing trend in the average bridging length of GNPa. As can be seen, the average length of bridged GNPs in the GNPREs processed by the gap distance of 20 μm is less than that observed for GNPREs obtained by using gap distance of 40 μm. Moreover, there is a linear correlation between the GNP content and average bridging length.

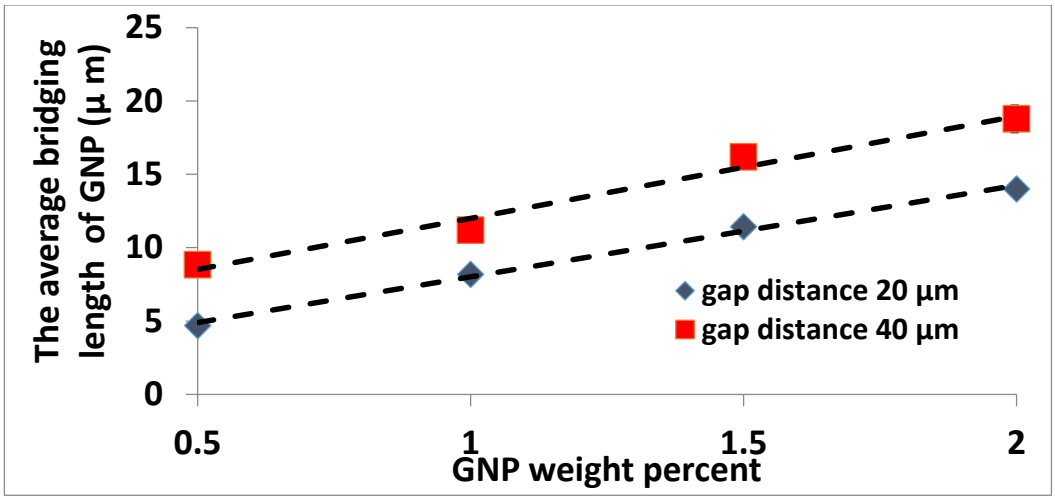

Figure 3-5. Variation in the average bridged length of GNPs for GNPREs with various GNP contents

The study of Gojny et al [18] showed that roller milling CNTs in a resin with decreasing gap distance (as low as 5 μm) produced nanocomposites with better mechanical properties. This finding suggests that the geometry of nanoparticle is another influencing factor in reaching the optimum roller gap distance. The main difference between CNTs and GNPs from dispersion point of view is their flexural stiffness (EI). By assuming a typical dimension for a multi-walled CNT (i.e., D_i=7.5 nm and D_o=15 nm) and the GNP dimensions used in the current study, it can be estimated that the average flexural stiffness of the GNPs used in this study is roughly 3000 times greater than that of typical CNTs. This indicates that CNTs are much more flexible than GNPs, which makes them less vulnerable to breakage under the bending load generated by the rollers. Therefore, it can be concluded that smaller gap distances can be used for processing CNT reinforced nanocomposites, but not for GNP reinforced nanocomposites.

It should be noted that the best results were obtained by the gap distances of 20 µm and 40 µm, respectively. In fact, processing of GNPRE by using 60 µm roller gap led to a decrease in the stiffness of the GNPRE in comparison to that of the neat resin. Therefore,

in order to evaluate the influence of dispersion and aspect ratio of GNPs on the electrical and thermal properties of the nanocomposite, for the remainder of this study, only GNPRE specimens produced by 20 µm and 40 µm gap distances are considered.

3.4.2 Electrical resistivity

Figure 3-6 shows the electrical resistivity of the neat resin and the GNPREs as a function of GNP content. GNPREs with low concentration of GNPs show more or less the same resistance as the neat resin does, and that there is no significant difference between the electrical conductivity of GNPREs made using the different roller gap distances. Beyond 1 wt% GNP inclusion, however, the resistivity decreases markedly. This sudden decrease in the electrical resistivity of GNPRE in a specific range of filler concentrations is usually referred to as the "electrical percolation threshold" (EPT). In this study, the EPT was determined to occur between 1 wt% and 1.5 wt% for both selected roller gaps.

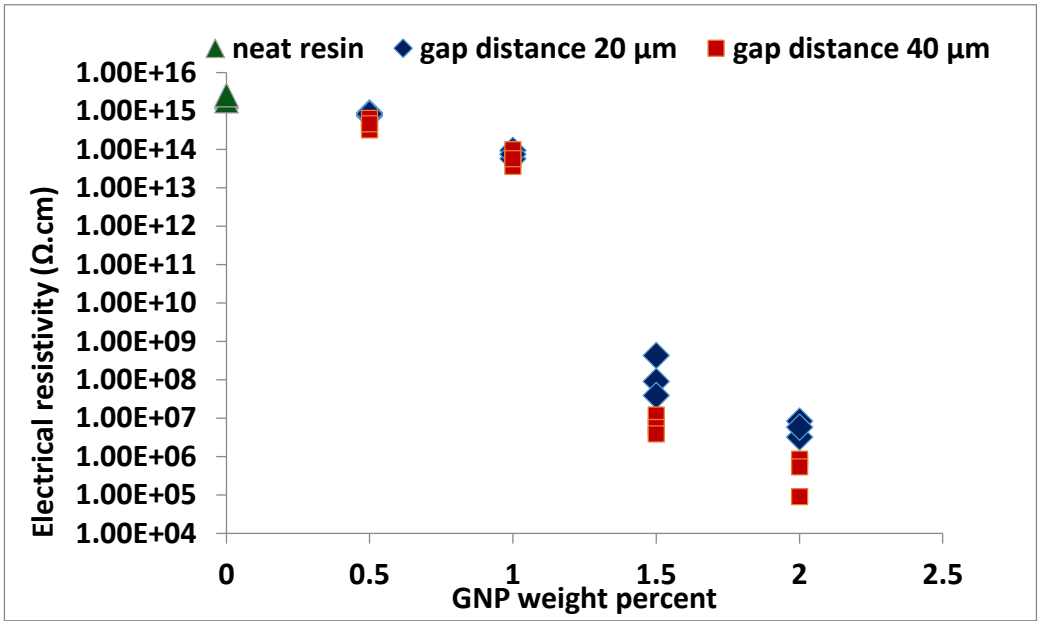

Figure 3-6. Influence of roller gap distance on the electrical resistivity of nanocomposites with various GNP contents

The EPT depends on nanoparticles' dimensions and the distance among them. There are several analytical and semi-empirical models available for predicting the EPT of nanocomposites. Some examples of such models are the "exclude volume model" [25], Lu and Mai's model [26] and a recently proposed model based on the average interparticle distance (IPD) [15]. The latter model is used to calculate the EPT of the 7 *nm* thick GNPs with the assumption that GNPs' diameter varies from 1 μm to 50 μm, based on the IPD model. The results are illustrated in Figure 3-7.

As the results reveals, in the case of GNPs considered here (with an average diameter of 25 μm), the IPD model predicted that the EPT would occur at 0.89 wt% GNP. However, the EPT was measured experimentally and found to be between 1 and 1.5 wt%. As shown in Figure 3-5, the average characteristic dimension of GNPs must have been reduced due to the calendering process. Thus, the EPT would be different from the value predicted by the IPD model, since the IPD model assumes uniform particle dispersion. Moreover, knowing the exact aspect ratio of nanoparticles is also important for obtaining an accurate prediction. However, the evaluation of the exact aspect ratio is very difficult, especially after the completion of the dispersion process. Therefore, in consideration of all the variables that are associated to actual GNPREs, the model is considered to provide predictions of the electrical threshold with reasonable and acceptable accuracy.

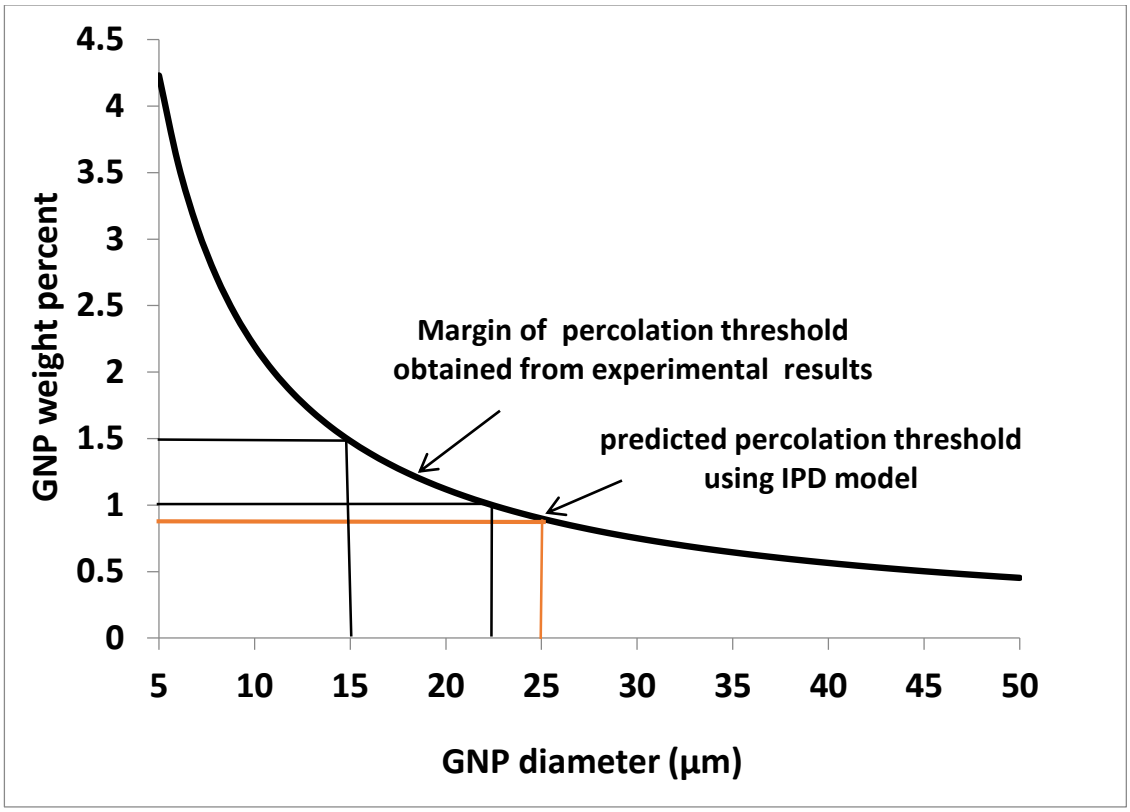

Figure 3-7. Comparison of the predicted (IPD model) percolation thresholds of GNPREs and experimentally obtained values

It should be noted that interparticle contiguity seems to be an essential condition to achieve EPT [27].To further explore how the electrical threshold is achieved, the SEM micrographs of the electrical specimens were investigated. For that, one specimen that was previously used for evaluating the electrical conductivity was selected from each group of GNPRE with different GNP contents. The specimen was then fractured in half under a bending load and the fracture surfaces were assessed using FE-SEM. Figure 3-8a shows the fracture surface of a typical GNPRE specimen with 0.5wt% GNP concentrate. The small arrows identify the dispersed GNPs in the matrix. As evident, the distances among the GNP are larger than the distance required for the electrons to be able to transfer from one GNP particle to another; as a result, the electrical resistivity of the nanocomposite with

0.5 wt% GNP concentration is quite similar to that of the neat epoxy. Although the distances among the GNPs in 1 wt% concentrate specimens are estimated to be less than those of the 0.5 wt% specimens (see Figure 3-8b), nevertheless no GNP clusters could be observed. It should be noted that the increase in the concentration of GNP could increase the probability of GNP clustering. Figure 3-8c (1.5 wt% GNP) and 8d (2 wt% GNP) indicates that the electrons could potentially move easily within the GNPs present in the clusters; as a result, the electrical resistivity of the GNPREs would be dramatically reduced.

It is also postulated that the average characteristic dimension of GNP (i.e., GNP's diameter), could play an important role in governing the EPT of a GNPREs. It is therefore believed that the use of smaller diameter GNPs would result in a relatively higher EPT; this criterion was demonstrated to hold for CNT-reinforced composites as demonstrated by Ayatollahi et al [27].

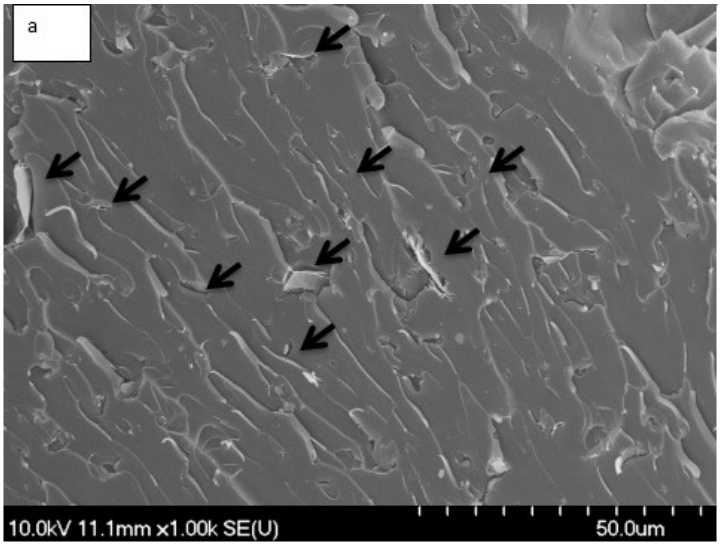

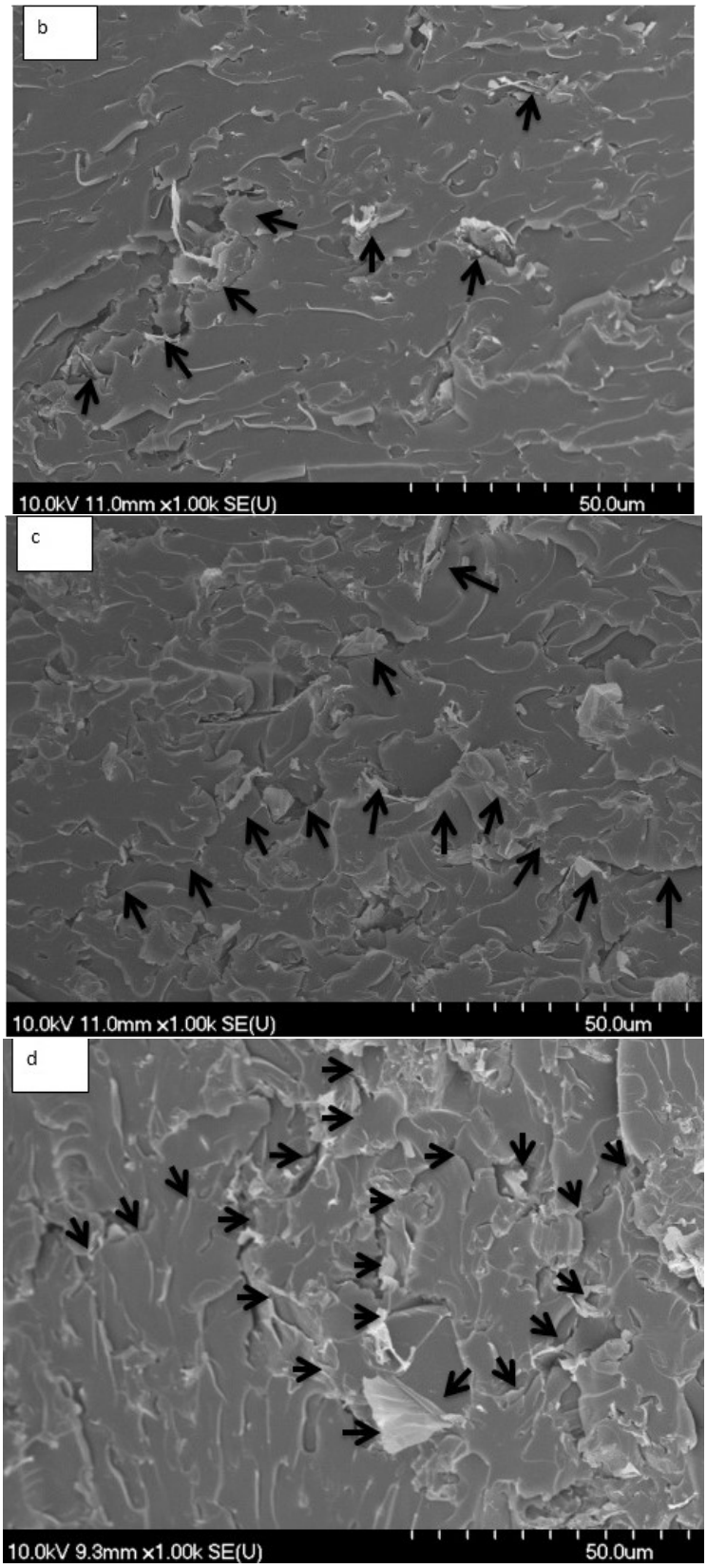

Figure 3-8. images of the fracture surfaces of the electrical conductivity in GNPRE specimens with GNP contents of (a) 0.5 wt%, (b) 1 wt%, (c) 1.5 wt% and (d) 2 wt%

3.4.3 Thermal conductivity

Table 3-1 reports the thermal conductivity of GNPREs evaluated at room temperature (25℃) and elevated temperature (80℃). The results indicate that the thermal conductivity of GNPREs increased by increasing the GNP content. The results follow the same trend when the conductivity was measured at both room and elevated temperatures. Furthermore, the change in the thermal conductivity of nanocomposite measured at 80℃ is lower than that measured at room temperature for the considered GNP contents (see Figure 3-9). This trend can be attributed to the fact that at higher temperatures, epoxy's thermal conductivity would increase.

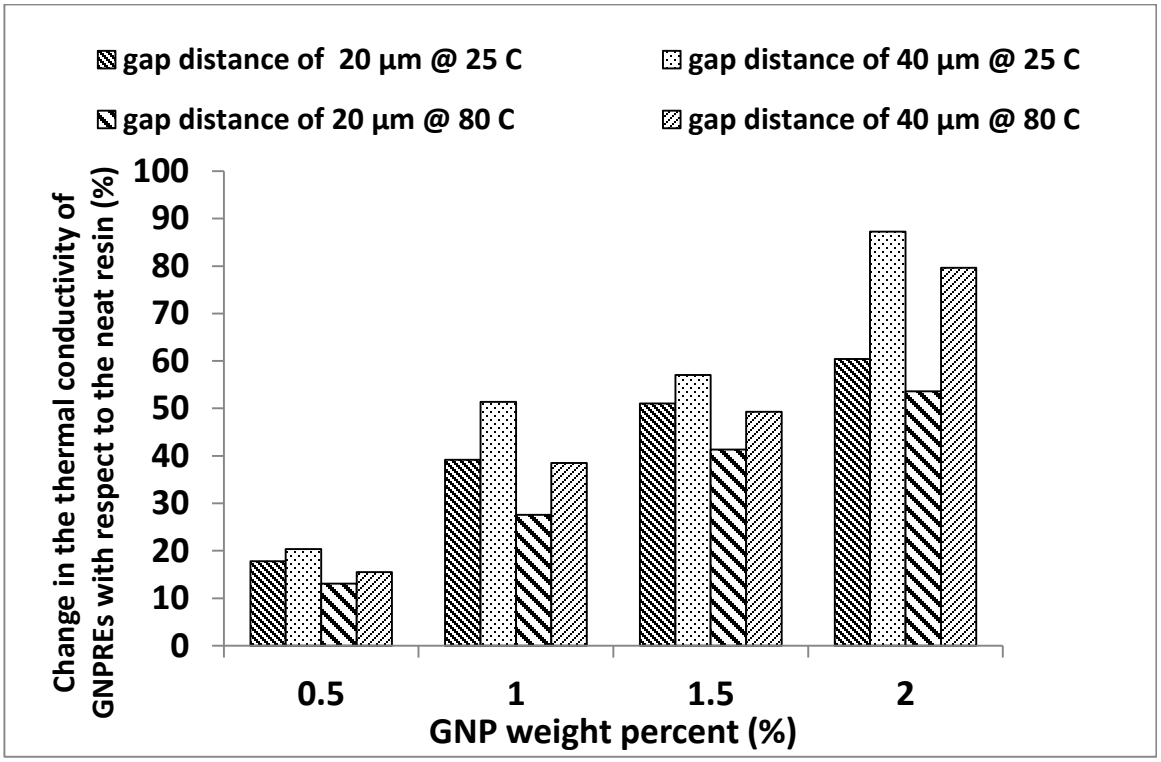

Figure 3-9. Influence of roller gap distance on the thermal conductivity of ECREs with different GNP contents (normalized with respect to the conductivity of neat epoxy)

It should be noted however that in general, neat epoxy resins are inherently poor thermal conductors. Similar to the electrical conductivity trend discussed earlier, addition of GNPs to these resins could create a conductive network, thereby increasing the thermal conductivity of resins. However, unlike in the case of electrical conductivity, full contiguity of GNPs is not essential for the development of a tangible change in the thermal conductivity of GNPREs. The heat propagation in GNPs is mainly facilitated by the acoustic phonon phenomenon. Therefore, a uniform network of GNPs resulting from optimal GNP dispersion could contribute to the steady increase in the thermal conductivity of the resultant GNPREs. In addition, nanoparticles' size could also influence the phonon diffusion through a conductive pathway [28]. The higher thermal conductivity of GNPRE, which obtained when a gap distance of 40 μm was used, can be ascribed to higher aspect ratio of GNP (see Figure 3-4b). Since the large size GNP could most likely create a more effective conductive network; as a result, the thermal conductivity of GNPREs hosting larger diameter GNPs should be higher than those reinforced with relatively smaller GNPs.

Table 3-1. Thermal properties of GNP-reinforced nanocomposites evaluated experimentally

GNP content (wt%)	Thermal conductivity (W/m.K)				Linear CTE ($\times 10^{-6}/℃$)	
	Room Temperature		80 ℃			
	Gap distance: 20 (μm)	Gap distance: 40 (μm)	Gap distance: 20 (μm)	Gap distance: 40 (μm)	Gap distance: 20 (μm)	Gap distance: 40 (μm)
0	0.221±0.016		0.250±0.006		74.87±1.21	
0.5	0.261±0.004	0.266±0.001	0.283±0.005	0.289±0.008	68.66±0.11	66.03±2.24
1	0.308±0.016	0.335±0.014	0.320±0.007	0.347±0.005	62.13±3.12	60.81±1.35
1.5	0.334±0.005	0.348±0.001	0.354±0.002	0.374±0.002	59.94±2.39	59.38±1.72
2	0.355±0.012	0.415±0.009	0.385±0.013	0.450±0.020	55.94±0.57	54.47±3.45

As stated earlier, several studies have reported properties of GNPREs that were produced using more expensive dispersion methods (i.e., processes that could not be considered as economical and functional for large-scale GNPRE production). By comparing the results reported in those studies and the experimental results reported in the present study, the following suggestions are offered. Using relatively high roller gap distances for processing GNPREs would not negatively influence the increasing trend seen in the thermal conductivity results. For example, Chatterji et al [16] utilized different processing techniques (i.e., solvent, ultrasonic and three-roll mill) in order to disperse the same commercially produced grade of GNP that has been used in the current study, in an epoxy resin. They observed an increase of 85% in thermal conductivity at 2 wt% GNP content, which corroborates closely to the findings of our study.

3.4.4 Linear coefficient of thermal expansion

The experimentally evaluated linear coefficient of thermal expansions (CTE) of the GNPREs are reported in Table 3-1 and also in Figure 3-10. The results indicate that GNPREs' CTE value decreased compared to that of the neat epoxy as the GNP concentration increased (see Figure 3-10). The CTE of the neat epoxy, which was evaluated to be approximately $75\times10^{-6}/℃$, was clearly reduced in the GNPRE specimens (Figure 3-10). The results indicate that there is an almost linear relationship between the CTE and the GNP content.

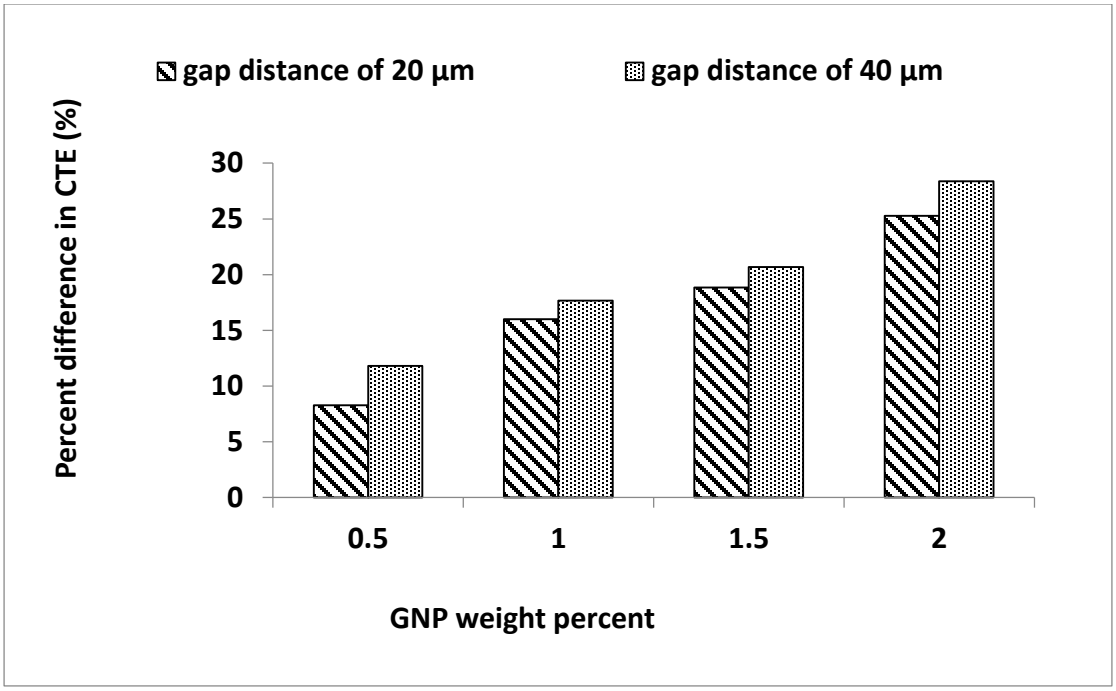

Figure 3-10. Influence of roller gap distance on the CTE of ECREs with different GNP contents (normalized with respect to the CTE of neat epoxy)

It should be noted that all CTE evaluations were performed at 80 ℃, which is well under the glass transition temperature, T_g, of the epoxy resin (i.e., 140 ℃). It should be noted that the CTE of a typical graphene sheet is approximately -0.5×10^{-6} /^{o}C , also measured at 80 ^{o}C (which incidentally remains the same up to temperature of 197 ^{o}C [29]). As a result of this negative CTE, the incorporation of GNPs into epoxy resins would clearly impede the expansion of epoxy molecules, which results in a significant reduction in GNPRE's CTE, at temperatures below the T_g.

In the current study, the GNPs were essentially randomly distributed in the epoxy resin. Therefore, a model that could accurately predict the CTE of such GNPREs should be capable of accounting for the geometry and size of the randomly distributed nanoparticles within the resin. Chow [30] extended the "mean field theory", which was

originally developed for evaluating the elastic modulus of fiber-reinforced composites, to evaluate the thermal expansion of composite materials. He suggested the use of following equations for calculating the longitudinal and transverse CTEs of a composite.

$$\alpha_L = \alpha_m + \frac{k_f}{k_m}\frac{(\gamma_f - \gamma_m)G_1 V_f}{2K_1G_3 + K_3G_1} \quad (8)$$

$$\alpha_T = \alpha_m + \frac{k_f}{k_m}\frac{(\gamma_f - \gamma_m)G_3 V_f}{2K_1G_3 + K_3G_1} \quad (9)$$

where α_m is the matrix linear CTE, k_f and k_m are the bulk moduli of nano filler and matrix, respectively, V_f is the filler volume fraction, γ_f and γ_m are the bulk thermal expansions of nano filler and matrix, respectively (where γ_f is equal to $2\alpha_{f,T} + \alpha_{f,L}$ and γ_m is taken as $3\alpha_m$) and finally, K_i and G_i are calculated using Equations 10 and 11.

$$K_i = 1 + \left(\frac{k_f}{k_m} - 1\right)\left[(1 - V_f)\beta_i + V_f\right] \quad (10)$$

$$G_i = 1 + \left(\frac{\mu_f}{\mu_m} - 1\right)\left[(1 - V_f)\theta_i + V_f\right] \quad (11)$$

In the above equations, μ is the shear modulus and β_i and θ_i are functions of GNP's characteristic ratio (i.e., $\rho = {}^{t}/_{D}$) and matrix's Poisson's ratio, respectively (see Appendix A of reference [30]).

The predicted results using the above equations are compared with the experimental results as shown in Figure 3-11. The results indicate that Chow's model predicted the CTE of the GNPREs conservatively. The experimentally obtained CTE for 2 wt% GNP is 55.94±1.73 ($10^{-6}/℃$), while the CTE calculated by Chow's model is 68.95 ($10^{-6}/℃$). It should be noted that Chow's model considers both the geometric dimensions and filler volume fraction. As seen, however, the results show that in the case of the GNPs used in this study, which have relatively high aspect ratios that result in $\rho \ll 1$, Chow's model

predictions exhibit an average discrepancy of 15% compared to the experimental values. The results showed that the Chow model was not a suitable model due to the nonlinearity in the variation of the CTE observed in our nanocomposites. Consequently, a nonlinear model was developed based on a statistical curve-fitting approach. It was demonstrated that the model could be used to predict the CTE of GNP-reinforced nanocomposite, as a function of GNP weight content, with a reasonable accuracy (Figure 3-11). The application of the proposed model shows 51% reduction in the CTE of GNPRE when 0.5 wt% GNP is used. Considering the aspect ratio of the used GNPs, the obtained value corroborates well with those reported by Wang et al [31].

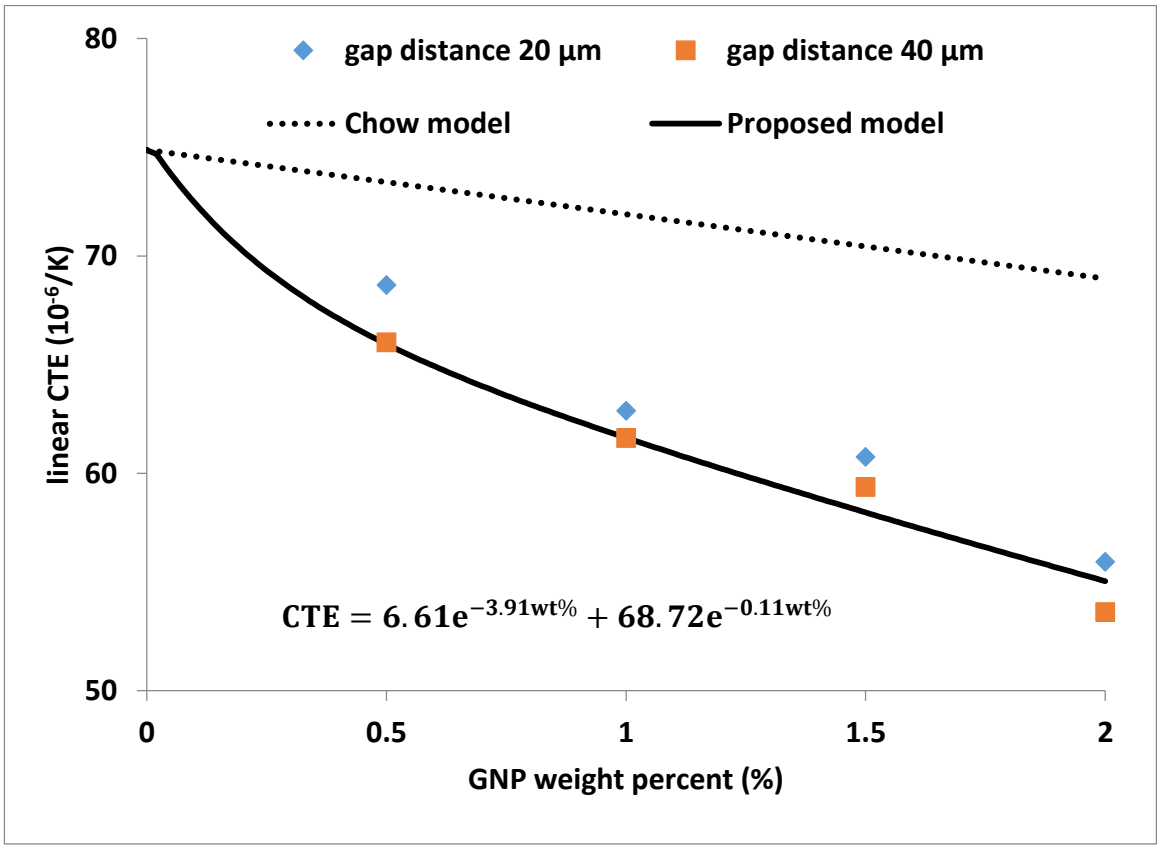

Figure 3-11. Comparison of the predicted CTE of GNPREs by Chow's model and those obtained by the proposed semi-empirical model

3.5 Multi-functional design aspects

Figure 3-12 shows the sensitivity of GNPREs' elastic and thermal properties as a function of GNP content. . As can be seen, the elastic modulus of the GNPREs is not appreciably improved by infusion of more GNPs in the resin. On the other hand, the thermal conductivity of GNPREs was increased from 22% to 89% percent with 0.5 wt% and 2 wt% of GNP, respectively. The change in the electrical resistivity also follows a specific trend when the resin included less than 1.5 wt% GNP. The electrical resistivity of GNPREs did not change significantly below 1.5 wt% GNP content, and the values are almost equal to that of the neat epoxy. On the other hand, when the GNP content exceeded that corresponding to the electrical percolation threshold, the electrical resistivity decreased abruptly from 10^{15} to 10^{6} $\Omega.m$. One can therefore design a nanocomposite that could satisfy a specific structural, thermal and/or electrical requirements by using the relationships illustrated in Figure 3-12.

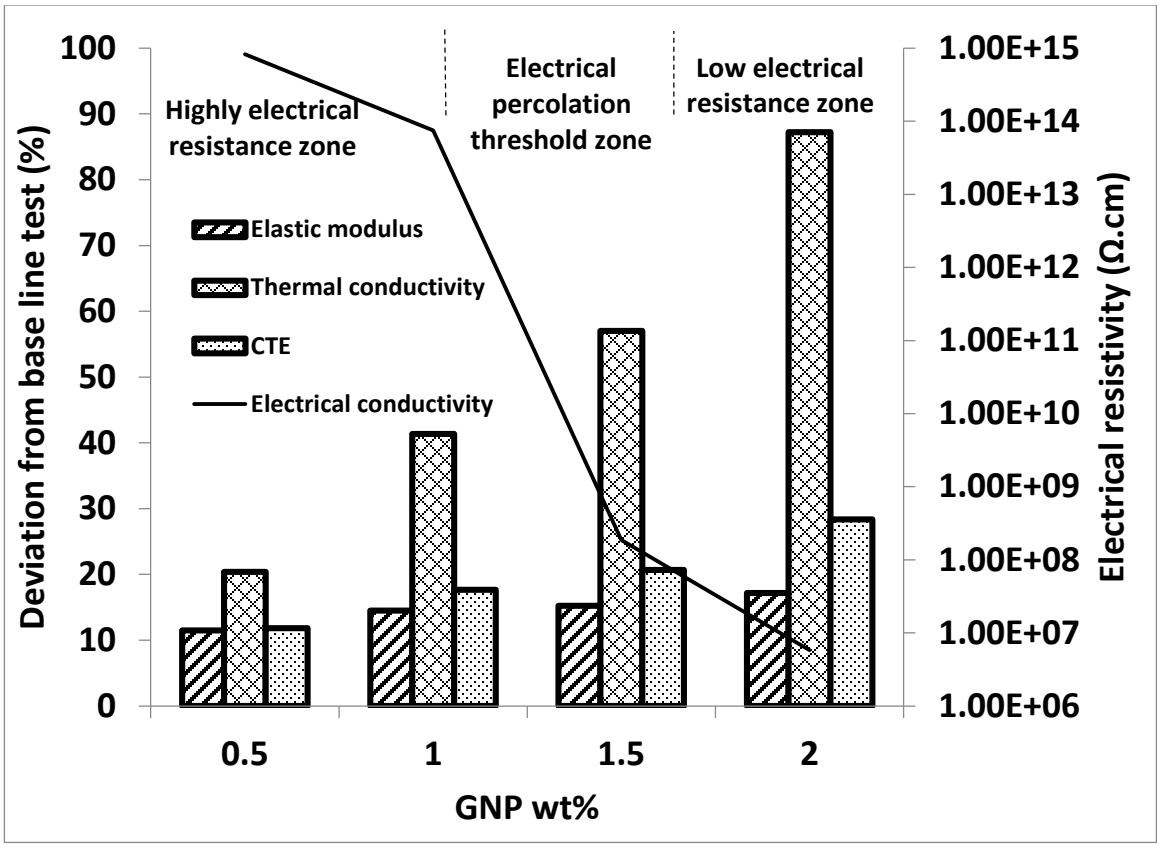

Figure 3-12. multi-functional effect of GNP on epoxy resin

3.6 Summary and Conclusion

In this study, graphene nanoparticle-reinforced epoxy nanocomposites (GNPRE) with various graphene weight contents were produced by using three-roll mill calendering technique. The effect of the adopted processing technique on the multi-functional properties of the GNPREs (i.e., the elastic modulus, electrical resistivity, thermal conductivity and linear coefficient of thermal expansion), was experimentally investigated. The analysis of the observed results prompted the concept of the optimum gap distance for production of optimal GNP reinforced nanocomposites in reference to nanoparticles' aspect ratio, geometry and content. This is believed to be the first time that this concept is being introduced. In summary, inclusion of 2 wt% GNP to the epoxy resin resulted in an increase of 9% and 12% in the elastic modulus of the GNPREs when roller gaps of 20 μm

and 40 μm were used, respectively. The general and modified Halpin-Tsai models were utilized for prediction of the moduli. Due to the models' poor predictive capability, these models were modified to account for the filler platelet's geometry. The results revealed that the adjusted modified 2D randomly oriented Halpin-Tsai model could produce more accurate results than its 3D form.

Results also illustrated that no significant change in the electrical resistivity could be observed in specimens with GNP contents of up to 1 wt%. In fact, the electrical conductivity threshold could be obtained by addition of 1.5 wt% GNP. IPD model's prediction of the electrical percolation threshold was also evaluated and compared to the experimentally obtained values, confirming that its predictions were reasonably accurate.

Moreover, the thermal conductivities of GNP-nanocomposites measured both at room and elevated temperatures were significantly increased even when only 0.5 wt% content of GNP was included in the resin. The increase in the thermal conductivity followed a linear trend as a function of GNP content. However, the increase in the thermal conductivity at elevated temperature was observed to be less than that when evaluated at room temperature.

The CTE value of the GNPREs measured by a dilatometer revealed that CTE of the GNP-nanocomposites decreased by 15% and 25% when 0.5 wt% and 2 wt% GNPs were included in the resin, respectively. It was also shown that the available analytical models, such as Chow's model, underestimated the CTE values of the nanocomposites. In addition, the total dispersion durations when the rollers' gap distances of 20 μm and 40 μm were used were 140 min and 60 minutes, respectively. However, the optimum roller gap distance for a uniform dispersion of CNT was found to be 5 μm, which corresponds to a dispersion

duration of 560 minutes. Therefore, when processing GNP-reinforced nanocomposites, the total time required for the dispersion process would be 9 times faster with the proposed gap distance in comparison to that required for processing CNT-reinforced nanocomposites. It should also be noted that in this research, a bench-top three-roll mill was used, which is suitable for laboratory scale production. This processing technique, however, has the capability and capacity to be scaled up to an industrial production scale.

Finally, the relationships of the various properties investigated in this study, as a function of GNP weight content were presented in the form of a chart. This chart can be used to select the appropriate GNP content to generate a GNP-reinforced nanocomposite that would offer optimal multi-functional properties for a given application.

3.7 Acknowledgments

This research was funded by the National Science and Engineering Research Council of Canada (NSERC) through the Collaborative Research and Training Experience (CREATE) program. The authors are grateful to the granting agency. The use of Dalhousie Institute for Research in Material (IRM) equipment, through Professor M.A. White (Chemistry Department, Dalhousie University) and Professor S. Corbin (Civil & Resource Engineering Department, Dalhousie University) is also gratefully acknowledged.

3.8 References

[1] Fim FdC, Guterres JM, Basso NRS, Galland GB. Polyethylene/graphite nanocomposites obtained by in situ polymerization. Journal of Polymer Science Part A: Polymer Chemistry. 2010;48:692-8.

[2] S. RR, D.C. L. Mechnaical and thermal properties of caron nanotubes. Carbon. 1995;33:6.

[3] Lanticse LJ, Tanabe Y, Matsui K, Kaburagi Y, Suda K, Hoteida M, et al. Shear-induced preferential alignment of carbon nanotubes resulted in anisotropic electrical conductivity of polymer composites. Carbon. 2006;44:3078-86.

[4] Yeh M-K, Tai N-H, Liu J-H. Mechanical behavior of phenolic-based composites reinforced with multi-walled carbon nanotubes. Carbon. 2006;44:1-9.

[5] Scott CD, Arepalli S, Nikolaev P, Smalley RE. Growth mechanisms for single-wall carbon nanotubes in a laser-ablation process. Appl Phys A. 2001;72:573-80.

[6] See CH, Harris AT. A Review of Carbon Nanotube Synthesis via Fluidized-Bed Chemical Vapor Deposition. Industrial & Engineering Chemistry Research. 2007;46:997-1012.

[7] Cho D, Lee S, Yang G, Fukushima H, Drzal LT. Dynamic Mechanical and Thermal Properties of Phenylethynyl-Terminated Polyimide Composites Reinforced With Expanded Graphite Nanoplatelets. Macromolecular Materials and Engineering. 2005;290:179-87.

[8] Viculis LM, Mack JJ, Mayer OM, Hahn HT, Kaner RB. Intercalation and exfoliation routes to graphite nanoplatelets. Journal of Materials Chemistry. 2005;15:974-8.

[9] Chatterjee S, Nuesch FA, Chu BT. Comparing carbon nanotubes and graphene nanoplatelets as reinforcements in polyamide 12 composites. Nanotechnology. 2011;22:275714.

[10] Li W, Dichiara A, Bai J. Carbon nanotube–graphene nanoplatelet hybrids as high-performance multifunctional reinforcements in epoxy composites. Composites Science and Technology. 2013;74:221-7.

[11] Bortz DR, Heras EG, Martin-Gullon I. Impressive Fatigue Life and Fracture Toughness Improvements in Graphene Oxide/Epoxy Composites. Macromolecules. 2012;45:238-45.

[12] Chatterjee S, Nafezarefi F, Tai NH, Schlagenhauf L, Nüesch FA, Chu BTT. Size and synergy effects of nanofiller hybrids including graphene nanoplatelets and carbon nanotubes in mechanical properties of epoxy composites. Carbon. 2012;50:5380-6.

[13] King JA, Klimek DR, Miskioglu I, Odegard GM. Mechanical properties of graphene nanoplatelet/epoxy composites. Journal of Applied Polymer Science. 2013;128:4217-23.

[14] Ramakrishna S, Lim TC, Inai R, Fujihara K. Modified Halpin-Tsai Equation for Clay-Reinforced Polymer Nanofiber. Mechanics of Advanced Materials and Structures. 2006;13:77-81.

[15] Li J, Kim J-K. Percolation threshold of conducting polymer composites containing 3D randomly distributed graphite nanoplatelets. Composites Science and Technology. 2007;67:2114-20.

[16] Chatterjee S, Wang JW, Kuo WS, Tai NH, Salzmann C, Li WL, et al. Mechanical reinforcement and thermal conductivity in expanded graphene nanoplatelets reinforced epoxy composites. Chemical Physics Letters. 2012;531:6-10.

[17] Thostenson ET, Chou T-W. Processing-structure-multi-functional property relationship in carbon nanotube/epoxy composites. Carbon. 2006;44:3022-9.

[18] Gojny FH, Wichmann MHG, Köpke U, Fiedler B, Schulte K. Carbon nanotube-reinforced epoxy-composites: enhanced stiffness and fracture toughness at low nanotube content. Composites Science and Technology. 2004;64:2363-71.

[19] ASTM D638 Standard test method for tensile properies of plastics. West conshohocken, PA: ASTM International; 2010.

[20] ASTM D257 Standard test method for DC resistance or conductance of insulating material. West Conshohocken, PA: ASTM International; 2007.

[21] ASTM D4496 Standard test method for D-C resistance or condutance of moderately conductive materials. West Conshoohoken, PA: ASTM International; 2004.

[22] Bryan C, Whitman CA, Johnson MB, Niven JF, Murray P, Bourque A, et al. Thermal conductivity of (Er_{1−x}Y_{x})_{2}Ti_{2}O_{7} pyrochlore oxide solid solutions. Physical Review B. 2012;86:054303.

[23] ASTM D228 Standard test Method for linear thermal expansion of solid material with a push-rod dilatometer. West conshohocken PA: ASTM international; 2011.

[24] Wong M, Paramsothy M, Xu XJ, Ren Y, Li S, Liao K. Physical interactions at carbon nanotube-polymer interface. Polymer. 2003;44:7757-64.

[25] Celzard A, McRae E, Deleuze C, Dufort M, Furdin G, Marêché JF. Critical concentration in percolating systems containing a high-aspect-ratio filler. Physical Review B. 1996;53:6209-14.

[26] Lu C, Mai YW. Influence of aspect ratio on barrier properties of polymer-clay nanocomposites. Physical review letters. 2005;95:088303.

[27] Ayatollahi MR, Shadlou S, Shokrieh MM, Chitsazzadeh M. Effect of multi-walled carbon nanotube aspect ratio on mechanical and electrical properties of epoxy-based nanocomposites. Polymer Testing. 2011;30:548-56.

[28] Yang S-Y, Ma C-CM, Teng C-C, Huang Y-W, Liao S-H, Huang Y-L, et al. Effect of functionalized carbon nanotubes on the thermal conductivity of epoxy composites. Carbon. 2010;48:592-603.

[29] Jiang H, Liu B, Huang Y, Hwang KC. Thermal Expansion of Single Wall Carbon Nanotubes. Journal of Engineering Materials and Technology. 2004;126:265.

[30] Chow TS. The effect of Particles shape on the mechanical properties of filled polymer. Journal of Material Science. 1980;15:15.

[31] Wang S, Tambraparni M, Qiu J, Tipton J, Dean D. Thermal Expansion of Graphene Composites. Macromolecules. 2009;42:5251-5.

Chapter 4: Fracture and toughening mechanisms of GNP-based nanocomposites in modes I and II fracture

B. Ahmadi-Moghadam and F. Taheri

Published in the Journal of Engineering Fracture Mechanics, in Press.

DOI: 10.1016/j.engfracmech.2014.08.008

4.1 Abstract

The objective of this study was to enhance the fracture response and toughness of epoxy resins in a cost-effective manner. Therefore, an experimental program was designed to examine the fracture response and toughness (both modes I and II fracture) of an epoxy resin reinforced with different concentrations of graphene-nanoplatelets and multi-wall carbon-nanotube. The resulting nanocomposites exhibited significant improvement in their mode-I fracture toughness, while their mode-II fracture toughness was slightly degraded. Scanning-electron and atomic-force microscopes produced micrographs revealed the alteration of the fracture and toughening mechanisms of the resin by evidence such as relatively larger plastic deformation, crack deflection, bridging and pinning in mode-I fracture. An empirical fracture mechanism criterion was also proposed.

4.2 Introduction

Fiber-reinforced composites (FRPs) have been known to offer remarkable in-plane mechanical properties. Notwithstanding, FRP laminates are critically susceptible to delamination, especially FRPs that are made with relatively brittle resins (e.g., epoxy resins), since in general, they have relatively low fracture toughness and weak fiber/ matrix interface bond strength. As a result, several nanofillers, such as rubber particles and nano clays, have been utilized in order to increase the toughness of epoxy resins. Although these nanofillers have shown to improve the toughness of the epoxy resins significantly, but in

turn, they also degrade the stiffness of the reinforced epoxy resins [1, 2] by a notable margin.

Graphene nanoplatelets (GNPs) are new generation of carbon nanofillers, used to modify the stiffness and electrical conductivity of epoxy resins [3]. GNPs have evidently more effective improvement on mode-I fracture toughness of epoxy resin in comparison to CNT-reinforced epoxy resins (CRERs). On the other hand, the electrical percolation threshold (EPT) of CRERs typically occurs at 0.25 wt% CNT inclusion [4]. However, by using even relatively much larger GNP particles, one could not achieve the EPT with less than 1 wt% GNP.

It should be noted that very few studies exists that report mode-II fracture toughness and characteristics of GNP-reinforced epoxy resins (GRERs). Shadlou et al [5] observed 13% reduction in mode-II fracture toughness of epoxy resin reinforced with 0.5 wt% graphite oxide (GO). Moreover, even fewer studies are available with respect to the synergy of GNP and CNT on the fracture toughness of epoxy resin. Chatterjee et al [6] compared the mode-I fracture toughness of a GNP-reinforced epoxy resin (GRER), and a hybrid CNT-GRER with 0.5 wt% nano-fillers content. The results showed that the highest value of fracture toughness was exhibited by the specimen whose CNT content was nine times of its GNP content. The results of our reviewed literature indicate that the main focus of the investigations that have explored the synergy of GNP and CNT has been to achieve higher electrical conductive nanocomposites with the lowest possible GNP content [7, 8].

To the best of authors' knowledge, there exists no detailed study in consideration of the fracture response and toughening mechanism of GRERs under both pure mode-I and mode-II fractures. Moreover, there is a distinct lack of information on the effect of synergy

of GNPs and CNTs on mode-II fracture toughness of resins, especially in nanocomposites with greater nano-fillers contents than those reported in the literature (i.e., higher than 0.5% wt). Consequently, in this research, the facture toughness of GRERs and CNT-GRERs under pure mode-I and mode-II fracture are experimentally assessed. In addition, the associated fracture and toughening mechanisms are investigated using a scanning electron microscope (SEM) and atomic force microscope (AFM). As a result, based on the observed process-zone characteristics of the GRERs a fracture and toughening mechanism is proposed in mode-II fracture.

4.3 Experiments

4.3.1 Materials

The GNPs used in this research had an average thickness of 7 nm and an average particle diameter of 25 μm, obtained from the XG Sciences (Lansing, MI). The CNTs were acquired from the US Research Nanomaterials Inc (Huston, TX). The CNT particles had an average length of 25 μm with diameter range of 5~15 nm, according to the vendor datasheet. Figure 4-1 shows microscopic views of representative samples of the GNPs and CNTs used in this investigation. The resin used in this investigation was a hot-cure and low viscosity epoxy resin, Araldite LY564, with its hardener, Aradure 2954, available through the Huntsman (West Point, MI).

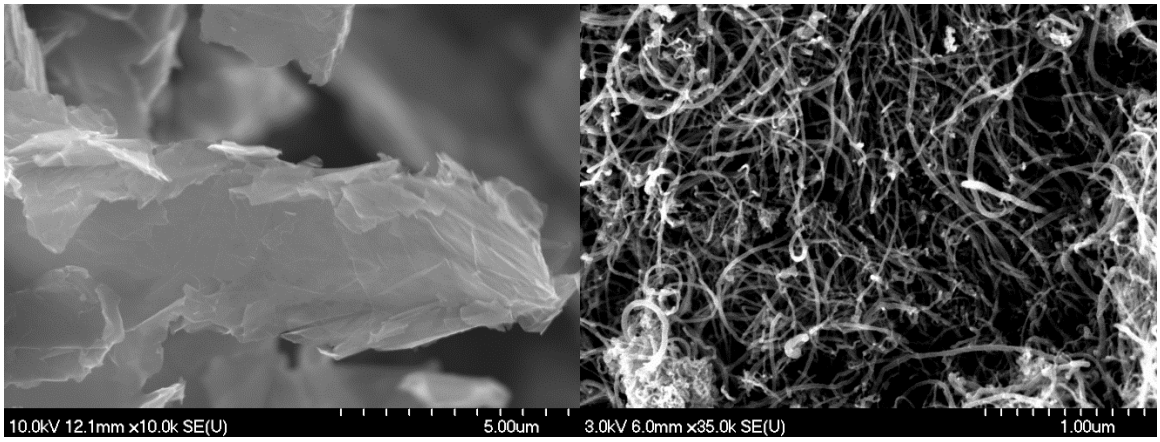

(a) (b)

Figure 4-1. SEM images of (a) GNPs and (b) CNTs

4.3.2 Specimen preparation

To fabricate the hybrid CNT-GRERs, firstly, the appropriate amounts of CNT were distributed into the resin using a mechanical stirrer operated at 2000 rpm for 15 minutes. Then, the mixed CNT-resin slurry was further processed through a three roll mill (Torrey Hill Technology, San Diego, CA) for three cycles. Subsequently, the appropriate amounts of GNPs were distributed into the CNT-resin slurry, also using the mechanical stirrer operated with speed of 2000 rpm for 15 minutes. The mixtures of CNT- and GNP- resins were further processed through the three-roll mill based on the GNP content. The number of calandering cycle used to process the hybrid CNT/GNP reinforced resins slurry was three, five and seven times for 0.2, 0.7 and 1.7 wt% GNP contents, respectively. It should be noted that the GRERs were processed with the same methodology, excluding the mentioned step for dispersing the CNTs in resin.

After the dispersion process, the appropriate amount of hardener was added to the resin and mixed for additional 15 minutes using the mechanical stirrer set at 150 rpm. The mixture was subsequently degassed in a chamber at -13.75 psi for 45 minutes. Finally, the

mixture was poured into the molds and cured at 80 ℃ for 1 hour and then post-cured at 140 ℃ for 8 hours.

4.3.3 Tests and methodology

ASTM D5045 single edge notch bend (SENB) configuration [9] was utilized to assess the mode-I fracture toughness (K_{IC}) of the nanocomposites. The dimensions of the specimens (Figure 4-2) were selected such to satisfy the plane strain criterion, as recommended by the standard, and the K_{IC} was calculated using equation (4-1.

$$K_{Ic} = \left(\frac{P_{max}}{B.W^{0.5}}\right) f\left(\frac{a}{w}\right) \tag{4-1}$$

In the above equation, P_{max} is the maximum load from the load-displacement curve; B and W are the specimen's thickness (10 mm) and width (20 mm), respectively, and $f\left(\frac{a}{w}\right)$ is a factor related to the geometry of the specimen, which can be calculated using the following equation.

$$f\left(\frac{a}{w}\right) = 6\left(\frac{a}{w}\right)^{1/2} \frac{\left[1.99 - \left(\frac{a}{w}\right)\left(1 - \frac{a}{w}\right)\left(2.15 - 3.93\frac{a}{w} + 2.7\left(\frac{a}{w}\right)^2\right)\right]}{\left(1 + 2\frac{a}{w}\right)\left(1 - \frac{a}{w}\right)^{3/2}} \tag{4-2}$$

The other variables are shown in Figure 4-2.

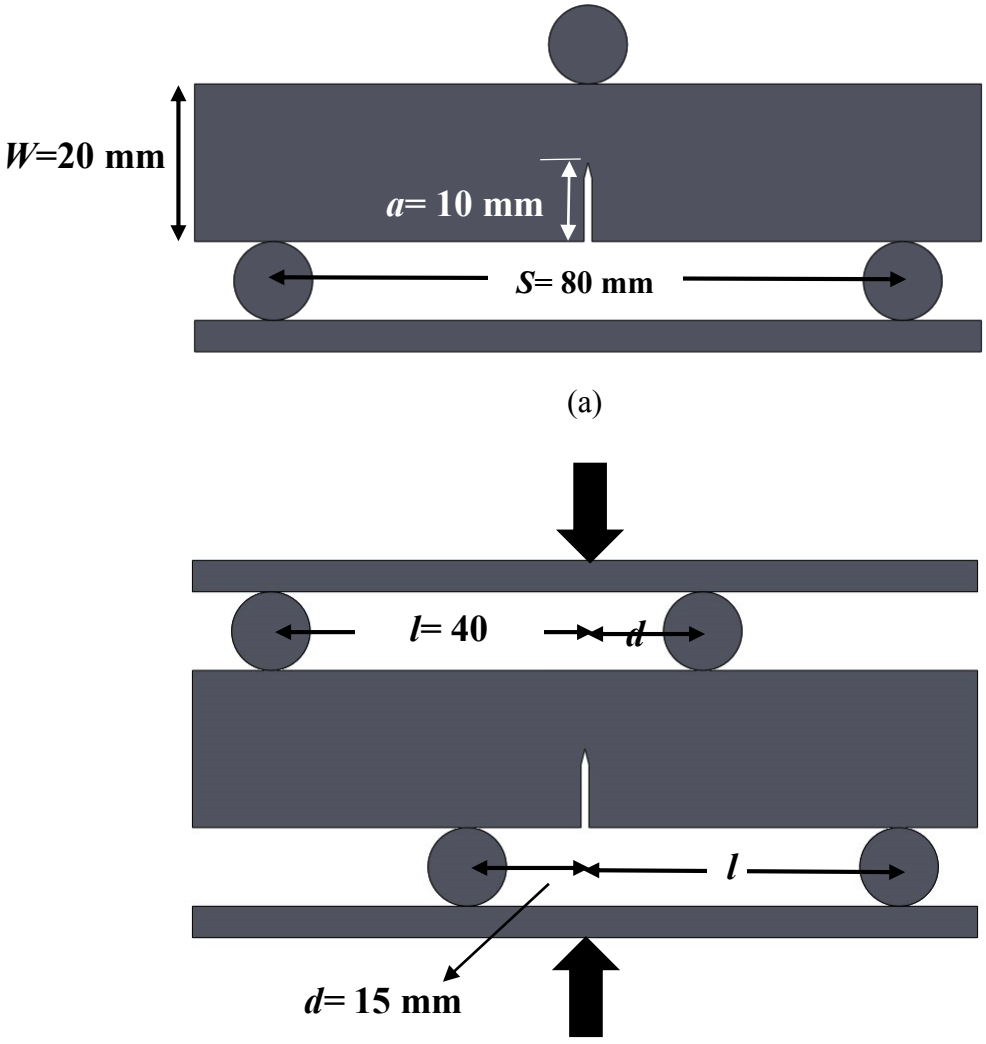

Figure 4-2. Scheme of fracture toughness specimens (a) for mode-I and (b) for mode-II

It should be noted that there exist no known standard test method for evaluating the mode-II fracture toughness of such epoxy nanocomposites under plane-strain condition. There are, however, at least three test methods used by various researchers to obtain K_{IIC}; they are: (i) the unsymmetric four-point bending test, (ii) the end loaded split laminate (ELS) test, and (iii) the Arcan test method, with the first one being more prevalently used [10]. Figure 4-2 shows the SENB and loading conditions for evaluating K_{IC} and K_{IIC}. A notable advantage of these test methods is that the same specimen configuration is used for

evaluating both K_{IC} and K_{IIC}. The K_{IIC} can be evaluated by using the following equation [10].

$$K_{IIC} = \frac{F}{B.w^{0.5}}\left(1 - \frac{d}{l}\right) f'\left(\frac{a}{w}\right) \tag{4-3}$$

where F is the largest magnitude of the load in the load–displacement curve, $f'\left(\frac{a}{w}\right)$ is a shape factor, which can be calculated by the following equation [10].

$$f'\left(\frac{a}{w}\right) = 9.763\left(\frac{a}{w}\right)^4 - 15.036\left(\frac{a}{w}\right)^3 + 8.667\left(\frac{a}{w}\right)^2 + 1.695\left(\frac{a}{w}\right) - 0.037 \tag{4-4}$$

and the other variables are shown in Figure 4-2.

4.4 Results

4.4.1 Fracture toughness

The evaluated Mode-I and mode-II fracture toughness values of the GRERs and CNT-GRERS reinforced nanocomposites are presented in Table 4-1. The mode-I fracture toughness of the neat epoxy (measured at 0.77 $MPa.\sqrt{m}$) increased linearly as a function of GNP wt% inclusion to as high as 1.48 $MPa.\sqrt{m}$ in GRERs with 3 wt% GNP (i.e., 90% increase in K_{Ic}). Nevertheless, the value of mode-II fracture toughness is considerably larger than the mode-I fracture toughness in all GRERs specimens, except those including 3 wt% GNPs. On the other hand, K_{IIC} showed a descending trend in the GRERs' specimens as the concentration of GNP increased (Figure 4-3).

Table 4-1.fracture toughness of GRERS and CNT-GRERs

	Neat epoxy	**0.5 wt%**		**1 wt%**		**2wt%**		**3 wt%**
	-	GNP	$GNP_{0.2wt\%}$ + $CNT_{0.3wt\%}$	GNP	$GNP_{0.7wt\%}$ + $CNT_{0.3wt\%}$	GNP	$GNP_{1.7wt\%}$ + $CNT_{0.3wt\%}$	GNP
K_{IC} $(Pa.\sqrt{m})$	0.77±0.02	0.96 ± 0.042	1.06 ± 0.045	1.06 ± 0.026	1.25 ± 0.075	1.30 ± 0.062	1.35 ± 0.085	1.46 ± 0.084
K_{IIC} $(Pa.\sqrt{m})$	1.71±0.06	1.68 ± 0.068	1.25 ± 0.033	1.61 ± 0.045	1.52 ± 0.019	1.50 ± 0.09	1.52 ± 0.064	1.49 ± 0.1

As the synergy of the GNP and CNT increased, the mode-I fracture toughness of the nanocomposites became larger than those observed for the GRER (Figure 4-3). Notwithstanding, K_{IIC} of the CNT-GRER specimens hosting the minimum GNP content (i.e., 0.2 wt%) actually degraded in comparison to neat resin's toughness; however, the toughness linearly increased by a notable margin when the concentration of GNPs exceeded that of CNT in the nanocomposites.

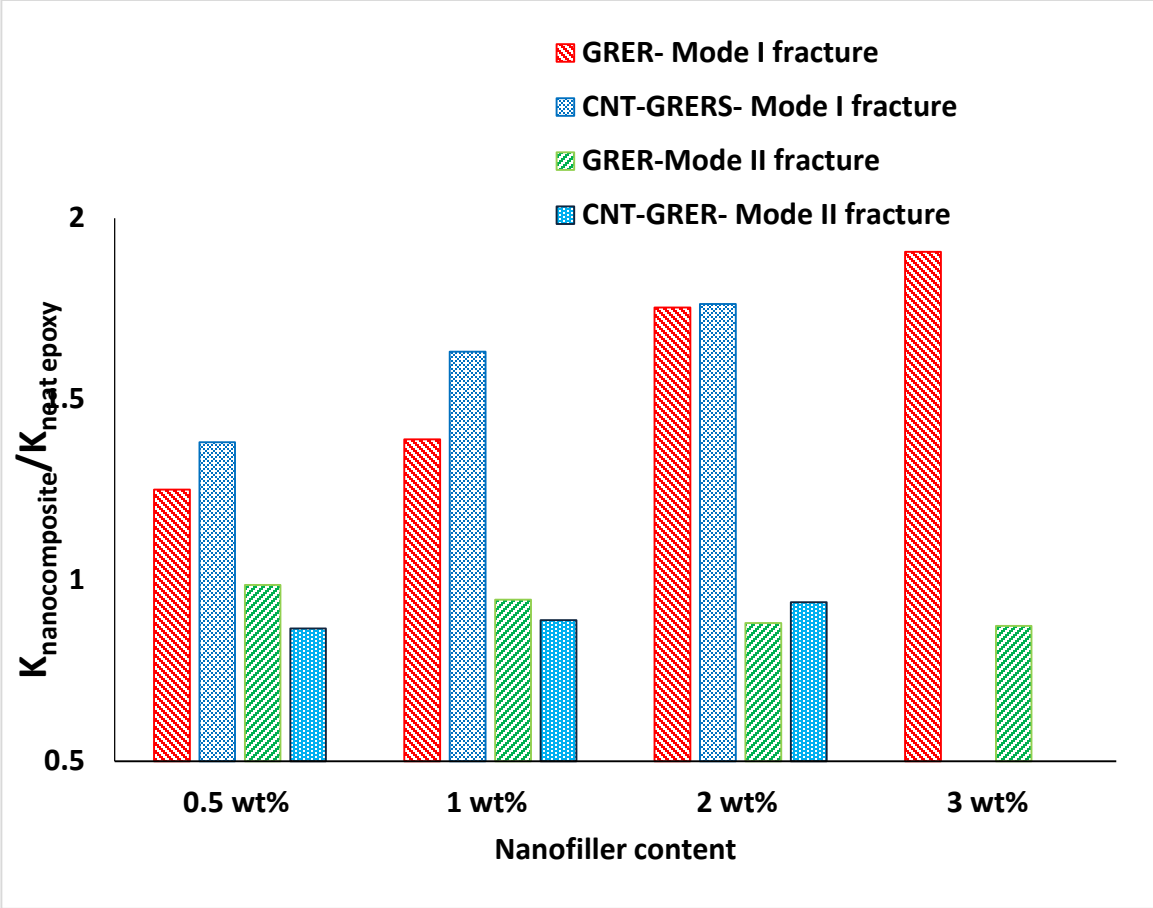

Figure 4-3. Normalized fracture toughness versus wt% content of nanoparticles

.

4.5 Fracture and toughening mechanism

4.5.1 Mode-I fracture

The presence of rigid and perfectly bonded fillers prompts different fracture and toughening mechanisms in a host resin. Some such mechanisms are the shear yielding, crack deflection, and crack pinning and bowing [11, 12]. When GNPs and CNTs are considered as rigid nanofillers when combined with polymers, since they are much stiffer than their host polymers. One could therefore expect to observe fracture toughening mechanisms similar to those observed in resins reinforced with other types of rigid fillers.

As stated earlier, GNPs have disk-like shape. Since they are randomly dispersed in the epoxy resin, a growing crack would be deflected as it encounters the rigid GNP particles. As a result, the crack is forced to move out of its initial propagation plane by tilting and /or twisting. Any such deflection would lead to local mixed-mode fracture (mixed-mode I-II, I-III or I-II-III), depending on the local state of stress, when considering 3D crack propagation). Consequently, the driving force required to propagate the crack under a mixed-mode condition would be larger than that required under mode-I condition. Therefore, the fracture toughness of GNP-reinforced resins would be increased. The aforementioned theory has been proven by Faber and Evans [13, 14] for resins reinforced with spherical fillers.

Figure 4-4 shows SEM micrographs of the fracture surfaces of nanocomposites reinforced with various amounts of nano-filler contents, within an area close to the crack tip). The mirror-like appearance of the fracture surface of the neat epoxy (Figure 4-4a) indicates a brittle mode-I fracture. Increasing the content of the nano-fillers causes a relatively rougher fracture surface of the nanocomposites. Note that GNPs have greater aspect ratios in comparison to other nanofillers (i.e., diameter/thickness > 3500); consequently, when a propagating cracks encounters a rigid GNP, especially in nanocomposites with high nanofiller content, the crack has to tilt or twist in greater angles in order to pass the GNP. As a result, more peaks and valleys would be created on the fracture surfaces.

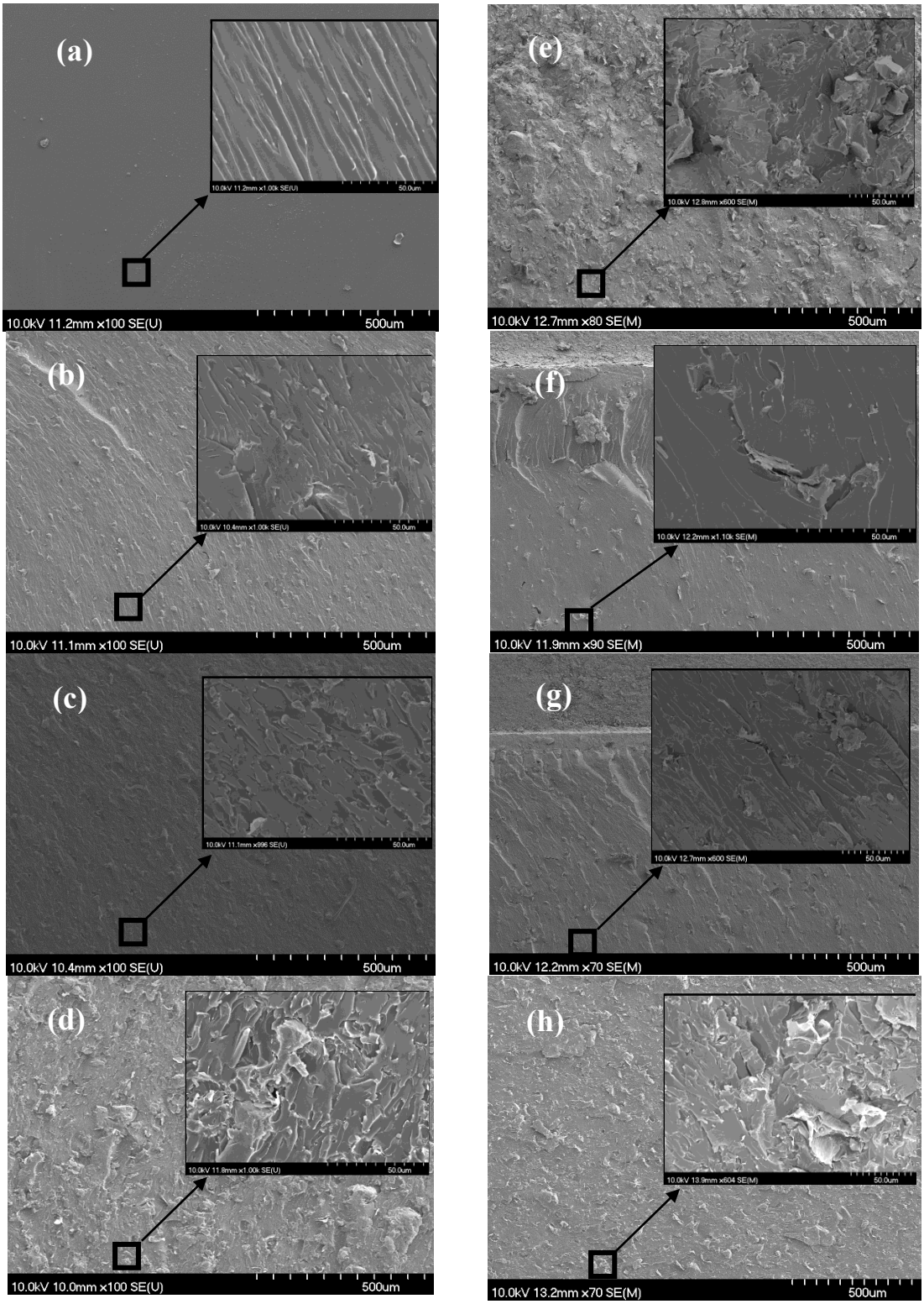

Figure 4-4. Fracture surfaces of GRERs: (a) neat resin, (b) 0.5 wt%, (c) 1wt% , (d) 2wt%, (e) 3wt% and CNT-GRERs, (f) 0.2 $wt\%_{GNP}$+0.3 $wt\%_{CNT}$, (g) 0.7 $wt\%_{GNP}$+0.3 $wt\%_{CNT}$, and (h) 1.7 $wt\%_{GNP}$+0.3 $wt\%_{CNT}$

Figure 4-4 also illustrates the evidence of some GNP particles that have been pulled out of one side of the fracture surface (see white arrows). This would indicate that those GNPs bridged the crack faces under mode-I (opening mode) fracture. Moreover, the arbitrary curvature of the GNPs provides added resistance against the pull-out forces. this phenomenon is called "mechanical lock", created by the physical constraint of individual GNPs by the surrounding matrix[15] The more is the GNP wt% content, the larger would be the pull-out forces; as a result, the summation of pull- out forces would increase the fracture energy required for crack propagation. Consequently, the fracture toughness of the host resin would be increased.

Crack deflection also results in larger fracture surfaces than those created by an un-deflected crack. The energy release rate is a function of the fracture surface area. In order to develop an effective relationship between the critical energy release rate of cracked nanocomposites and fracture areas, one should evaluate the roughness of several sections within the process zone (or the plastic zone) near the crack tip. For that, an AFM (JPK-NanoWizardII-Ultra, Berlin, Germany) was utilized to assess the roughness of several $30\ \mu m\ \times 30\ \mu m$ areas in the vicinity of the crack tips. The tapping method was used to image the scanned sections with relatively high resolution [16]. As shown in Figure 4-5, the average roughness of several $5\ \mu m\ \times 5\ \mu m$ sections near the crack tip were evaluated using the instrument's data-processing software.

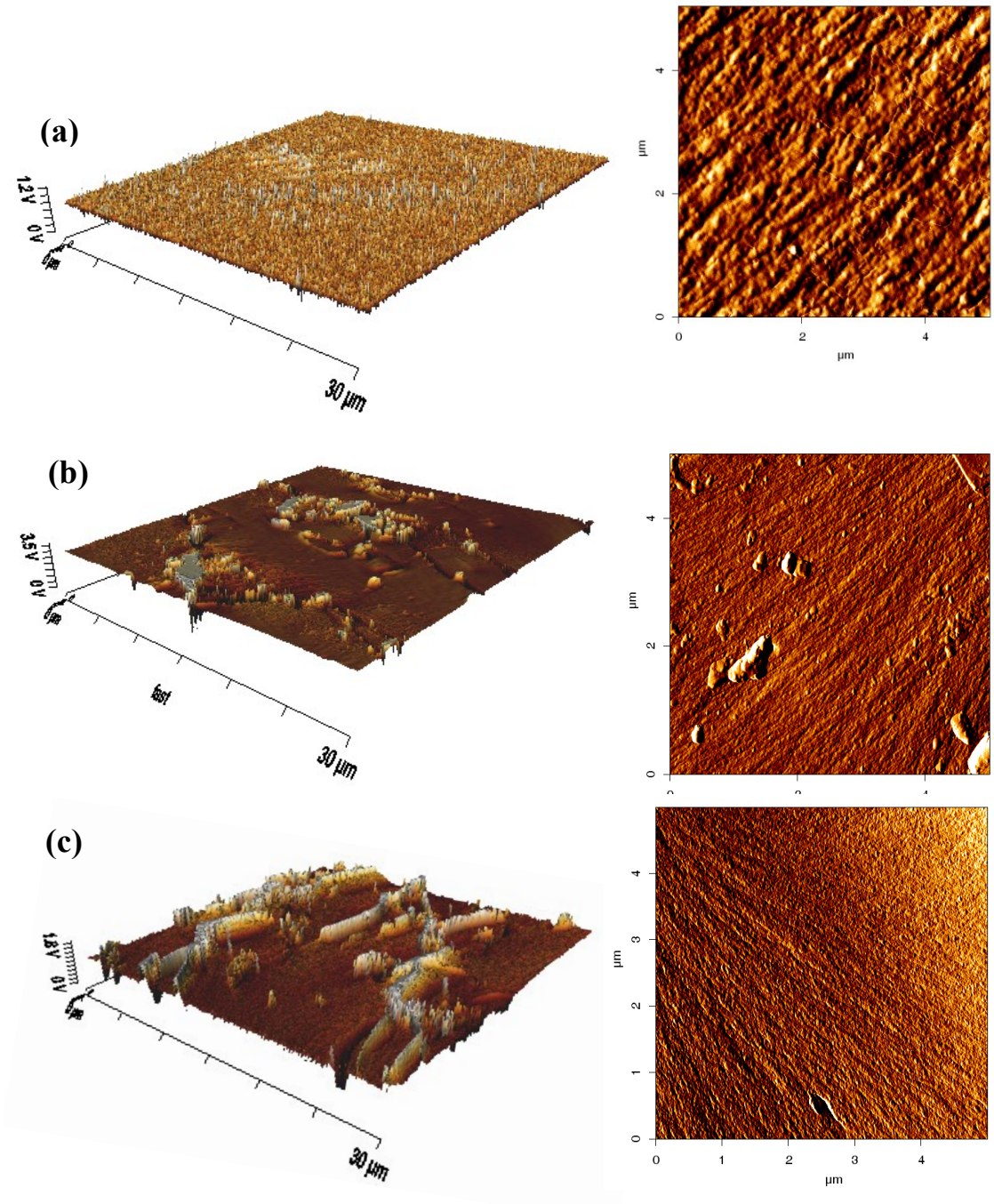

Figure 4-5. AFM micrographs of (a) neat epoxy, (b) epoxy with 0.5 wt% GRERs, and (c) epoxy with 2 wt% CNT-GRERS

Figure 4-6 presents the typical fracture surface roughness morphology of the GRER and CNT-GRER specimens. As seen, the surfaces have relatively rougher appearance in the nanocomposite specimens hosting high concentration of nanofillers.

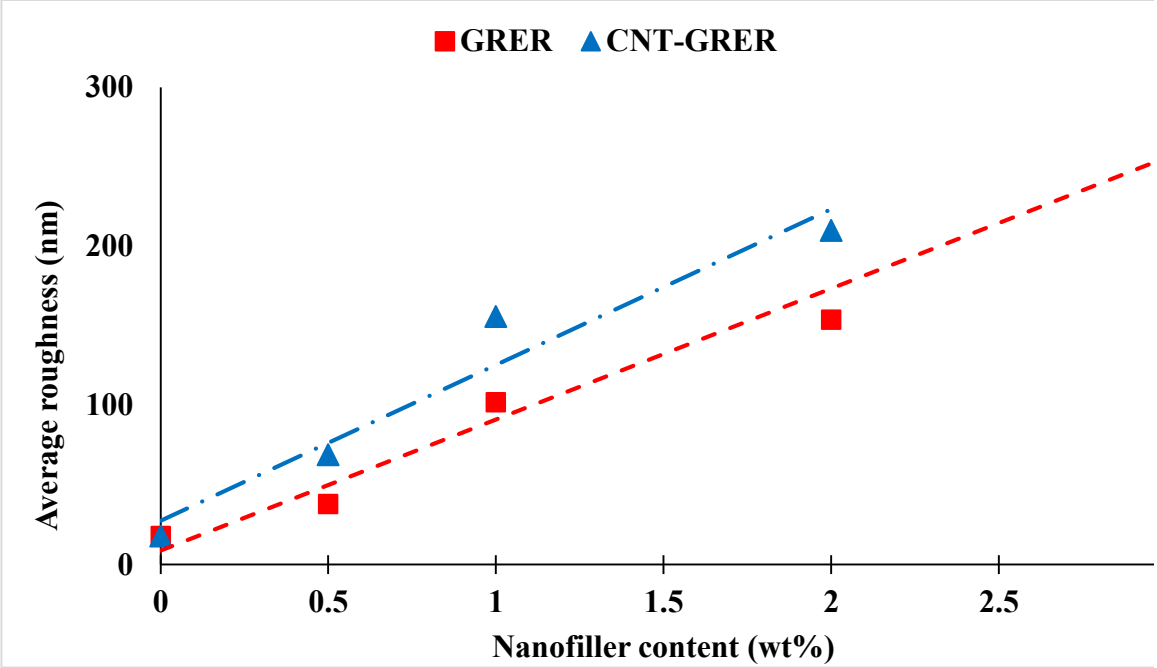

Figure 4-6. Fracture surface roughness of the epoxy nanocomposites

As briefly mentioned earlier, the shear yielding concept also plays an important role in the toughening mechanism of thermoset polymers. Rigid carbon nanoparticles such as GNPs and CNTs can prompt shear yielding in epoxy by facilitating the change in the stress state, which could ultimately transform the plane strain state of the material to plane stress condition. The former condition suppresses the yielding with a larger margin, thus resulting in a smaller plastic zone at the crack tip [17].

It should be noted that the plastic zone is a very small region surrounding the crack tip that rarely could be observed. On assessed fracture surfaces by SEM (Figure 4-7), an inconspicuous bulge region seen in front of a crack tip was seen repetitively in all specimens. The fracture pattern is obviously different rather that could be observed in other parts of fracture surfaces. Furthermore, the height of this area was different in specimens with different GNP content. Assuming this area as process zone, A statistical study was

therefore conducted to investigate the variation in the bulge size with the aid of SEM along the crack tip and the average value was plotted versus GNP content in Figure 4-8.

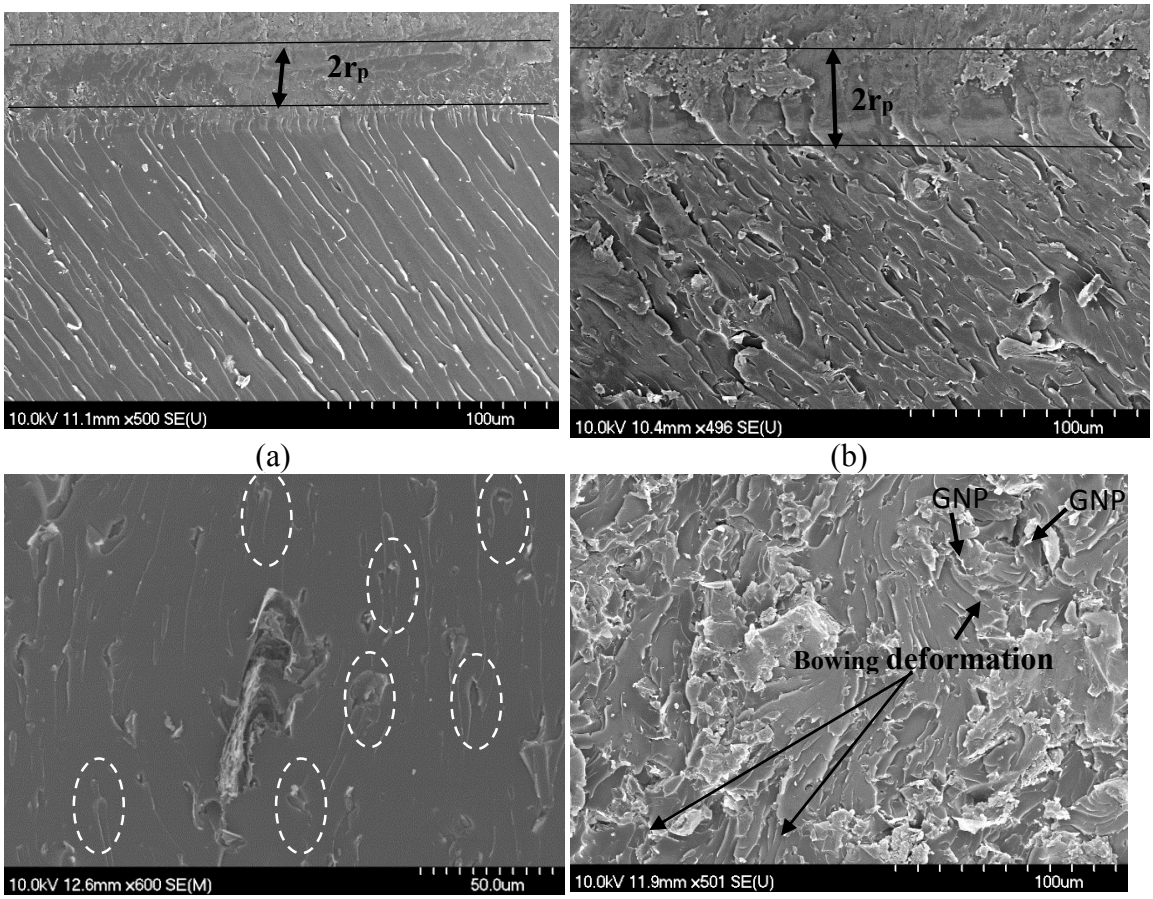

Figure 4-7. SEM micrographs of regions near the crack tip a) neat epoxy b) 0.5wt% GRERs and pinning and bowing toughening mechanism in c) 1wt% GRERs d) 2wt% GRERs (crack path is from the top to bottom of each figure)

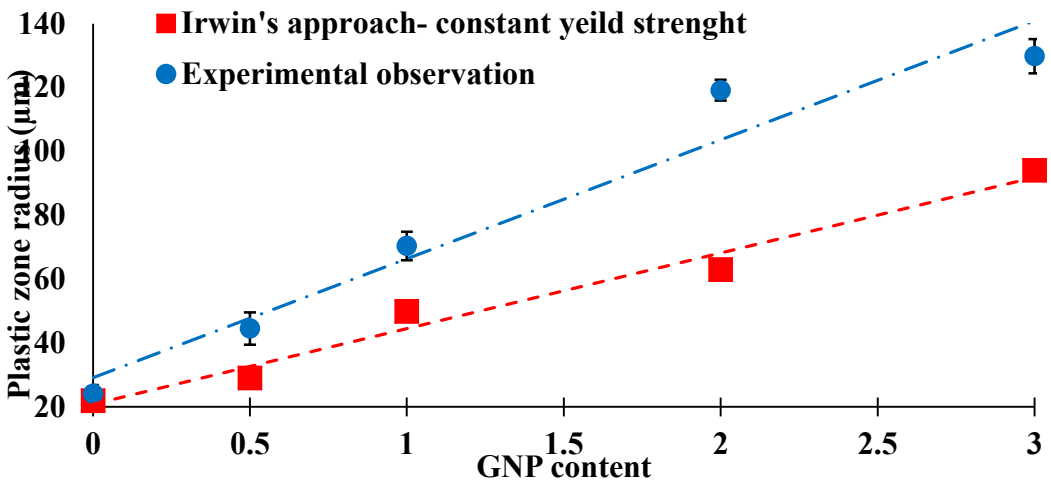

Figure 4-8. Variation of the plastic zone radius as a function of GNP content

The size of the process zone can be assessed by Irwing's approach [17]. Irwing relates the radius of the process zone (PZR), r_p, to material's toughness and yield strength, σ_y, by the following equation.

$$r_p = \frac{1}{6\pi}\left(\frac{K_{IC}}{\sigma_y}\right)^2 \tag{4-5}$$

Figure 4-8 shows the variation in plastic zone's radius evaluated for the GRER specimens as a function of GNP content, based on Irwins approach, and the experimental results (i.e., SEM). It should be noted that a constant value of yield strength was assumed for the nanocomposites when employing the Irwin equation. The results reveals a linear increase in the PZR from 21.9 μm in the neat epoxy to 94.0 μm, in nanocomposites reinforced with 3wt% GNPs.

Figure 4-8 shows good agreement between the results predicted by Irwin's equation and the experimental ones, only for the case of neat epoxy (with less than 8% deviation). The level of agreement in the results, however, suffers as the GNP content increases. This

could be indicative of the fact that Irwin's approach suited for predictions of PZR for brittle materials, which in general, exhibit a very small plastic zone. The fracture toughness of GRERs was increased when higher GNP contents were used. In some of the nanocomposites hosting higher GNP contents, the fracture toughness magnitude exceeded $1Pa.\sqrt{m}$, which suggest the nanocomposites gained ductility, hence developing a larger process zone region. It is believed this is the primary reason for Irwin's equation producing overestimated PZR in specimens hosting higher GNP contents.

The crack pinning was the other toughening mechanism observed on the fracture surfaces of the nanocomposites that included more than 1wt% nanoparticles (see Figure 4-7c). In this toughening mechanism, when a crack front encounters nanofillers, it would have to propagate through a path in between the nanoparticles, which could ultimately result in a bow shape deformation. As can be seen from the micrograph, the bow-shape crack front cannot be as clearly observed in specimens hosting 1wt% GNP particle (shown in Figure 4-7c) as compared with the specimens reinforced with 2wt% GNPs (see Figure 4-7d). Green [18] showed that crack pinning and bowing in epoxy resins reinforced with rigid spherical particles are affected by the particles' average diameter and the average distance among them. The results observed in our investigation indicate that not only is the crack front bowing affected by the distance among the GNPs (as seen on the fracture surfaces of the GNP nanocomposites), but it is also sensitive to the orientations of GNPs. GNPs are disk-like particles. Examination of the specimens' fracture surfaces revealed that the maximum resistance against crack propagation was attained when the majority of most GNPs' surface were aligned perpendicular to the fracture surfaces. One can then postulate that the higher is the aspect ratio of GNPs, the more likely would be the

crack pining and bowing; note that this condition holds only for nanocomposites which include more than a certain amount (wt%) of nanoparticles, such that the inter-particle distance criterion is not grossly violated.

4.5.2 Mode-II fracture

The shear yielding, which is considered as the main toughening mechanism, usually occurs in thermoset resins, when the value of the shear stress near the crack tip reaches a critical limit. Under mode-II fracture, a great amount of energy is expended to develop shear-bands as opposed due to crack extension. As a consequence, mode-II fracture toughness and fracture strength of thermoset resins are always greater than those under mode-I. This observation is supported by the results reported in Table 4-1 and Figure 4-3.

It should be emphasized that evaluation of fracture and toughening mechanisms under mode-II fracture is relatively more challenging when compared to mode-I fracture. When a crack, originally in the mode-II state, starts propagating, it often changes to opening mode (i.e., mode-I fracture). Therefore, shortly after the crack propagation starts, the observed fracture surface patterns become very similar to those observed for Mode-I fracture (Figure 4-4).

The rough surfaces and pulled-out GNPs at a distance relatively far away from the crack tip as seen in Figure 4-9 support the aforementioned statements in regard to the change in fracture mode observed in nanocomposites. Figure 4-9b to 9d illustrate the fracture surfaces, near the initial crack tip in the nanocomposite specimens that ultimately failed under mode-II fracture. In contrast, one can see several cavities and crushed resin regions in the vicinity of the crack tip on the fracture surfaces of the neat epoxy specimens (see Figure 4-9a). The examination of the fracture surfaces reveled that as the GNP content

increased, so did the density of crushed resin regions and cavitations in the process zone. These types of failure could not be observed in the process zone of the specimens that failed in Mode-I fracture. A closer examination of the status of GNPs and matrix in the process zones revealed that most GNPs were debonded from the resin in the direction of the applied shear stress. Subsequently, due to the much higher rigidity of GNP (compared to that of the matrix), the stresses caused several regions of the matrix located in front of GNPs to fracture (see Figure 4-9e and 9f). In consideration of all the differences observed in the process zone of the nanocomposites failed under Mode-I and Mode-II fracture, the following Mode-II fracture mechanism is believed to be associated with the GNP-based nanocomposite.

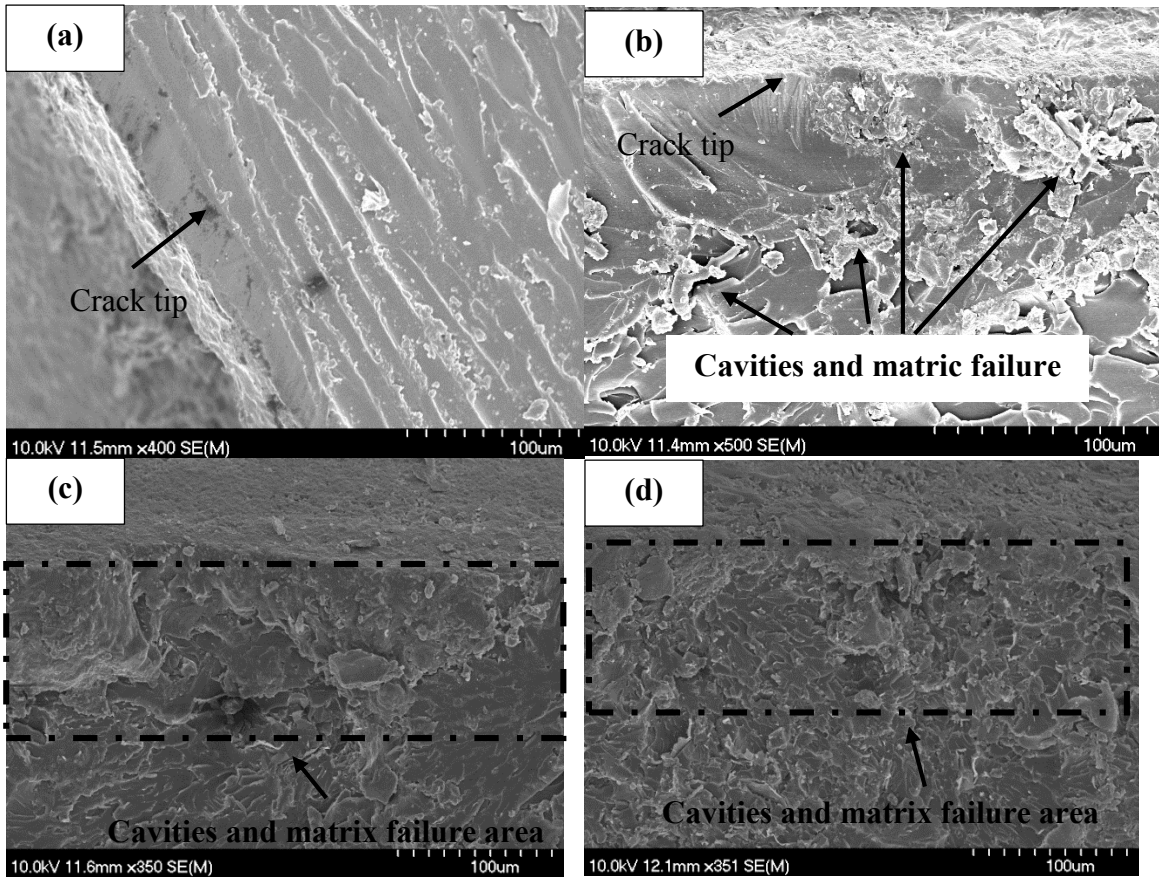

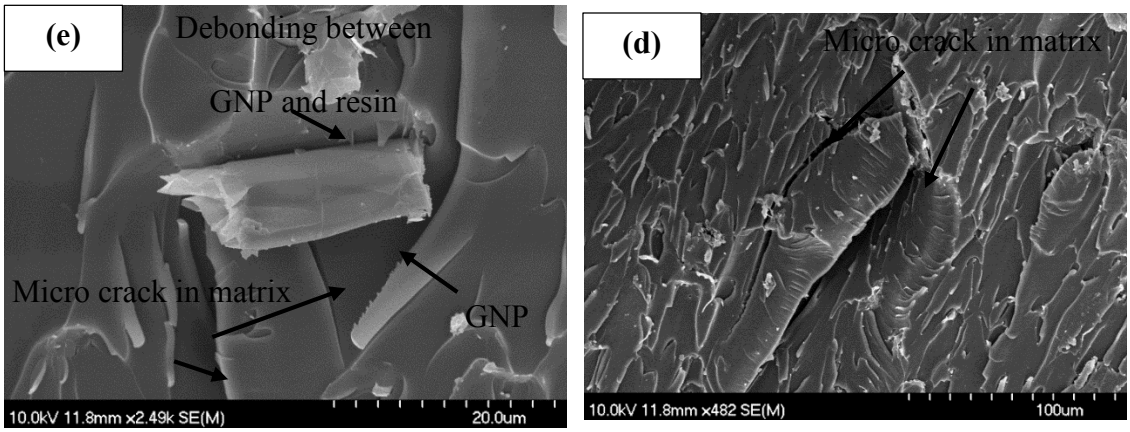

Figure 4-9. SEM micrographs of regions near the crack tip resulting into mode-II fracture a) neat epoxy b) 2wt% GNP

Knowing that GNPs generally possess much greater bending stiffness and strength than epoxy resins, as the shear stress within the process zone increases, the GNPs located within the zone bend and resist the stress, hence create stress concentration at their interfaces with the matrix. As the stress increases, since the GNPs can withstand much higher stress magnitudes than the matrix, when the stress surpasses the strength of the matrix, either the matrix/GNP interfaces would fail, or the matrix in the process zone region would fail cohesively. The accumulation of interface and cohesive failure in the process zone would in turn reduce the plastic deformation near the crack tip, thus decreasing the volume of the process zone. As a consequence, the crack propagation resistance and critical fracture toughness of the nanocomposite would be significantly degraded.

It should also be noted that while GNPs are often assumed to be disk-like particles, SEM images clearly show that GNPs have jagged-shaped perimeter or edges (see Figure 4-1). The jaggedly curved edges provide added resistance against the pull-out forces by the "mechanical lock" phenomenon and bridge the crack. As a result, they enhance the overall toughness of the resulting nanocomposite. Based on the same reasoning, the

contribution of GNPs under mode-II fracture state, which involves sliding of crack surface, becomes minimal.

4.6 Summary and conclusion

In this study, the fracture behavior of an epoxy resin reinforced with different concentrations of GNP particles, and with a hybrid of CNT and GNP particles were investigated and assessed. In addition, the enhancement in toughening mechanism of resin produced by the nanoparticles were evaluated using micrographs produced by SEM and AFM.

The results showed that GNPs could effectively and efficiently enhance mode-I fracture toughness of the epoxy resin; however, the resins' mode-II fracture toughness was slightly degraded, regardless of GNPs' %wt content. The inclusion of combined CNTs and GNPs improved the mode-I fracture toughness of the nanocomposites by a small margin in comparison to the GNP-reinforced nanocomposites. Moreover, the mode-II fracture toughness of the CNT/GNP-reinforced epoxy attained the lowest value when the ratio of GNP to CNT content was less than one (i.e., $GNP_{wt\%}/CNT_{wt\%}<1$).

The fracture surface assessment of the epoxy specimens reinforced with various wt% contents of GNPs and CNTs revealed that the presence of nanofillers increased the plastic deformation, and thus created more shear-bands in the vicinity of crack front under mode-I fracture. The fracture surfaces roughness, and the energy-release rate of the specimens tested under mode-I were also enhanced as the nanoparticles concentration increased. It was therefore identified that crack deflection would be one of the main toughening mechanisms in this type of nanocomposites. In addition, crack pinning and

bridging were observed to be the other mechanisms enhancing the nanocomposites toughness.

On the other hand, the creation of relatively smaller plastic zones, larger density of micro-cracks, nanoparticle/matrix debonding (especially near the crack tips), and the absence of filler-bridging (due to the nature of fracture mode), were the features clearly noted in specimens subjected to Mode-II fracture. In conclusion, in consideration of the collective effects of the above-mentioned phenomena, it could be concluded that overall, the inclusion of GNPs in the epoxy resins somehow has not improved the mode-II fracture toughness of the resin.

4.7 Acknowledgments

This research was funded by the National Science and Engineering Research Council of Canada (NSERC) through the Collaborative Research and Training Experience (CREATE) program. The authors are grateful to the granting agency. The authors also gratefully acknowledge Dr. Jan Rainey and Marie L. Tremblay (Department of Biochemistry & molecular Biology, Dalhousie University) for their cooperation in roughness assessment of the fracture surfaces by AFM.

4.8 References

[1] Bagheri R, Pearson RA. Role of particle cavitation in rubber-toughened epoxies: 1. Microvoid toughening. Polymer. 1996;37:4529-38.

[2] Brunner AJ, Necola A, Rees M, Gasser P, Kornmann X, Thomann R, et al. The influence of silicate-based nano-filler on the fracture toughness of epoxy resin. Engineering Fracture Mechanics. 2006;73:2336-45.

[3] Li B, Zhong W-H. Review on polymer/graphite nanoplatelet nanocomposites. J Mater Sci. 2011;46:5595-614.

[4] Al-Saleh MH, Sundararaj U. A review of vapor grown carbon nanofiber/polymer conductive composites. Carbon. 2009;47:2-22.

[5] Shadlou S, Alishahi E, Ayatollahi MR. Fracture behavior of epoxy nanocomposites reinforced with different carbon nano-reinforcements. Composite Structures. 2013;95:577-81.

[6] Chatterjee S, Nafezarefi F, Tai NH, Schlagenhauf L, Nüesch FA, Chu BTT. Size and synergy effects of nanofiller hybrids including graphene nanoplatelets and carbon nanotubes in mechanical properties of epoxy composites. Carbon. 2012;50:5380-6.

[7] Wei T, Song L, Zheng C, Wang K, Yan J, Shao B, et al. The synergy of a three filler combination in the conductivity of epoxy composites. Materials Letters. 2010;64:2376-9.

[8] Li J, Wong P-S, Kim J-K. Hybrid nanocomposites containing carbon nanotubes and graphite nanoplatelets. Materials Science and Engineering: A. 2008;483–484:660-3.

[9] Fim FdC, Guterres JM, Basso NRS, Galland GB. Polyethylene/graphite nanocomposites obtained by in situ polymerization. Journal of Polymer Science Part A: Polymer Chemistry. 2010;48:692-8.

[10] Ayatollahi MR, Shadlou S, Shokrieh MM. Mixed mode brittle fracture in epoxy/multi-walled carbon nanotube nanocomposites. Engineering Fracture Mechanics. 2011;78:2620-32.

[11] Kinloch AJ. Mechanics and mechanisms of fracture of thermosetting epoxy polymers. Epoxy Resins and Composites I: Springer Berlin Heidelberg; 1985. p. 45-67.

[12] Wetzel B, Rosso P, Haupert F, Friedrich K. Epoxy nanocomposites – fracture and toughening mechanisms. Engineering Fracture Mechanics. 2006;73:2375-98.

[13] Faber KT, Evans AG. Crack deflection processes—I. Theory. Acta Metallurgica. 1983;31:565-76.

[14] Faber KT, Evans AG. Crack deflection processes—II. Experiment. Acta Metallurgica. 1983;31:577-84.

[15] Wong M, Paramsothy M, Xu XJ, Ren Y, Li S, Liao K. Physical interactions at carbon nanotube-polymer interface. Polymer. 2003;44:7757-64.

[16] Simpson GJ, Sedin DL, Rowlen KL. Surface Roughness by Contact versus Tapping Mode Atomic Force Microscopy. Langmuir. 1999;15:1429-34.

[17] Anderson TL. Fracture Mechanics: Fundamentals and Applications, Third Edition: Taylor & Francis; 2005.

[18] Green D, Nicholson P, Embury JD. Fracture of a brittle particulate composite. J Mater Sci. 1979;14:1413-20.

Chapter 5: Effect of Functionalization of Graphene Nanoplatelets on the Mechanical Response of Graphene/ Epoxy Composites

B. Ahmadi-Moghadam, M. Sharafimasooleh, S. Shadlou and F. Taheri

In the journal of Materials and Design, in Press, 2014

DOI: 10.1016/j.matdes.2014.10.047

5.1 Abstract

This study introduces a new strategy for functionalizing graphene nanoplatelets (GNPs) by bonding a silane agent to its structure. In order to evaluate the efficacy of the proposed method, epoxy resin specimens reinforced with silane modified GNPs (G-Si) are prepared at different weight contents of nanoparticles along with three other types of GNPs (unmodified GNP, graphene oxide [GO], and amino functionalized GNP [G-NH_2]). The nanocomposites' mechanical properties, such as the elastic modulus, ultimate strength, modulus of toughness and fracture toughness are evaluated and compared for different types of functionalization. Raman spectroscopy, thermo-gravimetric analysis (TGA) and Fourier transform infrared spectroscopy (FTIR) are employed to characterize the chemical and structural changes of the functionalized GNPs. The results show that nanocomposites containing G-Si and G-NH_2 provide the best results for most of the mentioned properties. The functionalization of GNPs gives the most promising results for fracture toughness of epoxy, showing an 82% increase, and scanning electron microscopy (SEM) micrographs and X-ray diffraction (XRD) analysis reveal that an improved dispersion status is obtained by GNP functionalization.

5.2 Introduction

Graphene nanoplatelets (GNPs) are the new generation of carbon-based nanoparticles that feature remarkable mechanical, electrical and thermal properties [1], along with lower production costs than carbon nanotubes (CNTs) [2]. These characteristics have prompted numerous researchers to focus their efforts on investigating the enhancement of several physical properties of polymers reinforced with GNPs [3-5].

Similar to other types of carbon nanoparticles, the main challenges in the fabrication of GNP-based nanocomposites are achieving a homogeneous dispersion of GNPs in epoxy resin without damaging its structure and improving the quality of the interface between the GNPs and matrix. To address the former issue, the authors previously proposed an optimum and cost-effective dispersion method for GNP/epoxy nanocomposites by taking into account the structural differences between GNP and CNT [6].

In addition to the dispersion method, the functionalization of carbon nanoparticles has been established as an efficient means to achieve superior dispersion of nanoparticles in polymers [7-10]. The functional groups bonded to the surface of nanoparticles are usually chemically compatible with the host resin, thus providing a stronger interface between each nanoparticle and some polymeric matrices. For instance, Reed [11] recently reviewed the interface properties of functionalized CNTs and their matrix, showing that

the main reason for selecting a functional group is to match the surface energy of the filler materials to the polymer matrix.

Although there are a few studies on the functionalization of GNP in the literature, they mainly focused on the electrical and thermal properties of the resultant nanocomposites [12-14], while little attention has been given to their effect on the mechanical response of GNP-based nanocomposites [15, 16]. Moreover, while several attempts have been made towards the functionalization of CNTs, the literature suffers from a lack of a suitable functionalization technique for GNPs. To the best of the authors' knowledge, there has been no study on the functionalization of GNPs by a silane coupling agent (i.e., [3-glycidyloxypropyl] trimethoxysilane).

In this research, a new method is introduced for the functionalization of GNPs that uses a silane agent to increase GNPs' reinforcement efficiency for polymers. To investigate the structural and chemical changes of GNPs due to the functionalizing process, thermo-gravimetric analysis (TGA) and Raman spectroscopy were utilized. To compare the competency of the proposed silane function, nanocomposites reinforced with silane-functionalized GNPs (referred to as G-Si hereafter), along with three other types of GNPs, namely, unmodified GNPs (referred to as UG hereafter), graphene oxide GNP ((referred to as GO hereafter), and amino functionalized GNP (referred to as G-NH_2 hereafter).

Nanocomposites with different weight contents (i.e., 0.25, 0.5 and 1 wt%) of nanoparticles were prepared and their mechanical properties, including the tensile properties and fracture toughness, were assessed. Moreover, the effects of functionalization on the dispersion status of GNPs and the morphology of fracture surfaces were qualitatively investigated using scanning electron microscopy (SEM).

5.3 Methodology

5.3.1 Materials

The unmodified GNPs (UG) with an average thickness of 7 nm and average particle diameter of 25 μm, supplied by the XC Science (Lansing, MI), were used in this research. G-NH_2 with an average thickness of 5nm and average diameter of 8 μm were obtained through Cheap Tubes Inc. (Battleboro, VT). Araldite LY1564 (Bisphenole-A) epoxy resin was used throughout this study along with Aradur 2954 (cycloaliphatic polyamine) hardener, which is available through Huntsman Co. (West Point, GA). A purified silane coupling agent, (3-glycidyloxypropyl) trimethoxysilane, used for functionalizing the GNPs, was obtained from Sigma-Aldrich Canada Co. (Oakville, ON).

5.4 GNP functionalization method

To fabricate the G-Si, the first step was to reflux 1.0 g of UGs with 200 ml of 40% nitric acid for 4 hours at 80 ℃. The GNPs were then thoroughly washed with distilled water to remove untreated acid until the pH became neutral, resulting in GO. Next, 15.0 g of 98%

purified silane coupling agent, 15.0 g of methanol, 0.15 ml glacial acetic acid and 0.75 ml distilled water were mixed together, after which 20 ml of this mixture and 1.0 g of the GO obtained through the previous step were added to 200 ml of toluene and stirred at room temperature for 64 hours. The mixture was filtered and then washed first with toluene and subsequently with methanol to obtain G-Si. Finally, the G-Si was dried for 4 hours at 80℃.

5.5 Nanocomposite preparation

As stated, GNPs with four different surface modifications (namely, UG, G-NH_2, GO, and G-Si) were used in the present study. The same manufacturing method was utilized for nanocomposites reinforced with all types of GNPs. Firstly, nanoparticles were dispersed in the epoxy resin according to an established method using a three-roll mill [6] with different GNP weight contents (i.e., 0.25, 0.5 and 1 wt%). Then, the hardener was added to the GNP-resin slurry and mixed for 15 minutes using a mechanical stirrer at 150 rpm. The mixture was subsequently degassed, poured into molds, and cured at 60 ℃ for 1 hour, followed by post-curing at 120 ℃ for 8 hours.

5.6 Characterization

The untreated GNPs, and modified GNPs (GO and G-Si) were subjected to chemical analysis using TGA by a TG-209-F1-Libera thermogravimetric analyzer (NETSCH, Burlington, MA), Raman spectroscopy analysis by a DEXR Smart Raman Spectrometer (Thermo Scientific, Waltham, MA) and also FTIR analysis by Bruker Tensor 27 FTIR (Bruker, Madison, WI) to verify the effective bonding between the silane coupling agents and the GNPs.

Tensile tests were carried out according to the ASTM-D638 standard to assess the materials' tensile properties (i.e., the elastic modulus, ultimate strength, ultimate strain, and strain energy). In addition, the fracture toughness of pure epoxy and nanocomposites was evaluated according to ASTM-D5045. All mechanical tests were performed at room temperature using a MTS servo-hydraulic test machine (model 312.21) with a 100 kN load cell.

To further explore the influence of functionalization on the structure of GNPs, the dispersion quality of GNPs in nanocomposites and failure mechanisms, the fracture surfaces of pure epoxy and nanocomposites were thoroughly examined using the field emission SEM S-4700 (Hitachi, Dallas, TX). In addition, a high speed Bruker D8 Advanced XRD system (Bruker, Madison, WI) was used to extract the XRD signals of nano particles and nanocomposites to evaluate the dispersion quality of GNPs in nanocomposite.

5.7 Results and Discussion

5.7.1 Chemical analysis

The Raman spectra of UG, GO and G-Si excited with a 532 nm laser are shown in Figure 5-1. The spectra of unmodified GNPs consists of the G-band at about 1580 cm^{-1} and a weak defect band (known as the D-band) at about 1370 cm^{-1}. The G-band and D-band have different intensities and are shifted by functionalizing GNPs. The G-band shift could be indicative of a change in the amount and type of chemical groups attached to GNPs and/or increased oxygen content in the GNP structure [17]. It has been observed that when a GNP's thickness is increased, the G-band position shifts to a lower energy [18]. Although the D-band is normally very weak in both graphite and graphene in comparison to carbon

nanotubes [18], the intensity of the D-band (I_D) is directly proportional to the level of defects in the sample. In other words, the larger the I_D, the higher is the intensity of atomic-scale defects. The shift in the D-band after the functionalization process is negligible compared to the UGs, which could indicate that this process did not introduce extensive defect and damage to the GNPs' structure.

The ratio of I_D/I_G was increased by functionalization of GNPs with I_G being the intensity of the G-band (see Table 5-1). This may be attributable to the functionalization process that increases the GNPs' structural disorder intensity by formation of covalent bonds [19]. The increasing trend of I_D/I_G was also reported by Cho et al. [15] for other groups of chemical functions of GNPs.

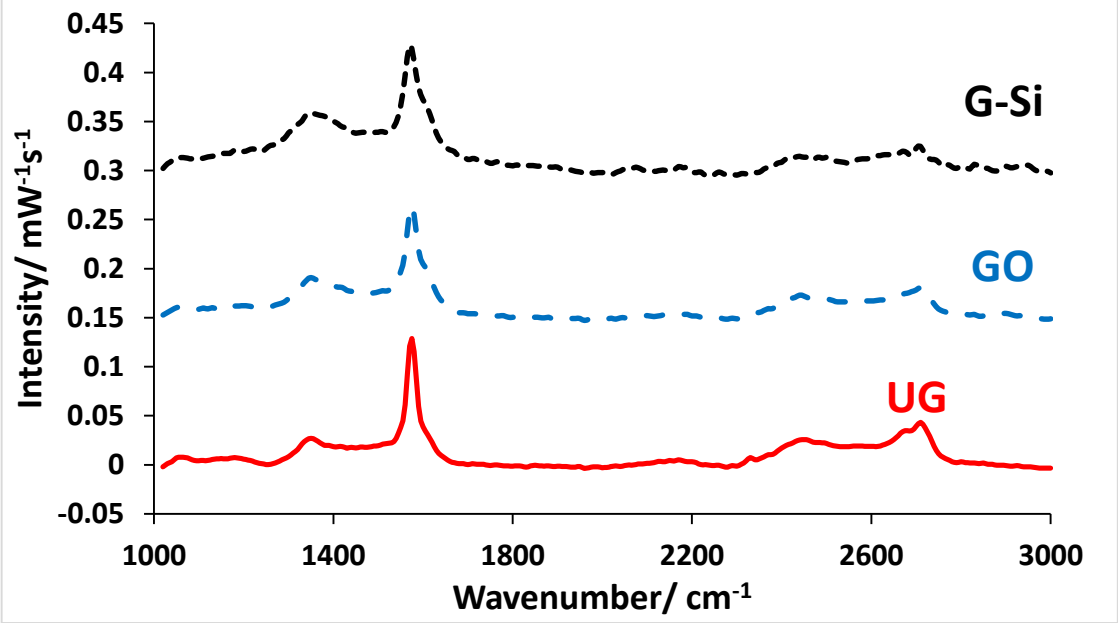

Figure 5-1.The Raman Spectra of as-received and functionalized GNPs

Table 5-1.Displacement and intensity ratios of GNPs obtained through the Raman spectroscopy

Specimen ID	D-band (cm^{-1})	G-band (cm^{-1})	I_D/I_G
UG	1371	1580	0.168
GO	1370	1579	0.296
G-Si	1370	1580	0.478

TGA analysis was also conducted to obtain further information with respect to the degree of functionalization achieved for the GNPs. Figure 5-2 illustrates the weight-loss curves of UG, GO, and G-Si. By increasing the temperature from 250 ℃ to 600 ℃, the weight loss of UG, GO and G-Si is 15%, 25% and 40%, respectively. Moreover, the residual weight of GO and G-Si is, respectively, 4% and 10% of the original weight of as-received GNP. The deferential weight-loss curve of pristine G-Si consists of a small peak at approximately 373 ℃ in addition to the main peak at 793 ℃. This secondary peak can also be observed in the deferential weight-loss curve of unmodified GNP, but it appeared at 420 ℃. As shown in Figure 5-3, silane does not exist in UGs whereas in G-Si, silane and oxygen are clearly recognized as major components after carbon. Therefore, the existence and shift of the secondary peak on the deferential weight-loss curve of G-Si could be indicative of bonding between GNP and the silane coupling agent. Considering the clear weight loss difference in the specific temperature range between the unmodified and functionalized GNPs, along with the remaining residual weight of processed GNPs and the existence and shift of secondary peaks in deferential weight-loss curve of functionalized GNPs, it could be concluded that the functional group was successfully bonded to the GNPs. Zhu et al. [20] obtained the same trend with silane-functionalized carbon nanotubes.

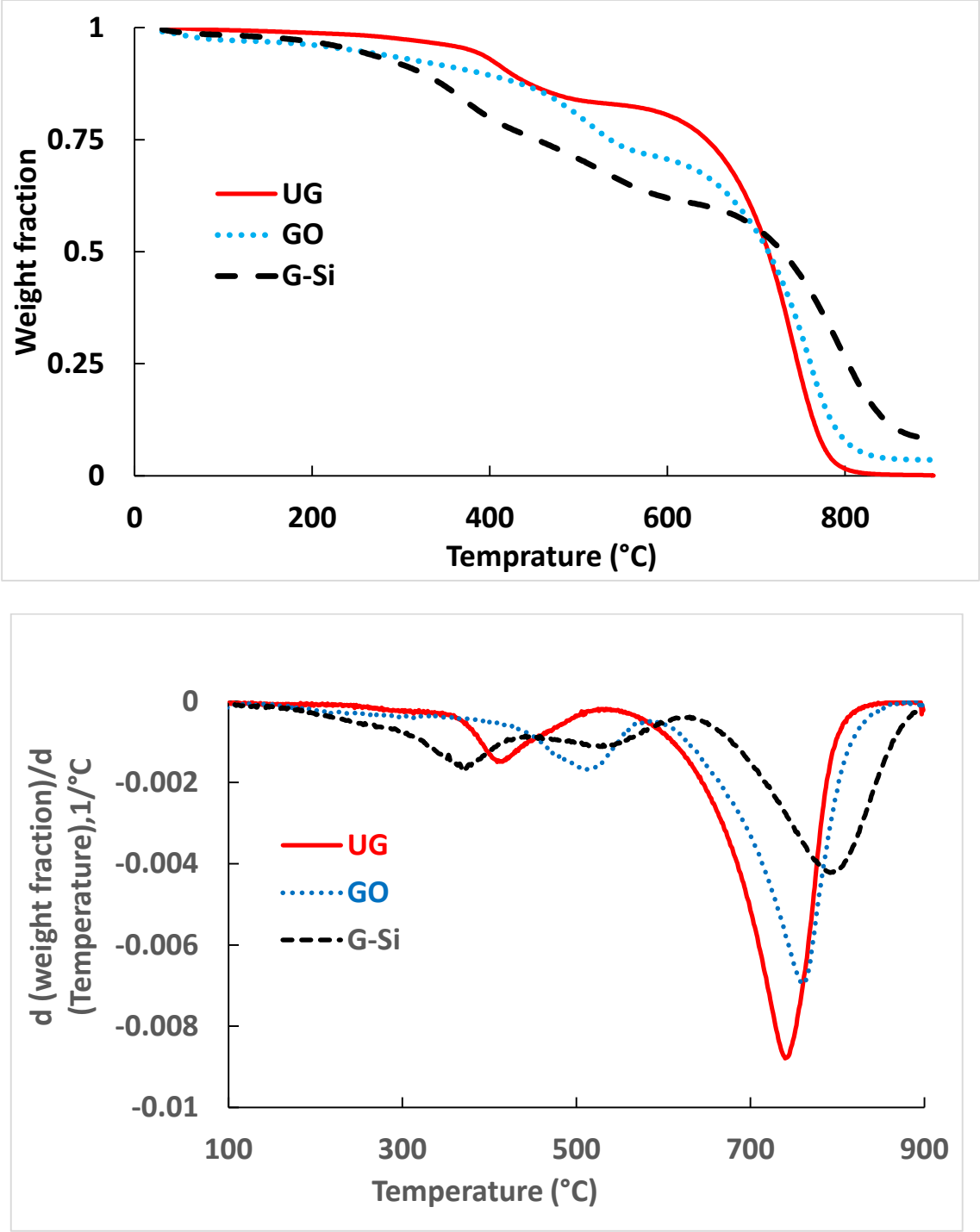

Figure 5-2. Weight-loss curves obtained by TGA

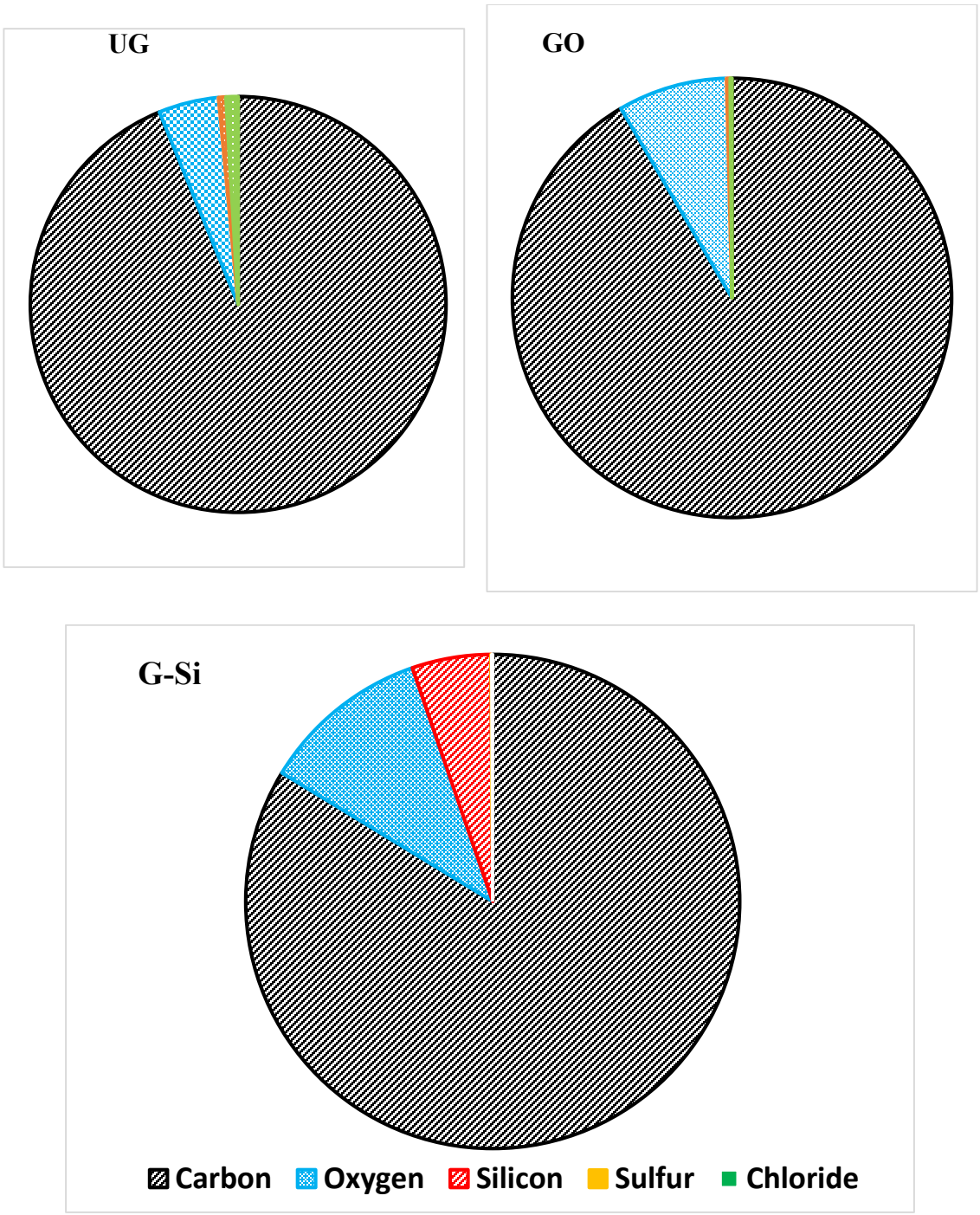

Figure 5-3. EDS obtained from SEM analysis of the unmodified and modified surfaces of GNPs

To improve the existence of chemical bond between the silane agent and GNP, the comparison of FTIR spectra of UG and G-Si is shown in Figure 5-4. In addition to all peaks

that could be observed in UG spectrum such as OH group at 3423 cm^{-1} and out-of-plane vibration of C=O at 1195 cm^{-1} and C-H band at 2922 cm^{-1} and 2854 cm^{-1}, the appearance of two new peaks at 1045 cm^{-1} and 1097 cm^{-1} assigned to the Si-O-Si and Si-O-C, respectively, indicates the successful chemical functionalization.

It should also be noted that G-NH_2 was directly purchased from a well-known vendor (i.e., Cheap Tube Ltd). In the case of this GNP, the authors relied on the following information provided by the vendor in reference to the primary functionality of the GNP. The GNP's main functionality is N=H and the other minor functionalities are N-H, O=C-N-H2 and C≡N. The authors did not carry out any tests to verify the aforementioned functionalities.

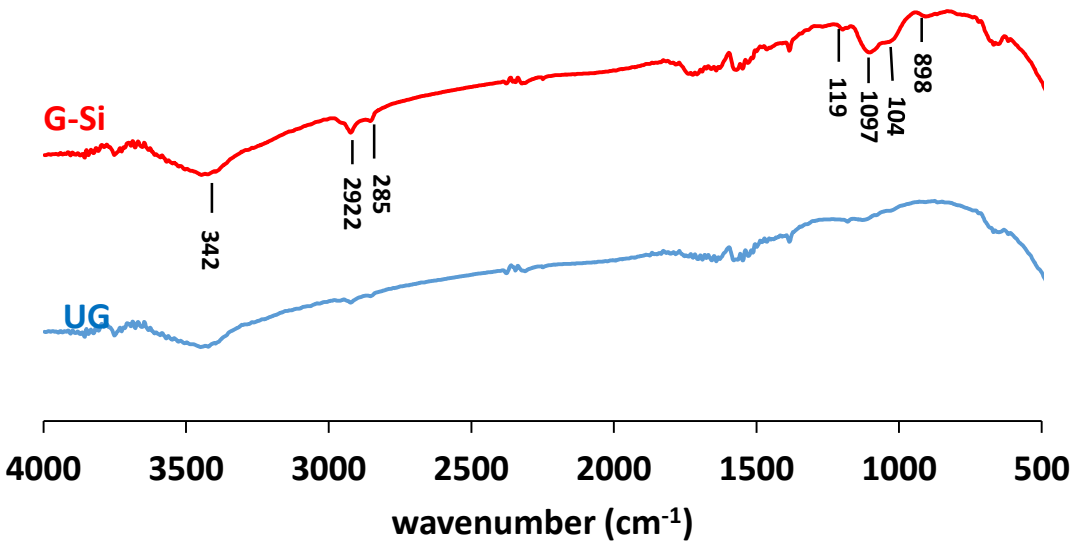

Figure 5-4. FTIR spectra of UG and G-Si functionalized GNPs

If the functionalization process is not conducted properly, it may lead to damage and fracturing of nanoparticles, thus reducing their effective length. On the other hand, it has been shown that the dimensions of GNPs could noticeably affect the mechanical properties of the resultant nanocomposites [21]; that is, the larger aspect ratios of nanoparticles could lead to higher mechanical properties of nanocomposites [6, 22].

As discussed earlier, the small changes in the D-band of the Raman spectra may indicate that the functionalization process did not introduce any defects to the GNPs' structure. To confirm this interpretation, high-magnitude SEM micrographs were taken from the unmodified and functionalized GNPs (see Figure 5-5). The extensive study of the SEM micrographs demonstrated no significant alteration in the GNPs' average diameter after functionalization. It is also noteworthy that the small shift of the G-band in the Raman spectra of all types of GNPs could indicate that the thickness of GNPs was not altered after the functionalizing process [18].

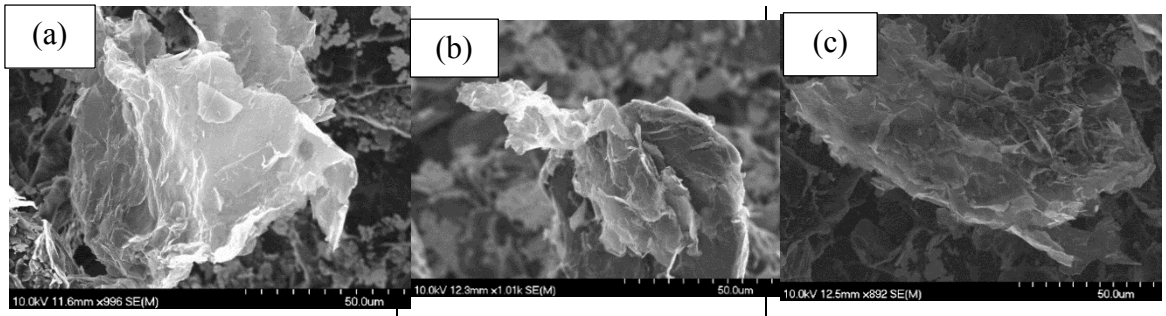

Figure 5-5. Typical SEM micrographs of GNPs: a) pristine GNP, and b) GO c) G-Si

5.7.2 Tensile properties

Following the successful functionalization of GNPs, the effect of different functionalized GNPs on the mechanical properties of the host resin were experimentally

investigated. Tensile tests were performed on dog-bone specimens, and various mechanical properties were extracted and compared.

The elastic modulus and the ultimate strength of the nanocomposites are depicted in Figure 5-6. The results reveal that, in general, the inclusion of GNPs has enhanced the elastic modulus of the host epoxy resin. In general, the functionalized nanocomposites reinforced with each %wt content of functionalized GNPs (i.e., G-Si and G-NH_2) provided a higher elastic modulus than that obtained using UG or GO. Moreover, the highest value for the elastic modulus of nanocomposites was obtained at 1 wt% for the G-Si nanocomposite. These results clearly demonstrate that the functionalization of GNP significantly impacts the stiffness of nanocomposites. However, at the lowest GNP content (i.e., 0.25 wt%), the elastic modulus of nanocomposites did not vary noticeably compared to that of the neat epoxy. By increasing the nanoparticle contents from 0.25 wt% to 0.5 wt%, an average growth of 14% in the elastic modulus was observed for nanocomposites hosting the surface functionalized GNPs and only 4% increase of elastic modulus obtained in nanocomposite hosting the as-received GNPs. However, by increasing the amount of nanoparticles from 0.5 wt% to 1 wt%, the enhancement in the nanocomposites' stiffness was not noticeable.

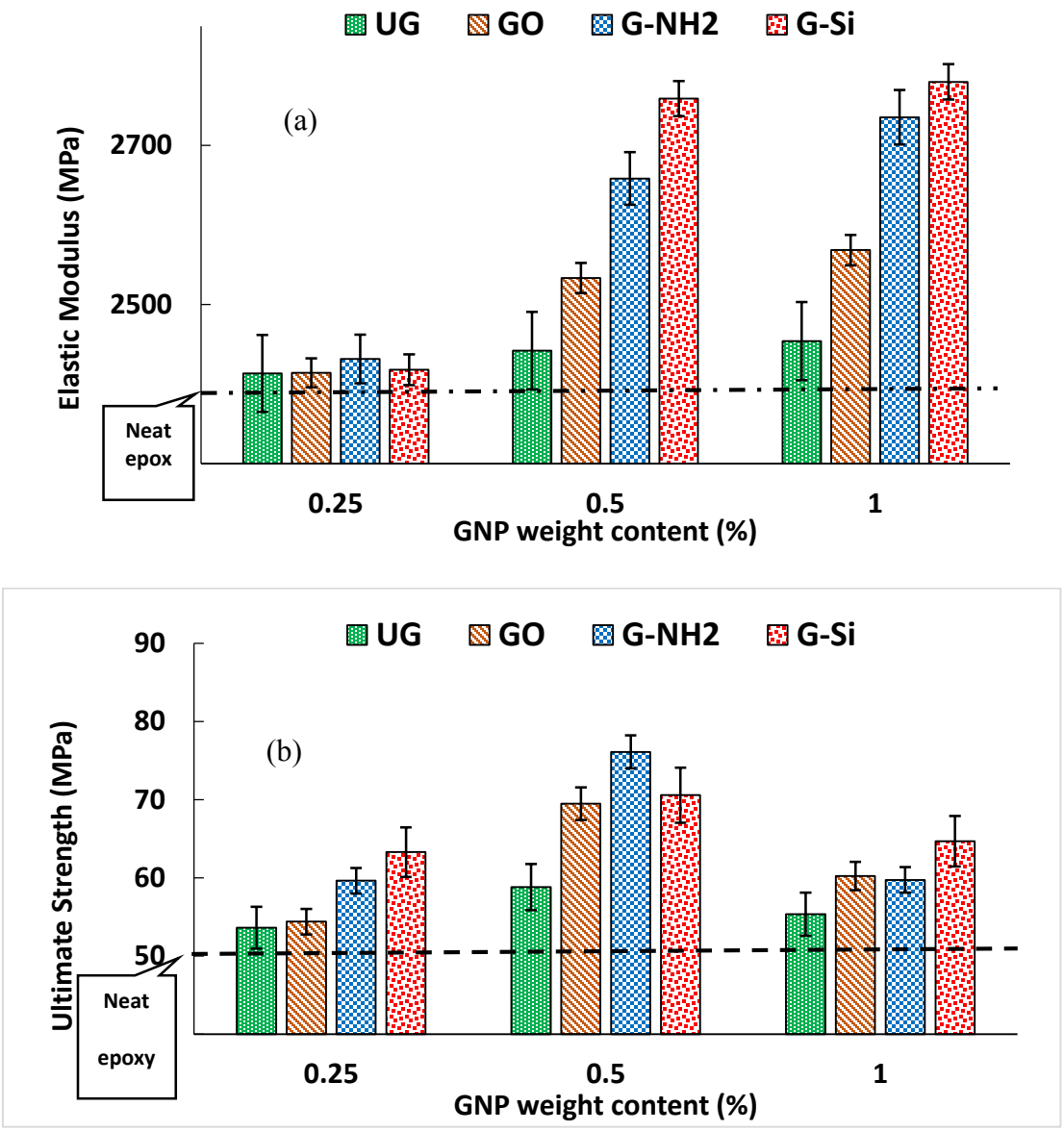

Figure 5-6. The tensile properties of neat epoxy and various types of nanocomposites (a) Elastic modulus (b) Ultimate strength

By inclusion of 0.25, 0.5 and 1 wt% of any type of GNPs in the epoxy, the ultimate strength of nanocomposites was increased by an average amount of 15%, 38% and 21%, respectively (see Figure 5-6(b)). Thus, it could be concluded that the inclusion of 0.5 wt% GNPs (regardless of the type of GNP), provided the best results in regard to

nanocomposites' ultimate strength. Figure 5-6) also illustrates that the functionalized GNPs, regardless of type, are more effective for increasing the ultimate strength of epoxy compared to non-processed GNPs.

5.7.3 Toughness and ductility

The ability of materials to absorb energy and deform plastically without fracturing could be characterized by evaluating the material's modulus of toughness (MT). An evaluation of MT in nanocomposites (Figure 5-7(a)) indicated that the highest MT was obtained at 0.5 wt% of GNP, regardless of the nanoparticle type. A comparative analysis of the results shown in Figure 5-7(a) reveals that the amino-functionalized GNPs produced the greatest enhancement on the absorbed energy of the nanocomposites, which in turn created the largest MT in nanocomposites. Moreover, the nanocomposites fabricated by surface functionalized GNP showed more capacity in absorbing energy (i.e., more MT), in comparison to those fabricated by as-received GNPs.

Figure 5-7(b) illustrates the plastic strain energy, normalized with respect to the total strain energy of each nanocomposite as an attribute of the capacity of the materials to undergo plastic deformation and exhibit ductility. The results indicate that approximately 35% of the entire absorbed energy was converted to plastic deformation in the neat epoxy resin specimens. In contrast, the inclusion of 0.25 wt% GNPs increased the plastic contribution towards the absorbed energy by a significant average margin of 65%. The best results were obtained from the nanocomposites containing G-Si and G-NH_2. Increasing the GNP content from 0.25 wt% to 0.5 wt% led to a significant growth in the absorbed plastic energy of the nanocomposites. However, with the addition of GNPs up to 1 wt%, the plastic energy did not change noticeably.

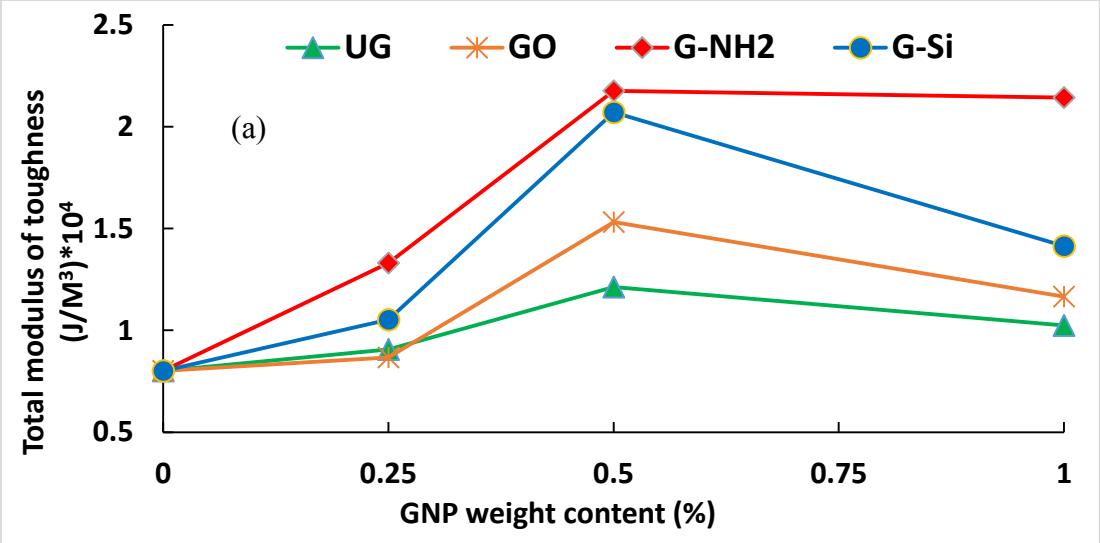

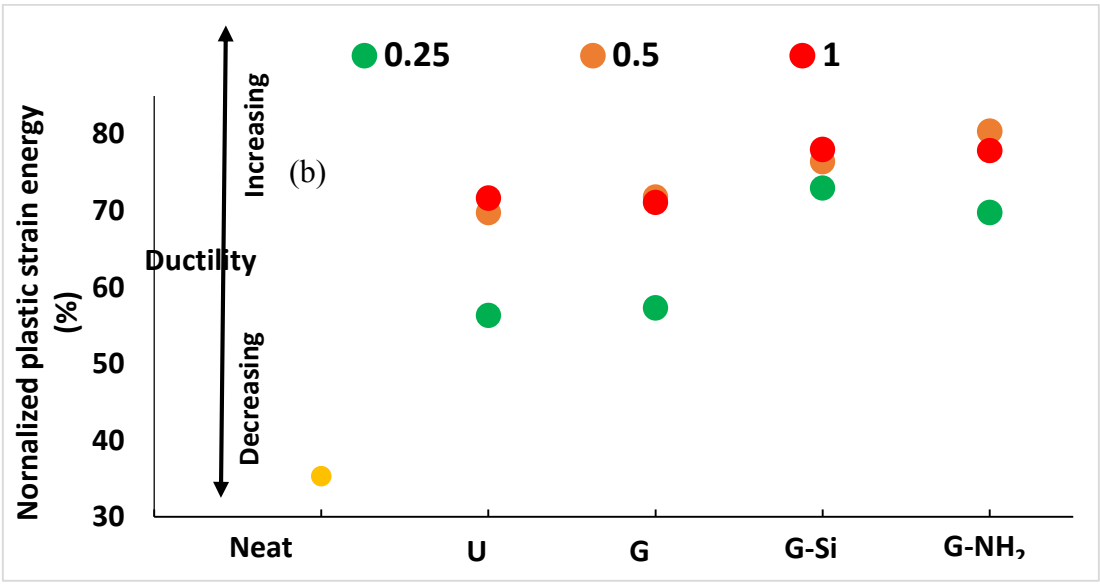

Figure 5-7. Data signifying ductility of nanocomposites (a) total modulus of toughness (b) normalized plastic strain energy

5.7.4 Fracture toughness

Fracture toughness tests were performed on the specimens made of pure epoxy and all the types of nanocomposites. The results, as depicted in Figure 5-8, indicate that in general, the incorporation of GNPs in epoxy increases its fracture toughness notably. By the addition of 0.25 wt% of any types of GNPs, the fracture toughness increased by an average of 15%. The nanocomposite reinforced with G-NH_2 provided the highest value in the mentioned GNP concentration. The maximum value for fracture toughness of nanocomposites obtained at 0.5 wt% by functionalized GNP. G-Si and G-NH_2 produced the highest efficiency in enhancement of fracture toughness of epoxy (i.e., 86% growth). By increasing the GNP content to 1 wt%, the fracture toughness degraded, regardless of the type of GNP used. A similar trend was reported for nanocomposites reinforced with carbon nanotubes [23].

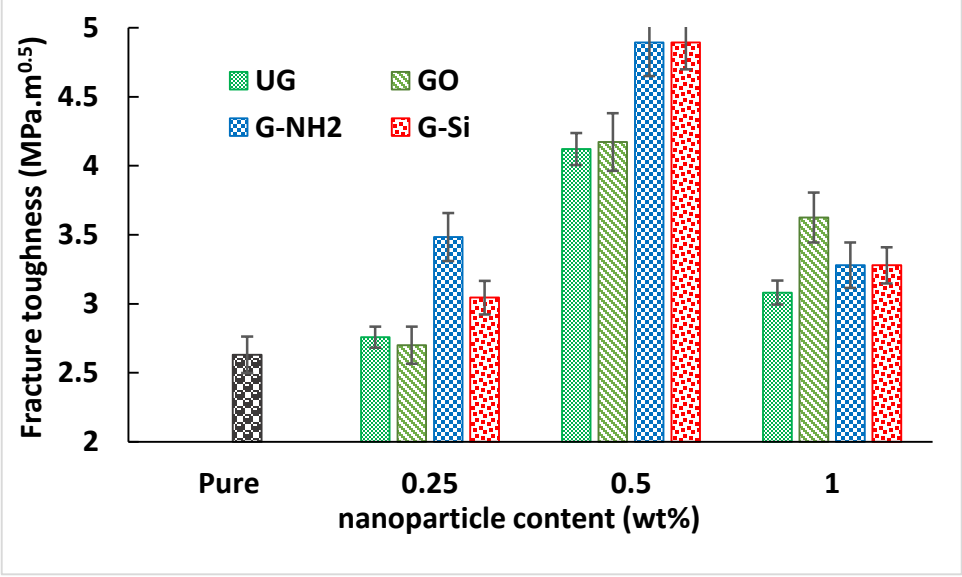

Figure 5-8. Fracture toughness of the neat epoxy and nanocomposites

In summary, the results indicate that functionalization clearly augments the efficiency of GNP as reinforcement. Among the different types of surface functionalizations tried on the GNPs (i.e., oxidation, amino-functionalization and silane-functionalization), the nanocomposites fabricated by G-NH_2 and G-Si treatments generally yielded better fracture toughness. Although, our trials indicated that at 1 wt% concentration, the GO produced the best outcomes when considering the fracture toughness values, the optimum collective mechanical properties (i.e., elastic modulus, ultimate strength and fracture toughness) were obtained by 0.5wt% G-NH_2 and G-Si functionalization within our trials. The functionalization of nanoparticles improves their effectiveness by primarily increasing the interface strength between the matrix and nanoparticles and also facilitating their dispersion in the matrix. The contribution of functionalization can be better understood by studying the mechanisms through which GNPs enhance the fracture toughness of their host resin. Some evidence for these mechanisms can be witnessed in the SEM micrographs that are presented in the next section.

5.8 Fracture Surface Micrographs

The roughness of the fracture surface of a specimen provides valuable information about the behavior (i.e., brittle or ductile) of the material and the crack deviation mechanism. Crack deviation takes place when micro-cracks encounter stiff GNPs, and consequently, has to by-pass them by seeking alternate paths. This in turn leads to a change in the crack growth plane, resulting in consumption of the energy. As illustrated in Figure 5-9, increasing the contents of any types of GNPs significantly increased the roughness of the surface compared to that in pure epoxy, which is clearly a sign of a crack

deviation mechanism. In contrast, the roughness of specimens enhanced with the same amount of GNPs of different types did not show any significant differences. This may be attributed to the fact that the number of crack deviations occurring during crack propagation has not been substantially altered by different functionalizations. This phenomenon is not contrary to one's expectations, since the number of deviated cracks is predominantly governed by the number of particles the crack encounter.

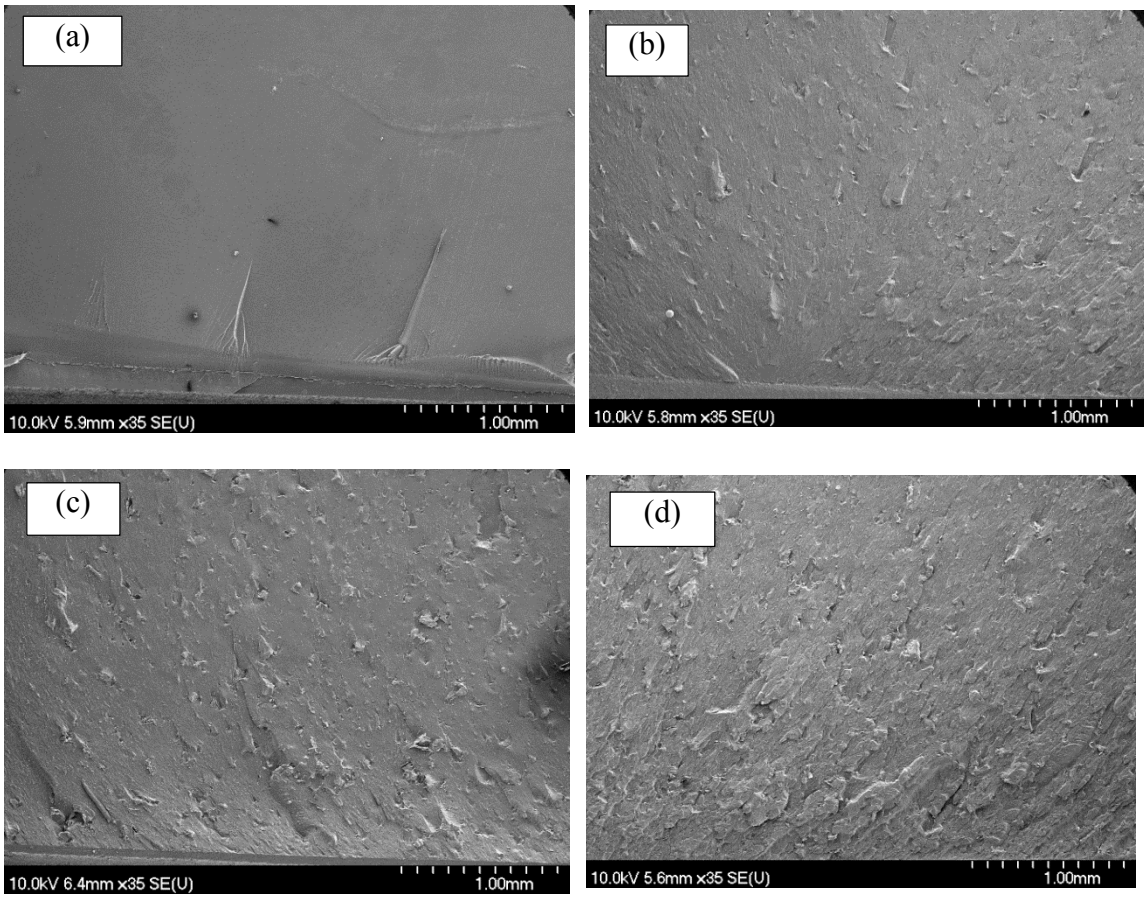

Figure 5-9. Low magnification micrographs of the fracture surfaces of (a) the neat epoxy and nanocomposites reinforced with (b) 0.25 wt%, (c) 0.5 wt%, and (d) 1 wt% GNP-Si (Note: the crack growth direction is from bottom to top)

Micrographs taken at higher magnifications revealed that the size and number of GNP agglomerations spotted in the specimens reinforced with GNP functionalized by UG

and GO were generally higher than those with G-Si and G-NH_2 (see Figure 5-10); however, a greater number of SEM micro-graphs are required to depict the dispersion quality of GNP in the matrix.

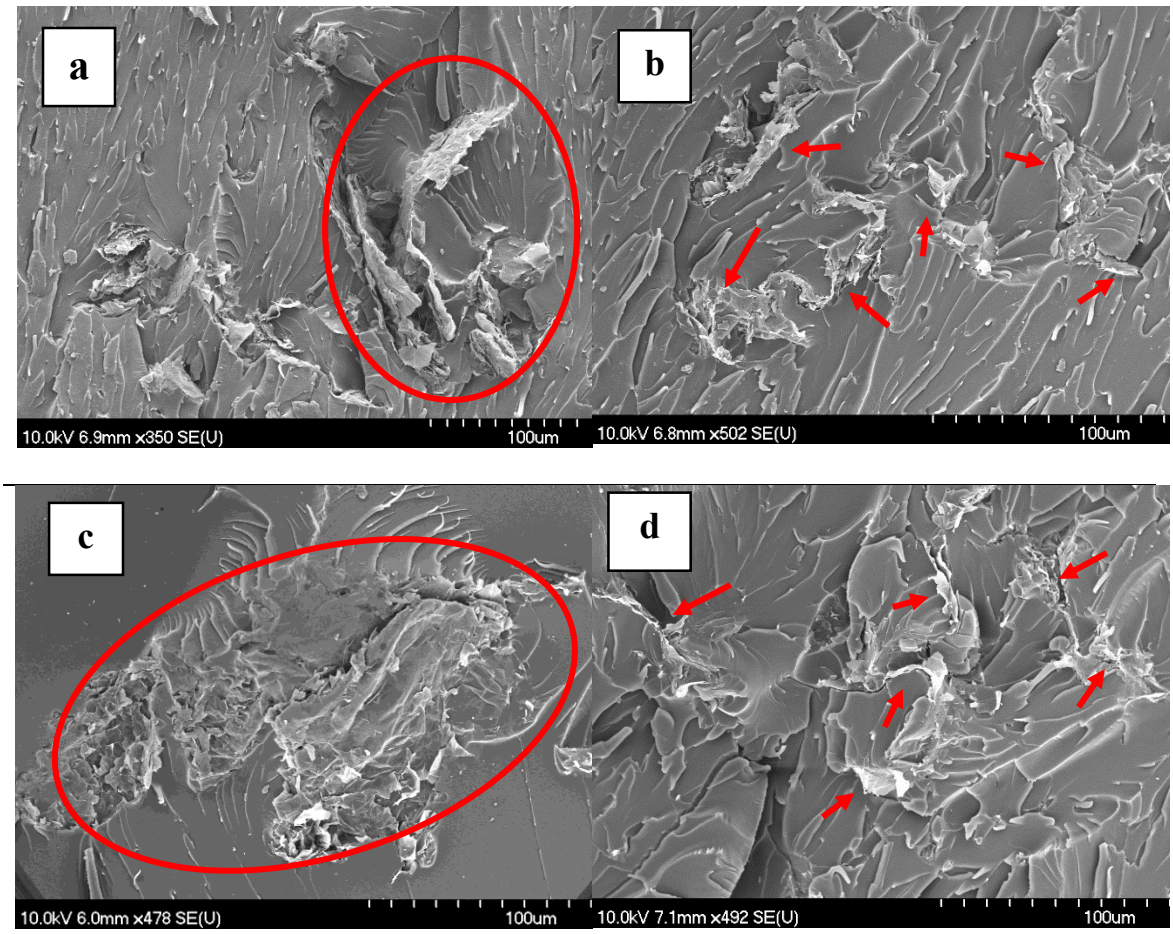

Figure 5-10. Typical dispersion status of nanocomposites reinforced with (a) 0.5 wt% UG, (b) 1wt% G-NH_2, (c) 0.5 wt% GO and (b) 1 wt% G-Si (Note: the crack growth direction is from bottom to top)

A comparative study of XRD patterns of nanocomposites fabricated with the as-received GNPs and differently method of GNP functionalization could globally illustrate the quality of GNP dispersion. In general, the disappearance of characteristics peaks of GNPs in XRD patterns of such nanocomposites would indicate that nanoparticles are

uniformly dispersed within the matrix [24]. Figure 5-11 shows the XRD patterns of the various nanocomposites processed in this study. As can be seen, there exists a peak at 26.6 degree in the XRD patterns of specimens fabricated by as-received GNPs and GO functionalized, which is considered as a characteristic feature of GNPs [25]. It should be noted that the XRD results confirm the patterns seen in the SEM images in Figure 5-10, for the above-mentioned GNPs; the results further confirm the evidence of some GNP agglomerations. It can be seen that the XRD patterns of nanocomposites fabricated by G-NH_2 and G-Si, as shown in Figure 5-11 resembles very closely to the XRD pattern of the neat epoxy. Further, the peak at 26.6^o for UG/epoxy composites cannot be seen for functionalized graphene/epoxy composites. This indicates that functionalized graphene shows, better dispersion than unmodified graphene. These results point to the effect of functionalization on the dispersion status of the GNPs. Improved GNP dispersion is one of the factors that enhances the mechanical properties of nanocomposites reinforced with GNPS functionalized with G-Si and G-NH_2.

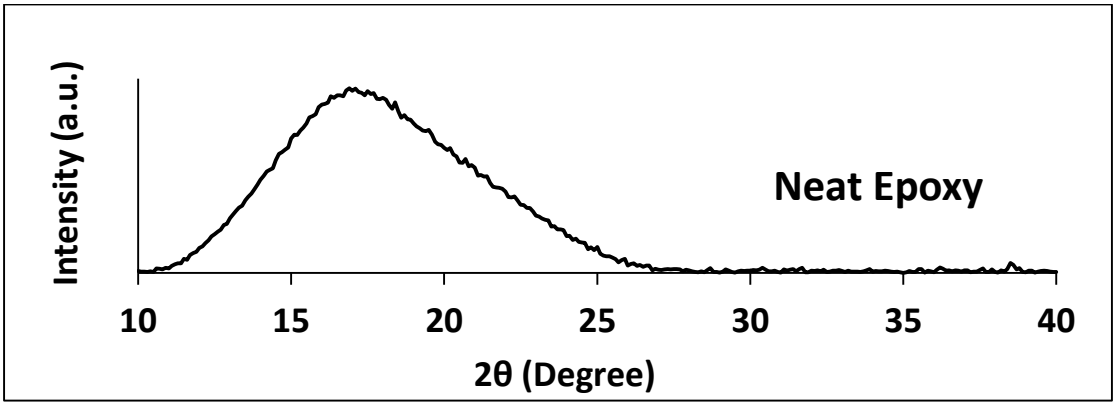

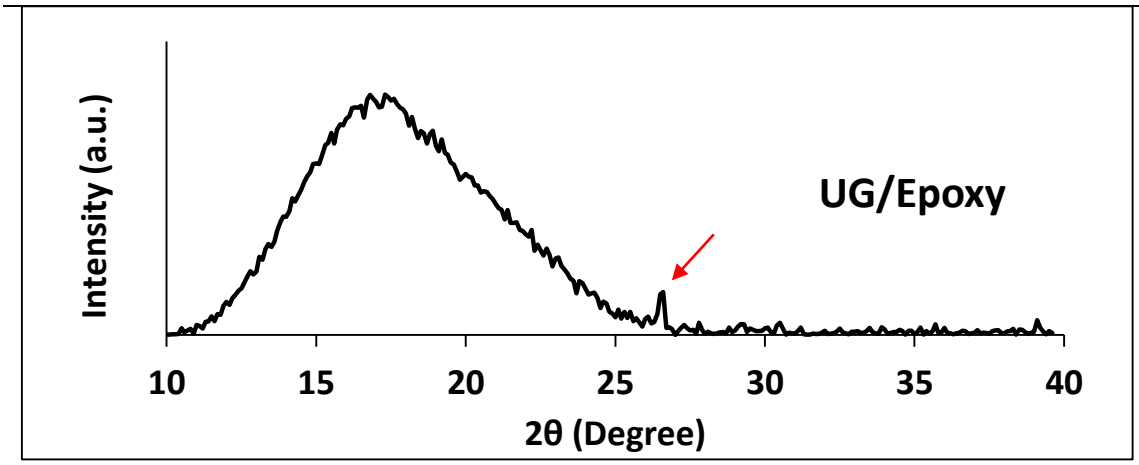
Intensity (a.u.)
UG/Epoxy
10
15
20
25
30
35
40
2θ (Degree)

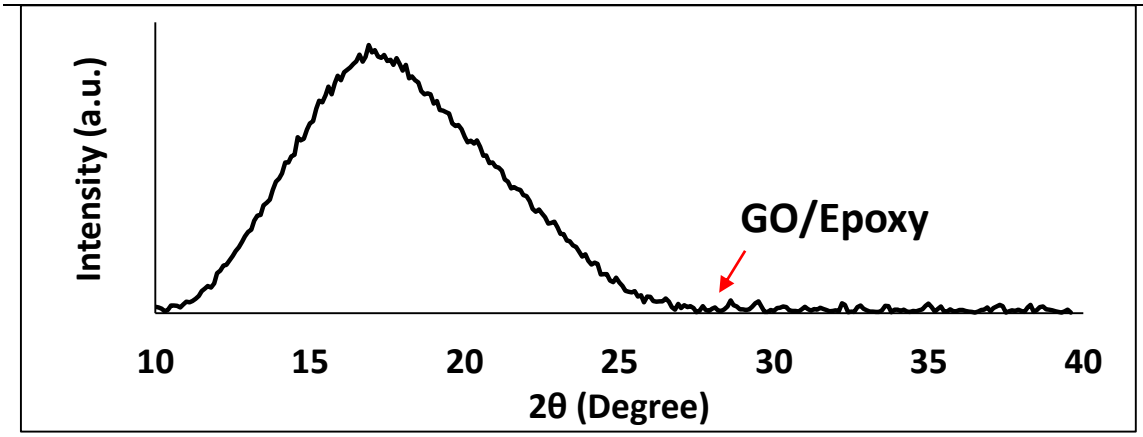
Intensity (a.u.)
GO/Epoxy
10
15
20
25
30
35
40
2θ (Degree)

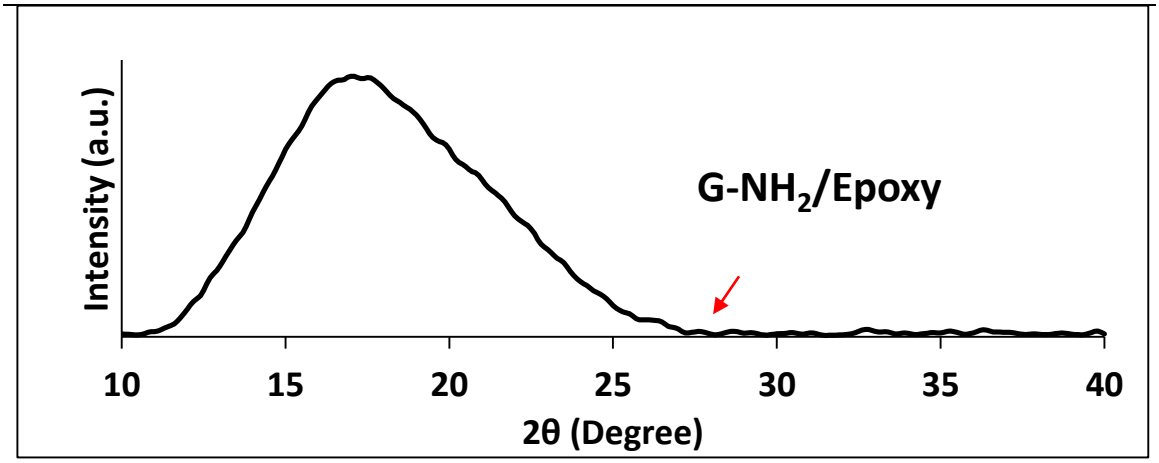
Intensity (a.u.)
G-NH2/Epoxy
10
15
20
25
30
35
40
2θ (Degree)

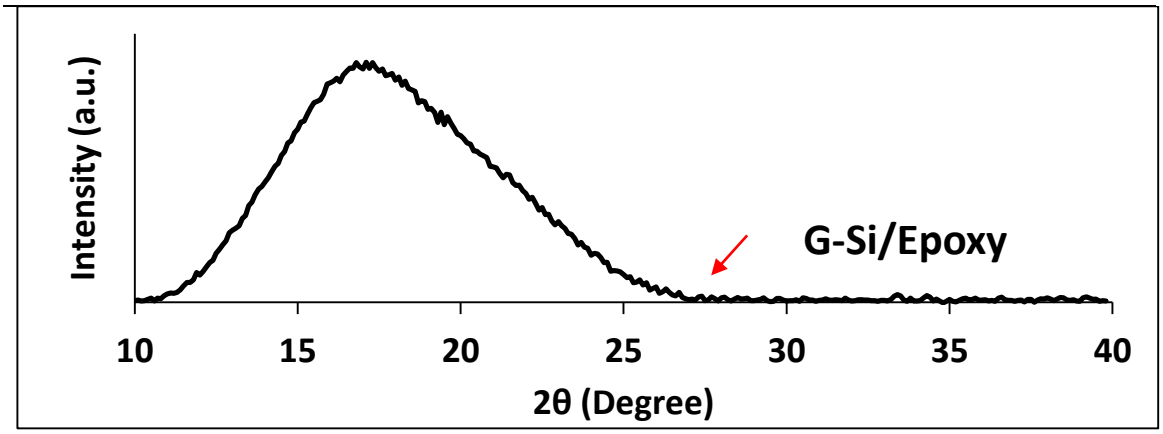

Figure 5-11. XRD patterns of GN- reinforced nanocomposites

Another mechanism that has an evident effect on increasing the fracture toughness of nanocomposites is crack bridging. This mechanism plays a more significant role when nanoparticles have high aspect ratios. When a nanoparticle bridges between two fracture surfaces, it may either fracture or pull out of one of the surfaces, depending on the nanoparticle's embedded length, interfacial strength, angle to fracture surface, and flexibility. It is believed that the functionalization of GNPs enhances the fracture toughness of the host resin, mainly through the crack-bridging mechanism, which can be enhanced by improving the interfacial strength between the GNPs and the epoxy. A higher interfacial strength would obviously delay GNPs' pullout action, thus increasing the required fracture energy. Evidence of crack-bridging mechanisms could be seen throughout examination of the fracture surfaces. This is evidenced by the pulled-out GNPs (shown in Figure 5-12(a) and/or the grooves remaining on the opposite surface (Figure 5-12(b)). The gap observed between the pulled-out GNPs and epoxy in Figure 5-12(a) can be due either to pulled-out GNPs from the other surface, or from local plastic deformation of the epoxy. This latter mechanism would occur when the angle between the GNP and the fracture plane is not

orthogonal, as a result of which the GNP would squeeze its surrounding polymer during the pull-out process.

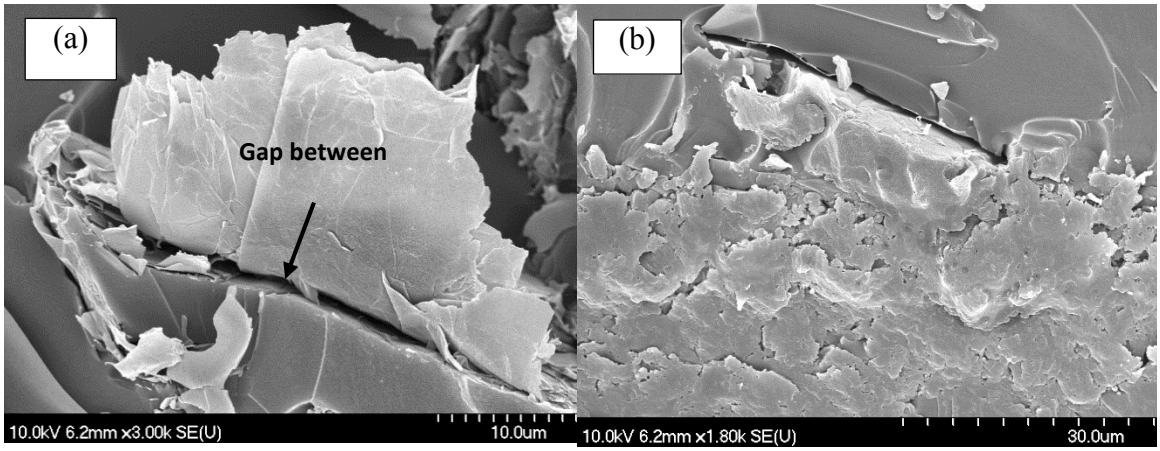

Figure 5-12. Crack-bridging mechanism in nanocomposites reinforced with (a) 0.5 wt% GO and (b) 0.5 wt% G-NH_2 (Note: the crack growth direction is from bottom to top)

5.9 Conclusions

A silane coupling agent was bonded to GNP through an oxidation and functionalization process, after which the mechanical properties of an epoxy resin reinforced with unmodified GNPs and processed GNPs (i.e., GO, G-Si and G-NH_2) were experimentally assessed. Thermo-gravimetric analysis, the Raman spectroscopy and Fourier transform infrared spectroscopy were utilized to confirm the successful bonding of the silane agent to GNPs. Furthermore, a field emission scanning electron microscope (SEM) was used to obtain more details about the effect of functionalization on the GNPs dispersion quality and failure mechanisms by evaluating the fracture surfaces of the nanocomposites.

The Raman spectra of functionalized and non-functionalized GNPs revealed that the main characteristic peaks (i.e., G-band and D-band) were shifted and the intensity ratio of D-band to G-band (i.e., I_D/I_G) was noticeably increased in the functionalized GNPs. This could be indicative of the existence of a covalent bond between the silane agent and GNPs. On the other hand, TGA analysis of the functionalized GNPs showed that weight loss and residual weight obtained from functionalized GNPs were more than that obtained from the unmodified GNPs, which could be another clue to the existence of a bond between GNPs and the silane agent. Finally, the existence of two new peaks (i.e., at wavenumber 1045 cm^{-1} and 1097 cm^{-1}), obtained by the FTIR spectrum for the silane functionalized GNP, further confirms the successful chemical functionalization.

The elastic modulus and fracture toughness of nanocomposites fabricated by 0.5 wt% of functionalized GNPs were enhanced 15% and 82%, respectively. The inclusion of 0.5 wt% GNPs also increased the ultimate strength of the host resin by 38% in average, while the effect of functionalized GNPs produced strength values greater than this average. In addition, the ductility of the host epoxy resin was increased by the inclusion of all types of GNPs. However, the contribution of G-Si and G-NH was more significant than that of non-processed GNPs.

5.10 Acknowledgments

This research was funded by the National Science and Engineering Research Council of Canada (NSERC) through the Collaborative Research and Training Experience (CREATE) program. The authors are grateful to the granting agency. The authors also gratefully acknowledge Dr. Christa Brosseau and Scott Harroun (Department of Chemistry, Saint Mary's University) for their cooperation in the Raman spectroscopy

assessment. In addition, the use of Dalhousie Institute for Research in Material (IRM) equipment, through Professor M.A. White (Chemistry Department, Dalhousie University) is also gratefully acknowledged.

5.11 References

[1] Novoselov KS, Geim AK, Morozov SV, Jiang D, Zhang Y, Dubonos SV, et al. Electric Field Effect in Atomically Thin Carbon Films. Science. 2004;306:666-9.

[2] Scott CD, Arepalli S, Nikolaev P, Smalley RE. Growth mechanisms for single-wall carbon nanotubes in a laser-ablation process. Appl Phys A. 2001;72:573-80.

[3] King JA, Klimek DR, Miskioglu I, Odegard GM. Mechanical properties of graphene nanoplatelet/epoxy composites. Journal of Applied Polymer Science. 2013;128:4217-23.

[4] Chatterjee S, Wang JW, Kuo WS, Tai NH, Salzmann C, Li WL, et al. Mechanical reinforcement and thermal conductivity in expanded graphene nanoplatelets reinforced epoxy composites. Chemical Physics Letters. 2012;531:6-10.

[5] Soltannia B, Taheri F. Static, quasi-static and high loading rate effects on graphene nano-reinforced adhesively bonded single-lap joints. International Journal of Composite Materials. 2013;3:181-90.

[6] Ahmadi-Moghadam B, Taheri F. Effect of processing parameters on the structure and multi-functional performance of epoxy/GNP-nanocomposites. J Mater Sci. 2014;49:6180-90.

[7] Ma P-C, Siddiqui NA, Marom G, Kim J-K. Dispersion and functionalization of carbon nanotubes for polymer-based nanocomposites: A review. Composites Part A: Applied Science and Manufacturing. 2010;41:1345-67.

[8] Wang Z, Colorad HA, Guo Z-H, Kim H, Park C-L, Hahn HT, et al. Effective functionalization of carbon nanotubes for bisphenol F epoxy matrix composites. Materials Research. 2012;15:510-6.

[9] Montazeri A. The effect of functionalization on the viscoelastic behavior of multi-wall carbon nanotube/epoxy composites. Materials & Design. 2013;45:510-7.

[10] Cui L-J, Wang Y-B, Xiu W-J, Wang W-Y, Xu L-H, Xu X-B, et al. Effect of functionalization of multi-walled carbon nanotube on the curing behavior and mechanical property of multi-walled carbon nanotube/epoxy composites. Materials & Design. 2013;49:279-84.

[11] Reed CW. The Chemistry and Physics of the Interface Region and Functionalization. In: Nelson JK, editor. Dielectric Polymer Nanocomposites: Springer US; 2010. p. 95-131.

[12] Karthick R, Brindha M, Selvaraj M, Ramu S. Stable colloidal dispersion of functionalized reduced graphene oxide in aqueous medium for transparent conductive film. Journal of Colloid and Interface Science. 2013;406:69-74.

[13] Dao TD, Hong J-E, Ryu K-S, Jeong HM. Super-tough functionalized graphene paper as a high-capacity anode for lithium ion batteries. Chemical Engineering Journal. 2014;250:257-66.

[14] Zhang S-P, Liu B, Li C-Y, Chen W, Yao Z-J, Yao D-T, et al. Enhanced dispersibility and thermal stability of β-cyclodextrin functionalized graphene. Chinese Chemical Letters. 2014;25:355-8.

[15] Yadav SK, Cho JW. Functionalized graphene nanoplatelets for enhanced mechanical and thermal properties of polyurethane nanocomposites. Applied Surface Science. 2013;266:360-7.

[16] Yuan B, Bao C, Song L, Hong N, Liew KM, Hu Y. Preparation of functionalized graphene oxide/polypropylene nanocomposite with significantly improved thermal stability and studies on the crystallization behavior and mechanical properties. Chemical Engineering Journal. 2014;237:411-20.[17] Chiu PW, Duesberg GS, Dettlaff-Weglikowska U, Roth S. Interconnection of carbon nanotubes by chemical functionalization. Applied Physics Letters. 2002;80:3811-3.

[18] Hodkiewicz J. Characterizing graphene with Raman spectroscopy. Thermo Fisher Scientific; 2010.

[19] Yadav SK, Mahapatra SS, Cho JW, Lee JY. Functionalization of Multiwalled Carbon Nanotubes with Poly(styrene-b-(ethylene-co-butylene)-b-styrene) by Click Coupling. The Journal of Physical Chemistry C. 2010;114:11395-400.

[20] Zhu Y, Bakis CE, Adair JH. Effects of carbon nanofiller functionalization and distribution on interlaminar fracture toughness of multi-scale reinforced polymer composites. Carbon. 2012;50:1316-31.

[21] Chatterjee S, Nafezarefi F, Tai NH, Schlagenhauf L, Nüesch FA, Chu BTT. Size and synergy effects of nanofiller hybrids including graphene nanoplatelets and carbon nanotubes in mechanical properties of epoxy composites. Carbon. 2012;50:5380-6.

[22] Ayatollahi MR, Shadlou S, Shokrieh MM. Correlation between aspect ratio of MWCNTs and mixed mode fracture of epoxy based nanocomposites. Materials Science and Engineering: A. 2011;528:6173-8.

[23] Ayatollahi MR, Shadlou S, Shokrieh MM. Fracture toughness of epoxy/multi-walled carbon nanotube nano-composites under bending and shear loading conditions. Materials & Design. 2011;32:2115-24.

[24] Liang J, Huang Y, Zhang L, Wang Y, Ma Y, Guo T, et al. Molecular-Level Dispersion of Graphene into Poly(vinyl alcohol) and Effective Reinforcement of their Nanocomposites. Advanced Functional Materials. 2009;19:2297-302.

[25] John WZ. Graphite. Graphite, Graphene, and Their Polymer Nanocomposites: CRC Press; 2012. p. 1-58.

Chapter 6: Influence of graphene nanoplatelets on modes I, II and III interlaminar fracture toughness of reinforced polymer composites

B. Ahmadi-Moghadam and F. Taheri

Accepted for publication (pending minor revisions) in the Journal of Engineering Fracture Mechanics, Winter 2015

6.1 Abstract

The potential capability of graphene nanoplatelets (GNPs), with diverse surface functional groups for the purpose of enhancing the interlaminar fracture toughness of E-glass/epoxy composites was assessed. The GNPs included unmodified GNPs, and two chemically functionalized GNPs. Comparisons were made based on modes I, II and III interlaminar fracture toughness values. The results indicated that the interlaminar fracture toughness was increased significantly under mode I fracture, but not as much for the other modes. Based on the microscopic evaluation of the fracture surfaces, the inclusion of the functionalized GNPs generated the most resilient fiber/resin interface, thus, effectively inhibiting the crack propagation.

6.2 Introduction

Fiber-reinforced polymer composites (FRPs) have been known to offer remarkable in-plane mechanical properties. Notwithstanding, FRPs are critically susceptible to delamination, especially those that are fabricated with relatively brittle resins (e.g., epoxy resins). This is because, in general, such resins inherently have low strain capacity in comparison to the limiting strain of the fibers they commonly host, low fracture toughness [1], and weak fiber/matrix interface bond strength [2]. As a result, various types of nanopartciles, such as carbon nanotubes (CNTs), have been included in epoxies in an

attempt to enhance their toughness [3-5]. Indeed, CNTs have been widely used to enhance the fracture response of FRP under modes I and II fracture [6-9].

Although CNTs have the potential to enhance the fracture toughness of FRPs, some studies have shown that the inclusion of CNTs in FRP composites could adversely affect the fracture toughness of the host FRP structure [10, 11]. Two possible reasons for the adverse reactions are (i) the filtering effect of micro fibers during resin transport, and (ii) the agglomeration of nanopartciles [12]. An agglomeration, depending on its configuration, could act as a void or a flaw, thus degrading the mechanical performance of the nanocomposite.

In comparison to the tubular shape of CNTs, graphene nanoplatelets (GNPs) are disk-like configuration of carbon nanopartciles. They have been mainly used to modify the stiffness and electrical conductivity of epoxy resins [13]. In reference to the enhancement gained in the fracture toughness of resins, it has been shown that GNPs, in general, provide more significant improvement in the fracture toughness of epoxy resins in comparison to CNTs, (when compared at the same weight content) [14, 15]. The mechanical performances of GNP/epoxy composites could also be further enhanced by the surface functionalization technique. For instance, the authors and their co-workers [16] recently demonstrated that silane and amino-functionalized GNPs produced a more effective improvement in the elastic modulus and mode-I fracture toughness of epoxy resins in comparison to as-received (i.e., unmodified) GNP-reinforced epoxy resins.

Although the positive effects of GNPs on the mechanical performance of epoxy resins (particularly on their fracture toughness) have been demonstrated in several studies, nonetheless, to the best of the authors' knowledge, no detailed study has investigated the

fracture response of multi-scale polymer composites reinforced with GNPs. In this research, therefore, a systematic investigation is conducted to assess the fracture responses of E-glass fiber-reinforced epoxy laminates, with their mid-plane resin layer having been modified with 0.5 wt% of different types of GNPs (i.e., unmodified and functionalized GNP). Modes I and II fracture test specimens are manufactured and tested according to the standard practices, and mode III fracture ILF toughness of laminates is evaluated by a newly introduced torsion test. To establish the enhancing effect of GNPs with respect to the energy release rate of the laminates and their failure modes, the fracture surfaces of nanocomposites are also examined with the aid of a scanning electron microscope (SEM).

6.3 Experiments

6.3.1 Materials

As-received/unmodified GNPs (referred to as UG, hereafter) with an average thickness of 7 nm and an average particle diameter of 25 μm, were acquired from the XC Science (Lansing, MI), were used in this research. NH_2 functionalized GNPs (referred to G-NH_2 hereafter) with an average thickness of 5nm and an average diameter of 8 μm were obtained through the Cheap Tubes Inc. (Battleboro, VT). Araldite LY1564 (Bisphenole-A) epoxy resin was used throughout this study, along with Aradur 2954 (cycloaliphatic polyamine) hardener, which is available through the Huntsman Co. (West Point, GA). GNPs with other functionality groups used in this study, such as those functionalized by graphene oxide (GO) and glycidyloxypropyl-trimethoxysilane graphene nanoplatelets (G-Si), were produced based on a method established by the author and his co-workers (see reference 16 for details). The aforementioned functionalized GNPs will be referred to as GO and G-Si, respectively, hereafter.

6.3.2 Specimen preparation

The test specimens for determining the fracture toughness due to delamination (i.e., ILFT) were extracted from 200 mm × 200 mm of E-glass-epoxy FRP plates, hosting a manually embedded delamination with an initial length of 60 mm. The procedure for fabricating each plate and producing the delamination is as follows:

- Sixteen 200 mm × 200 mm sheets of unidirectional E-glass cloth were cut to size and then stacked to form two 8-layer plates, maintaining a parallel fiber orientation (i.e., unidirectional).
- The plates were subsequently impregnated with the neat epoxy resin, using the VARTM (vacuum assistant resin-transfer molding) method.
- While still wet, an ultra-thin layer of Teflon cloth was placed at a specific location, along one edge of each of the mating plates, in order to generate the initial delaminated region.
- Since assessing the effect of GNPs on the interlaminar fracture toughness of laminate was the main objective of this research, a pre-determined amount of either neat epoxy resin or GNP-reinforced epoxy resin, prepared as per the authors protocols detailed in their previous research [13], was applied to one of the mating surfaces of each pair of 8-layer plates.
- Subsequently, each of the above plates was mated with its pair, such that the resin-applied surface formed the bonded interface, thus generating the final so-called delaminated composite plate.

- At this juncture, each assembly was consolidated and the extra resin was extracted using the vacuum-bagging technique. The mated plates were then cured at 60 ℃ for 2 hours and post-cured at 120 ℃ for eight hours.
- The test specimens were subsequently extracted, in appropriate sizes as per the standards, from the bonded composite plates with the aid of a semi-automated diamond tip rotary saw, continuously cooled with water.

The optical micro-graphs, shown in Figure 6-1, evidence a uniform distribution of the resins around the fibers at the mid-plane of the specimens.

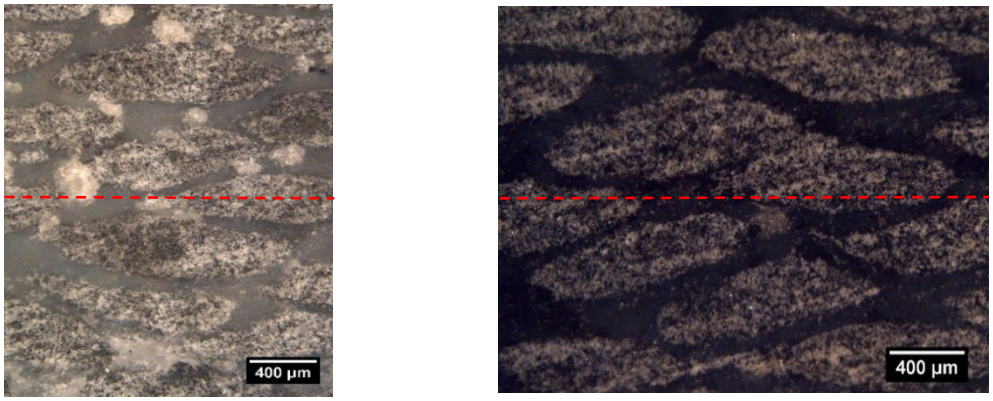

Figure 6-1. Optical images of the cross-sections at the interface region of FRPs bonded with (a) neat epoxy and (b) with epoxy reinforced with 0.5 wt% Si-G

6.3.3 Test methodology

Mode I interlaminar fracture toughness tests were carried out as per ASTM D5528 [17]. Double cantilever beams (DCBs) with dimensions of 150 × 25 × 3.5 mm and initial crack lengths of 45 mm were loaded through two loading blocks adhered to the end of each specimen, using a servo-hydraulic test machine. The tests were conducted in displacement control mode (5 mm/min). Mode I interlaminar fracture toughness (ILFT) was calculated

according to the following equation, which is known as the modified compliance calibration method [17]:

$$G_I = \frac{3P^2C^{2/3}}{2A_1bh} \tag{6-1}$$

in which P is the load corresponding to the defined crack length, C is compliance (i.e., crosshead displacement over the load corresponding to a defined crack length), A_1 is the slope of the line on the least-square plot of the crack length, normalized by specimen thickness as a function of the cube root of compliance, b and h are specimen's width and thickness, respectively.

The same configuration of a DCB specimen, but with an initial crack length of 30 mm, was used to evaluate the mode II ILFT. The specimens were loaded in a 3-point flexure under displacement control loading regime (1 mm/min), according to a previous study done by Zhu et al. [12]. Equation (6-2) was used to calculate mode II ILFT according to a compliance calibration method, as specified in [18].

$$G_{II} = \frac{3P^2Ba^2}{16bh^3} \tag{6-2}$$

where P is the load corresponding to the defined crack length, a, and B is the slope of the straight line fitted to the data points in a $C(8bh^3)$ versus a^3 plot.

Given the lack of a standard for evaluating the mode III fracture toughness of FRP composites, an edge crack torsion method, as proposed by Lee [19] was conducted to assess mode III ILFT, with some modifications to it. The test procedure and related calculations are summarized as follows.

The edge-crack torsion (ECT) specimens (Figure 6-2a) with a dimension of 40×80×5.5 mm and an initial crack length of 13 mm were extracted from a plate with a layup of $[90^o/(\pm 45^o)_2(\mp 45^o)_2/90^o]_s$. The manufacturing technique for fabrication of this laminate is identical to that explained previously. The specific laminate layup prompts the specimens to show linear behavior under torsion load prior to reaching the critical load for crack propagation. Moreover, the (± 45) plies in the specimens provide sufficient torsional stiffness to the specimens. Consequently, the ECT specimen is sufficiently compliant to allow G_{IIIC} (i.e., mode III critical energy release rate) to be readily evaluated by the compliance calibration method [19].

It should be noted that if the aforementioned specimen configuration becomes subjected to a pure torsion load, its crack tip would undergo a pure mode III loading. Consequently, a fixture (Figure 6-2b) was designed to facilitate the application of pure torsion loading into the specimen through a torsion test machine. The torsion load was transferred to the specimens through two pins, each having a curved surface in contact with one end of the specimen, while the other end was restrained from rotating by two other similarly shaped pins (see Figure 6-2a). A “Low Torque Tinius Olsen” horizontal torsion machine, with a maximum applied torque capacity of 1100 N.m, was used in the rotation control mode (2.5 degree/s).

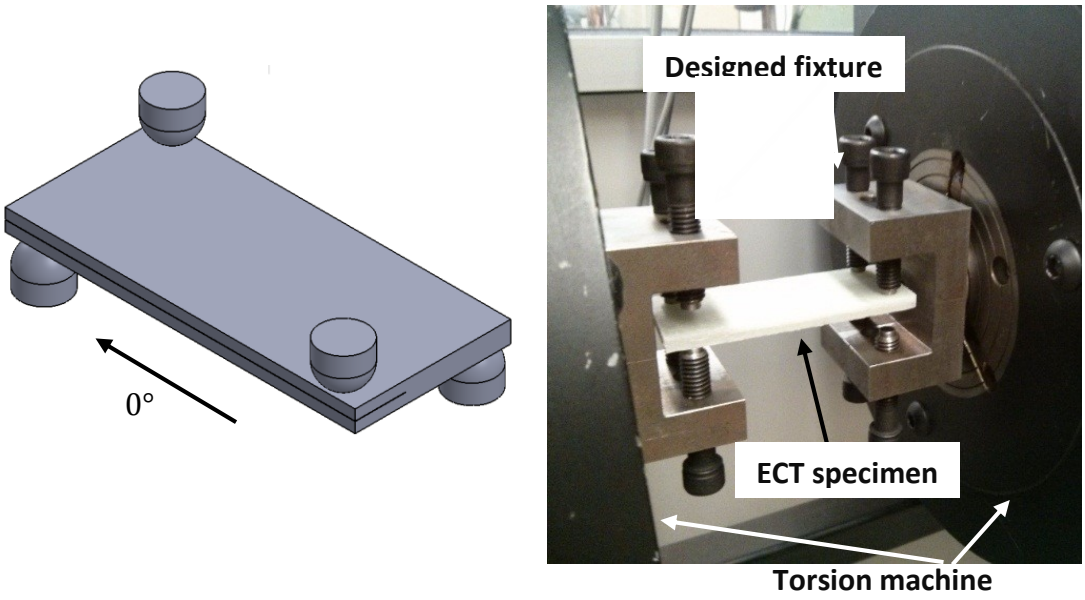

(a) (b)

Figure 6-2. (a) The schematic of the ECT specimen; (b) actual test set up

Equation (6-3) was used to calculate mode III ILFT.

$$G_{III} = \frac{3T^2 C_\theta}{8LW\left(1 - \left(\frac{3}{4}\right)\left(\frac{a}{W}\right)\right)} \tag{6-3}$$

in which T is the torque corresponding to a predefined crack length, C_θ is the calibrated torsional compliance, L is the twist length (i.e., the longitudinal distance between the two supporting pins of the fixture), W is specimen's width, and a is the crack length.

To obtain C_θ as a function of crack length, ECT specimens with different crack lengths (0, 7, 13, 20 and 25 mm) were manufactured and C_θ was evaluated through the torque versus angle curve obtained for each crack length. A straight line was then fitted on the data plotted in the form of $1/C_\theta$ versus a/w, and the coefficients A and B were evaluated as per Equation (6-4) in below.

$$1/C_\theta = A + B(\frac{a}{W}) \quad (6\text{-}4)$$

The values of A and B were evaluated for the base line test specimens (i.e., specimens without GNPs), as 2253 (N/cm) and -1815.91 (N/cm), respectively. It should be noted that the obtained values of A and B were used for calculating the parameter C_θ of the GNP-reinforced specimens.

Table 6-1 shows the averages of maximum loads obtained from the DCB and ENF tests corresponding with modes I and II ILF assessment. The table also reports the maximum torque obtained from applying a torsion load on the ECT specimens to evaluate Mode III ILF. Figure 6-3 shows typical load-displacement (Figure 6-3 a and b) and torque-angle (Figure 6-3c) curves obtained from the tests.

Table 6-1. Average values of the maximum applied loads and torques for assessing modes I, II and III ILF

		Mode I (N)	Mode II (N)	Mode III (N.m)
Neat Epoxy		41.93±3.4	496.78±18.12	24.11±1.15
0.5 wt%	UG	42.75±1.8	511.08±25.15	24.10±3.24
	GO	45.35±4.6	558.2±11.17	24.33±1.87
	G-NH2	54.64±2.3	571.96±14.66	25.66±2.18
	G-Si	56.62±3.8	747.07±35.12	24.92±1.07

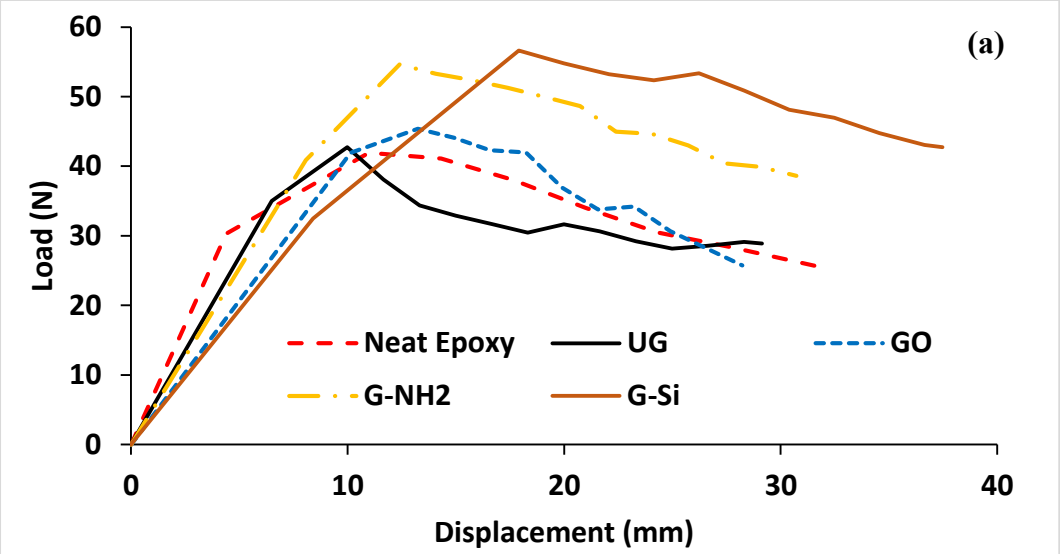
(a)
Load (N)
Displacement (mm)
Neat Epoxy
UG
GO
G-NH2
G-Si

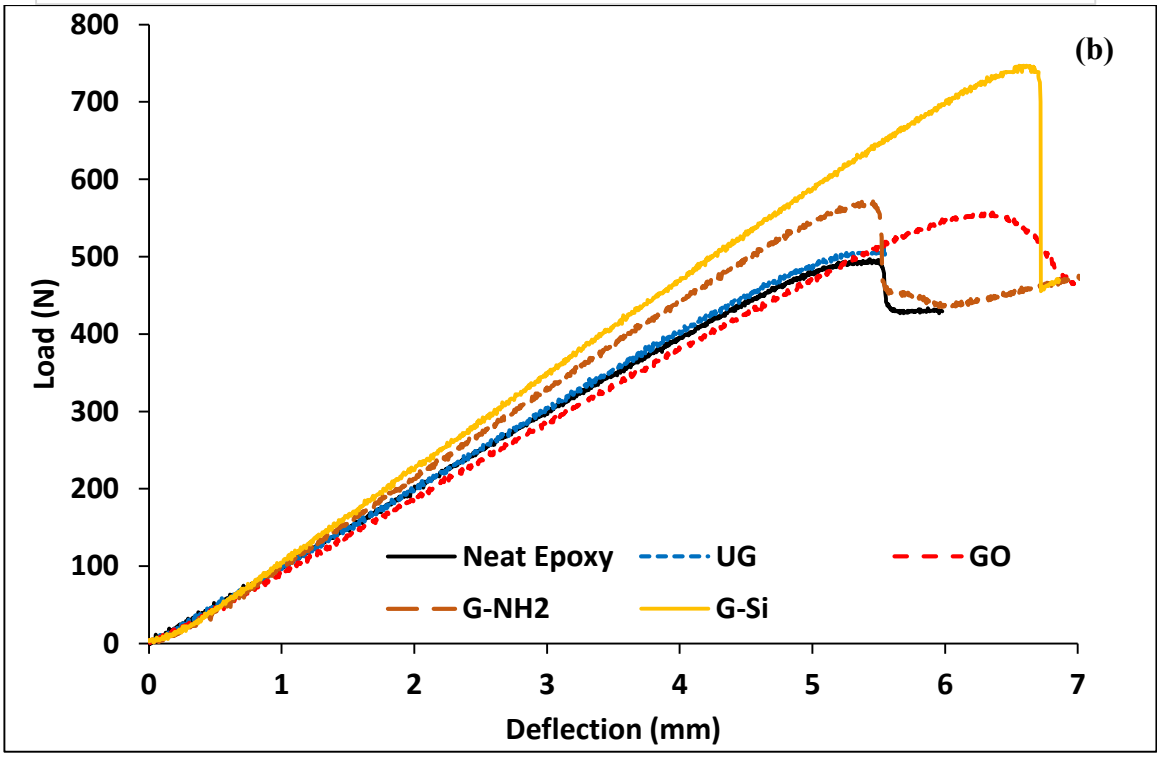
(b)
Load (N)
Deflection (mm)
Neat Epoxy
UG
GO
G-NH2
G-Si

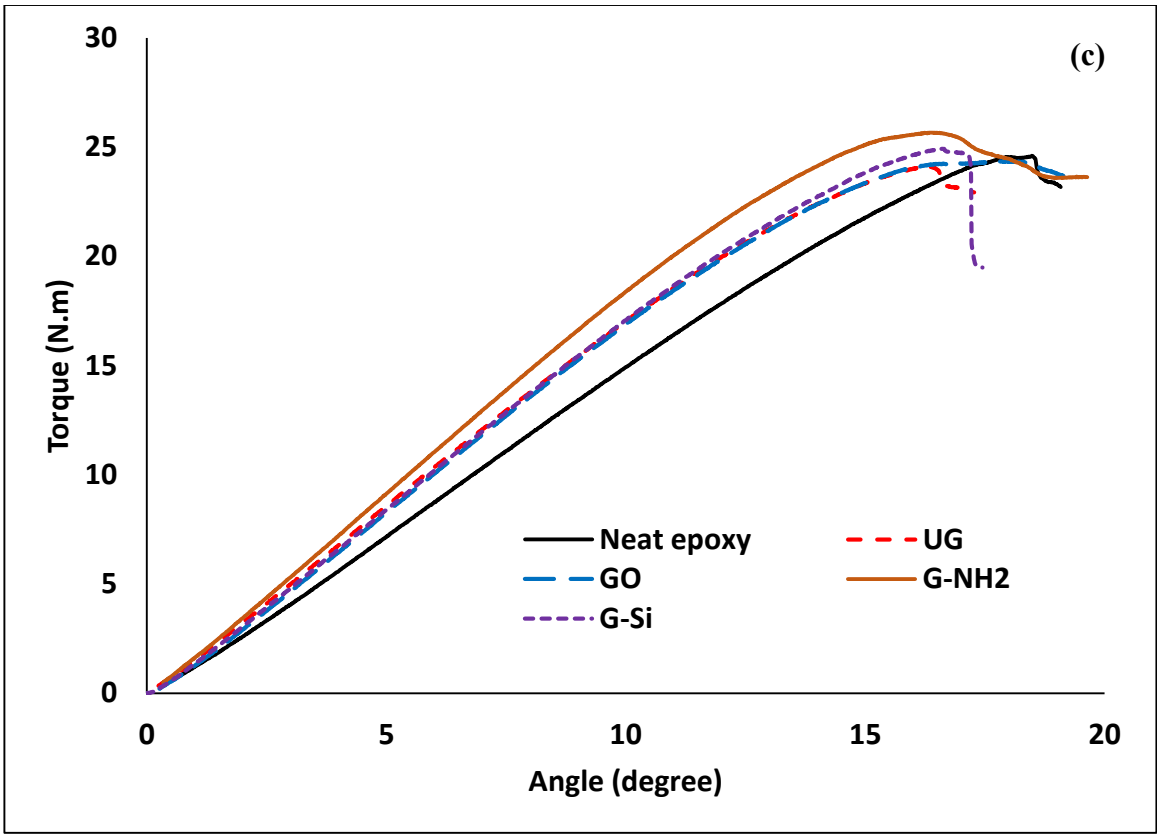

Figure 6-3. Representative load-displacement curves of a) Mode I b) Mode II and torque-angle curve (for Mode III) ILF assessment

6.4 Results and Discussion

6.4.1 Mode I-ILFT

As seen by the results shown in Figure 6-4, the inclusion of all forms of the GNPs managed to enhance the mode I critical energy release rate (CERR) of the FRPs. The results indicate that the inclusion of UG in the mid-resin increased the CERR of the FRP laminates by 11%, while the G-NH_2 and G-Si increased the CERR by 33% and 39%, respectively. It should be noted that the illustrated CERRs in Figure 6-4 represent the value of the energy corresponding to the onset of crack propagation in the specimens (for more details, see [17]). As mentioned earlier, the CERR in FRPs is primarily governed by the matrix fracture toughness, and in the cases where GNP-reinforced resins are used, also governed by the

interface strength of GNPs and the resin. As a result, based on the findings outlined in authors' earlier work [16], the largest CERR value was anticipated to be associated with either the G-NH_2 or G-Si reinforced epoxy resins. Moreover, the presence of the silane brought the surface energies of the matrix and E-glass fibers (made of silicon) closer to one-another; consequently, the more enhanced fiber/matrix interaction led to further improvement in the value of CERR.

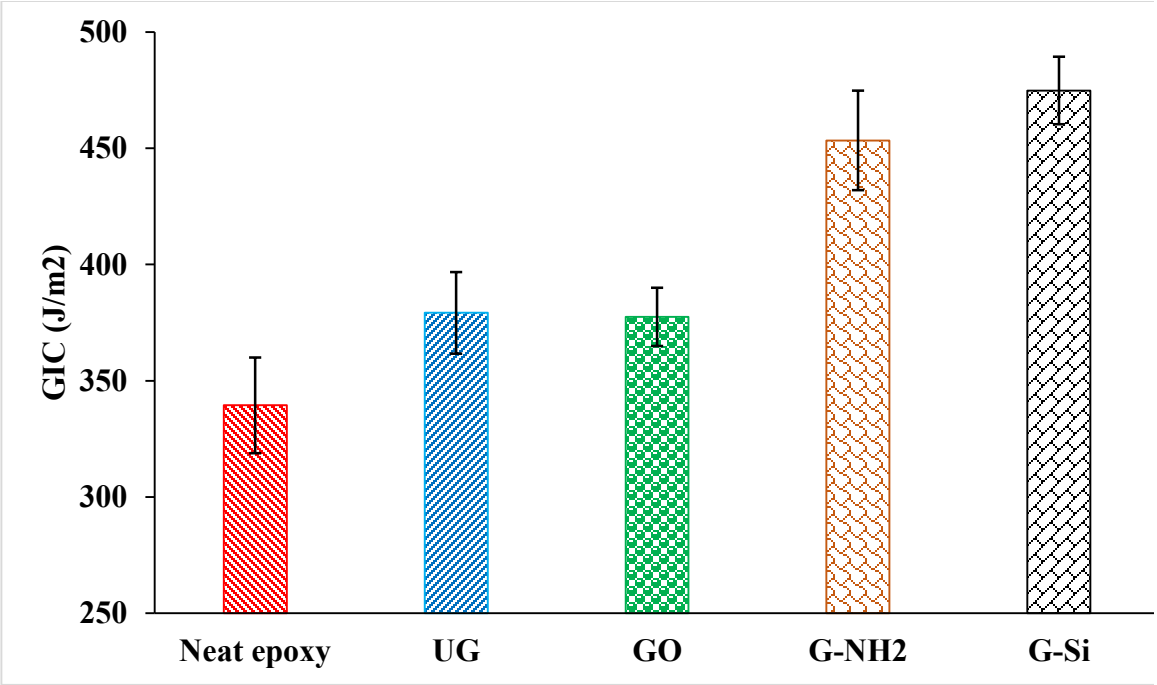

Figure 6-4. Mode I critical energy release rates of FRP plates adhered by the neat resin and various GNP-reinforced resins

The mode I fracture-resistant curve of the E-glass/epoxy laminated composites mated with 0.5 wt% UG, GO, G-NH_2 and G-Si are compared with a fracture-resistant curve of the plates mated with the neat resin, as shown in Figure 6-5. In general, mode I energy release rate of the FRPs increased abruptly in value within the first 7 mm of crack propagation, regardless of the existence of nanoparticles. The ILFTs reached a plateau

(referred to as G_{Ip}, hereafter), within 10 to 20 mm of delamination's advancement. Therefore, G_{Ip} is considered herein to be the propagation fracture toughness of the FRPs.

The horizontal lines seen in Figure 6-5 , point to the values of CERRs at the onset of the crack (delamination) propagation of the DCB specimens, which were mated with UG- and GO-reinforced resins. The results show that the CERRs did not increase significantly along their fracture plane (i.e., 11% and 4% increases were observed corresponding to the onset and propagation phases, respectively). However, when considering the G_{Ip} of DCB specimens, one can note a slight reduction in the CERR of the specimens mated with the as-received (or unmodified) GNP-reinforced resin. A significant improvement in the onset of CERR was observed in DCB specimens that hosted either G-NH_2- or G-Si-reinforced resin in their fracture plane (i.e., 33% and 39% improvements, respectively). The inclusion of G-Si in the resin produced the greatest improvement in the CERR during the crack propagation stage (i.e., 33%) of the FRPs.

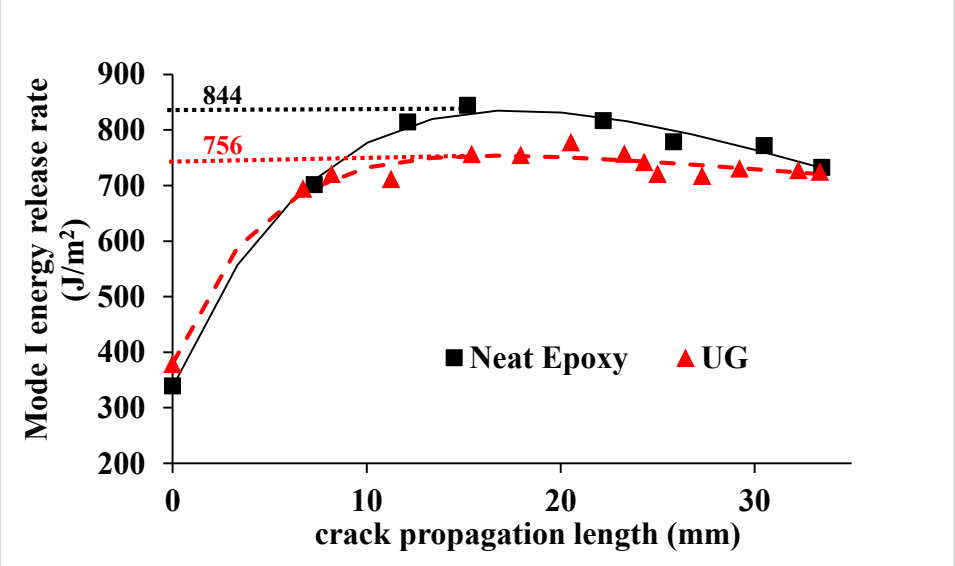

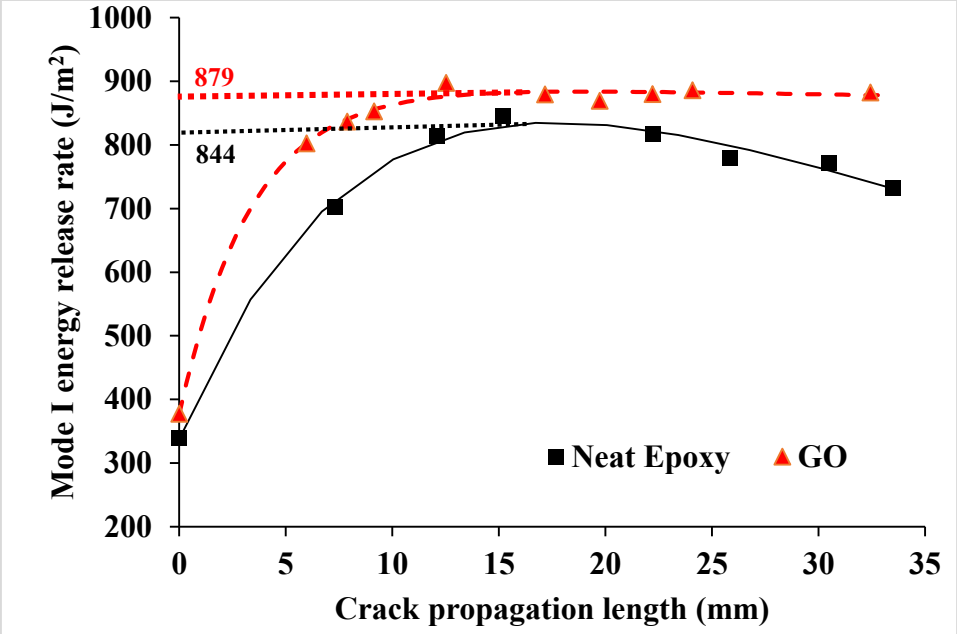
Mode I energy release rate (J/m²)
1000
900
800
700
600
500
400
300
200
879
844
Neat Epoxy
GO
0
5
10
15
20
25
30
35
Crack propagation length (mm)

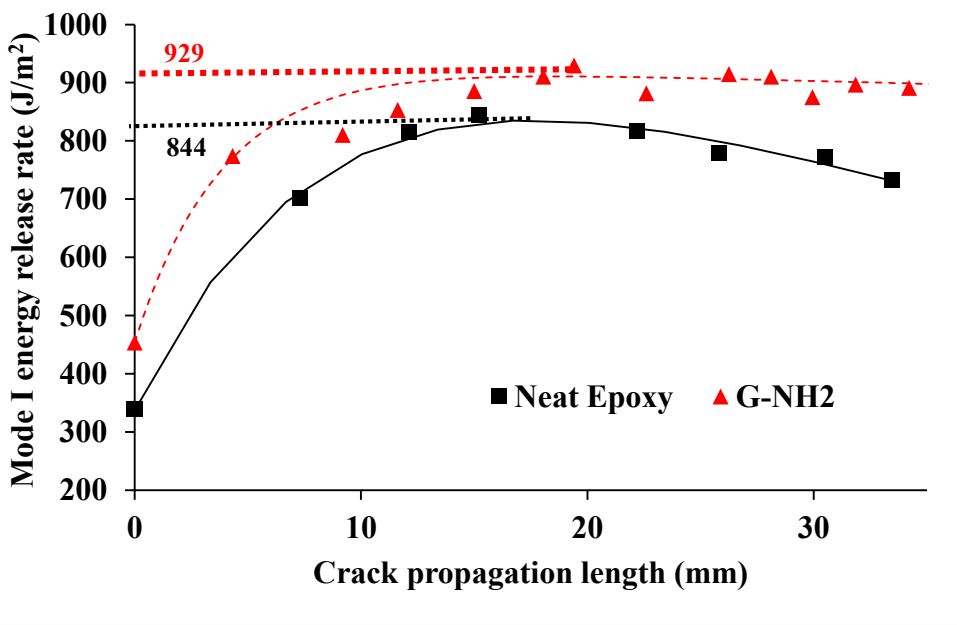
Mode I energy release rate (J/m²)
1000
900
800
700
600
500
400
300
200
929
844
Neat Epoxy
G-NH2
0
10
20
30
Crack propagation length (mm)

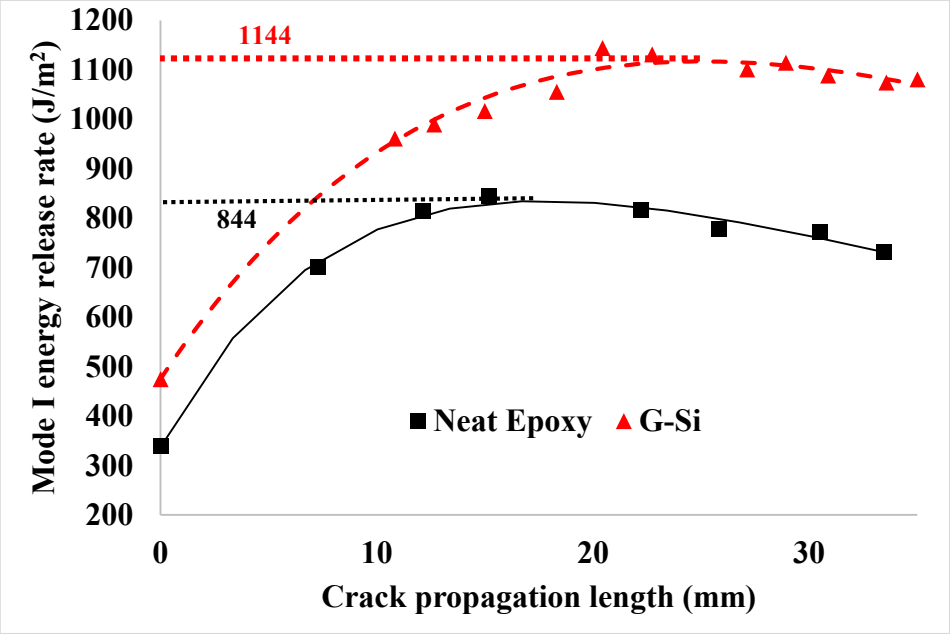

Figure 6-5. Mode I fracture-resistant curves of the DCB specimens

6.4.2 Mode II ILFT

To evaluate the mode II ILFT of FRP laminates based on the compliance calibration method, the compliance of each specimen with respect to the different crack lengths should be evaluated as described in reference [12]. Figure 6-6 shows the compliance of ENF specimens mated with resins, with and without nanopartciles, respectively, versus the crack length. The results revealed that the compliance of all specimens was increased linearly with respect to the crack propagation. Moreover, the unmodified GNP-reinforced resin did not affect the compliance of FRP laminate in comparison to the laminates mated with the neat epoxy. The same ineffectiveness was observed when the resin that contained GO was used to mate the FRP laminates. The greatest improvements, however, were obtained by adding G-NH_2 and G-Si to the resin at the fracture plane. The compliance curve corresponding to the mode II ILFT specimens represents the bending stiffness of the specimens. As for the bending stiffness enhancement, the resins reinforced with

functionalized GNPs (G-NH_2 and G-Si) enhanced the bending stiffness of the cracked specimens by approximately 26%.

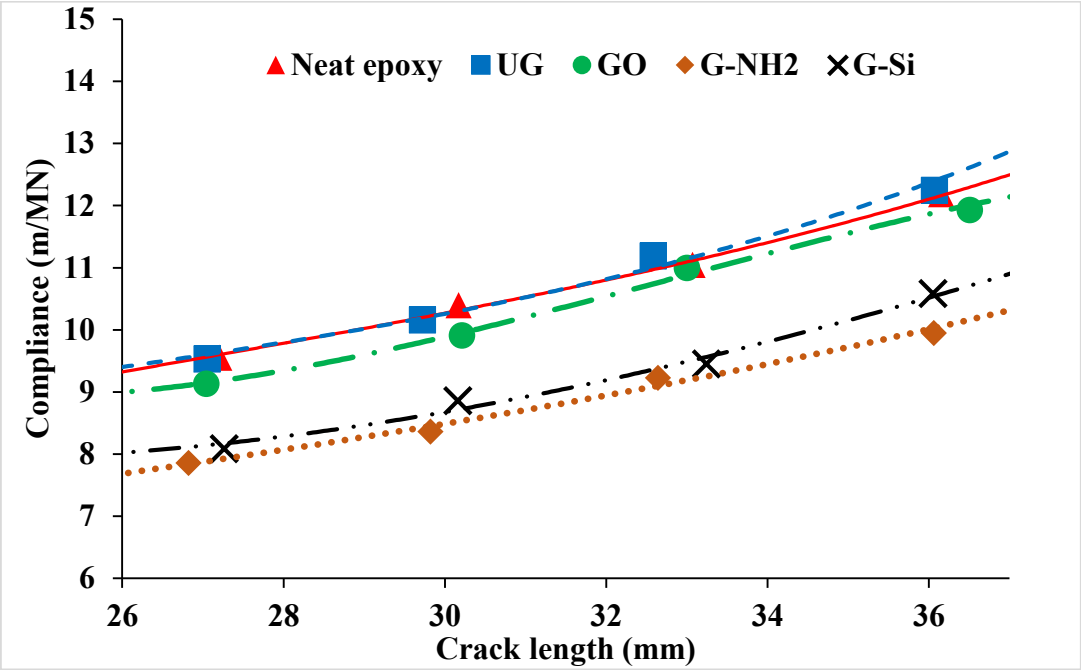

Figure 6-6. Compliance of the ECT specimens made by neat resin and various types of GNP-reinforced resins

The onset mode II CERRs of specimens with and without nanopartciles are shown in Figure 6-7. The existence of UG within the fracture plane of specimens adversely affected the mode II ILFT of the specimens. The authors have shown in their previous study [14] that even the use of unmodified GNPs resulted in a slight decrease in mode II fracture toughness of GNP/epoxy nanocomposites. Consequently, the reduction of mode II fracture toughness of the matrix could lead to the reduction of mode II ILFT of the specimens reinforced by UG-reinforced resin. The inclusion of G-NH_2 and G-Si increased the in-plane shear fracture toughness of FRP laminates by 12% and 11%, respectively. By observing the mode II ILFT results, one could postulate that the efficiency of GNPs in

enhancing the ILFT of FRP laminates at the in-plane shear fracture mode is less than what could be attained for the opening fracture mode.

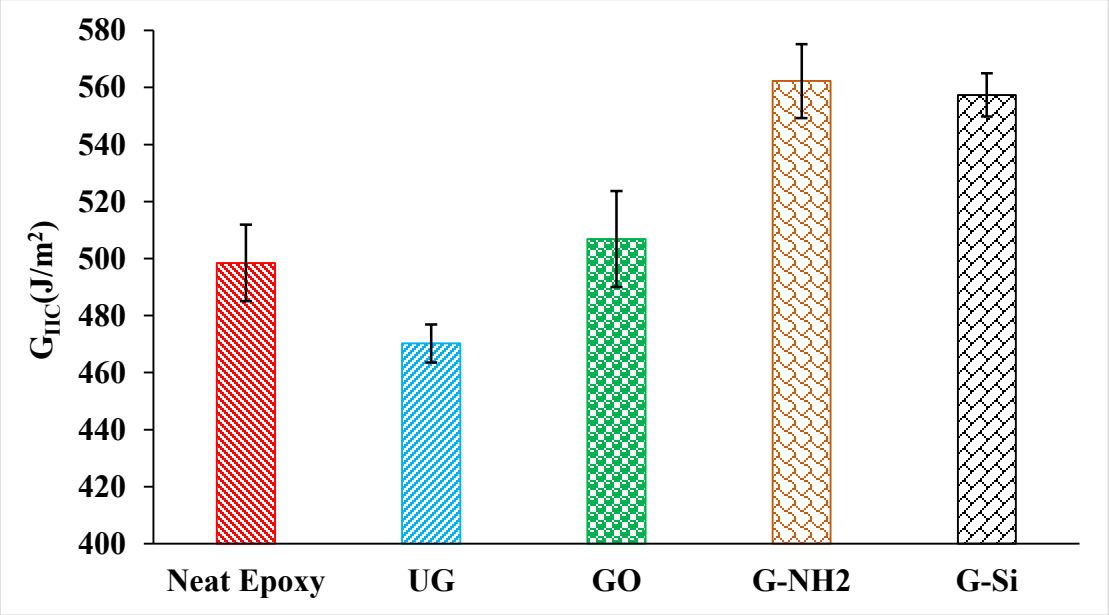

Figure 6-7. Mode II critical energy release rates of FRP plates adhered by neat epoxy resin and various GNP-reinforced epoxy resins

6.4.3 Mode III ILFT

As shown in Figure 6-8, the trend that was observed for mode II ILFT of the FRP laminates reinforced with nanopartciles is also observed for the laminates under mode III ILFT. The inclusion of G-NH_2 and G-Si in the resin increased the value of G_{IIIC} by 24% and 19%, respectively. Comparatively, the efficiency of the functionalized GNPs under mode III ILFT is observed to be greater than that observed under mode II ILFT, but still is less than that observed under mode I ILFT. The main fracture mechanism of GNP modified FRPs in mode I fracture is GNP bridging due to the nature of fracture mode (i.e., opening mode). Since the crack surfaces slide on one-anther in modes II and III fracture, thus, GNPs

never get the opportunity to infuse their contribution and increase the fracture resistance of cracks by creating a bridge between the two surfaces of cracks. The fracture mechanism of GNP/FRP composites are comprehensively discussed in next section.

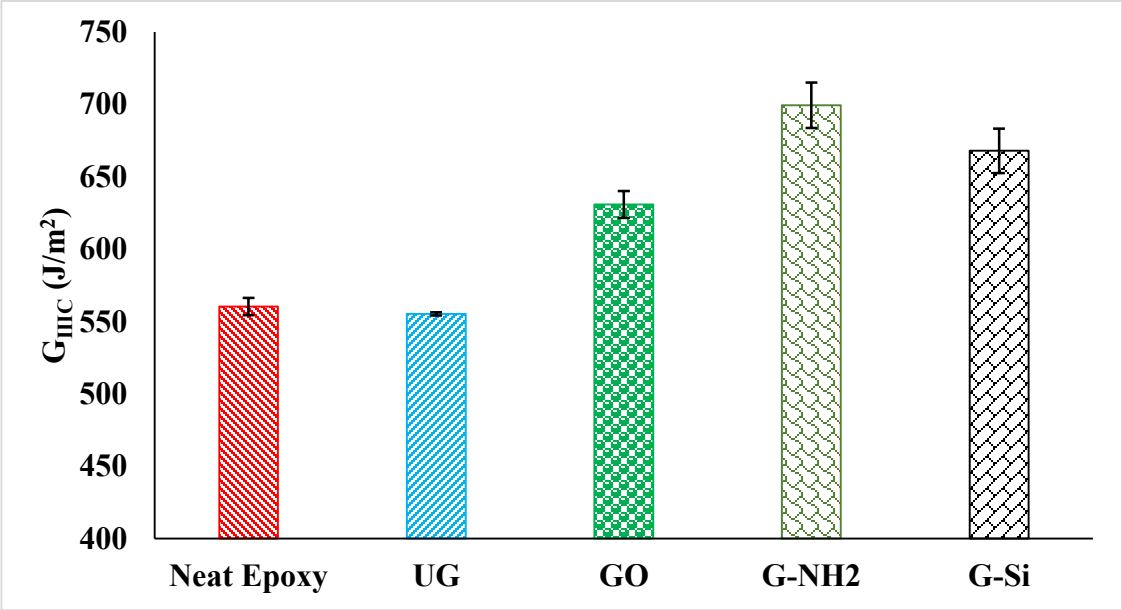

Figure 6-8. Mode III critical energy release rates of FRP plates adhered by the neat and various GNP-reinforced epoxy resins

6.5 Fracture surface micrographs

As stated earlier, the number of available studies considering modes II and III ILFT of FRP composites is far less in comparison to those that have considered the mode I ILFT. This is mainly due to the complex micro-scale fracture mechanism involved with the modes II and III ILF. In dealing with the aforementioned complex mechanics, the fracture surfaces of FRP laminates were also assessed by SEM to further explore the influence of GNPs on the interlaminar fracture mechanics of FRP laminates. Figure 6-9 (a) and (c) represent small regions near the crack tip on the fracture surfaces of plates bonded with the

neat epoxy and UG-reinforced epoxy resin, respectively, which were tested under mode I fracture. The specimens that were mated with the neat epoxy exhibited smooth fracture surfaces, while inclusion of UGs roughened the fracture surfaces as seen in Figure 6-9(c). Consequently, the fracture surface area was increased, which could be the cause of greater mode I CERR in the UG-reinforced FRPs.

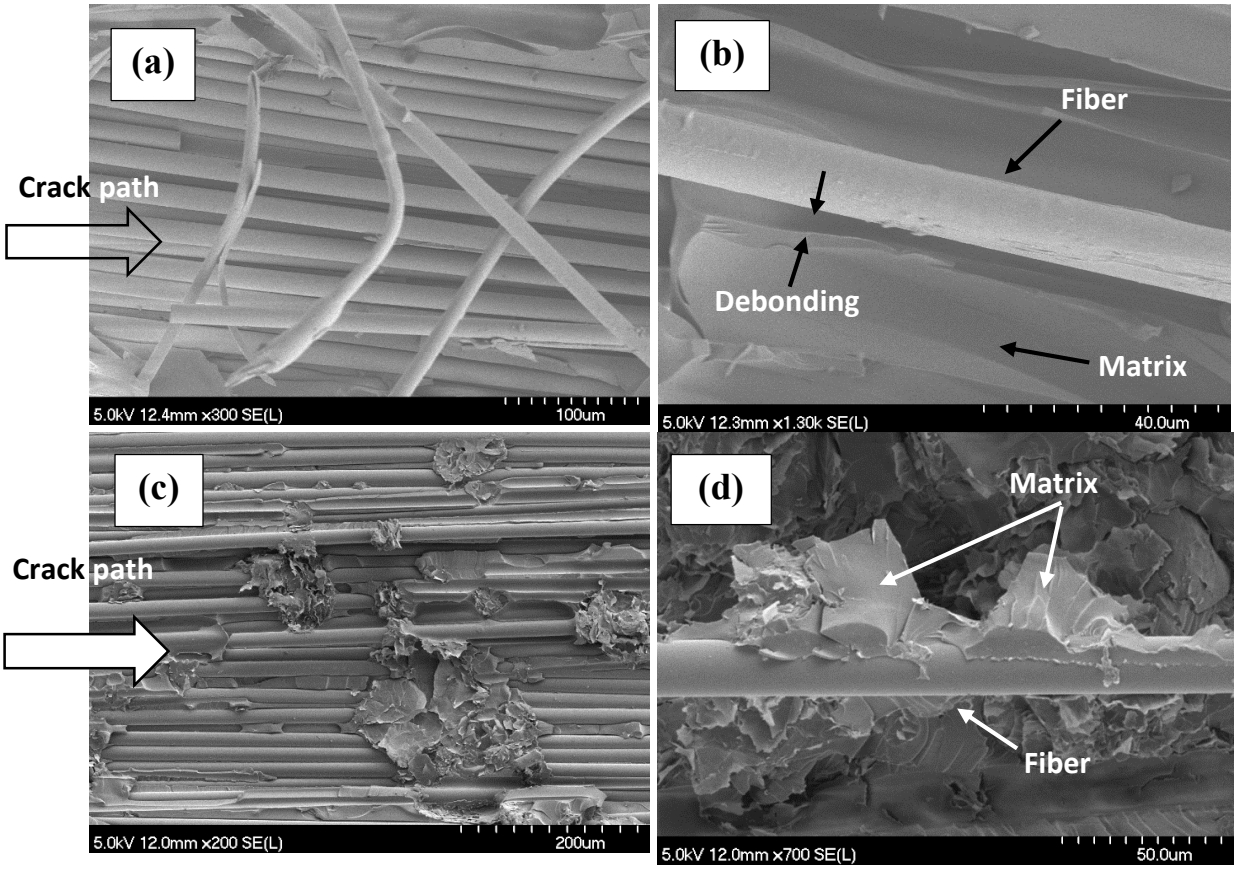

Figure 6-9. Fracture surfaces of FRP specimens bonded with: (a) and (b) neat epoxy, and (c) and (d) epoxy reinforced with 0.5 wt% Si-G

The presence of resin lumps around the fibers in the UG reinforced specimen seen in the pictures clearly indicates that crack propagation was diverted as it encountered the UG, and that the crack could not propagate into the interface of the fiber and matrix. As the consequence of crack diversion, additional energy was required to advance the crack

in FRP specimens bonded with UG. Figure 6-9(b)) indicate debonding to be the main mode of damage (see the gap in Figure 6-9(bin FRP specimens bonded by the neat epoxy. In contrast, the continuous contact of the GNP-modified matrix and fibers, as seen in Figure 6-9(d), is an indicative of the resiliency of the fiber/matrix interface.

Moreover, a typical SEM image of the fibers embedded within the resin which was reinforced by the silane agent functionalized GNPs is illustrated in Figure 6-10. As seen, the clear interaction of resin and fibers, visible in the figure, could rarely be observed in specimens mated with the unmodified GNPs (see Figure 6-9(d)). It can also be clearly seen that the G-Si functionalization has enhanced the adhesion of GNPs to their host resin. Moreover, the image also evidences the pulling of some of the silane functionalized GNPs out of their host resin on the fracture plane. This would indicate that the presence of silicon on the surfaces of GNPS promoted better adhesion of GNPs to the glass fibers. As a result, the increase in the fiber/matrix interface contact is postulated to generate greater values of CERR (at the onset) in the FRPs, regardless of the fracture mode.

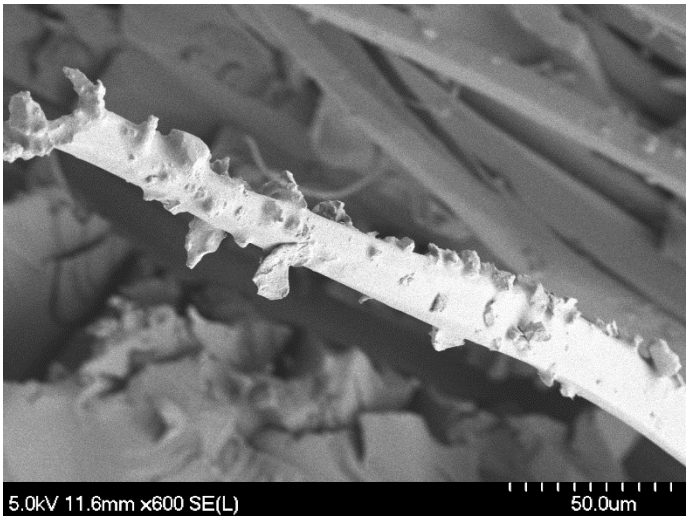

Figure 6-10. SEM image evidencing the excellent adhesion of G-Si to fibers

Figure 6-11(a) shows the fracture surface of FRP composite mated with the neat epoxy. As seen, small segments of the matrix have remained amongst the fibers on the fracture surface. The shapes of remaining matrix segments indicate that the failure occurred within the resin in the form of micro-cracks, and then the micro-cracks propagated toward the interface, and subsequently coalesced. Thus, the matrix possessing a relatively higher fracture toughness could resist against the nucleation of micro-cracks and stronger adhesion between fibers and matrix could result in a higher mode II CERR. As described in [14], the unmodified GNPs adversely affected the mode II ILFT of GNP-reinforced resin. Here, similarly, as a consequence of reduction in the matrix fracture toughness in FRP composites mated with UG-reinforced resin, mode II CERR values were degraded, as seen in the results illustrated in Figure 6-7. The results indicate that the values of mode II CERR is greater in FRPs mated with functionalized GNP-reinforced resins in comparison to that bonded with the neat epoxy resin. As discussed, this is a consequence of a stronger fiber/matrix interface. The positive improvement in CERR values obtained under mode II fracture in specimens that were mated with functionalized GNP-reinforced resins is observed to be, however, less than the CERR values observed under mode I fracture. This is attributed to the fact that the ILFT of the FRP composites subject to mode II fracture is mainly influenced by the nucleation of macro-cracks in the matrix rather than crack propagation along the fiber/matrix interface.

As shown in Figure 6-11(b), the main fracture mechanisms observed under mode III fracture are fiber pullout and fiber bridging. The incorporation of functionalized GNPs could enhance the fiber/matrix interface bond, thus consuming more energy to pull the GNPs out of the matrix. This observation supports the results shown in Figure 6-8, which

confirmed that the functionalized GNPs did indeed produce more enhancement in the interlaminar fracture response of FRPs under mode III fracture.

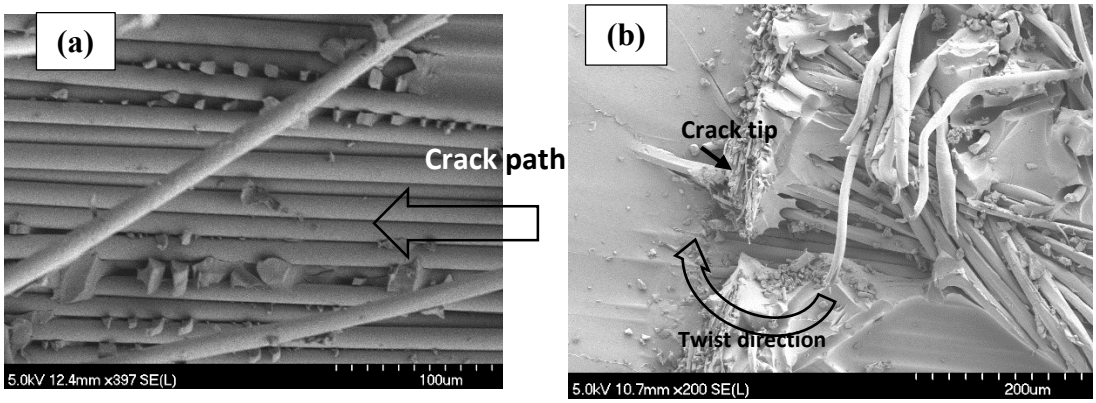

Figure 6-11. SEM micrographs of fracture surfaces of FRP composite mated with the neat epoxy tested under (a) mode II fracture (b) mode III fracture

6.6 Summary and conclusion

The interlaminar fracture toughness of FRP composites plates mated with unmodified epoxy resin and epoxy resins reinforced with various functionalized GNPs were assessed under modes I, II and III fracture, and the results were compared. SEM micrographs of the fracture surfaces were utilized to further appraise the effect of GNP functionalization on the fracture and toughening mechanisms of FRP composites tested under different modes of fracture. To the best of authors' knowledge, the current study presents the first-time evaluation of ILFT of FRPs that use resins reinforced with GNPs.

In addition, to evaluate mode III ILFT of FRP laminates, a new test procedure was developed and proposed. In this procedure, a relatively thin and small FRP specimen with lay-up of $[90^o/(\pm 45^o)_2(\mp 45^o)_2/90^o]_s$, hosting a length-wise delamination in its mid-plane, is subjected to a pure torsion load. Mode III ILFT of the specimen can then be calculated based on the compliance calibration method, because the laminate exhibits sufficient torsional stiffness.

Experimental results revealed that the FRPs that were mated with the functionalized GNP-reinforced resins exhibited improved modes I, II and III ILFT, by a significant margin. Moreover, the most effective enhancement of functionalized GNPs was observed in specimens that were subjected to mode I fracture, in comparison to those that were subjected to modes II and III fracture. Moreover, not only the inclusion of the as-received or unmodified GNPs in resin did not improve the mode ILFT of FRPs, but in fact, the inclusion of UGs in the resin adversely affected modes II and III ILFT of FRPs.

SEM images of the fracture surfaces of FRP specimens revealed that the presence of GNPs in the resin roughened the fracture surfaces, and thereby increasing the ILFT of the bonded interfaces. In addition, GNPs functionalization improved the surface energy of GNPs, causing a stronger GNP/resin interface bond. This phenomenon was verified by the presence of a layer of resin on the surfaces of GNPs that were functionalized by silane agent.

6.7 Acknowledgements

This research was funded by the National Science and Engineering Research Council of Canada (NSERC) through the Collaborative Research and Training Experience (CREATE) program. The authors are grateful to the granting agency.

6.8 References

[1] Goodman SH. 6 - Epoxy Resins. In: Goodman SH, editor. Handbook of Thermoset Plastics (Second Edition). Westwood, NJ: William Andrew Publishing; 1999. p. 193-268.
[2] Piggott MR. Load Bearing Fibre Composites: Kluwer Academic Publishers; 2002.
[3] Ayatollahi MR, Shadlou S, Shokrieh MM, Chitsazzadeh M. Effect of multi-walled carbon nanotube aspect ratio on mechanical and electrical properties of epoxy-based nanocomposites. Polymer Testing. 2011;30:548-56.
[4] Srikanth I, Kumar S, Kumar A, Ghosal P, Subrahmanyam C. Effect of amino functionalized MWCNT on the crosslink density, fracture toughness of epoxy and

mechanical properties of carbon–epoxy composites. Composites Part A: Applied Science and Manufacturing. 2012;43:2083-6.
[5] Wernik JM, Meguid SA. On the mechanical characterization of carbon nanotube reinforced epoxy adhesives. Materials & Design. 2014;59:19-32.
[6] Almuhammadi K, Alfano M, Yang Y, Lubineau G. Analysis of interlaminar fracture toughness and damage mechanisms in composite laminates reinforced with sprayed multi-walled carbon nanotubes. Materials & Design. 2014;53:921-7.
[7] Falzon BG, Hawkins SC, Huynh CP, Radjef R, Brown C. An investigation of Mode I and Mode II fracture toughness enhancement using aligned carbon nanotubes forests at the crack interface. Composite Structures. 2013;106:65-73.
[8] Wicks SS, Wang W, Williams MR, Wardle BL. Multi-scale Interlaminar Fracture Mechanisms in Woven Composite Laminates Reinforced with Aligned Carbon Nanotubes. Composites Science and Technology.
[9] Yu B, Jiang Z, Tang X-Z, Yue CY, Yang J. Enhanced interphase between epoxy matrix and carbon fiber with carbon nanotube-modified silane coating. Composites Science and Technology. 2014;99:131-40.
[10] Fan Z, Santare MH, Advani SG. Interlaminar shear strength of glass fiber reinforced epoxy composites enhanced with multi-walled carbon nanotubes. Composites Part A: Applied Science and Manufacturing. 2008;39:540-54.
[11] Tugrul Seyhan A, Tanoglu M, Schulte K. Mode I and mode II fracture toughness of E-glass non-crimp fabric/carbon nanotube (CNT) modified polymer based composites. Engineering Fracture Mechanics. 2008;75:5151-62.
[12] Zhu Y, Bakis CE, Adair JH. Effects of carbon nanofiller functionalization and distribution on interlaminar fracture toughness of multi-scale reinforced polymer composites. Carbon. 2012;50:1316-31.
[13] Ahmadi-Moghadam B, Taheri F. Effect of processing parameters on the structure and multi-functional performance of epoxy/GNP-nanocomposites. J Mater Sci. 2014;49:6180-90.
[14] Ahmadi-Moghadam B, Taheri F. Fracture and toughening mechanisms of GNP-based nanocomposites in modes I and II fracture. Engineering Fracture Mechanics.
[15] Shadlou S, Alishahi E, Ayatollahi MR. Fracture behavior of epoxy nanocomposites reinforced with different carbon nano-reinforcements. Composite Structures. 2013;95:577-81.
[16] Ahmadi-Moghadam B, Taheri F. Effect of Functionalization of Graphene Nanoplatelets on the Mechanical Response of Graphene/ Epoxy Composites. Journal of Materials and Design. 2014;In press.
[17] ASTM. ASTM D5528-13, Standar test method for mode I interlaminar fracture toughness of unidirectional fiber reinforced polymer matrix composites. West Conshohocken, PA: ASTM international; 2013.
[18] Deo RB. Composite materials: testing and design: ASTM; 1996.
[19] Lee SM. An edge crack torsion method for mode III delamination fracture test. Journal of Composites, Technology & Research. 1993;15:193-201.

Chapter 7: An effective means for Evaluating Mixed-Mode I/III Stress Intensity Factors using Single Edge Notch Beam Specimen

Babak Ahmadi-Moghadam and Farid Taheri

Published in the Journal of Strain Analysis for Engineering Design, Volume 48, Issue 4, PP 245-257, 2013

7.1 Abstract

The main objective of this study is to produce a set of practical equations, by which one could evaluate I/III mixed mode stress intensity factor by conducting a simple mode-I single edge notch bend specimen test as per ASTM D5054. To establish the proposed equations, a comprehensive finite element analysis is conducted to map the stress intensity factors' distribution through the thickness of the specimen with the aim of establishing the most effective loading condition for evaluating the mode stress intensity factors. An experimental investigation is also conducted to obtain the ultimate fracture load and establishing the fracture mechanism under the mixed-mode loading state. A set of correction factors is also proposed, which accounts for the influence of orientation of the initial crack and the applied load on the stress intensity factors.

7.2 Introduction

Epoxy resins and adhesives are widely used in various industrial applications in fabricating advanced fiber reinforced polymer composites parts and their assemblage. Macro-defects and cracks could be developed in these materials during part fabrications, mainly because of air bubbles remain within the resin during fabrication, due to impact of tools and other foreign objects [1], as well as due to formation of curing induced residual thermal stresses (causing shrinkage) [2]. The cracks would propagate from these defects and result into catastrophic failure of the part and/or the whole structure.

Assessments of crack bodies are often based on the utilization of the stress intensity factors (SIFs) obtained on pure facture modes (i.e., mode I, II and III); this is despite the fact that most crack bodies are subject to mixed mode status. Therefore the assessment of a crack body under mixed modes condition would lead to more realistic and effective assessment strategies. It should be noted that some studies have been performed with the aim of assessing mixed-mode I-II and I-III fracture modes, and developing appropriate equations for evaluating mixed-mode fracture toughnesses [3-5]. Nevertheless, the proposed assessment methods are involved with complex shape specimens and test fixtures, in turn increasing the overall cost of such assessments (especially for assessing mixed-mode I-III fracture) [6].

Several comprehensive research works have been conducted to assess the fracture behavior of bulk adhesives and neat resins under pure mode I fracture. Analytical solutions have been developed [7] for calculating the stress intensity factor, and standardized experimental configuration and measurement techniques have been proposed (see for instance ASTM D5054 [8]). As stated, most of the relevant efforts have been expended on establishing mode-I fracture related criteria, mainly because a large percentile of structural failures gets initiated by mode I crack propagation (especially in brittle materials). However, there are several real-life applications in which cracks are seldom subjected to pure mode-I loading status.

Consequently, the evaluation of the fracture response under mix-modes is important. Even the investigations that have considered mixed mode fracture have mainly focused on in-plane shear in combination to the crack opening mode [9-11]. A survey of the pertinent literature has revealed that there are only a few works conducted in consideration of mixed-

mode I/III fracture in bulk epoxy resin. Chen et al [12] assessed the fracture behavior of bulk epoxy resin under pure mode I and pure mode III loading conditions. They demonstrated that the critical value of mode III SIF is almost equal to the critical mode I SIF, and the strain energy theory's prediction was in good agreement with their experimental results. Most of such works have tried to modify the existing crack initiation and propagation criteria, thereby considering mode III fracture [13, 14] or have developed local criteria to clarify the effect of fragmentation along the crack tip [15].

It would be therefore desirable to be able to assess the SIFs under mixed mode conditions by using a simple tests specimen configuration and test set up. This practical requirement, in addition to the lack of performed investigations on characterizing bulk epoxy resin's fracture behavior under mixed mode I/III condition, motivated the work presented in this manuscript.

It should be noted that in response to the lack of specific standards, several specimen configurations and test setups have been proposed for measuring SIF under mixed-mode I/III. Chell and Grivan [16] and Varadarajan et al [17] geared up an experimental test setup in which a portion of the applied tensile stress could be translated to in-plane and out of plane shear stresses using a single edge notch beam (SENB). This was accomplished by altering the load direction versus the crack front. Davenport and Smith [18] extended the single punch shear test to mixed mode I/II by allowing the load to be applied in a diverse direction onto the SENB specimen. In addition, circumferentially notched cylindrical bar (CNCB) specimens were subjected to a combined tension and torsion loading state in order to evaluate the fracture behavior of poly methyl methacrylat, PMMA, in mixed mode I/III.

A modified compact tension specimen configuration was proposed by Kumar et al. [19] for evaluating I/III mixed mode fracture toughness of an aluminum alloy. The crack orientation angle (the complement of the angle between the trajectory of the applied line load orientation and the crack front) was used to establish the ratio of mode III to mode I fracture. Furthermore, a correction factor was proposed such that by its application to the mode I fracture toughness, one could obtain K_{1c} and K_{3c}. Manoharan and Lewardowski [6] utilized a through thickness single edge inclined notch specimen to characterize the fracture behavior of a particular reinforced aluminum alloy composite under combined mode I and III fracture. The specimen configuration was inspired from that recommended by the ASTM E399 [20]. Liu et al [21] conducted an experimental investigation on several CNCB specimens made of a brittle (PMMA) and a ductile (aluminum 7075) material to evaluate the propensity of a crack to make transition from one mode (e.g., mode I fracture) to another mode of fracture (e.g., mode III fracture) as function of increasing torsion stress versus normal stress. Their results revealed that tensile type fracture occurred in PMMA, while both tensile and shear failure modes were observed in aluminum specimen.

In the previous investigations, the loading conditions had been varied, and in some cases, specimens with an inclined crack were utilized; however there exists no specific standard for measuring the critical stress intensity factor under I-III mixed-mode condition. ASTM D5054 [8] provides the standard test method for evaluating the plane strain fracture toughness in plastic materials under pure mode I loading. It would be more desirable and effective if one could use the same specimen configuration (i.e. the SENB specimen) and obtain mixed-mode I-III critical SIFs, while being able to evaluate the pure mode I fracture toughness with the same basic specimen configuration as test apparatus as well. It is

therefore the main objective of this study to produce a set of practical equations, by which one could evaluate I/III mixed mode SIFs of bulk epoxy resin by conducting a simple mode-I SENB specimen test as per ASTM D5054 [8]. In order to establish the equations, the SENB specimens bearing an inclined crack front (with respect to the through-thickness axis of the specimen) has been used, loaded with a line load, also in the same orientation of the crack front. Similar configuration has been used by other investigators for evaluating polymers' I-II mixed-mode fracture toughness (see for instance Ayatollahi et al [22]).

The configuration of the specimen hosting an inclined single edge-notch in which the crack orientation angle is at angle θ with respect to the through-thickness axis (Z-axis as shown in Figure 7-1) of the specimen. The application of loading illustrated in the Figure 1 would result in both the opening and twisting modes of the crack tip. The orientation of angle θ would of course govern the contribution of each loading mode. When $\theta = 0^{o}$ (i.e, the crack is perpendicular to the specimen axis), it is a pure mode I fracture; however, the contribution of the shear force is not negligible, particularly in the vicinity of the free surfaces. The SENB configuration as per ASTM D5054 [8] is selected with the commonly used dimensions (Figure 7-1) for measuring fracture toughness under pure mode-I loading.

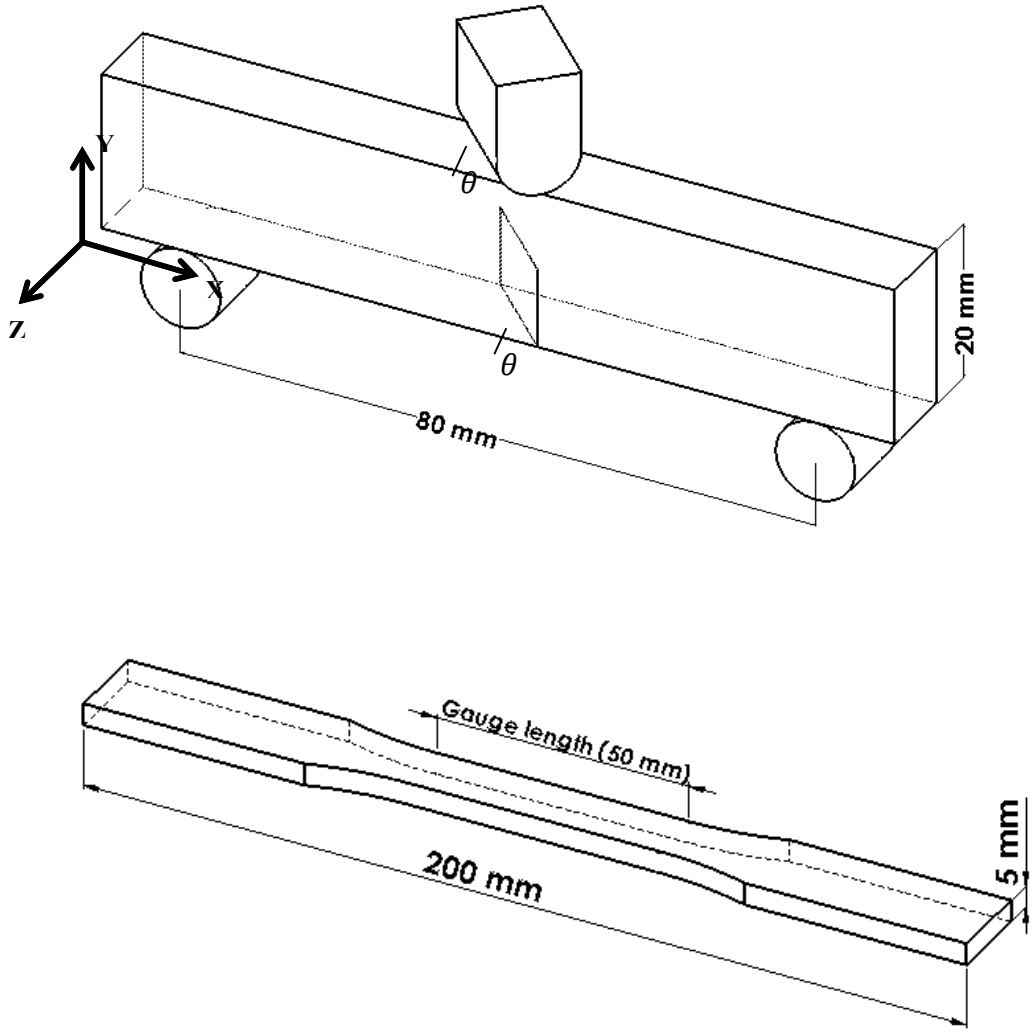

Figure 7-1. Schematics of a: the proposed specimen, boundary condition and loading condition for evaluating K_{1c} and K_{3c} using three point bend test(isometric view) and b: the tensile test specimen as per ASTM D638

As also stated, a comprehensive FE study was performed with two main aims. Firstly, to evaluate the dependency of mixed mode SIF to crack orientation angle. Secondly, to demonstrate the somewhat uniform through-thickness distribution of K_1 and K_3. The results of the investigation led to the development of two correction factors. The

application of these factors to the available relationship used for calculating the mode I critical SIF, K_{IC}, would result in the establishment of the values of K_{1c} and K_{3c}.

An experimental investigation was performed to establish the integrity and accuracy of the results obtained from the FE analysis, as well as establishing the integrity of the proposed equations. The investigation included the evaluation of the stress-strain response of the epoxy adhesive under uniaxial loading state as per ASTM D638 [23]. Then, three-point bend test was conducted as per ASTM D5054 [8] on SENB specimens having various crack front orientation angle with the aim of to establishing their ultimate fracture capacity and SIFs.

7.3 Finite element analysis

7.3.1 Modeling Strategy

Due to the lack of unified effective analytical expressions for calculating of K_{1c} and K_{3c}, a finite element framework was established to assess the SIF distribution within the cracked body. Among the several available methods for calculating the SIF, such as the contour integral and virtual crack growth methods, the contour integral technique was utilized through the ABAQUS FE commercial code. The SENB specimen was modelled using the reduced integrated higher order brick (C3D20R) element of the ABAQUS. The seam crack and focused mesh techniques were used to configure the contour integral region (see Figure 7-2). A layer of wedge elements surrounded by hex elements were used to generate the so-called "focused mesh" configuration at the crack tip region, as shown in Figure 7-2. To model the crack tip singularity, the mid-side nodes nearest the node forming the crack front were moved to the quarter distance nearer to the crack front nodes. The analysis was performed for a model in which $a/\mathrm{W} = 0.5$ (where a is the crack length and

w is specimen's height), while the crack front orientation angle, θ, was varied from 0º to 60º with 15º interval. Table 7-1shows the material properties used in the FE analysis.

Table 7-1. Mechanical properties of LY564/Aradure 2954

Elastic modulus	Yield stress	Ultimate stress	Poison ratio
2.65 (GPa)	67 (MPa)	87 (MPa)	0.35

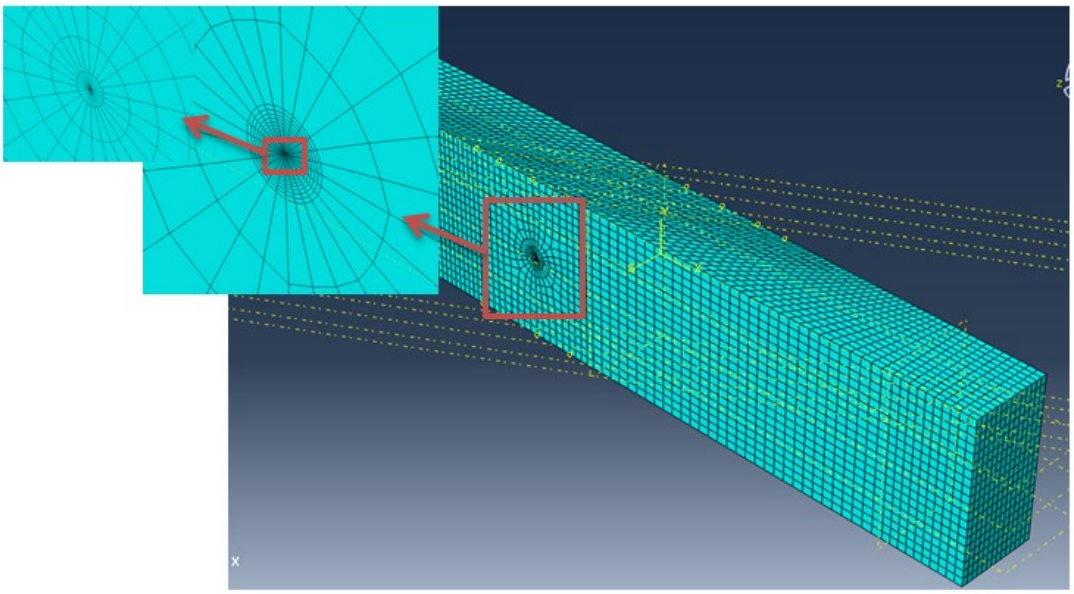

Figure 7-2. the FE mesh

7.3.2 SIF distribution

The expression for evaluating mode-I critical stress intensity factor is as follows [7].

$$K_{IC} = \frac{P_{max}}{BW^{\frac{1}{2}}} f(\frac{a}{W}) \qquad 7\text{-}1$$

in which P_{max} is the fracture load, B is beam's width, W is the beam's height, a is the crack length and $f(\frac{a}{W})$ is a geometry correction factor. For the case of the selected specimen geometry, in which S/W=4, $f(\frac{a}{W})$ is evaluated using the following equation. S is the length of support span (note that the S/W=4 has been implicitly included in the coefficient that appears after the equal sign (i.e., 6), in the following equation):

$$f\left(\frac{a}{W}\right) = 6\left(\frac{a}{W}\right)^{\frac{1}{2}} \frac{\left[1.99 - \left(\frac{a}{W}\right)\left(1 - \frac{a}{W}\right)\left(2.15 - 3.93\frac{a}{W} + 2.7\left(\frac{a}{W}\right)^2\right)\right]}{\left(1 - 2\frac{a}{W}\right)\left(1 - \frac{a}{W}\right)^{\frac{3}{2}}} \qquad 7\text{-}2$$

The FE predictions for the SENB specimen with mode I crack and loading configuration are shown in Figure 7-3. As seen, FE results indicate that K_1 attains its maximum value at mid-thickness plane of the specimen, and the FE produced magnitude is equal to 95% of that produced by the analytical expression (see Figure 7-5). Furthermore, three dimensional effect is observed in the distribution of K_I stress intensity factor; in fact, K_I's value suddenly decreases near the free surfaces of the specimen, by as much as 23%. This phenomenon is well-known (see for instance Sukumar et al [24]). The results also indicate that K_2 and K_3 values are nil throughout the thickness. The variation of the SIFs along the thickness of the specimen for the crack front orientation angle θ = 30° is illustrated in Figure 7-4. The results indicate that when the crack front orientation angle increased from 0° to 45°, not only did the value of K_1 decreased, but also K_2 and K_3 attained

significant values, especially as one nears the free surfaces. Of course, from theoretical perspective, the value of K_2 should be nil at specimen's mid-thickness; however, the FE results indicate that while K_2 is zero at that location, but attains a relatively large value as one moves toward the free surfaces. In fact, the value of K_2 suddenly dropped to 50% of its maximum value (on the specimen's surfaces) within 1 mm distance away from the free surfaces, and then gradually decreases to zero at the mid-plane of the specimen (through-the-thickness). K_1 however holds almost a constant value within approximately 90% of the thickness (the variation in this region is less than 10%).

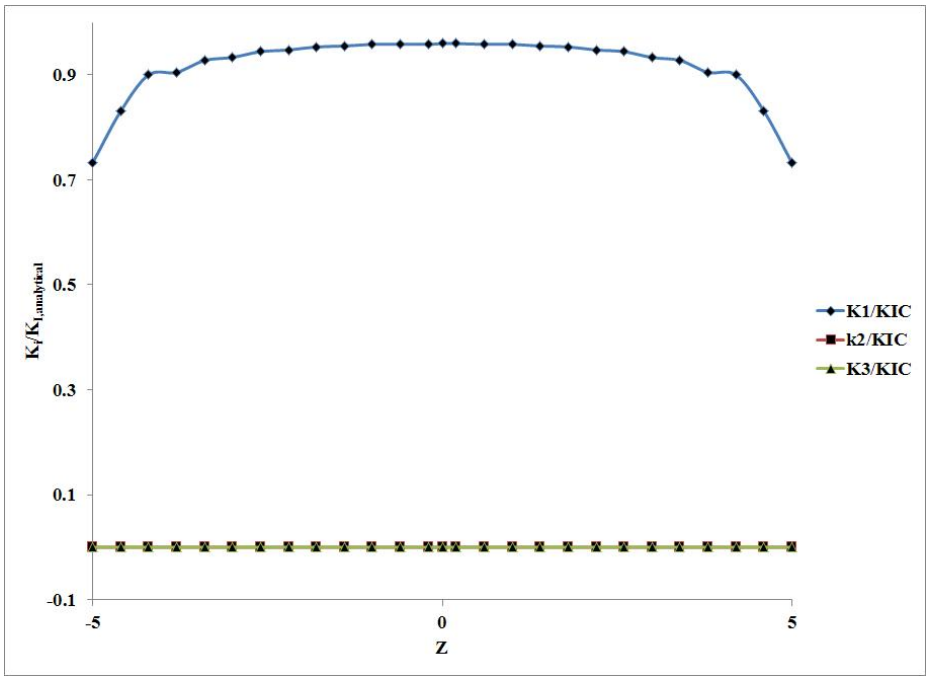

Figure 7-3. Through-thickness variation of SIFs evaluated by FE for mode I crack normalized with respect to theoretical value of K_I

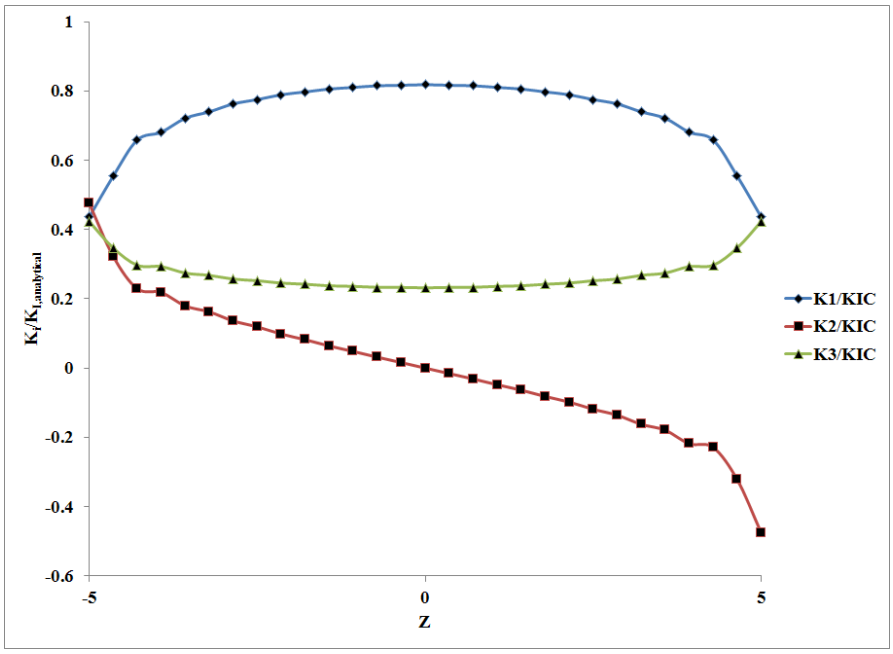

Figure 7-4. variation of the SIFs along the thickness of the specimen for the crack front orientation angle θ= 30^o

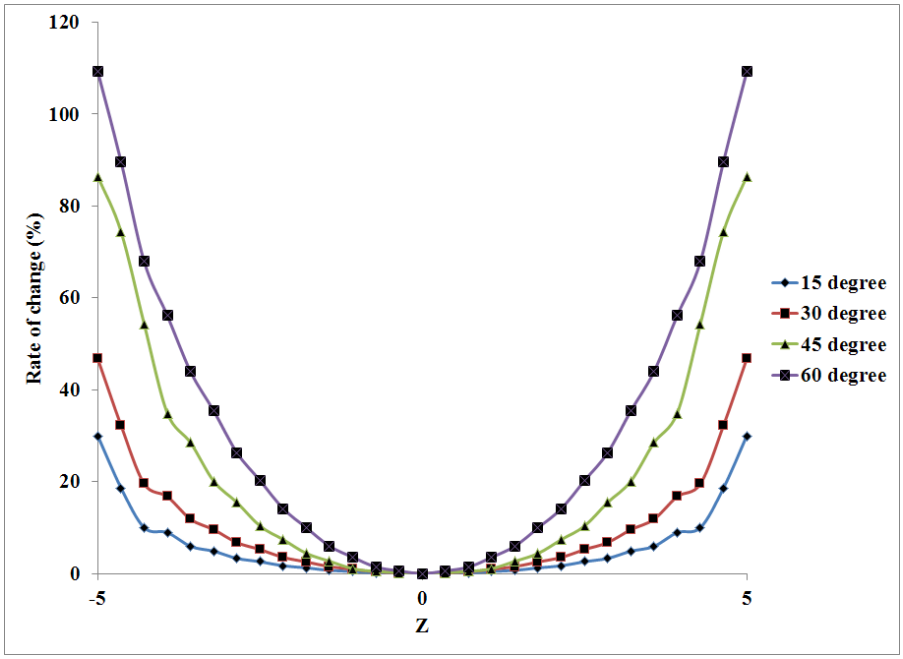

(a)

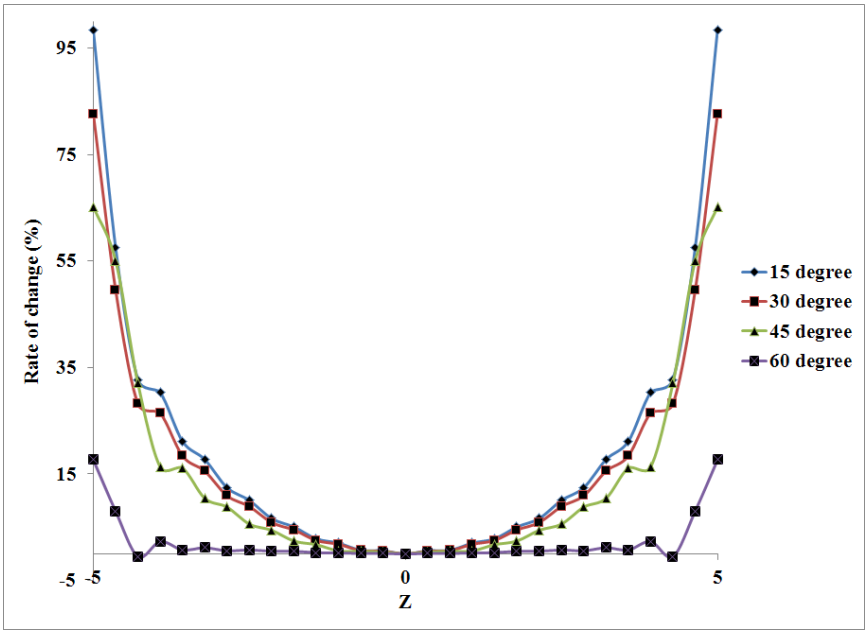

(b)

Figure 7-5. Percent change in the through -thickness variation of SIF for various crack front orientation angles with respect to mode I SIF- (a) K_1 variation (b) K_3 variation

The percent change in the values of K_1 and K_3, with respect to the theoretical value of Ks at mid-thickness, evaluated for various crack front orientation angles, are illustrated in Figure 7-5. As seen, there is a more gradual change in the through-thickness variation of K_1, for all crack orientation angles, while K_3 changes rather abruptly for all the crack orientation, and less for the 60^o orientation.

To further demonstrate that K_3 is much more dominant than K_2, FE results showing the through-thickness distribution of K_2 and K_3 for all the crack orientations are illustrated in Figure 7-6. As can be seen the values of K_3 are much greater than K_2 (in terms of comparison of the ratios of ratio of K_3/K_1 to K_2/K_1 within a region 0.5 mm away from the free surfaces), indicative of the fact that K_1 and K_3 would be the effective modes causing failure for most crack orientation angles. The negative value of K_3 as shown in Figure 6 for $\theta = 60^o$ is as a result of the opposing shear stresses developed near the either surfaces

of the specimens. The existence of these stresses would cause the crack not to propagate from crack's tip at these regions. This fact will be substantiated later by experimental results in the next section. Furthermore, the results near the free surfaces should be disregarded because the classical SIFs could not be defined at free surfaces due the severe and abrupt change in the strain distribution (also known as the "near the free surfaces/corner singularity" (see Bazant and Estenssare [25]).

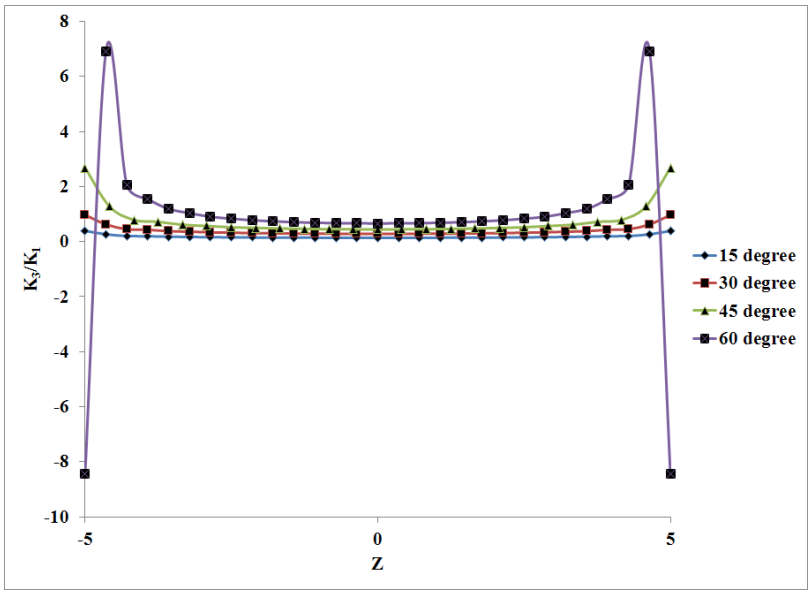

(a)

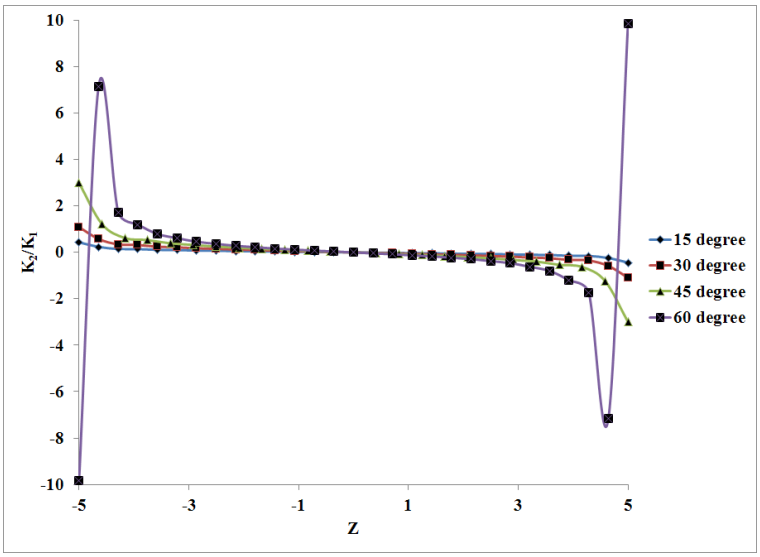

(b)

Figure 7-6. Through-thickness variation of (a) K_3 and (b) K_2 for all crack orientation angles

To better understand the influence of line-load angle on the magnitude of K_2 SIF, further investigation was carried out. Figure 7-7 shows the effect of the applied line-load angle on the value of K_2 through specimens' thickness. The variation is illustrated by plotting the variation S, defining by $\frac{K_{2\ (at\ \theta=0)} - K_{2\ (at\ \theta=crack\ angle)}}{K_{2\ (at\ \theta=0)}}$. The results reveal that K_2 would be reduced from 8.5%-11.5% at the vicinity of the free surfaces and from 14%-23% near the mid-thickness, when the load was applied parallel to the pre-crack front's orientation. Furthermore, the values of through-thickness variation of K_2 decreased when the line-load assumed the same orientation as that of the crack front.

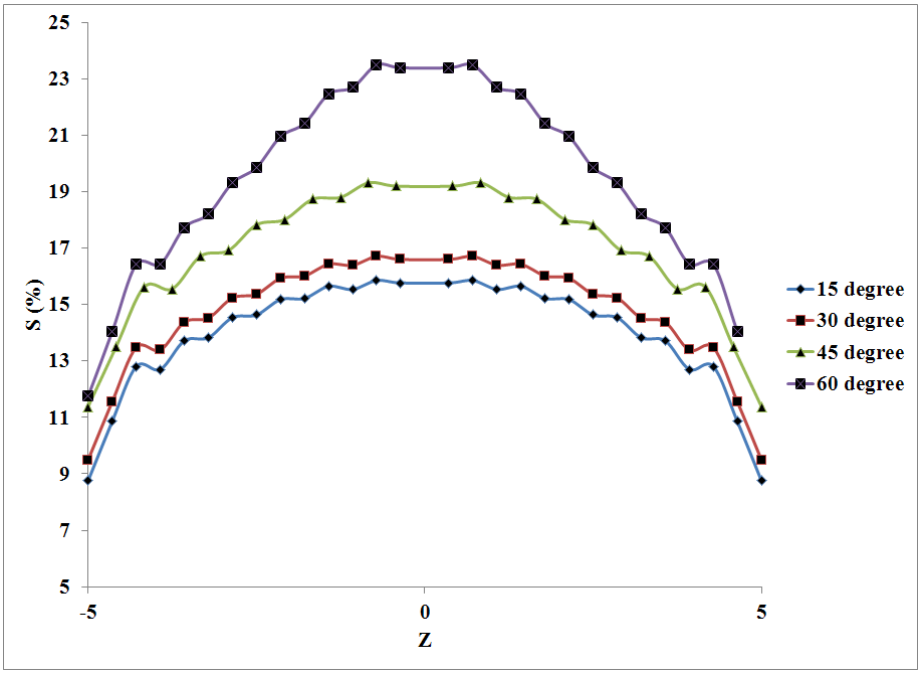

Figure 7-7. Variation in the through-thickness distribution of K_2 when line -oad is at the same angle as the cack front for various crack front angles

The above results are used in the development of a simple and effective relationships for establishing the SIFs K_1 and K_3 for crack fronts oriented at an arbitrary angle θ. For that two correction factors, namely $g(\theta)$ and $h(\theta)$ are proposed, as follows:

$$g(\theta) = A + Bcos(\theta) + Csin(\theta) \qquad 7\text{-}3$$

$$h(\theta) = A' + B'cos(\theta) + C'sin(\theta) \qquad 7\text{-}4$$

where A, B, C, $A^{'}$, $B^{'}$ and $A^{'}$, are constants that are established by performing a regression analysis to the data reported in Table 7-2, in which the K_1 and K_3 represent the assessed SIFs at the mid-thickness of the specimen. The $g(\theta)$ and $h(\theta)$ factor relates K_1 and K_3 to crack front orientation angle (θ), respectively, using the following equations:

$$K_1 = \frac{P}{BW^{\frac{1}{2}}} f_1(\frac{a}{W})[0.34 + 0.66cos(\theta) - 0.22sin(\theta)] \quad 7\text{-}5$$

$$K_3 = \frac{P}{BW^{\frac{1}{2}}} f_1(\frac{a}{W})[-0.24 + 0.24cos(\theta) + 0.51sin(\theta)] \quad 7\text{-}6$$

$f_1(\frac{a}{W})$ term appearing in the above equations is calculated using equation 7-2. Once the values of K_{iC} are calculated, one can then evaluate the values of G_{iC} (under the plane strain condition) by the following equations:

$$G_1 = {K_1}^2(1 - \upsilon^2)/E \quad 7\text{-}7$$

$$G_3 = {K_3}^2(1 + \upsilon)/E \quad 7\text{-}8$$

Table 7-2. The values of K_1 and K_3 at the mid-thickness, obtained through the FE analysis

Angle (degree)	0	15	30	45	60
$\frac{K_1}{K_{IC}}$	1	0.938	0.819	0.621	0.492
$\frac{K_3}{K_{IC}}$	0	0.129	0.231	0.279	0.325

7.4 Experimental Investigation

7.4.1 Materials and Specimen preparation

A high strength epoxy resin (Araldite LY564/ Aradur 2954) was used to prepare the test specimens. The mechanical properties of used epoxy are shown in Table 1. LY564 resin was mixed with Aradur 2954 hardener with the weight ratio of 100:35, and was then stirred by a mechanical stirrer at 700 rpm for five minutes. To remove the existing bubbles, the resin was left in a container in a vacuum chamber for 60 minutes at 91.5 kPa vacuum. Moulds were made to accommodate two test specimen configurations; the dog bone tensile specimen (as per ASTM D638 [23]) and the single edge notch bend (SENB) specimen configuration (as per ASTM D5054 [8]). These moulds were then filled by the resin and cured in an oven at $60^{\circ}C$ for two hours, followed by post curing it at $120^{\circ}C$ for eight hours. A special jig was designed to make the inclined pre-notch in each specimen using a 0.28 mm thick jeweller saw. After creation of the notch by the saw, the notch was sharpened using a fine razor blade.

7.4.2 Test set-up

An Instron servo-hydraulic test machine (model 8500) with a 5 kN load cell was used to load the specimens and load, actuator and support's displacements data was collected through a proper data acquisition system and stored in a PC. The test speed was at 2 mm/min and 1 mm/min for the tensile and three point-bend tests, respectively. Three specimens were tested at each pre-crack orientation angle. A master loading device was designed in order to apply the load in the same orientation as that of the pre-crack front. Figure 7-8 shows test setup and apparatus.

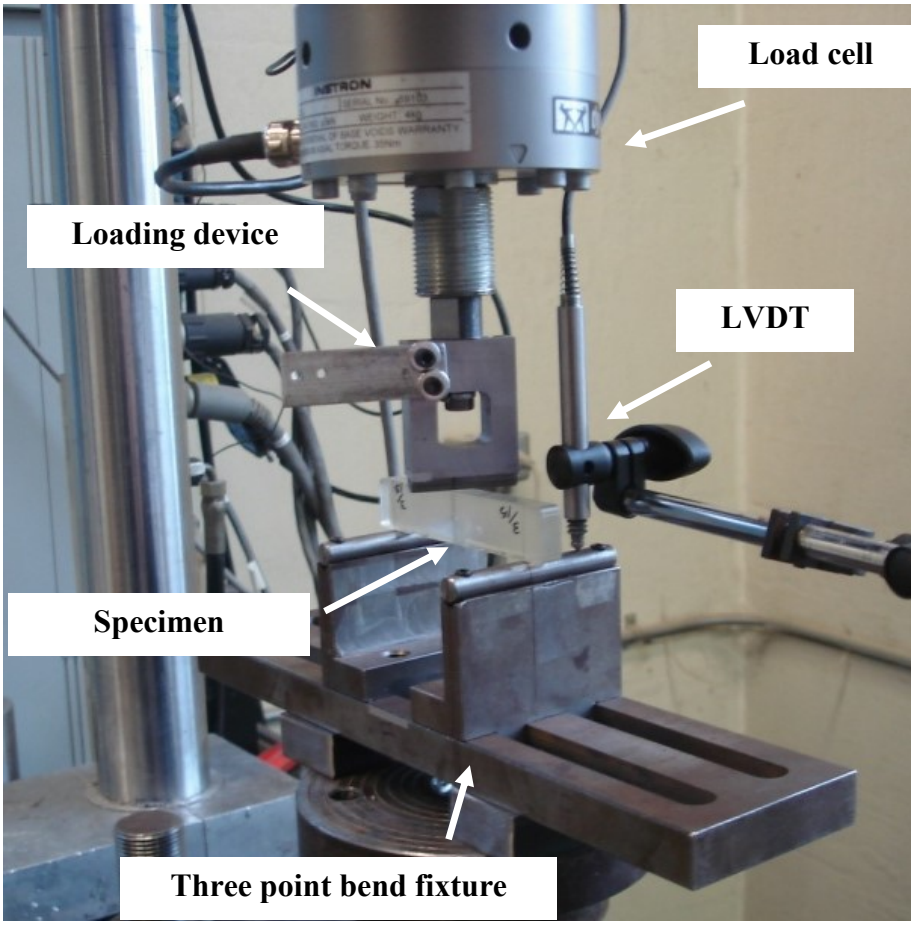

Figure 7-8. Three point bend test setup and apparatus

7.4.3 Experimental results

The uniaxial stress-strain results obtained from testing the dog-bone specimen exhibited a nonlinear elastic-plastic response for the resin, as illustrated in Figure 7-9. Although the tensile test exhibits a nonlinear elastic-plastic response of the studied resin, all tested specimens failed in a brittle manner and the fracture surfaces were flat without any shear lips. Furthermore, there was no noticeable permanent reduction in specimens' cross-section area to be measured. This would indicate that the assumption of quasi brittle

behaviour is valid for the material; as a result, one can use the linear elastic fracture mechanics for evaluating the crack tip SIFs [26].

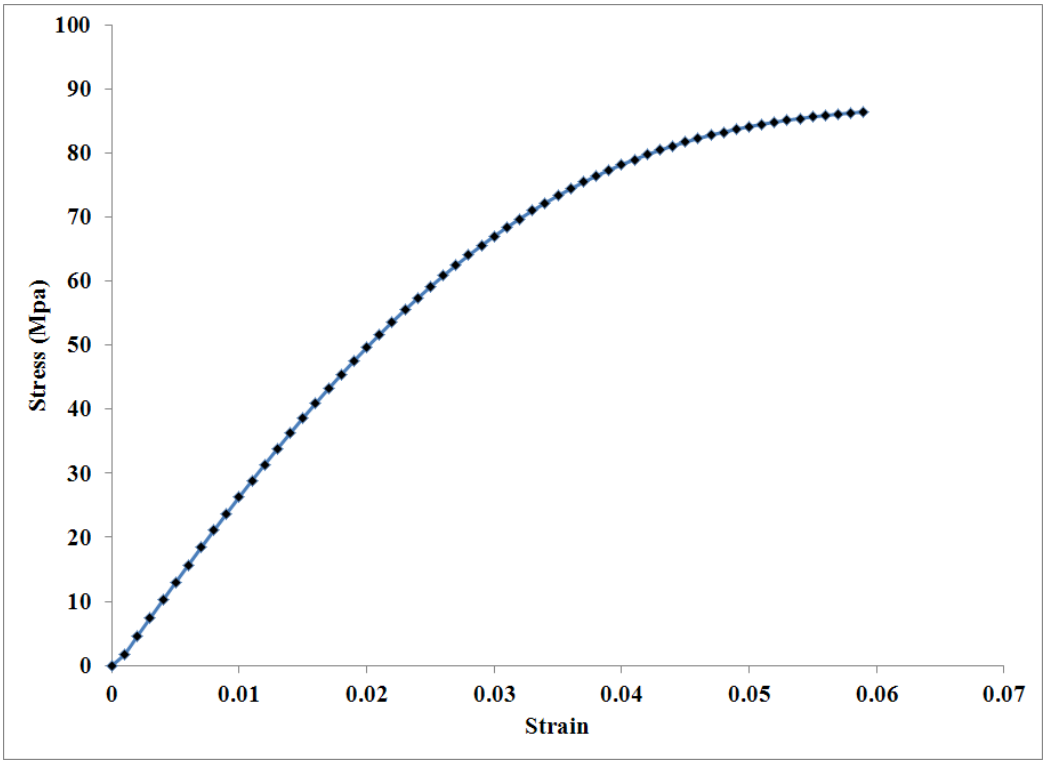

Figure 7-9. Uniaxial stress-strain response of LY564-Aradur 2954

As stated earlier, by establishing the value of P_{max} from the three point bend tests for specimens with θ=0° pre-crack, the values of K_{1C} and K_{3C} could be calculated for a specimen having its pre-crack oriented at any arbitrary orientation angle θ by setting the appropriate value of θ in Equations 7-5 and 7-6. Figure 7-10 shows the load-displacement curves for specimens having various pre-crack orientation angle, θ. As shown, the magnitude of the load for $\theta = 60°$ is much higher than that anticipated. The examination of the failure surface on the failed specimens revealed that the crack actually did not propagate from the crack tip in the vicinity of the free surfaces, thus, the failure occurred

at higher load levels than anticipated. This failure pattern was consistent in all specimens with $\theta = 60°$ crack orientation, Figure 7-11 illustrates a typical failed specimen with a pre-crack orientation angle of $\theta = 60°$. The above-discussed failure mechanism can be observed though the illustrated failure surface.

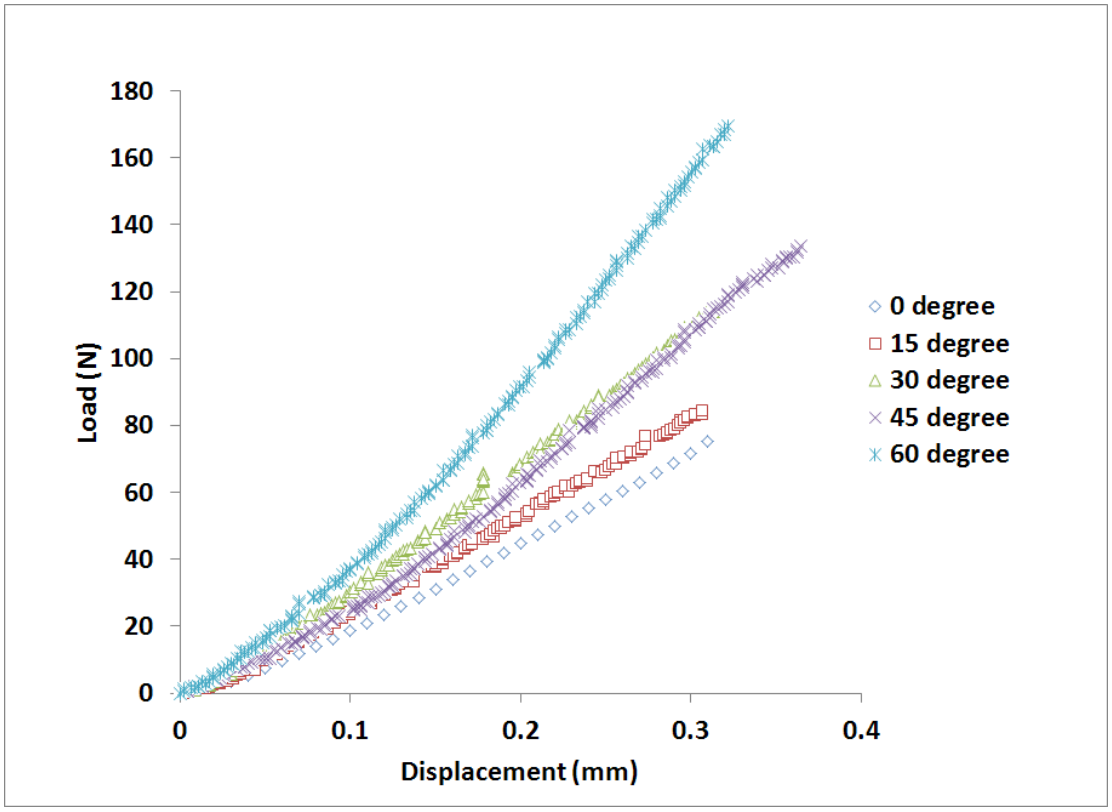

Figure 7-10. Load-displacement response of the SENB specimens having various crack orientation angle.

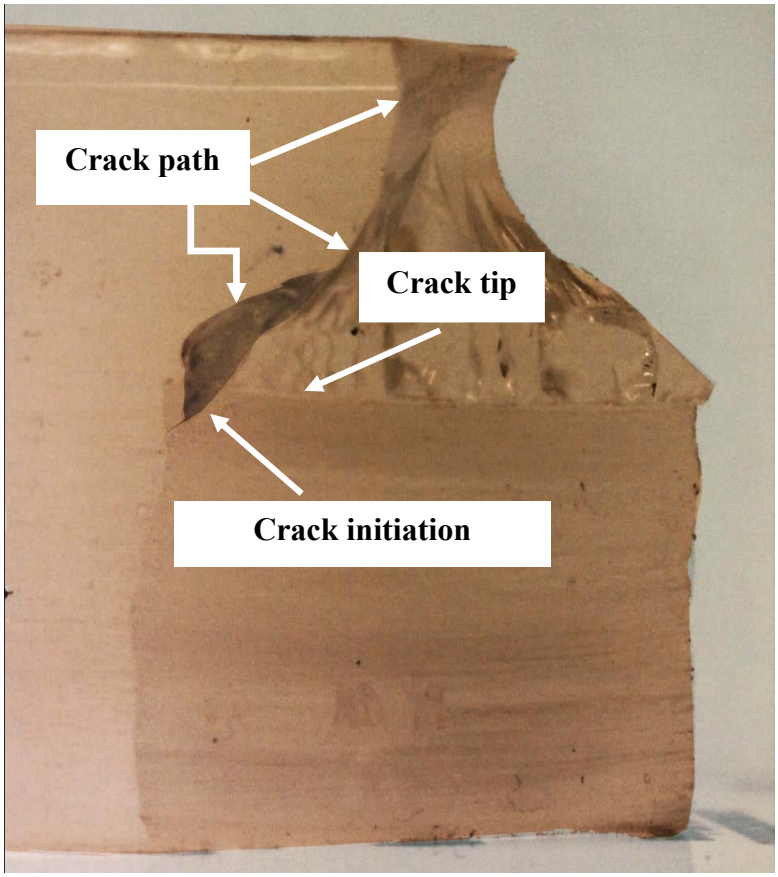

Figure 7-11. Typical failure morphology observed in specimens hosting a pre-crack orientation of $\theta = 60^{o}$

As per ASTM D5054 [8], the value of P_{max} would be the maximum load value seen in curves shown in Figure 7-12. By substituting P_{max} and appropriate crack angle and specimen geometric information in Equations 5 and 6, one can calculate K_{1C} and K_{3C} for the given pre-crack angle. Figure 7-12 shows the variation of $K_{1C}/\ K_{IC,theoritical}$ versus $K_{3C}/\ K_{IC,theoritical}$ for different crack orientations. K_{1C} and K_{3C} are the critical SIFs at the mid-thickness of specimen. As seen, an increase in the crack angle in turn increased the contribution of mode III fracture, also increased the magnitude of K_I. Since an increase in crack's angle would lead to an increase in the fracture surface area (due to inclination of the fracture plane), consequently, the value of the actual (experimentally obtained) K_{IC}

would be larger than the theoretical one. This would be mainly due to the friction between the crack surfaces in the actual specimen, which is not accounted within the simulation. In addition, the fracture area is larger than the assumed planar due to rough appearances. It should be noted that the investigated epoxy resin is a brittle material; such materials tend to fracture under pure mode I [6] (i.e., mode I fracture contribution becomes dominant, even under a mix-mode fracture state). The effect of this phenomenon can be seen in the results, since even at higher fracture angles, the contribution of K_{1C} is significant and almost to K_{3C}.

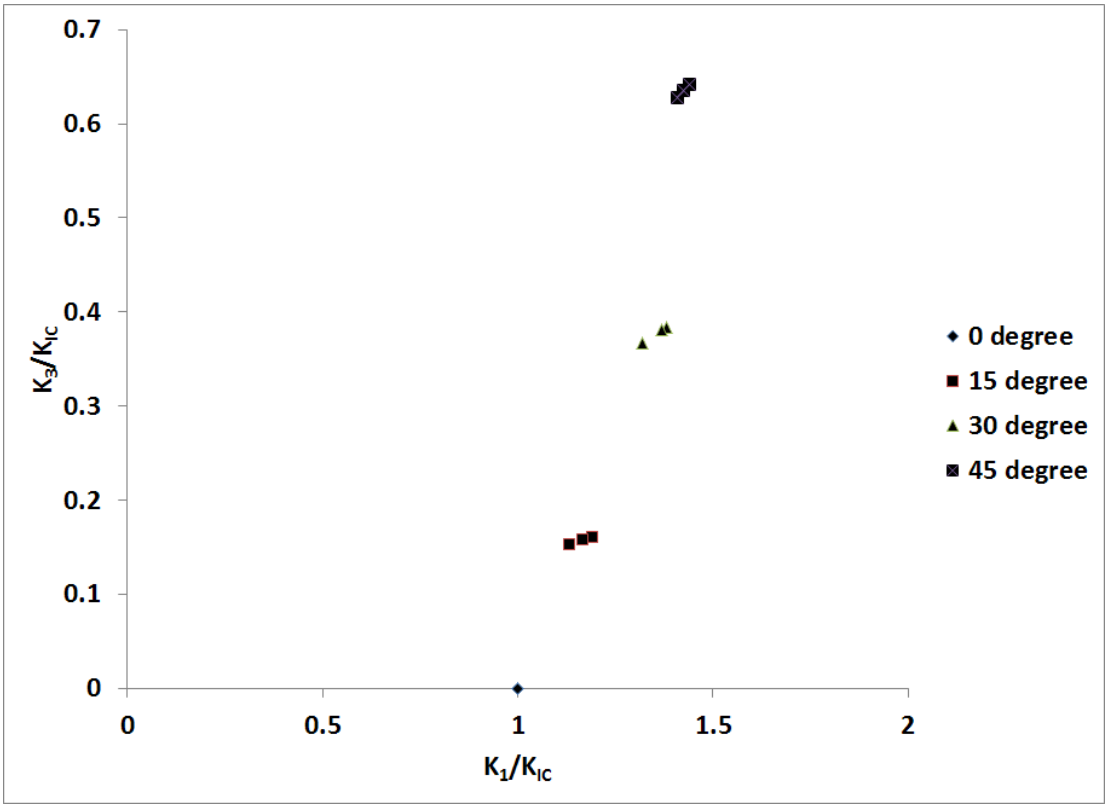

Figure 7-12. Variation of the experimentally obtained critical mixed-mode I/III SIF

It should be noted that since the fracture was not initiated from the crack tip in $\theta = 60^{o}$ specimens, the results for this group of specimens was not reported in the graph of Figure 12.

Figure 7-13 shows the front view of crack kink angle and the fracture surface of the specimens. When $\theta = 0^{o}$, crack evolved continually along the initial crack front. The shiny and mirror-like crack surface (Figure 7-13Fb) indicates the brittle nature of the pure mode I fracture. Furthermore, the thumb nail shaped crack front illustrates the relatively large thickness of the specimens. For $\theta > 0^{o}$, not only did the crack propagated with in an angle with respect to the initial crack front, but also the crack front twisted along the direction of propagation. Lazarus et al [27] observed the same behavior in PMMA and concluded that the crack front would twist such that it would finally approach to the mode I plane of the specimens. The increase in crack angle θ resulted in crack's transition from an approximately single faceted propagation of the crack to a multi-faceted propagation morphology crack evolution occurred (Figure 7-13d,f and h). The formation of such multi-facets has also been observed by Sommer [28] in brittle material when the material underwent more torsional stress (i.e., mode III loading) as opposed to those having been subjected to predominantly in-plane stress (mode I loading). One can therefore conclude that formation of these multi-faceted appearance (also referred to as "factory roof" pattern), is an indicative of domination of mode III loading in studied specimens.

a

b

c

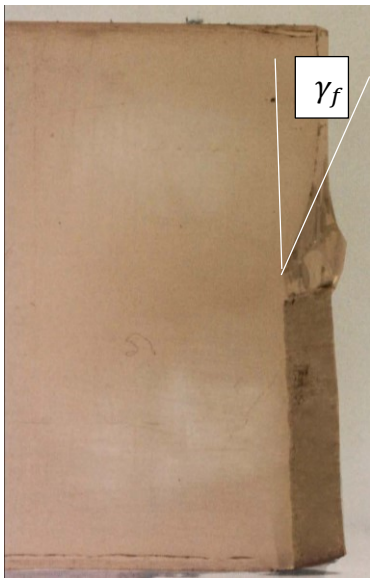

d

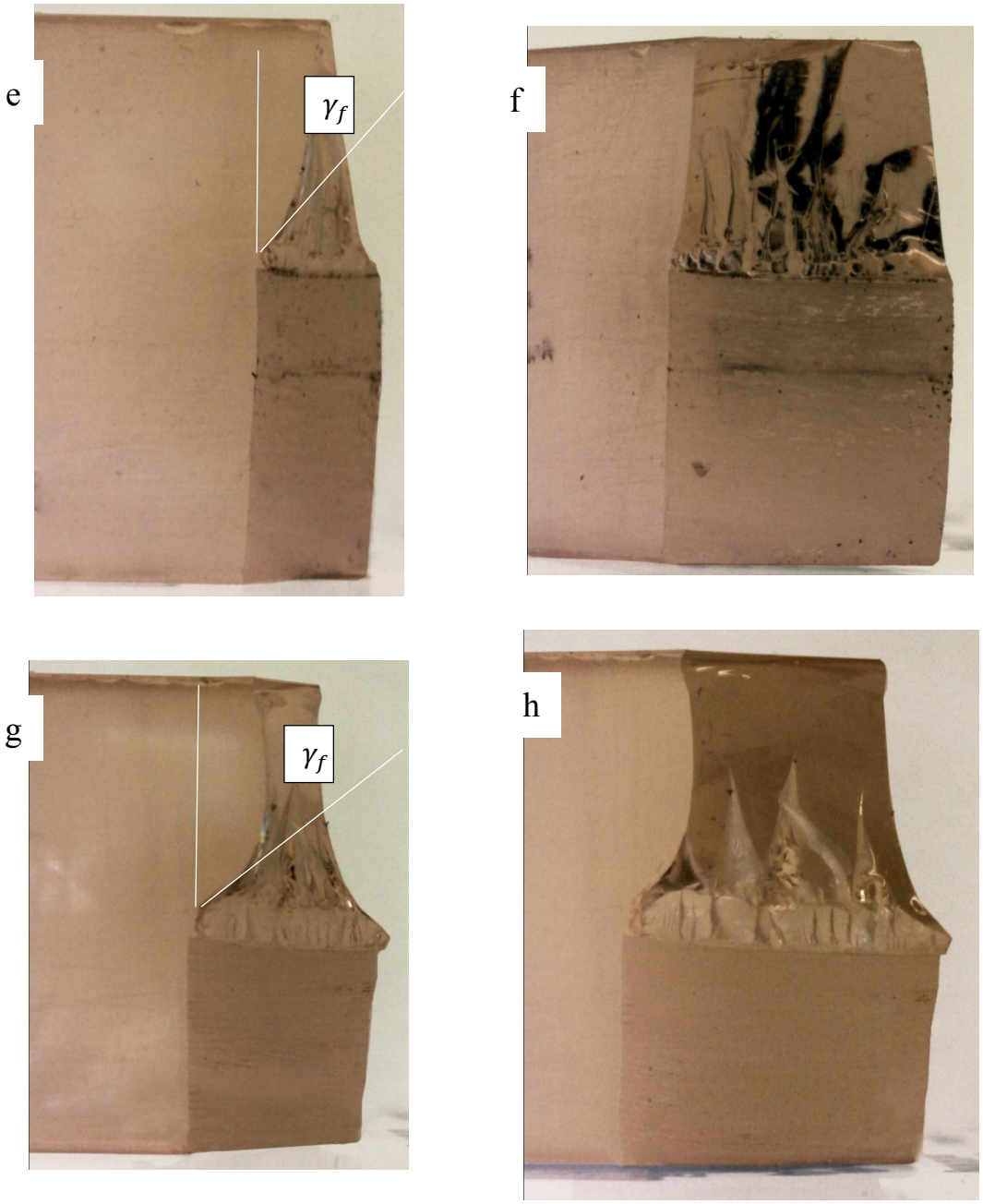

Figure 7-13. Crack surface and crack kink angle:a, b) pure mode one, c,d) $\theta = 15°$, e, f) $\theta = 30°$ and g, h $\theta = 45°$

To assess the crack initiation and propagation, one may utilize the mixed mode fracture mechanics criteria. There exist two sets of criteria: (i) local-based and (ii) global-based. Local criteria, such as the maximum tangential stress criterion (MTS), require the

value of K_i (i=1, 2, 3) at each point through the thickness of specimens, obtained from a 3D analysis; the global criteria, however, require the average value of K_i (see for example Lazarus et al [14]).

Schollmanm et al [13] developed the maximum tangential stress criterion (MTS) based on a 3D analysis, by considering K_3 (3DMTS). According to this criterion, the crack would grow radially from the crack front along the direction perpendicular to the plane where the principal stress attains its maximum value. One can link the crack kink angle, γ, as shown in Figure 7-13 to SIFs using the following expression.

$$
\begin{aligned}
&-6K_1 tan(\gamma/2) - K_2\big(6 - 12tan^2(\gamma/2)\big) \\
&\quad + \Big\{[4K_1 - 12K_2 tan(\gamma/2)]\big[-6K_1 tan(\gamma/2) \\
&\quad - K_2\big(6 - 12tan^2(\gamma/2)\big)\big] \\
&\quad - 32{K_3}^2 tan(\gamma/2).\big(1 \\
&\quad + tan^2(\gamma/2)\big)^2\Big\}.\Big\{[4K_1 - 12K_2 tan(\gamma/2)]^2 \\
&\quad + 64{K_3}^2\big(1 + tan^2(\gamma/2)\big)^2\Big\}^{-1/2} = 0
\end{aligned}
\qquad \text{7-9}
$$

Lazarus et al [14] proposed two global criteria starting from the assumption that the twisting of the crack front occurs due to the existence of mode III fracture. Their criteria were developed by maximizing the mean value of the total energy release rate (MVG) and minimizing the mean value of mode I SIF (MVK) along the crack front with respect to the kink angle, γ. According to the above-mentioned criteria (i.e., MVK and MVG), the angle γ can be linked to the ratio of $\frac{K_3}{K_1}$, using the following equations, respectively:

$$\gamma = \frac{8\frac{h}{d}}{1 + \frac{16\sqrt{2}}{2\pi}\sqrt{\frac{h}{a}} - \frac{5}{12}\frac{h}{a} + \frac{6}{\pi}\frac{2-3\upsilon}{2-\upsilon}\frac{h}{d}} \times \frac{k_3}{k_1} \qquad 7\text{-}10$$

$$\gamma = \frac{4\frac{h}{d}}{(2-\upsilon)\left(\frac{1}{3} + \frac{4}{3\pi}\sqrt{\frac{2h}{a}} - \frac{16}{3\pi^2}\frac{h}{a} + \frac{2}{\pi}\frac{2-3\upsilon}{2-\upsilon}\frac{h}{d}\right)} \times \frac{k_3}{k_1} \qquad 7\text{-}11$$

where a is the crack length, d is the half thickness of specimen, υ is the poison ratio and h is a characteristic length related to the twisting angle of the crack (for details see Lazarus et al [14]).

The kink angle, γ_f (for our specimens) was measured at z=5 and converted to its value on crack coordinate system (γ) using following equation.

$$\cos\gamma = \frac{\cos\gamma_f}{\sqrt{\sin^2\theta + \cos^2\theta\sin^2\gamma_f}} \qquad 7\text{-}12$$

By substituting the average value of K_3 and kK_1 in Equations 9-11, the value of the kink angle could be predicted. Figure 7-14 shows the comparison of the kink angle computer by the above-mentioned method and those measured. As can be seen, there are large error margin between the kink angle values obtained through the incorporation of the 3DMTS criterion and the experimental results. On the other hand, the angles obtained based on the MVK and MVG criteria are in good agreement with the experimental results.

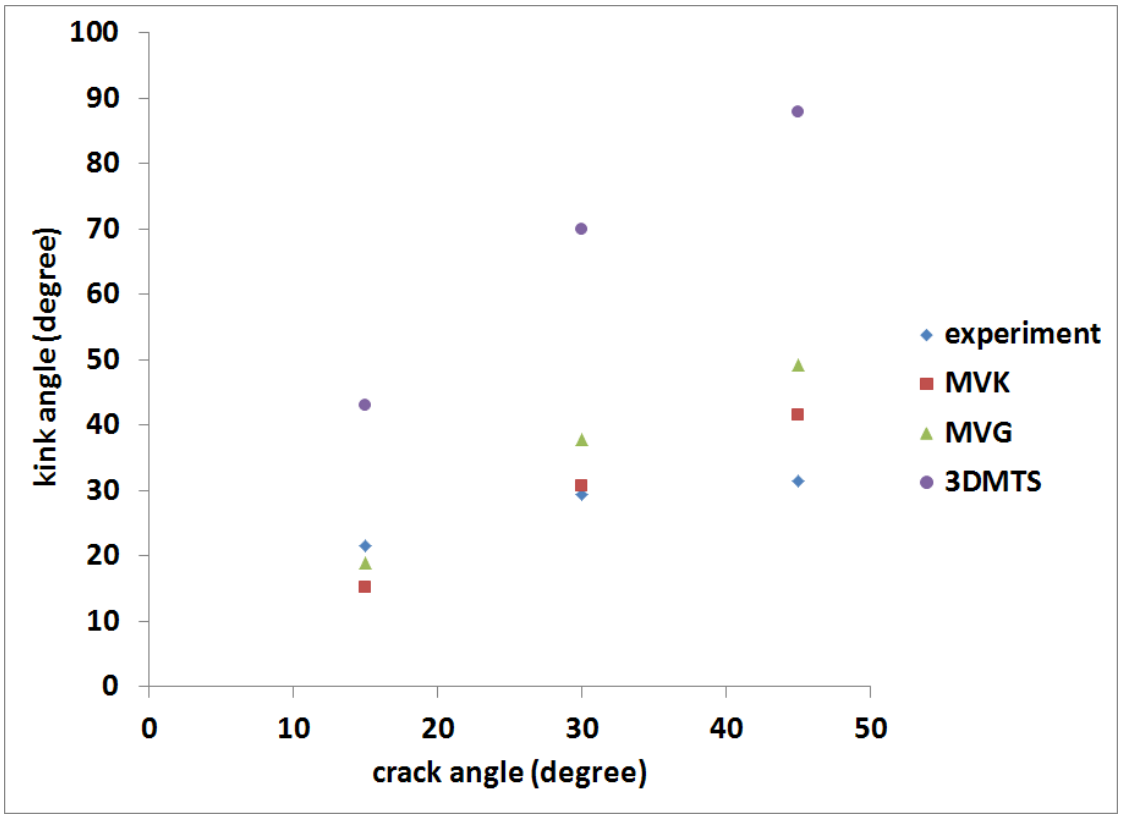

Figure 7-14. Crack kink angle

It should be noted that one can expect the maximum error in the prediction of kink angle at the measured locations because one cannot dismiss the role of K_2 near the free surfaces of the specimens; nonetheless the MVK and MVG methods could accurately predict the kink angle values. In addition, the global-based criteria accounts for the effect of the facet originated due to mode III loading by parameter, h, (see equations 10 and 11); therefore comparing the situations where K_3 is the more predominant in comparison to K_2 further reveals that the most effective fracture modes in the tested specimens were modes I and III. Moreover, the through-the-thickness variation of K_1 and K_3 were more-or-less uniform, and that is why the specimens fracture response could be characterized by the global criteria.

7.5 Conclusions

A modified single edge notch bend specimen configuration was utilized to evaluate the fracture behavior of an epoxy resin under mixed-mode I/III. The fundamental specimen configuration is identical to the SENB specimen as per ASTM D5054 [8], but in the proposed specimen, the crack takes an orientation angle with respect to the through-thickness axis of the specimen. The use of proposed specimen provides several advantages. Firstly, the fracture behavior of material in both mode I and mixed mode (I/II and I/III) could be assessed with the same specimen configuration and loading apparatus. This eliminates the need for more complex apparatus that are currently utilized in conducting tests for establishing mixed mode fracture toughness of materials. Secondly, as it was illustrated by our results, in the proposed specimen configuration, the contribution of K_3 was more dominant in comparison to the contribution of K_2 on all crack fronts, regardless of the crack orientation angle (with exception to a small region near the specimens' surfaces). It was also observed that applying the line-load in the same orientation as that of the pre-crack front would dramatically reduce the contribution of K_2, consequently validating the condition of $K_2 \ll K_3$ within a large area through-the-thickness of the specimen. The authors therefore suggest that the creation of a pair of side grooves on the two outer surfaces of the specimen should constrain the crack front to be extended under a relatively constant K_3 ratio, thereby eliminating the effect of K_2 that develops near the surfaces. This postulation will be pursued I the next phase of our study.

7.6 Acknowledgment

The financial support of the National Science and Engineering Resource of Canada (NSERC) through the CREAT program is gratefully appreciated.

7.7 References

[1] Zhu H, Wu B, Li D, Zhang D, Chen Y. Influence of Voids on the Tensile Performance of Carbon/epoxy Fabric Laminates. Journal of Materials Science & Technology. 2011;27:69-73.

[2] White SR, Hahn HT. Cure Cycle Optimization for the Reduction of Processing-Induced Residual Stresses in Composite Materials. Journal of Composite Materials. 1993;27:1352-78.

[3] Suresh S, Tschegg EK. Combined Mode I-Mode III Fracture of Fatigue-Precracked Alumina. Journal of the American Ceramic Society. 1987;70:726-33.

[4] Xu G, Bower AF, Ortiz M. An analysis of non-planar crack growth under mixed mode loading. International Journal of Solids and Structures. 1994;31:2167-93.

[5] BS EN ISO 12737: Determination of Plain-Strain Fracture Toughness of Metallic Materials. . BSI; 2011.

[6] Manoharan M, Lewandowski JJ. Combined Mode I-Mode III Fracture Toughness of a Particulate Reinforced Metal-Matrix Composite. Journal of Composite Materials. 1991;25:831-41.

[7] Anderson TL. Fracture Mechanics: Fundamentals and Applications, Third Edition: Taylor & Francis; 2005.

[8] ASTM D5054. Standard test methods for plane-strain fracture toughness and strain energy release rate of plastic material. West Conshohocken, PA: ASTM; 2007.

[9] Bian L-C, Kim KS. The minimum plastic zone radius criterion for crack initiation direction applied to surface cracks and through-cracks under mixed mode loading. International Journal of Fatigue. 2004;26:1169-78.

[10] Bian L, Taheri F. Fatigue fracture criteria and microstructures of magnesium alloy plates. Materials Science and Engineering: A. 2008;487:74-85.

[11] S. BS, K. PK, S. HM. Finite element modeling of crack initiation in mixed-mode (I/II). Journal of Solid Mechanics. 2010;3:231-47.

[12] Chen Z, Adams RD, da Silva LM. Fracture toughness of bulk adhesives in mode I and mode III and curing effect. Int J Fract. 2011;167:221-34.

[13] Schöllmann M, Richard H, Kullmer G, Fulland M. A new criterion for the prediction of crack development in multiaxially loaded structures. Int J Fract. 2002;117:129-41.

[14] Lazarus V, Buchholz FG, Fulland M, Wiebesiek J. Comparison of predictions by mode II or mode III criteria on crack front twisting in three or four point bending experiments. Int J Fract. 2008;153:141-51.

[15] Lin B, Mear ME, Ravi-Chandar K. Criterion for initiation of cracks under mixed-mode I + III loading. Int J Fract. 2010;165:175-88.

[16] Chell GG, Girvan E. An experimental technique for fast fracture testing in mixed mode. Int J Fract. 1978;14:R81-R3.

[17] Varadarajan R, Thurston A, Lewandowski J. Increased Toughness of Zirconium-Based Bulk Metallic Glasses Tested under Mixed Mode Conditions. Metall and Mat Trans A. 2010;41:149-58.

[18] Davenport JCW, Smith DJ. A STUDY OF SUPERIMPOSED FRACTURE MODES I, II AND III ON PMMA. Fatigue & Fracture of Engineering Materials & Structures. 1993;16:1125-33.

[19] A.M. K, J.P. H, R. H, X. F. A Suggested Test Procedure to Measure Mixed Mode I–III Fracture Toughness of Brittle Materials. Journal of Testing and Evaluation. 1994;23:327-34.

[20] ASTM E399. Standard test method for linear-elastic plane strain fracture toughness K_IC of metallic material. West Conshohocken, PA: ASTM; 2009.

[21] Liu S, Chao YJ, Zhu X. Tensile-shear transition in mixed mode I/III fracture. International Journal of Solids and Structures. 2004;41:6147-72.

[22] Ayatollahi MR, Shadlou S, Shokrieh MM. Mixed mode brittle fracture in epoxy/multi-walled carbon nanotube nanocomposites. Engineering Fracture Mechanics. 2011;78:2620-32.

[23] ASTM D638. Standard test method for tensile properties of plastic. West Conshohocken, PA ASTM; 2010.

[24] Sukumar N, Moës N, Moran B, Belytschko T. Extended finite element method for three-dimensional crack modelling. International Journal for Numerical Methods in Engineering. 2000;48:1549-70.

[25] Bažant ZP, Estenssoro LF. Surface singularity and crack propagation. International Journal of Solids and Structures. 1979;15:405-26.

[26] Chao Y, Liu S. On the failure of cracks under mixed-mode loads. Int J Fract. 1997;87:201-23.

[27] Lazarus V, Leblond J-B, Mouchrif S-E. Crack front rotation and segmentation in mixed mode I+III or I+II+III. Part II: Comparison with experiments. Journal of the Mechanics and Physics of Solids. 2001;49:1421-43.

[28] Sommer E. Formation of fracture ‘lances’ in glass. Engineering Fracture Mechanics. 1969;1:539-46.

Chapter 8: The Effect of Strain-Rate on the Tensile and Compressive Behavior of Graphene Reinforced Epoxy/ Nanocomposites

Sahin Shadlou, B. Ahmadi-Moghadam and Farid Taheri

Published in the Journal of Materials and Design, Volume 54, PP439-447, 2014

8.1 Abstract

The effect of strain rate on the mechanical behavior of epoxy reinforced with graphene nanoplatelets (GNPs) is investigated. Nanocomposites containing various amounts of GNP are prepared and tested at four different strain rates (0.01, 0.1, 1 and 10/s) under compressive and tensile loading regimes. The results show that incorporation of GNP highly affects the behavior of epoxy. The fracture surfaces of tensile specimens are also investigated using scanning electron microscopy (SEM) to discern the surface features and dispersion state of GNP. Finally, the predictive capability of some of the available models for evaluating the strength of nanocomposites are assessed and compared against the experimental results. Moreover, a modification factor to the widely used Halpin-Tsai model is proposed to improve the accuracy of the model when evaluating the Young's modulus of nanocomposites at various strain rates.

8.2 Introduction

A large number of studies have been carried out to explore various aspects of nanocomposites reinforced with carbon nanotube (CNT) [1, 2], carbon nanofiber (CNF) [3] and nanodiamond [4] in past two decades. The recent discovery of graphene nanoplatelets as a new breed of carbon nanoparticle with its extraordinary physical properties, however, has led to generation of a new class of nanocomposites. In addition to the impressive thermal and electrical properties of GNP, the mechanical properties of the sp^2 bonding network in the GNP structure render them as suitable nanoparticles for

enhancing the mechanical properties of polymers [5]. The recent advances in processing techniques has facilitated less costly and more environmentally friendly production of bulk GNPs [6], thereby increasing the potential of use of GNP based nanocomposites in various industrial applications. Chen and Lin [7] proposed a non-toxic, non-polluting and friendly to the environment for preparation process of GNP and obtained GNP with good structure and dispersibility.

Polymeric materials, either in the form of bulk or as adhesives, may be subjected to dynamic or impulse loading conditions. Strain rate has been known to affect the mechanical behavior of polymers quite significantly [8]; therefore, a deep understanding about the effect of strain rate on polymers properties is crucial in the design and safe in-service performance of polymeric structural components. The effects of strain rate and temperature on pure polymers and composites have been studied by several researchers [9]. Goglio et al [10] also investigated the dynamic mechanical response of two epoxy adhesives, in form of bulk materials, under tensile and compressive loadings exerted through a servo-hydraulic universal testing machine, as well as a tension-compression Hopkinson bar apparatus. However, their attempt for utilizing the Cowper-Symonds and Johnson-Cook models to fit their experimental data led to unacceptable results. Mcclung and Ruggles [11] studied the inelastic deformation response in polymerization of a high-temperature thermoset polymer. They observed that the influence of strain rate changed material's response during tensile loading and unloading and the strain recovery response. The material showed positive, non-linear strain rate sensitivity under monotonic loading. In addition, a nonlinear behavior was observed during unloading, regardless of the strain rate. They also reported that the strain recovery at zero stress is also highly affected by the

strain rate. A few researchers have also investigated the effect of strain rate on composite materials. Jacob et al [12] have provided a nice review on works conducted to investigate the strain rate dependency of mechanical properties of polymer composite materials.

While there have been several studies that have evaluated the effect of strain rate on pure polymers, there is a very limited number of studies on the effect of strain rate on polymers reinforced with nanoparticles. Among the available studies that have investigated the response of nanoparticle reinforced polymers under different strain rates, the emphasis has mainly been on organoclay [13]. For instance, Jo and Naguib [14] studied the tensile behavior of a high-density polyethylene/clay nanocomposite foam with different cystallinity. They found out that although the Young's modulus of the foams was improved by the increase in its crystallinity, the rate of improvement decreased at higher strain rates. They also proposed a viscoelastic stress-strain behavior for the foam. Moreover, Argento et al [15] compared the loading rate effect on energy dissipation characteristics of bio-(sisal fiber) and nano-(nanoclay) cellular composite systems to conventional materials. Although they observed that the biocomposite systems showed unique energy dissipation characteristics and muted rate dependency (while the nanocomposite system did not), they could not identify the mechanism(s) that caused the trend. In another study Shen et al [16] indented the surfaces of polymer/clay nanocomposite at different strain rates. They found that strain rate had almost no effect on the elastic moduli of the neat system and the nanocomposites.

There have also been some strain rate studies on nanocomposites reinforced with CNT. Kakoee et al [17] investigated the effect of CNTs on the mechanical properties of epoxy based nanocomposites. They observed that addition of CNT to epoxy led to decrease

in compressive young modulus and fracture energy. However, at higher strain rates inclusion of CNT increased these properties 3% and 30.5% respectively. The strain rate effect in syntactic nanocomposite foams was studied by Al-Sharab et al [18] split-Hopkinson pressure bar at strain rates in the range 825-1670 1/s. They reported 20-40% increase in the strength of nanocomposite at higher strain rates. However, to the best of authors' knowledge, there has not been any research exploring the influence of rate effect on response of nanocomposites reinforced with GNPs.

In this study, therefore, the influence of various strain rates on the tensile and compressive responses of pure epoxy and GNP-reinforced epoxy nanocomposites is investigated. Nanocomposites with various GNP contents (i.e., 0.25, 0.5 and 1 wt%) are prepared and tested under strain rates of 0.01, 0.1, 1, 10/s. The fracture surfaces of the tensile specimens were investigated using the SEM micrographs. In addition, the capability of some of the available models for predicting the yield strength of the composite at different strain rates were assessed and compared against the results obtained experimentally. Moreover, a modification factor for the Halpin-Tsai model was proposed to improve the predictive accuracy of the model in regard to evaluating the Young's modulus of nanocomposites, with a particular emphasis on the strain rate.

8.3 Experiments

8.3.1 Materials and specimen preparation

Araldite LY 564 (Bisphenole-A) epoxy resin was used throughout this study along with Aradure 2954 (cycloaliphatic polyamine) hardener. This epoxy system is available through Huntsman Co. (West Point, Point, GA). GNPs used for this research were supplied by XG scientific (Lansing, MI). According to the supplier, they have an average thickness

of 7 nm and a mean particle diameter of 25 μm. In order to prepare the specimens, the desired amount of GNPs (i.e. 0.25, 0.5 and 1 wt%) was added to the monomer and mixed using a mechanical stirrer for 15 minutes at 2000 rpm. To obtain a uniform dispersion of GNPs within the resin, the mixture was then processed using a three-roll mill homogenizer (Torrey Hill Technology, San Diego, CA). The milling cycles for the mixture containing 0.25, 0.5 and 1 wt% GNP were at 1, 2 and 4 cycles, respectively. Finally, the hardener was added into the mixture, and after degassing, the slurry was cast in the desired molds.

8.3.2 Mechanical characterization

The monotonic tensile tests were performed on coupons according to ASTM: D638 standard [19], except for those used for assessing the strain rates. The tensile tests were performed using an MTS servo-hydraulic test machine with a 100 *kN* load cell. A dynamic extensometer was also used to measure the displacement accurately. Cylindrical shaped specimens with a diameter of 8.5 mm and length of 9 mm were employed to assess the compressive properties, using an Instron servo-hydraulic test machine (model 8500) with a 25 *kN* load cell. The tests were performed at strain rates of 0.01, 0.1, 1, 10/s; thus appropriate cross-head displacements were chosen based upon the nature of test and dimension of each specimen.

8.3.3 Scanning electron microscope

A field emission scanning electron microscope, FE-SEM, (Hitachi S-4700, Dallas, TX) was used to investigate the fracture surfaces of the nanocomposites and neat epoxy specimens, as well as the status of GNP dispersion within the resin.

8.4 Results and Discussion

8.4.1 Compression tests

Typical stress-strain curves for the neat epoxy and nanocomposites are depicted in Figure 8-1. Only one curve for each case is presented to ease the comparison of the results. As can be seen, the Young's modulus and yield strength of the materials increased as the strain rate increased. The neat epoxy exhibited a similar response in all strain rates; a linear elastic response in the initial loading stage, followed by minor nonlinear behavior up to the yielding point, followed by an insignificant strain softening and subsequently exhibited a dramatic strain hardening. On the other hand, the behavior of nanocomposites is different to some extent. It appears that the composite underwent no strain softening, and that after the yielding point, it exhibited strain hardening.

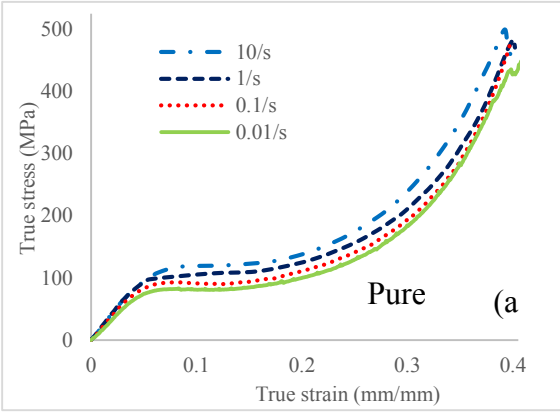

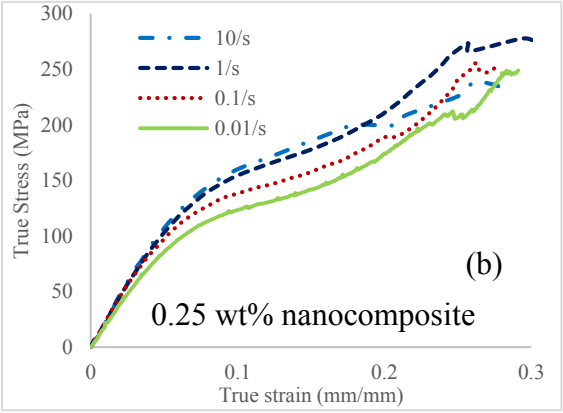

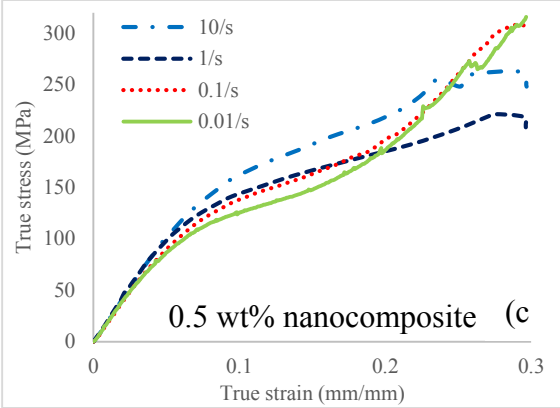

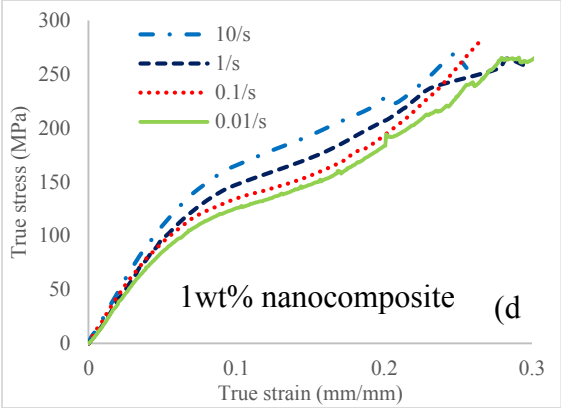

Figure 8-1. Typical experimental uniaxial compression true stress-strain curves for (a) neat epoxy (b) 0.25 wt% nanocomposite (c) 0.5 wt% nanocomposite (d) 1 wt% nanocomposite

The general trend for all nanocomposites containing different amounts of GNP is similar. The difference in strain hardening behavior of all materials at higher strain rates can be attributed to adiabatic heating effect, which has been reported to be significant at strain rate of 0.01/s or higher [20]. This effect seems to be more noticeable for nanocomposites, which might be due to higher conductivity of these materials owing to inclusion of GNPs. It is also noteworthy to mention that flaws like agglomeration of GNPs, entrapped gasses and other defects would have influence in this portion of materials' response.

Figure 8-2 presents a clearer comparison between the stress-strain curves of the neat epoxy and nanocomposites. While the fracture strain for pure epoxy is around 0.4 mm/mm, the value decreases to 0.3 in the case of nanocomposites, which signifies a transition from ductile to brittle behavior. However, a noticeable raise can be observed in the plastic flow of the nanocomposites compared to neat epoxy. The toughness of the neat epoxy and nanocomposites for strain rate of 0.01/s was evaluated by measuring the area under the corresponding stress-strain curve. The toughness value for the neat epoxy is 62 MPa and approximately 47 MPa for the nanocomposites. Nevertheless, if one assumes

strain of 0.2 as the limiting strain for use of the materials as structural adhesives, then the toughness of the nanocomposites at this limit would be 1.5 times that of the neat epoxy.

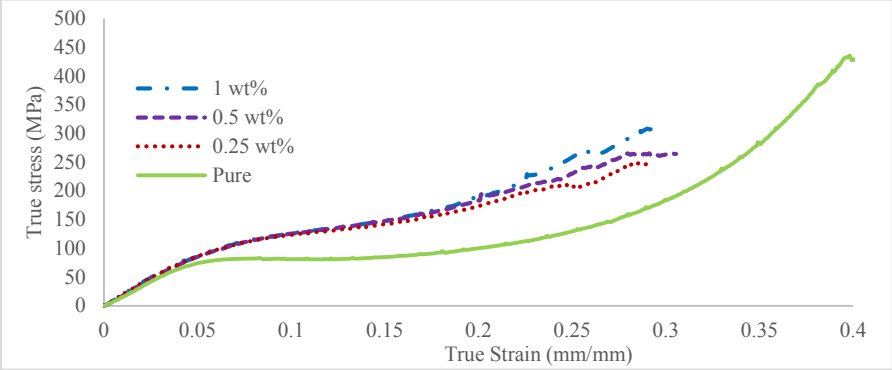

Figure 8-2. Comparison of the stress-strain curve for pure epoxy and nanocomposites at strain rate of 0.01/s

The observed values of yield strength and Young's modulus for all materials are presented in Figure 8-3. It should be noted that these values were obtained from the engineering stress-strain curves. The results depict a noticeable increase in both the yield strength and Young's modulus of material as a function of increasing strain rate. Moreover, comparison of the results at a given strain rate indicates that the addition of GNPs improved these properties. However, it can be inferred from the results that the efficiency gained through the GNPs as a reinforcement decreases at higher strain rates.

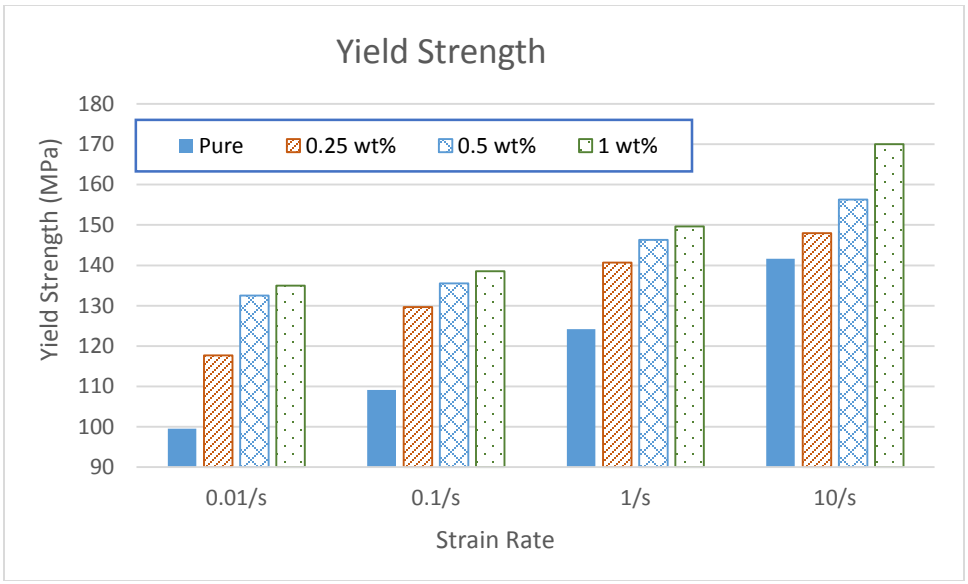

(a)

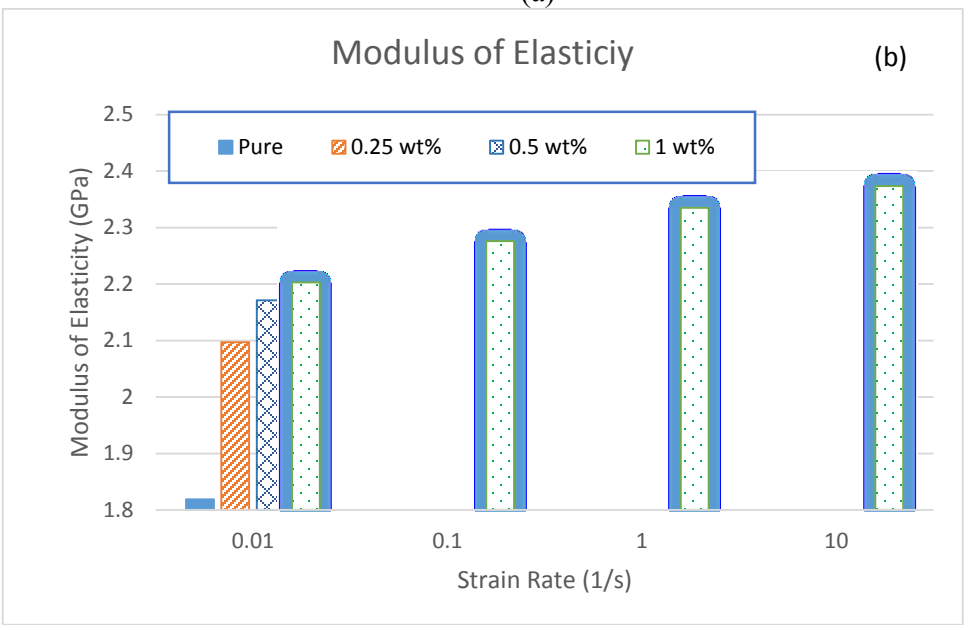

(b)

Figure 8-3. Comparison of the mechanical properties of the neat epoxy and nanocomposites evaluated at various strain rates; (a) yield strength (b) Young's modulus

It is believed that the increase in the mechanical properties at higher strain rates is on account of the reduction in molecular mobility of epoxy chains, which results to stiffer chains [21]. On the other hand, inclusion of GNP to neat epoxy apparently produces a similar effect [22]. In fact, the GNP particles with their higher stiffness (i.e. compared to

neat epoxy) get located within the spaces existing among the polymer chains, thus reducing chains' flexibility. This in turn causes a reduction in the positive reinforcing efficiency of GNPs at higher strain rates, since it is postulated that the polymer chains have already been stiffened under the application of higher strain rates. In other words, as an analogy, at higher strain rates, the matrix acts as if it is a new and relatively stiffer epoxy. This corroborates with the fact that the positive reinforcing attributes of nanoparticles diminish as the stiffness of the host matrix increases [23].

8.4.2 Tensile test

Typical stress-strain curves for each group of materials obtained under tensile loading are illustrated in Figure 8-4. All materials exhibit much lower ductility under tension compared with their compression response. In addition, the ultimate strength in tension is much lower than those exhibited under compression.

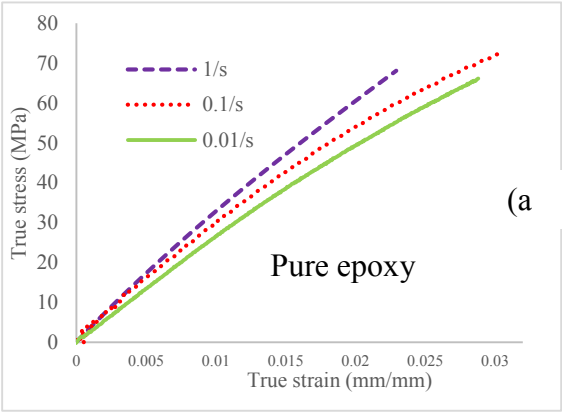

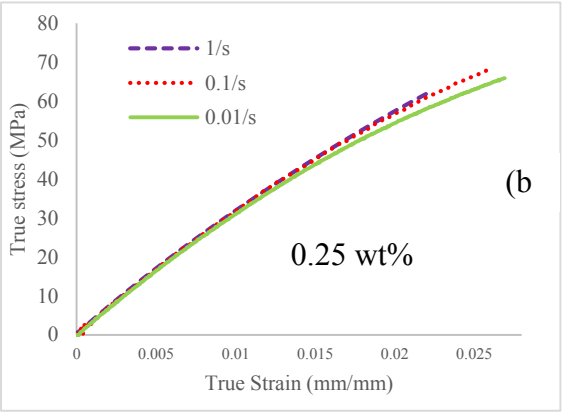

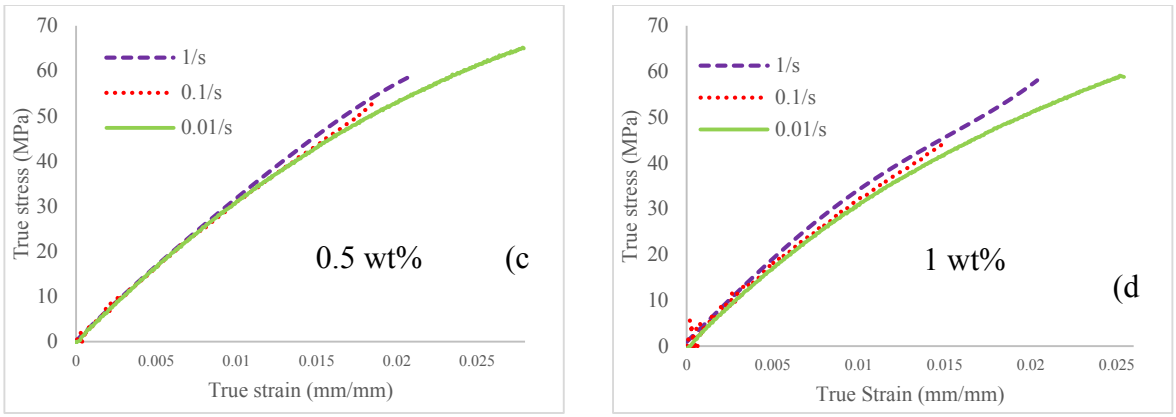

Figure 8-4. Typical uniaxial tensile true stress-strain curves for (a) neat epoxy (b) 0.25 wt% nanocomposite (c) 0.5 wt% nanocomposite (d) 1 wt% nanocomposite

It can be seen that here is no distinct yielding point on the curves. This is attributed to the semi-brittle nature of this epoxy when subjected to tension, especially at higher strain rates, and when hosting the GNPs. However, for comparative purposes, the yield strength of the neat epoxy at strain rate of 0.01/s was measured at 0.2% proof strain, and compared against the values obtained from the stress-strain curve under compressive loadings. This value was determined to be 63 MPa for the neat epoxy, which happens to be 35% less than the corresponding value under compression. The reduction in the yield strength under tension can be attributed to the influence of hydrostatic pressure, as discusses in detail by Spitzing and Richmond [24]. Spitzing and Richmond proposed the following equation [24]:

$$\sigma_y^p = \sigma_y^0 + \alpha_p P \tag{8-1}$$

where σ_y^p is the absolute value of the yield stress under hydrostatic pressure p, $\sigma_y^0$is the yield stress under zero hydro static pressure and α_p is the sensitivity coefficient. The hydrostatic pressure can be obtained by:

$$P = -\frac{1}{3}\sum_{i=1,2,3}\sigma_i \tag{8-2}$$

where σ_i refers to the stress components. In uniaxial tension p takes a negative sign, (i.e. $-\sigma_y^t/3$) and in uniaxial compression p is positive (i.e. $\sigma_y^c/3$) which is the reason for obtaining higher yield strength in compression.

The values for the Young's modulus of all materials evaluated under various strain rates are shown in Figure 8-5. The general trends in data are similar to that obtained when materials were subjected to compression test (i.e. increase of the properties at higher strain rates and GNP contents). However, the percentages of the increase under tension are lower than those tested under compression. This is attributed to the degrees of freedom of the epoxy chains. Under tension, the degrees of freedom is lower than under compression. This is because the chains are more aligned along the axial direction when subjected to a tensile loading, while they will be mainly aligned in the radial direction under a compressive loading. Given the stiffening mechanism produced by inclusion of the GNPs (as explained earlier), it appears that the relatively lower degrees of freedom of chains in compression allow the GNP particles to have a higher impact upon the behavior of polymers. In addition, the flaws within the system such as GNPs agglomeration and entrapped gases are believed to cause less detriment to the resin under compressive loading than under tensile loading.

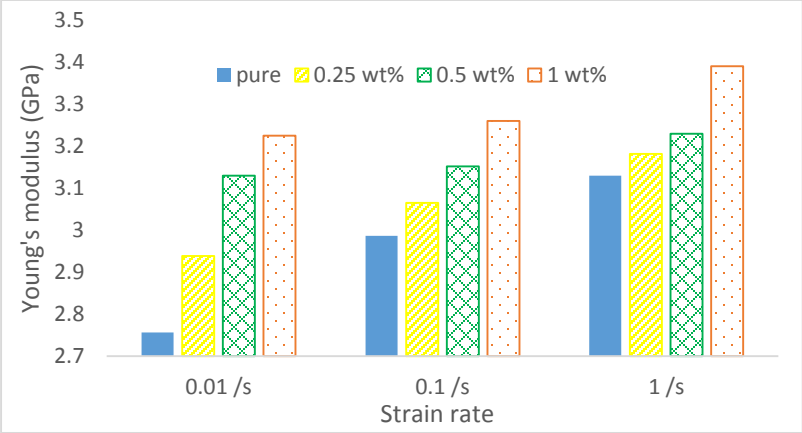

Figure 8-5. Comparison of the Young's modulus for the neat epoxy and nanocomposites evaluated at various strain rates

It should also be noted that the values of the tensile modulus are larger than those measured under compression, while intuitively one would expect similar values regardless of the loading sense. However, it appears that the dimensions (and the number of voids within the larger body) plays a role in these cases. To shed more light onto this phenomenon, thinner and longer specimens were fabricated and tested under compression. The values of the resulting modulus of elasticity were determined to become closer to those obtained under tensile loading.

8.5 SEM analysis

For better understanding the strain rate effect on the mechanical response of polymers, the SEM images of the fracture surfaces of the tensile specimens tested under the different strain rates were captured. The fracture surfaces of the neat epoxy at various strain rates are illustrated in Figure 8-6. It can be observed that generally, the roughness of fracture surface increases at higher strain rates, leading to more irregular cleavages with deeper valleys; these signify more sudden fractures.

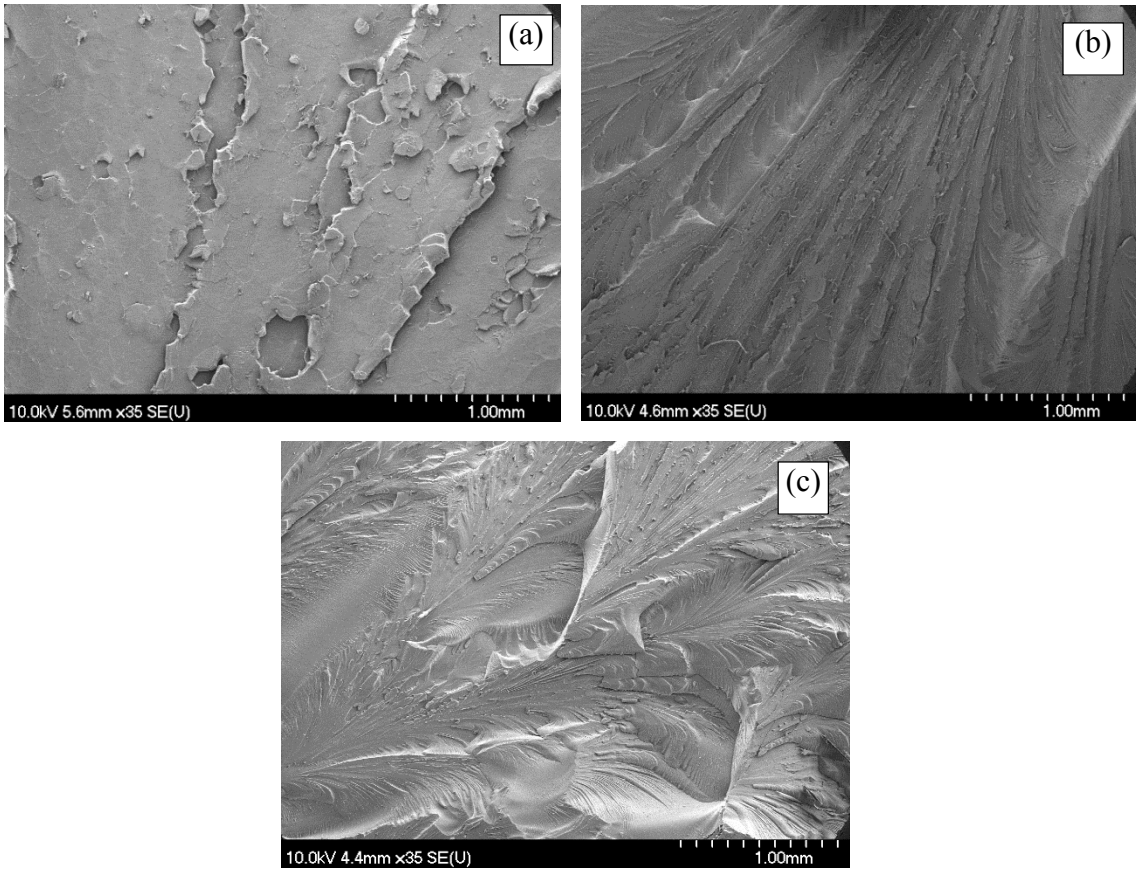

Figure 8-6. SEM micrographs of the failure surfaces of the neat epoxy test under tensile loading at strain rate of (a) 0.01/s (b) 0.1/s (c) 1/s

The fracture surfaces of the neat epoxy and nanocomposites are compared in Figure 8-7 (a,b). The roughness in the fracture surfaces of the nanocomposites is clearly higher than that of the pure epoxy. The cleavages observed on the fracture surfaces of nanocomposite specimens can be divided into two groups of deep and shallow cleavages. The pattern of the deep cleavages is fairly similar to that observed in the pure epoxy specimens. On the other hand, the density of the shallow cleavages in nanocomposite specimens is relatively much higher, which can be attributed to presence of GNPs within

the matrix. This supposition is justified by further exploring the fracture surface at a higher magnification (see Figure 8-7 (c,d)). Presence of the nanoparticles at the border of the shallowest cleavages can be observed. In fact, the graphene particles are the reason for change to the direction of fracture plane and creating cleavages. The GNP particles, which intersect with fracture plane, bridge between the two fracture surfaces and will either break (see Figure 8-7 (e)) or pull out of the other surface, which leaves a hole in turn (see Figure 8-7 (f)).

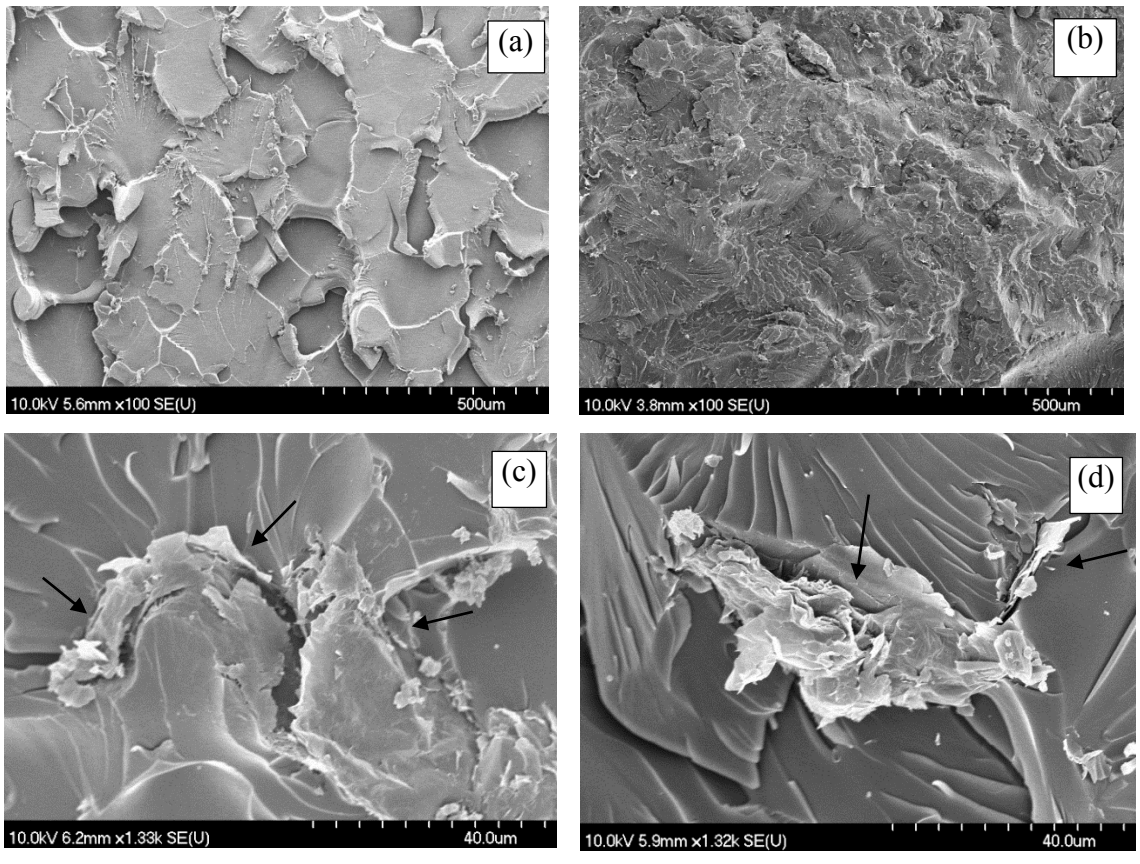

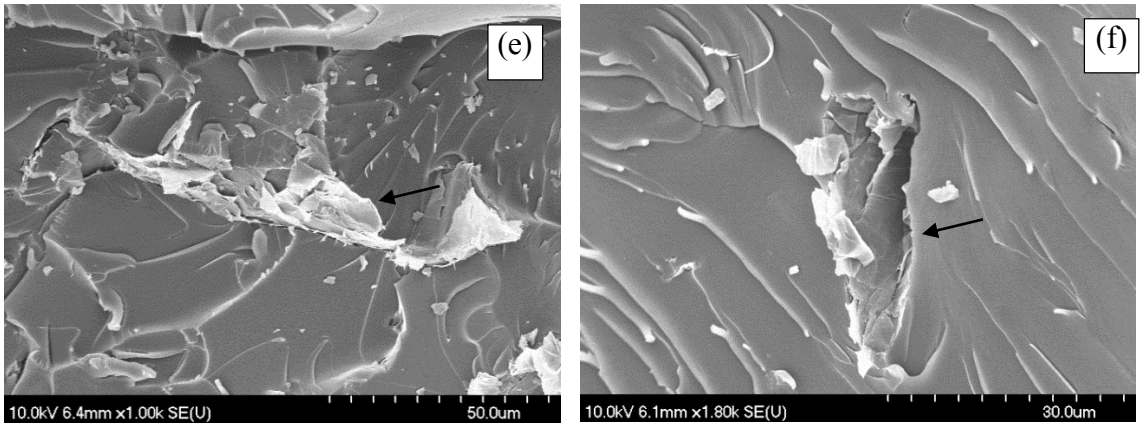

Figure 8-7. SEM micrographs of the failure surfaces of various specimens tested under tensile loading condition at strain rate of 0.01/s; (a) pure epoxy (b-f) 0.5 wt% nanocomposite

GNP dispersion status in nanocomposites was also investigated using SEM. Except for some local agglomerates, especially at higher GNP contents, a uniform GNP dispersion in the nanocomposites was obtained, which confirms the suitability and aptness of the dispersion technique and the number of calendering cycles used for processing the nanocomposites.

8.6 Mechanical Properties Prediction Models

8.6.1 Prediction of the Yield Strength

The objective of this portion of the study is to identify and/or propose a model that could predict the yield strength of the materials at different strain rates with a good accuracy. For that, first, the integrity of some of the available models were assessed by considering their performance in relation to the neat epoxy used in our study. The models considered are as follows.

8.6.1.1 Johnson-Cook model

The Johnson-Cook model suggests a logarithmic trend for the variation of a materials' yield strength as a function of the strain rate; it is presented mathematically as follows [25]:

$$\sigma_y = \sigma_y^{ref}\left(1 + a\,Ln\left(\frac{\dot{\varepsilon}_p^{eff}}{\dot{\varepsilon}_0}\right)\right) \tag{8-3}$$

where σ_y^{ref} is the yield strength evaluated under a static loading rate, $\dot{\varepsilon}_p^{eff}$ is the effective plastic strain rate, $\dot{\varepsilon}_0$ is the reference strain rate and a is a constant.

8.6.1.2 Cowper-Symonds model

This is a two-parameter exponential model, proposed by Cowper-Symonds [26]:

$$\sigma_y = \sigma_y^{ref}\left(1 + \left(\frac{\dot{\varepsilon}_p^{eff}}{C}\right)^{\frac{1}{P}}\right) \tag{8-4}$$

where P and C are constants.

The following models were proposed for predicting the yield strength of both pure polymers and polymers containing a second phase.

8.6.1.3 Modified Eyring's model

Several models have been proposed for prediction of the effect of temperature and strain rate on yield strength of polymers [27]. A cooperative type model that accounts for the presence of a second phase or reinforcement in materials, which has been widely used by other investigators, is the model proposed by Richeton et al.[28]:

$$\frac{\sigma_y}{T}=\frac{\sigma_i(0)-m.T}{T}+\frac{2k}{V_{eff}}\sinh^{-1}\left(\frac{\dot{\varepsilon}}{\dot{\varepsilon}_0\exp\left(\frac{\Delta H_{eff}}{kT}\right)}\right)^{1/n} \quad (8\text{-}5)$$

where σ_y is yield strength, T is the absolute temperature, k is the Boltzmann's constant, V_{eff} is an effective activation volume, ΔH_{eff} is an effective activation energy, $\dot{\varepsilon}$ is the strain rate, $\dot{\varepsilon}_0$ is the pre-exponential constant, $\sigma_i(0)$ is the internal stress at 0 K, m is a material parameter roughly equal to $\sigma_i(0)/T_g$ and n describes the cooperative character of the yield process. The effective activation volume and effective activation energy can be evaluated by:

$$\Delta H_{eff}=\frac{\varphi\Delta H_M\Delta H_G}{\Omega\Delta H_G+(1-\Omega)\Delta H_M}+(1-\varphi)\Delta H_G \quad (8\text{-}6)$$

$$V_{eff}=\frac{\varphi V_M V_G}{\Omega V_G+(1-\Omega)V_M}+(1-\varphi)V_G \quad (8\text{-}7)$$

where the parameters with M index are related to matrix (i.e. here, the epoxy) and those with G index are related to the second phase (here, the GNPs). The two parameters φ and Ω represent the state of mixing of filler in the matrix. However, only one of them is independent; they are related to the volume fraction of matrix, f_M, and GNP, f_G, with the following relations:

$$\begin{cases} f_M=\varphi.\Omega \\ f_G=1-\varphi.\Omega \end{cases} \quad (8\text{-}8)$$

8.6.1.4 Matadi et al Model

To directly include the effect of nano-reinforcements in the yield strength prediction, Matadi et al [13] suggested the use of a correction term in the abovementioned model instead of using the terms related to the effective activation energy and effective activation volume in Eq. (8-5). Their revised formulation is as follows:

$$\frac{\sigma_y}{T}=\left[\frac{1-f_G}{1+2.5f_G}Exp\left(Bf_G\right)\right]\left[\frac{\sigma_i(0)-m.T}{T}+\frac{2k}{V_M}\sinh^{-1}\left(\frac{\dot{\varepsilon}}{\dot{\varepsilon}_0\exp\left(-\frac{\Delta H_M}{kT}\right)}\right)^{1/n}\right] \quad (8\text{-}9)$$

where B is a constant.

The predictions of each of the models mentioned above applied to both the neat epoxy and nanocomposites are shown in Figure 8-8. As can be seen, all the models provided an acceptable prediction for the yield strength for the epoxy; however, Cowper Symonds' model provided the best predictions.

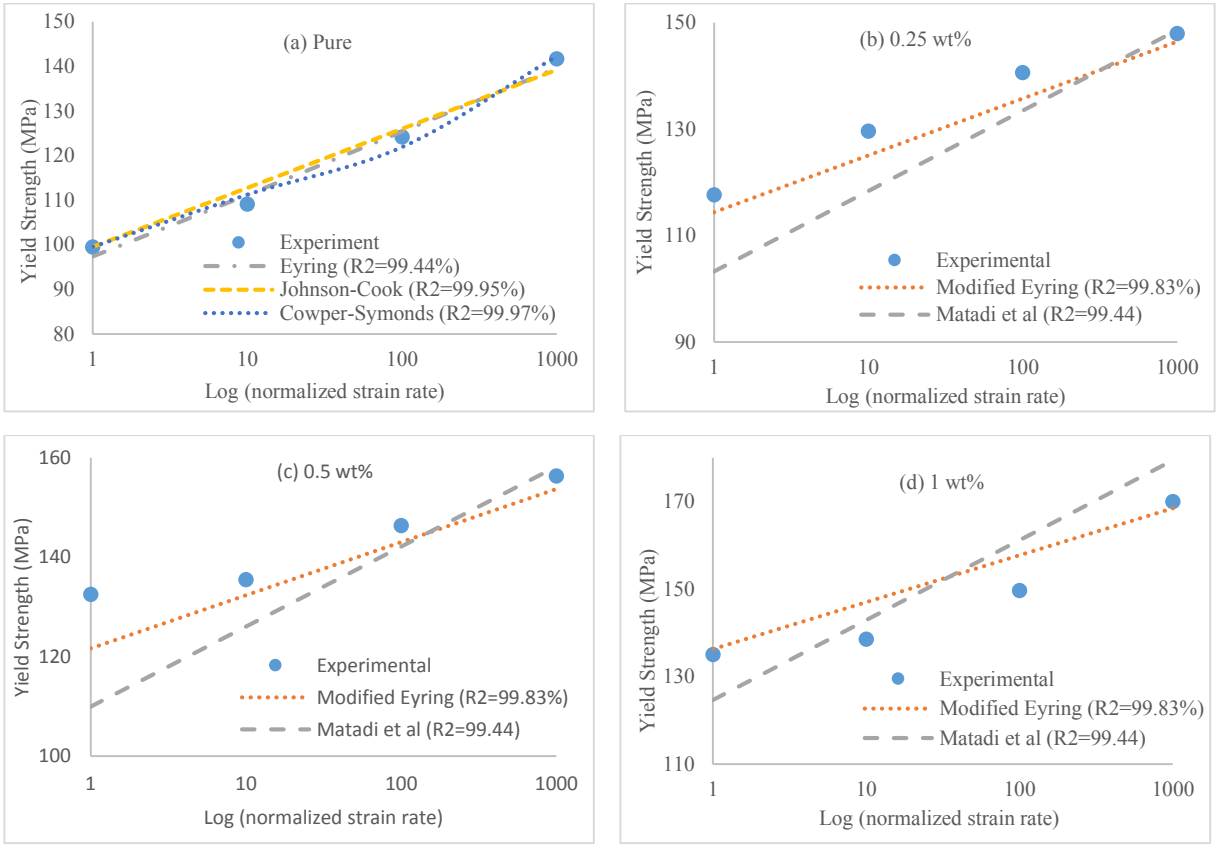

Figure 8-8. Comparison of the prediction of the models in variation of the yield strength as a function of strain rate; (a) pure epoxy (b) 0.25 wt% nanocomposite (b) 0.5 wt% nanocomposite (c) 1 wt% nanocomposite

Moreover, in the case of the nanocomposites, the modified Eyring provided a better prediction than the model proposed by Matadi et al. One can see large discrepancies between the modified Eyring model's predictions and the experimental values at some specific strain rates; in general, nonetheless, the model provides acceptable predictions for the yield strength of GNP-reinforced nanocomposites tested at various strain rates. Please note that all the required constants by the models are reported in Table 8-1.

Table 8-1. Values of the parameters required by the models

Models	Parameters
Johnson-Cook model	$C = 0.0577$
Cowper-Symonds model	$C = 20310 \quad \& \quad P = 3.56$
Modified Eyring's model	$\Delta H_M = 87.37\,kJ/mol$ $\quad V_M = 84.44\times10^{-29}\,m^3$ $\Delta H_G = 3071.93\,kJ/mol$ $\quad \varphi = 0.99$ $\quad \sigma_0 = 57.58\,MPa$ $V_G = 1.71\times10^{-29}\,m^3$ $\quad$ n = 2.32 $\quad$ m = 0.372
Matadi et al model	$\Delta H_M = 87.39\,kJ/mol$ $\quad V_M = 84.44\times10^{-29}\,m^3$ $\sigma_0 = 57.06\,MPa$ $\quad$ n = 1.56 $B = 53.75$ $\quad$ m = 0.63

8.7 Prediction of the Young's modulus

In this section, the Richeton et al's Model, which is a widely used model for predicting the influence of strain rate on material's Young's modulus, is presented. The integrity of the model, and the approach used for applying this model for predicting the effect of strain rate on the stiffness of nanocomposites are also discussed.

Richeton et al's [29] proposed the following equation to account for the effect of strain rate on Young's modulus of polymers:

$$E = E^{ref}\left(1 + s\,Log\left(\frac{\dot{\varepsilon}}{\dot{\varepsilon}_0}\right)\right) \qquad (8\text{-}10)$$

where E^{ref} is the Young's modulus at strain rate of $\dot{\varepsilon}_0$ and s is a constant which should be determined based on experimental results. The results produced by this model for the materials considered in this study are presented in Figure 8-9. The comparison of the results presented in Figure 8-9 (a) indicates that this model could accurately predict the Young's modulus of the neat epoxy.

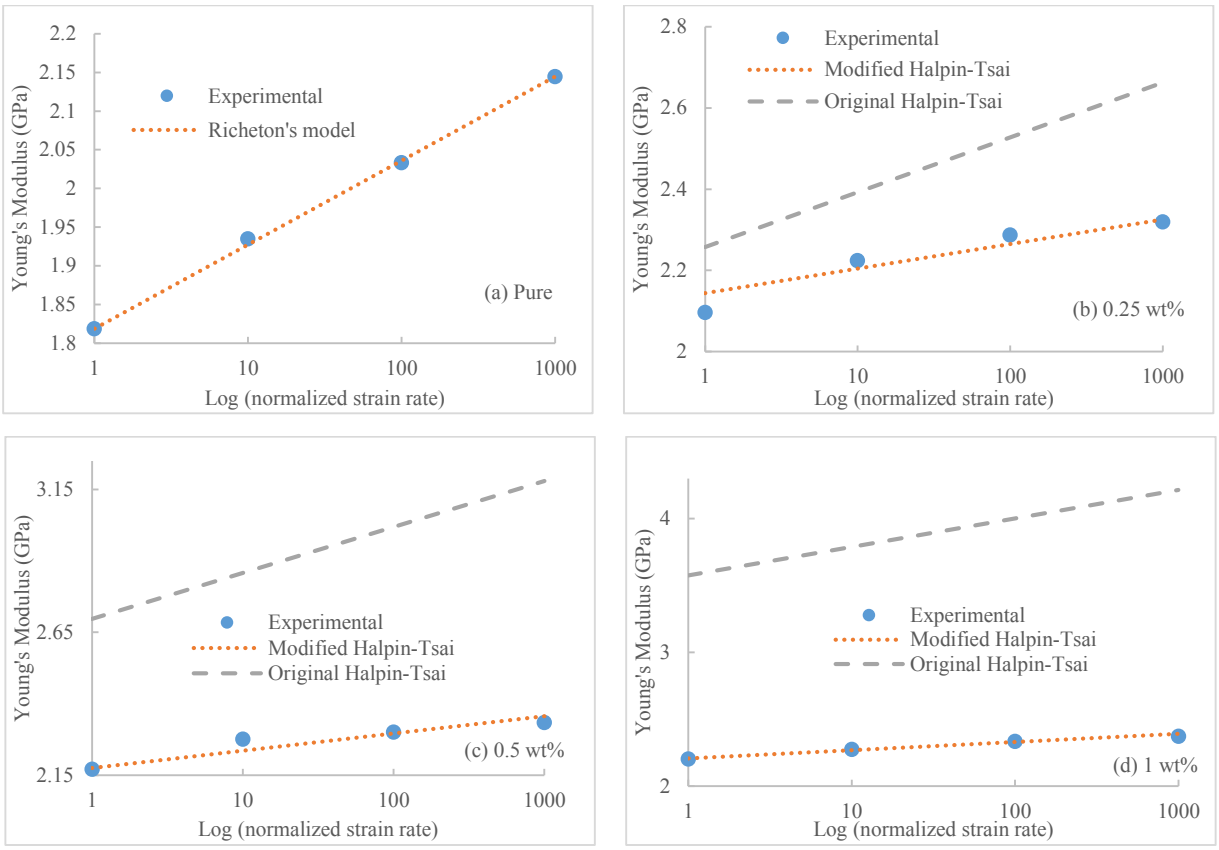

Figure 8-9. Comparison of the models' prediction of Young's modulus of (a) pure epoxy (b) 0.25 wt% nanocomposite (b) 0.5 wt% nanocomposite (c) 1 wt% nanocomposite, at different strain rates

To predict the Young's modulus of the nanocomposites, the following approach is used. First, the Halpin-Tsai model is used to calculate the Young's modulus of the

composites. This model predicts the Young's modulus of composites in their quasi-static state. This model assumes uniform distribution of the reinforcements within the host polymer, and no imperfection in the host matrix. The model predicts the maximum Young's modulus of the composite according to the following equation:

$$E_C = \left(\frac{3}{8} \frac{1+2(\lambda)\eta_l V_f}{1-\eta_l V_f} + \frac{5}{8} \frac{1+2\eta_T V_f}{1-\eta_T V_f} \right) E_m \tag{8-11}$$

in which

$$\eta_l = \frac{E_f / E_m - 1}{E_f / E_m + 2(\lambda)}, \quad \eta_T = \frac{E_f / E_m - 1}{E_f / E_m + 2} \quad , \lambda = l_f / d_f \tag{8-12}$$

where E_C is the Young's modulus of the composite, l_f and d_f are the length and the average diameter of the reinforcements (GNPs), E_f is the Young's modulus of the reinforcements, E_m is the Young's modulus of the matrix (epoxy), and V_f is reinforcements' volume content.

As stated earlier, since this model is developed to predict the Young's modulus at a quasi-static state, to predict the Young's modulus of a nanocomposite at a given strain rate, one should first obtain the value of matrix's modulus at the desired rate using Eq (8-10), and then evaluate the elastic modulus of the nanocomposite by using Eq (2-1).

The estimations of the Young's modulus of the materials considered in this study, using the original Halpin-Tsai model, are shown in Figure 8-9 (b-d). As expected, the Halpin-Tsai model overestimates the results by a large margin, with further observation that the higher the GNP content, the larger is the difference between the experimental results and models' predictions. The large discrepancies are due to the model's underlying assumption (i.e., uniform distribution of reinforcement, and no provision for any imperfection in the matrix e.g., entrapped gas, etc.).

To tackle this problem a modification factor is proposed by the authors to the original Halpin-Tsai model. The revised equation takes the following form:

$$E_C = \left(\frac{3}{8} \frac{1+2(\lambda)\eta_l V_f^{eff}}{1-\eta_l V_f^{eff}} + \frac{5}{8} \frac{1+2\eta_T V_f^{eff}}{1-\eta_T V_f^{eff}} \right) E_m^R \tag{8-13}$$

where

$$\eta_l = \frac{E_f / E_m^R - 1}{E_f / E_m^R + 2(\lambda)}, \quad \eta_T = \frac{E_f / E_m^R - 1}{E_f / E_m^R + 2} \quad , \lambda = l_f / d_f \tag{8-14}$$

$$V_f^{eff} = C_{m1} (V_f)^{C_{m2}} \tag{8-15}$$

$$E_m^R = E_m \left(1 + s\, Log \left(\frac{\cdot}{\cdot} \right) \right. \tag{8-16}$$

in which C_{m1} and C_{m2} are material constants which can be calculated based on experimental results. The predictions by the modified model are also presented in Figure 8-9 (b-d). The comparison of results shows that this model is perfectly capable of predicting the Young's modulus of nanocomposites. The evaluated constants for this model are presented in Table 8-2.

Table 8-2. Model parameters for Young's modulus

Models	Parameters	
	Compression	Tension
Richeton et al for pure epoxy	$s = 0.026$	$s = 0.031$
Modified Halpin-Tsai	$s = 0.014$	$s = 0.019$
	$C_{m1} = 0.0022$	$C_{m1} = 0.0079$
	$C_{m2} = 0.130$	$C_{m2} = 0.130$

It should be noted that the same model was used for predicting the Young's modulus of the composites when tested under tensile loads, yielding good agreements. For

the sake of clarity, the predictions of tensile modulus are not presented in Figure 8-9; however, the constants are presented in Table 8-2.

8.8 Conclusions

The effect of strain rate on the response of GNP-reinforced epoxy nanocomposites with various GNP contents, under tensile and compressive loading conditions, were investigated. The results showed that the yield strength and Young's modulus of both the neat epoxy and nanocomposites increased at higher strain rates. Moreover, it was also demonstrated that the beneficial attribute of GNP reinforcements decreased at higher strain rates. In addition, it was observed that strain rate played a more noticeable role under compressive loading in comparison to tensile loading.

By incorporation of GNPs into the epoxy, a transition from ductile to brittle was observed in the mechanical response of epoxy. This transition was observed to be more severe under compressive loading state. Furthermore, the plastic flow behaviour in the nanocomposites were exhibited to be different from that of the neat epoxy. In fact, the stress softening observed in the stress-strain response of the neat epoxy (after yielding point) disappears in the case of nanocomposites.

In addition, the integrity of some of the more widely used models developed for predicting the yielding strength and Young's modulus of pure epoxy and nanocomposites as a function of strain rate were evaluated and compared against the experimental data obtained in this study. As a result, a modification to the Halpin-Tsai model was proposed in order to enable it to predict the Young's modulus of nanocomposites at different strain rates with an acceptable accuracy.

8.9 Acknowledgments

This research was funded by the National Science and Engineering Research Council of Canada (NSERC). Partial funding of NSERC, through the Collaborative Research and Training Experience (CREATE) program is acknowledged. The authors are grateful to the granting agency.

8.10 Reference

[1] Ayatollahi MR, Doagou-Rad S, Shadlou S. Nano-/Microscale Investigation of Tribological and Mechanical Properties of Epoxy/MWNT Nanocomposites. Macromolecular Materials and Engineering. 2012;297:689-701.
[2] Ayatollahi M, Shadlou S, Shokrieh M. Fracture toughness of epoxy/multi-walled carbon nanotube nano-composites under bending and shear loading conditions. Materials & Design. 2011;32:2115-24.
[3] Alishahi E, Shadlou S, Doagou-R S, Ayatollahi MR. Effects of Carbon Nanoreinforcements of Different Shapes on the Mechanical Properties of Epoxy-Based Nanocomposites. Macromolecular Materials and Engineering. 2012.
[4] Ayatollahi M, Alishahi E, Shadlou S. Mechanical behavior of nanodiamond/epoxy nanocomposites. International journal of fracture. 2011;170:95-100.
[5] Li Y, Pan D, Chen S, Wang Q, Pan G, Wang T. In situ polymerization and mechanical, thermal properties of polyurethane/graphene oxide/epoxy nanocomposites. Materials & Design. 2013;47:850-6.
[6] Yoo K, Takei Y, Kim S, Chiashi S, Maruyama S, Matsumoto K, et al. Direct physical exfoliation of few-layer graphene from graphite grown on a nickel foil using polydimethylsiloxane with tunable elasticity and adhesion. Nanotechnology. 2013;24:205302.
[7] Chen DZ, Lin XM. Preparation of Graphene by Green Reduction Method and Characterization. Advanced Materials Research. 2013;807:515-20.
[8] Richeton J, Ahzi S, Vecchio KS, Jiang FC, Adharapurapu RR. Influence of temperature and strain rate on the mechanical behavior of three amorphous polymers: Characterization and modeling of the compressive yield stress. International Journal of Solids and Structures. 2006;43:2318-35.
[9] Gómez-del Río T, Salazar A, Rodríguez J. Effect of strain rate and temperature on tensile properties of ethylene–propylene block copolymers. Materials & Design. 2012;42:301-7.
[10] Goglio L, Peroni M, Rossetto M. Effect of the strain rate on the mechanical behaviour of epoxy adhesives. Key Engineering Materials. 2007;347:671-6.
[11] McClung AJ, Ruggles-Wrenn MB. Strain rate dependence and short-term relaxation behavior of a thermoset polymer at elevated temperature: experiment and modeling. Journal of pressure vessel technology. 2009;131.

[12] Jacob GC, Starbuck JM, Fellers JF, Simunovic S, Boeman RG. Strain rate effects on the mechanical properties of polymer composite materials. Journal of Applied Polymer Science. 2004;94:296-301.
[13] Matadi Boumbimba R, Wang K, Bahlouli N, Ahzi S, Rémond Y, Addiego F. Experimental investigation and micromechanical modeling of high strain rate compressive yield stress of a melt mixing polypropylene organoclay nanocomposites. Mechanics of Materials. 2012;52:58-68.
[14] Jo C, Naguib HE. Modeling the effect of strain rate on the mechanical properties of HDPE/Clay Nanocomposite foams. Polymers & polymer composites. 2008;16:561-75.
[15] Argento A, Kim W, Lee EC, Harris AM, Mielewski DF. Rate dependencies and energy absorption characteristics of nanoreinforced, biofiber, and microcellular polymer composites. Polymer Composites. 2011;32:1423-9.
[16] Shen L, Phang IY, Liu T, Zeng K. Nanoindentation and morphological studies on nylon 66/organoclay nanocomposites. II. Effect of strain rate. Polymer. 2004;45:8221-9.
[17] KAKOEE A, SHABAN A, KHATIBI AA. Experimental investigation of Compressive modulus, ultimate strain and fracture energy of epoxy based nanocomposite reinforced with carbon nanotubes, under conditions of high strain rate. methods. 2012;13:18-20.
[18] Al-Sharab J, Joshi B, Gupta N. The effect of multiwall carbon nanotubes (MWCNT) on the high strain rate compressive properties of syntactic nanocomposite foams. Microscopy and Microanalysis. 2012;18:1644-5.
[19] D638-10 AS. Standard Test Method for Tensile Properties of Plastics. West Conshohocken, PA: ASTM International, www.astm.org; 2010.
[20] Richeton J, Ahzi S, Vecchio K, Jiang F, Adharapurapu R. Influence of temperature and strain rate on the mechanical behavior of three amorphous polymers: Characterization and modeling of the compressive yield stress. International journal of solids and structures. 2006;43:2318-35.
[21] Bauwens J. Relation between the compression yield stress and the mechanical loss peak of bisphenol-A-polycarbonate in the β transition range. Journal of Materials Science. 1972;7:577-84.
[22] Ayatollahi M, Shadlou S, Shokrieh M, Chitsazzadeh M. Effect of multi-walled carbon nanotube aspect ratio on mechanical and electrical properties of epoxy-based nanocomposites. Polymer Testing. 2011;30:548-56.
[23] Ci L, Bai J. The reinforcement role of carbon nanotubes in epoxy composites with different matrix stiffness. Composites Science and Technology. 2006;66:599-603.
[24] Spitzig W, Richmond O. Effect of hydrostatic pressure on the deformation behavior of polyethylene and polycarbonate in tension and in compression. Polymer Engineering & Science. 1979;19:1129-39.
[25] Johnson GR, Cook WH. Fracture characteristics of three metals subjected to various strains, strain rates, temperatures and pressures. Engineering Fracture Mechanics. 1985;21:31-48.
[26] Cowper G, Symonds P. Strain hardening and effects in the impact loading of cantilever beams. Tech Rep Brown University Division of Applied Mathematics, Technical rept no 28. 1957.
[27] Pascault J-P, Sautereau H, Verdu J, Williams RJ. Thermosetting polymers: CRC Press; 2002.

[28] Gueguen O, Richeton J, Ahzi S, Makradi A. Micromechanically based formulation of the cooperative model for the yield behavior of semi-crystalline polymers. Acta Materialia. 2008;56:1650-5.
[29] Richeton J, Ahzi S, Vecchio K, Jiang F, Makradi A. Modeling and validation of the large deformation inelastic response of amorphous polymers over a wide range of temperatures and strain rates. International journal of solids and structures. 2007;44:7938-54.

Chapter 9: Conclusion

9.1 Conclusions

The overall goal of this study was to develop a highly resilient adhesive using graphene nanoplatelets. Several achievements were made through the course of the work conducted to accomplish the goal of this project. In summary, the fracture and toughening mechanisms of both GNP-reinforced epoxy and FRP composites formed by the GNP-reinforced epoxy applied at a strategic location (layer) were investigated. In addition, the mechanical properties of GNP-based nanocomposites were assessed under different loading rates. The specific outcomes of the investigations are summarized as follows:

1. The inclusion of GNPs to the epoxy resin resulted into a noticeable improvement in the stiffness of the resin. This was achieved by establishing the optimum gap distance for the three-roll mill used for dispersing the GNPs within the resin, with careful consideration of nanoparticles' aspect ratios, geometry and wt% content. As a result, the total time required for the dispersion process of the GNPs within the resin was improved by nine-fold. This was achieved by optimizing the gap distance of the three-roll mill (i.e., 20 μm and 40 μm) in the case of GNPs, in comparison to 5 μm gap required for processing CNT-reinforced nanocomposites. Thus, the production cost of GNP-based nanocomposites could be reduced by a significant margin.
2. The inclusion of GNPs within the resin also generated a significant improvement in the thermal conductivity of the resulting nanocomposite. In fact, the thermal conductivities of GNP-reinforced resin measured both at room, and elevated temperatures were significantly increased, even when only 0.5 wt% content of GNPs

was included in the resin. However, the elastic modulus of the modified adhesive did not change noticeably when 0.5wt% of the as-received GNP (i.e., without any surface modification) was added to the epoxy resin. Moreover, the electrical conductivity threshold was obtained by addition of 1.5 wt% GNPs to the adhesive.

3. The observed results revealed that the coefficient of thermal expansion (CTE) of the GNP-nanocomposites decreased by 15% and 25%, when 0.5 wt% and 2 wt% GNPs were added to the resin, respectively. Therefore, one could expect a lesser mismatch of the CTE of matrix and fibers in FRP structures; as a result lower magnitudes of thermal residual stresses would be generated within the FRP composites formed by the modified resin.
4. GNPs could effectively and efficiently enhance mode-I fracture toughness of the epoxy resin; however, the resin's mode-II fracture toughness was slightly degraded, regardless of GNPs' wt% content. The inclusion of combined CNTs and GNPs also further improved the mode-I fracture toughness of the nanocomposites, but by a small margin in comparison to the GNP-reinforced resin. Moreover, the mode-II fracture toughness of the CNT/GNP-reinforced epoxy attained the lowest value when the ratio of GNP to CNT content was less than one (i.e., $GNP_{wt\%}/CNT_{wt\%}<1$).
5. The quantitative and qualitative fracture surface assessment of the epoxy specimens reinforced with various wt% contents of GNPs and CNTs revealed that the presence of nanofillers increased the plastic deformation, and thus created more shear-bands in the vicinity of crack front under mode-I. The fracture surfaces' roughness, and the energy-release rate of the specimens tested under mode-I was also enhanced as the nanoparticles concentration increased. It was therefore identified that crack

deflection would be one of the main toughening mechanisms in this type of nanocomposites. In addition, crack pinning and bridging were observed to be the other mechanisms responsible for enhancing toughness of the nanocomposites.

6. The creation of relatively smaller plastic zones, larger density of micro-cracks, nanoparticle/matrix debonding (especially near the crack tips), and the absence of filler-bridging (due to nature of the fracture mode), were the features clearly noted in specimens subjected to Mode-II fracture. In conclusion, in consideration of the collective effects of the above-mentioned phenomena, it could be concluded that overall, the inclusion of GNPs in the epoxy resins somehow could not improve the mode-II fracture toughness of the resin.

7. It should be noted that the use of silane agent used for functionalizing GNPs, and the incorporated method of functionalization were both employed for the first time. The results of chemical analysis showed a clear shift of the main characteristic peaks in the Raman spectra. Moreover, the intensity ratio of the D-band to G-band of the spectra of functionalized and non-functionalized GNPs were also increased. In addition, a clear difference of weight loss and residual weight obtained from TGA analysis of unmodified GNPs and functionalized GNPs and also the existence of two new characteristic peaks obtained by the FTIR spectrum for the silane functionalized GNPs were also observed. All these features could be used in future investigations to establish the success of generation of a perfect bond between GNPs and silane agent.

8. As expected, the elastic modulus and fracture toughness of nanocomposites fabricated by 0.5 wt% of functionalized GNPs were enhanced by 15% and 82%,

respectively. In comparison, the as-received (unmodified) GNPs could improve the stiffness and fracture toughness of the nanocomposites by lower margins (4% and 45%), respectively. The inclusion of 0.5 wt% GNPs also increased the ultimate strength of the host resin by 38% in average; however, not to the extent that the functionalized GNPs could produce. In addition, the ductility of the host epoxy resin could also be improved by other methods of functionalization (i.e., G-NH_2); however, again, not to the same extent as was achieved by the silane functionalization, but the response was better than that produced by the as-received GNPs.

9. To evaluate mode III IFT of the FRP laminates, a new test procedure was developed and proposed. In the proposed method, a thin FRP laminated specimen, with the layup of $[90/(\pm 45)_2(\mp 45)_2/90]_s$, which also hosted an edge crack at the mid-thickness, is subjected to pure torsion. Mode III IFT of specimens can then be calculated based on the compliance calibration technique, since the selected layup generate sufficient torsional stiffness in the laminate, thereby subjecting the delamination to pure mode III fracture.
10. The observed experimental results revealed that the inclusion of functionalized GNPs-reinforced resin could significantly improve modes I, II and III IFTs of the FRP composites formed by the resin. It should, however, be noted that the functionalized GNPs produced more improvement in mode I fracture, as opposed in mode II or III IFTs. Moreover, inclusion of the as-received (untreated) GNPs could not enhance the morphology of the mode I fracture plane of the FRP composite

specimens; in fact, they adversely affected modes II and III IFT response of the specimens.

11. Fracture surface assessment of FRP laminated specimens revealed that existence of GNPs within the resin roughened the fracture surfaces, thus promoting better fiber/matrix adhesion. In addition, GNPs' functionalization altered the surface energy of the GNPs, thereby improving the GNP/matrix adhesion.
12. The pure modes I, II, and mix-modes I/II and I/III fracture responses of adhesive could be evaluated by using the same single-edge notch bend (SENB) specimen configuration as noted in ASTM D5054. The modified SENB specimen proposed in this study for evaluating the mixed-mode I/III fracture toughness is identical to the SENB specimen configuration commonly used to evaluate pure mode I fracture toughness of materials. However, in the proposed specimen, the initial crack is created in an appropriate orientation with respect to the through-thickness axis of the specimen. As a result, in the proposed specimen configuration, the contribution of mode III fracture becomes more dominant in comparison to the contribution of mode II fracture on all crack fronts, except near the specimen surfaces. Therefore, the creation of a pair of side grooves on the two outer surfaces of the specimen was suggested. This scheme eliminates the effect of mode II fracture that usually develops near the surfaces.
13. The effects of strain rate on the response of GNP-reinforced epoxy nanocomposites with various GNP contents, under both tensile and compressive loading conditions were also experimentally investigated. The results indicated that both the neat epoxy and GNP-reinforced-epoxy exhibited greater apparent strength and stiffness when

subjected to higher strain rates. Moreover, it was also demonstrated that the beneficial attribute of GNP reinforcements decreased at higher strain rates. In addition, it was observed that strain rate played a more noticeable role when the material was subjected to compressive loading in contrast to tensile loading.

14. The incorporation of GNPs into the epoxy, however, decreased the ductility of the epoxy. This transition was observed to be more severe under the compressive loading state. Furthermore, the plastic flow behaviour in the nanocomposites were observed to be different from that observed in the neat epoxy. In fact, the stress softening observed in the stress-strain response of the neat epoxy (i.e., that occurring after the yielding stage), disappeared in the case of GNP-reinforced resin.
15. The integrity of some of the more widely used models developed for predicting the yield strength and Young's modulus of pure epoxy and nanocomposites as a function of strain rate were evaluated and compared against the experimental data obtained in this study. As a result, a modification to the Halpin-Tsai model was proposed, in order to enable it to predict the stiffness of nanocomposites, at different strain rates, with better accuracy.

9.2 Recommendations for future works

As an extension to the work conducted in this thesis, the following tasks are recommended to be carried out in the future.

- Adhesively bonded joints (ABJs) are increasingly used to mate adherends that have different mechanical properties. The resulting difference in the CTEs of the adhesive and adherends can induced significant thermal residual stresses in such ABJs. ABJs that are formed by hot-cured adhesives, could develop residual stresses with significant

magnitudes during their fabrication process; these stresses remain in the joints throughout their service lives. On the other hand, comparatively, ABJs made with cold-cured adhesives would not retain a significant magnitude of residual stresses. Nevertheless, when such joints become subjected to environmental loadings, their performance become exasperated due to the mismatch of their thermal properties.

The author postulates that one could resolve the issue by incorporation of GNPs within the mating adhesives. The preliminary results of this research have revealed that GNPs could significantly improve the thermal conductivity and coefficient of thermal expansion of their host adhesive. As an extension to this work, therefore, one should investigate the performance of ABJs formed by GNP-reinforced adhesives, under elevated and cryogenic temperatures.

- As stated in chapter 3, GNP-based nanocomposites exhibited high electrical conductivity beyond their electrical threshold. In addition, GNPs are piezo-resistive materials; thus, their electrical resistivity would change by variation in their strain. Consequently, from the theoretical perspective, one should be able to measure the strain components' magnitude in GNP-reinforced nanocomposites by measuring the variation in their electrical resistance under a given loading state. This could potentially enable one to establish the initiation and advancement of damage. This possibility is very interesting; in that, it would enable one to monitor the health of structures made of such a nanocomposite without the use of any type sensors. The author has done some preliminary investigation on this front, and has obtained encouraging results. The main challenges encountered were the very low magnitude of change in the electrical resistance as a result of the applied loading, as well as the intervention of high ambient

noises. These challenges could be mitigated; therefore, making the persuasion of the technique a worthy endeavor.

- The author has also is of the opinion that the experience gained by monitoring the strain rate effect on the mechanical properties of GNP-based adhesives can be effectively extended toward predicting the response of GNP-reinforced ABJs at various strain rates. It should be noted that the author has experimentally investigated the effect of strain rate on tubular ABJs, mating FRP adherends with neat epoxy and GNP-reinforced epoxy adhesives under various torsional strain rates. The preliminary results revealed notable differences in the maximum load carrying capacity and load-displacement response of the joints.

  To further explore the response of such joints, it is recommended to generate a systematic finite element modeling framework, perhaps using the cohesive zone approach, to predict the behavior of the ABJs under different stain rates. For this, one should develop a user-defined subroutine to accommodate the stain rate dependent material properties for analyzing the joints' response. In addition, a traction-separation model (also a cohesive zone-based methodology) can be used to accommodate the strain rate dependency according to the data that could be generated by monitoring the torque and angular-displacement behaviour of the joints.

- Finally, the following complementary research works are strongly recommended in order to extend the findings of this research:

  I. A systematic investigation of fracture surfaces of GNP/epoxy composites should be carried out using micrographs, in order to establish an index by which one could quantitatively define the quality of GNP dispersion in resins.

II. The electrical percolation threshold of GNP/epoxy composites was found to be a function of the GNP content, as well as the dispersion quality of GNP in a given resin. Consequently, the electrical conductivity of GNP-reinforced nanocomposite could be indicative of the global quality of GNP dispersion in resins. The author, therefore, suggests more research, by which one could draw a correlation between the electrical percolation threshold and the quality of GNP dispersion in resins.

III. The results obtained in this research showed that the classical fracture mechanics predicted the plastic zone radius of GNP/epoxy composites in a conservative manner. Therefore, appropriate modification should be applied to the Irwin's equation so that the process zone region around the crack tip in GNP-reinforced nanocomposite could be characterized in a more accurate manner.

References

Zhang S-P, Liu B, Li C-Y, Chen W, Yao Z-J, Yao D-T, et al. Enhanced dispersibility and thermal stability of β-cyclodextrin functionalized graphene. Chinese Chemical Letters. 2014;25:355-8.

Yuan B, Bao C, Song L, Hong N, Liew KM, Hu Y. Preparation of functionalized graphene oxide/polypropylene nanocomposite with significantly improved thermal stability and studies on the crystallization behavior and mechanical properties. Chemical Engineering Journal. 2014;237:411-20.

Yu B, Jiang Z, Tang X-Z, Yue CY, Yang J. Enhanced interphase between epoxy matrix and carbon fiber with carbon nanotube-modified silane coating. Composites Science and Technology. 2014;99:131-40.

Wernik JM, Meguid SA. On the mechanical characterization of carbon nanotube reinforced epoxy adhesives. Materials & Design. 2014;59:19-32.

Technology THU. Ultrasonic lab devices and industrial processors, www.hielscher.com Germany2014.

Shadlou S, Ahmadi-Moghadam B, Taheri F. Nano-Enhanced Adhesives. Reviews of Adhesion and Adhesives. 2014;2:371-412.

Dao TD, Hong J-E, Ryu K-S, Jeong HM. Super-tough functionalized graphene paper as a high-capacity anode for lithium ion batteries. Chemical Engineering Journal. 2014;250:257-66.

Company HCRS. High speed dispersers, http://www.pharmaceuticalonline.com. NY2014.

Almuhammadi K, Alfano M, Yang Y, Lubineau G. Analysis of interlaminar fracture toughness and damage mechanisms in composite laminates reinforced with sprayed multi-walled carbon nanotubes. Materials & Design. 2014;53:921-7.

Ahmadi-Moghadam B, Taheri F. Effect of Functionalization of Graphene Nanoplatelets on the Mechanical Response of Graphene/ Epoxy Composites. Journal of Materials and Design. 2014;In press.

Ahmadi-Moghadam B, Taheri F. Effect of processing parameters on the structure and multi-functional performance of epoxy/GNP-nanocomposites. J Mater Sci. 2014;49:6180-90.

Ahmadi-Moghadam B, Taheri F. Development of Hybridized Graphene Nanoplatelets/Fiber-Reinforced Composites with Enhanced Interlaminar Fracture Toughness. 10th Canada-Japan Workshop on Composite. Vancouver, Canada2014.

Ahmadi-Moghadam B, Taheri F. Fracture and toughening mechanisms of GNP-based nanocomposites in modes I and II fracture. Engineering Fracture Mechanics. 2014.

H. Charles Ross & Son Company, NY, High speed dispersers, http://www.pharmaceuticalonline.com 2014.

Nanoparticle, http://en.wikipedia.org/wiki/Nanoparticle. 2014.

http://www.nanodiaproducts.com/diamond-products/suspensions/, suspension nano diamond. 2014.

Yoo K, Takei Y, Kim S, Chiashi S, Maruyama S, Matsumoto K, et al. Direct physical exfoliation of few-layer graphene from graphite grown on a nickel foil using polydimethylsiloxane with tunable elasticity and adhesion. Nanotechnology. 2013;24:205302.

Yadav SK, Cho JW. Functionalized graphene nanoplatelets for enhanced mechanical and thermal properties of polyurethane nanocomposites. Applied Surface Science. 2013;266:360-7.

Turvey GJ. Testing of pultruded glass fibre-reinforced polymer (GFRP) composite materials and structures. In: Bai J, editor. Advanced Fibre-Reinforced Polymer (FRP) Composites for Structural Applications: Woodhead Publishing; 2013. p. 440-508.

Taheri F. 18 - Advanced fiber-reinforced polymer (FRP) composites for the manufacture and rehabilitation of pipes and tanks in the oil and gas industry. In: Bai J, editor. Advanced Fibre-Reinforced Polymer (FRP) Composites for Structural Applications: Woodhead Publishing; 2013. p. 662-704.

Soltannia B, Taheri F. Static, quasi-static and high loading rate effects on graphene nano-reinforced adhesively bonded single-lap joints. International Journal of Composite Materials. 2013;3:181-90.

Soltannia B, Taheri F. Static, Quasi-Static and High Loading Rate Effects on Graphene Nano-Reinforced Adhesively Bonded Single-Lap Joints. International Journal of Composite Materials. 2013;3:181-90.

Shadlou S, Alishahi E, Ayatollahi MR. Fracture behavior of epoxy nanocomposites reinforced with different carbon nano-reinforcements. Composite Structures. 2013;95:577-81.

Shadlou S, Alishahi E, Ayatollahi M. Fracture behavior of epoxy nanocomposites reinforced with different carbon nano-reinforcements. Composite Structures. 2013;95:577-81.

Pinto AM, Martins J, Moreira JA, Mendes AM, Magalhães FD. Dispersion of graphene nanoplatelets in poly(vinyl acetate) latex and effect on adhesive bond strength. Polymer International. 2013;62:928-35.

Montazeri A. The effect of functionalization on the viscoelastic behavior of multi-wall carbon nanotube/epoxy composites. Materials & Design. 2013;45:510-7.

Li Y, Pan D, Chen S, Wang Q, Pan G, Wang T. In situ polymerization and mechanical, thermal properties of polyurethane/graphene oxide/epoxy nanocomposites. Materials & Design. 2013;47:850-6.

Li W, Dichiara A, Bai J. Carbon nanotube–graphene nanoplatelet hybrids as high-performance multifunctional reinforcements in epoxy composites. Composites Science and Technology. 2013;74:221-7.

King JA, Klimek DR, Miskioglu I, Odegard GM. Mechanical properties of graphene nanoplatelet/epoxy composites. Journal of Applied Polymer Science. 2013;128:4217-23.

Khan U, May P, Porwal H, Nawaz K, Coleman JN. Improved Adhesive Strength and Toughness of Polyvinyl Acetate Glue on Addition of Small Quantities of Graphene. ACS Applied Materials & Interfaces. 2013;5:1423-8.

Karthick R, Brindha M, Selvaraj M, Ramu S. Stable colloidal dispersion of functionalized reduced graphene oxide in aqueous medium for transparent conductive film. Journal of Colloid and Interface Science. 2013;406:69-74.

Falzon BG, Hawkins SC, Huynh CP, Radjef R, Brown C. An investigation of Mode I and Mode II fracture toughness enhancement using aligned carbon nanotubes forests at the crack interface. Composite Structures. 2013;106:65-73.

Cui L-J, Wang Y-B, Xiu W-J, Wang W-Y, Xu L-H, Xu X-B, et al. Effect of functionalization of multi-walled carbon nanotube on the curing behavior and mechanical property of multi-walled carbon nanotube/epoxy composites. Materials & Design. 2013;49:279-84.

Chen DZ, Lin XM. Preparation of Graphene by Green Reduction Method and Characterization. Advanced Materials Research. 2013;807:515-20.

Bai J, Frollini E, Silva CG, Ramires EC, Miskolczi N, Sarasini F, et al. Contributor contact details. In: Bai J, editor. Advanced Fibre-Reinforced Polymer (FRP) Composites for Structural Applications: Woodhead Publishing; 2013. p. xv-xviii.

Zhu Y, Bakis CE, Adair JH. Effects of carbon nanofiller functionalization and distribution on interlaminar fracture toughness of multi-scale reinforced polymer composites. Carbon. 2012;50:1316-31.

Wang Z, Colorad HA, Guo Z-H, Kim H, Park C-L, Hahn HT, et al. Effective functionalization of carbon nanotubes for bisphenol F epoxy matrix composites. Materials Research. 2012;15:510-6.

Srikanth I, Kumar S, Kumar A, Ghosal P, Subrahmanyam C. Effect of amino functionalized MWCNT on the crosslink density, fracture toughness of epoxy and mechanical properties of carbon–epoxy composites. Composites Part A: Applied Science and Manufacturing. 2012;43:2083-6.

Shokrieh MM, Kefayati AR, Chitsazzadeh M. Fabrication and mechanical properties of clay/epoxy nanocomposite and its polymer concrete. Materials & Design. 2012;40:443-52.

Matadi Boumbimba R, Wang K, Bahlouli N, Ahzi S, Rémond Y, Addiego F. Experimental investigation and micromechanical modeling of high strain rate compressive yield stress of a melt mixing polypropylene organoclay nanocomposites. Mechanics of Materials. 2012;52:58-68.

KAKOEE A, SHABAN A, KHATIBI AA. Experimental investigation of Compressive modulus, ultimate strain and fracture energy of epoxy based nanocomposite reinforced with carbon nanotubes, under conditions of high strain rate. methods. 2012;13:18-20.

John WZ. Graphite. Graphite, Graphene, and Their Polymer Nanocomposites: CRC Press; 2012. p. 1-58.

Gómez-del Río T, Salazar A, Rodríguez J. Effect of strain rate and temperature on tensile properties of ethylene–propylene block copolymers. Materials & Design. 2012;42:301-7.

Eslami S, Taheri-Behrooz F, Taheri F. Long-term hygrothermal response of perforated GFRP plates with/without application of constant external loading. Polymer Composites. 2012;33:467-75.

Chatterjee S, Wang JW, Kuo WS, Tai NH, Salzmann C, Li WL, et al. Mechanical reinforcement and thermal conductivity in expanded graphene nanoplatelets reinforced epoxy composites. Chemical Physics Letters. 2012;531:6-10.

Chatterjee S, Nafezarefi F, Tai NH, Schlagenhauf L, Nüesch FA, Chu BTT. Size and synergy effects of nanofiller hybrids including graphene nanoplatelets and carbon nanotubes in mechanical properties of epoxy composites. Carbon. 2012;50:5380-6.

Bryan C, Whitman CA, Johnson MB, Niven JF, Murray P, Bourque A, et al. Thermal conductivity of (Er_{1−x}Y_{x})_{2}Ti_{2}O_{7} pyrochlore oxide solid solutions. Physical Review B. 2012;86:054303.

Bortz DR, Heras EG, Martin-Gullon I. Impressive Fatigue Life and Fracture Toughness Improvements in Graphene Oxide/Epoxy Composites. Macromolecules. 2012;45:238-45.

Ayatollahi MR, Doagou-Rad S, Shadlou S. Nano-/Microscale Investigation of Tribological and Mechanical Properties of Epoxy/MWNT Nanocomposites. Macromolecular Materials and Engineering. 2012;297:689-701.

Al-Sharab J, Joshi B, Gupta N. The effect of multiwall carbon nanotubes (MWCNT) on the high strain rate compressive properties of syntactic nanocomposite foams. Microscopy and Microanalysis. 2012;18:1644-5.

Alishahi E, Shadlou S, Doagou-R S, Ayatollahi MR. Effects of Carbon Nanoreinforcements of Different Shapes on the Mechanical Properties of Epoxy-Based Nanocomposites. Macromolecular Materials and Engineering. 2012.

Zhu H, Wu B, Li D, Zhang D, Chen Y. Influence of Voids on the Tensile Performance of Carbon/epoxy Fabric Laminates. Journal of Materials Science & Technology. 2011;27:69-73.

Lim AS, Melrose ZR, Thostenson ET, Chou T-W. Damage sensing of adhesively-bonded hybrid composite/steel joints using carbon nanotubes. Composites Science and Technology. 2011;71:1183-9.

Li B, Zhong W-H. Review on polymer/graphite nanoplatelet nanocomposites. J Mater Sci. 2011;46:5595-614.

Gude MR, Prolongo SG, Gómez-del Río T, Ureña A. Mode-I adhesive fracture energy of carbon fibre composite joints with nanoreinforced epoxy adhesives. International Journal of Adhesion and Adhesives. 2011;31:695-703.

Chen Z, Adams RD, da Silva LM. Fracture toughness of bulk adhesives in mode I and mode III and curing effect. International Journal of Fracture. 2011;167:221-34.

Chatterjee S, Nuesch FA, Chu BT. Comparing carbon nanotubes and graphene nanoplatelets as reinforcements in polyamide 12 composites. Nanotechnology. 2011;22:275714.

Burkholder GL, Kwon YW, Pollak RD. Effect of carbon nanotube reinforcement on fracture strength of composite adhesive joints. J Mater Sci. 2011;46:3370-7.

Ayatollahi MR, Shokrieh MM, Shadlou S, Kefayati AR, Chitsazzadeh M. Mechanical and electrical properties of epoxy/multi-walled carbon nanotube/nanoclay nanocomposites. Iran Polym J. 2011;20:835-43.

Ayatollahi MR, Shadlou S, Shokrieh MM, Chitsazzadeh M. Effect of multi-walled carbon nanotube aspect ratio on mechanical and electrical properties of epoxy-based nanocomposites. Polymer Testing. 2011;30:548-56.

Ayatollahi MR, Shadlou S, Shokrieh MM. Mixed mode brittle fracture in epoxy/multi-walled carbon nanotube nanocomposites. Engineering Fracture Mechanics. 2011;78:2620-32.

Ayatollahi MR, Shadlou S, Shokrieh MM. Fracture toughness of epoxy/multi-walled carbon nanotube nano-composites under bending and shear loading conditions. Materials & Design. 2011;32:2115-24.

Ayatollahi MR, Shadlou S, Shokrieh MM. Correlation between aspect ratio of MWCNTs and mixed mode fracture of epoxy based nanocomposites. Materials Science and Engineering: A. 2011;528:6173-8.

Ayatollahi M, Alishahi E, Shadlou S. Mechanical behavior of nanodiamond/epoxy nanocomposites. International journal of fracture. 2011;170:95-100.

Argento A, Kim W, Lee EC, Harris AM, Mielewski DF. Rate dependencies and energy absorption characteristics of nanoreinforced, biofiber, and microcellular polymer composites. Polymer Composites. 2011;32:1423-9.

BS EN ISO 12737: Determination of Plain-Strain Fracture Toughness of Metallic Materials. . BSI; 2011.

ASTM D228 Standard test Method for linear thermal expansion of solid material with a push-rod dilatometer. West conshohocken PA: ASTM international; 2011.

http://www.azom.com/, Polymer adhesives – advantages of adhesive bonding over alternative assembly techniques by Master Bond. 2011.

Yu S, Tong MN, Critchlow G. Use of carbon nanotubes reinforced epoxy as adhesives to join aluminum plates. Materials & Design. 2010;31:S126-S9.

Yang S-Y, Ma C-CM, Teng C-C, Huang Y-W, Liao S-H, Huang Y-L, et al. Effect of functionalized carbon nanotubes on the thermal conductivity of epoxy composites. Carbon. 2010;48:592-603.

Yadav SK, Mahapatra SS, Cho JW, Lee JY. Functionalization of Multiwalled Carbon Nanotubes with Poly(styrene-b-(ethylene-co-butylene)-b-styrene) by Click Coupling. The Journal of Physical Chemistry C. 2010;114:11395-400.

Wei T, Song L, Zheng C, Wang K, Yan J, Shao B, et al. The synergy of a three filler combination in the conductivity of epoxy composites. Materials Letters. 2010;64:2376-9.

Varadarajan R, Thurston A, Lewandowski J. Increased Toughness of Zirconium-Based Bulk Metallic Glasses Tested under Mixed Mode Conditions. Metall and Mat Trans A. 2010;41:149-58.

S. BS, K. PK, S. HM. Finite element modeling of crack initiation in mixed-mode (I/II). Journal of Solid Mechanics. 2010;3:231-47.

Reed CW. The Chemistry and Physics of the Interface Region and Functionalization. In: Nelson JK, editor. Dielectric Polymer Nanocomposites: Springer US; 2010. p. 95-131.

Montazeri A, Javadpour J, Khavandi A, Tcharkhtchi A, Mohajeri A. Mechanical properties of multi-walled carbon nanotube/epoxy composites. Materials & Design. 2010;31:4202-8.

Ma P-C, Siddiqui NA, Marom G, Kim J-K. Dispersion and functionalization of carbon nanotubes for polymer-based nanocomposites: A review. Composites Part A: Applied Science and Manufacturing. 2010;41:1345-67.

Lin B, Mear ME, Ravi-Chandar K. Criterion for initiation of cracks under mixed-mode I + III loading. International Journal of Fracture. 2010;165:175-88.

Korotcenkov G. Chemical Sensors: Fundamentals of Sensing Materials Volume 2: Nanos

tructured Materials: Momentum Press; 2010.

Kim H, Miura Y, Macosko CW. Graphene/polyurethane nanocomposites for improved gas barrier and electrical conductivity. Chemistry of Materials. 2010;22:3441-50.

Hodkiewicz J. Characterizing graphene with Raman spectroscopy. Thermo Fisher Scientific; 2010.

Fim FdC, Guterres JM, Basso NRS, Galland GB. Polyethylene/graphite nanocomposites obtained by in situ polymerization. Journal of Polymer Science Part A: Polymer Chemistry. 2010;48:692-8.

ASTM D638 Standard test method for tensile properies of plastics. West conshohocken, PA: ASTM International; 2010.

http://www.vircon-composites.com/2_3_2.asp. Adhesive Bonding. 2010.

Yu S, Tong MN, Critchlow G. Wedge test of carbon-nanotube-reinforced epoxy adhesive joints. Journal of Applied Polymer Science. 2009;111:2957-62.

Wang S, Tambraparni M, Qiu J, Tipton J, Dean D. Thermal Expansion of Graphene Composites. Macromolecules. 2009;42:5251-5.

Prolongo SG, Gude MR, Sanchez J, Ureña A. Nanoreinforced Epoxy Adhesives for Aerospace Industry. The Journal of Adhesion. 2009;85:180-99.

Park SW, Lee DG. Strength of Double Lap Joints Bonded With Carbon Black Reinforced Adhesive Under Cryogenic Environment. Journal of Adhesion Science and Technology. 2009;23:619-38.

Park SW, Kim BC, Lee DG. Tensile Strength of Joints Bonded With a Nano-particle-Reinforced Adhesive. Journal of Adhesion Science and Technology. 2009;23:95-113.

McClung AJ, Ruggles-Wrenn MB. Strain rate dependence and short-term relaxation behavior of a thermoset polymer at elevated temperature: experiment and modeling. Journal of pressure vessel technology. 2009;131.

Liang J, Huang Y, Zhang L, Wang Y, Ma Y, Guo T, et al. Molecular-Level Dispersion of Graphene into Poly(vinyl alcohol) and Effective Reinforcement of their Nanocomposites. Advanced Functional Materials. 2009;19:2297-302.

Hosseinzadeh R. Analysis and enhancement of tubular bonded joints subject to torsion: Dalhousie University; 2009.

Choudalakis G, Gotsis AD. Permeability of polymer/clay nanocomposites: A review. European Polymer Journal. 2009;45:967-84.

Bauhofer W, Kovacs JZ. A review and analysis of electrical percolation in carbon nanotube polymer composites. Composites Science and Technology. 2009;69:1486-98.

Al-Saleh MH, Sundararaj U. A review of vapor grown carbon nanofiber/polymer conductive composites. Carbon. 2009;47:2-22.

ASTM E399. Standard test method for linear-elastic plane strain fracture toughness K_IC of metallic material. West Conshohocken, PA: ASTM; 2009.

Tugrul Seyhan A, Tanoglu M, Schulte K. Mode I and mode II fracture toughness of E-glass non-crimp fabric/carbon nanotube (CNT) modified polymer based composites. Engineering Fracture Mechanics. 2008;75:5151-62.

Li J, Wong P-S, Kim J-K. Hybrid nanocomposites containing carbon nanotubes and graphite nanoplatelets. Materials Science and Engineering: A. 2008;483–484:660-3.

Lazarus V, Buchholz FG, Fulland M, Wiebesiek J. Comparison of predictions by mode II or mode III criteria on crack front twisting in three or four point bending experiments. International Journal of Fracture. 2008;153:141-51.

Jo C, Naguib HE. Modeling the effect of strain rate on the mechanical properties of HDPE/Clay Nanocomposite foams. Polymers & polymer composites. 2008;16:561-75.

Gueguen O, Richeton J, Ahzi S, Makradi A. Micromechanically based formulation of the cooperative model for the yield behavior of semi-crystalline polymers. Acta Materialia. 2008;56:1650-5.

Fan Z, Santare MH, Advani SG. Interlaminar shear strength of glass fiber reinforced epoxy composites enhanced with multi-walled carbon nanotubes. Composites Part A: Applied Science and Manufacturing. 2008;39:540-54.

Bian L, Taheri F. Fatigue fracture criteria and microstructures of magnesium alloy plates. Materials Science and Engineering: A. 2008;487:74-85.

Benzaid R, Chevalier J, Saâdaoui M, Fantozzi G, Nawa M, Diaz LA, et al. Fracture toughness, strength and slow crack growth in a ceria stabilized zirconia–alumina nanocomposite for medical applications. Biomaterials. 2008;29:3636-41.

See CH, Harris AT. A Review of Carbon Nanotube Synthesis via Fluidized-Bed Chemical Vapor Deposition. Industrial & Engineering Chemistry Research. 2007;46:997-1012.

Saeed MB, Zhan M-S. Adhesive strength of nano-size particles filled thermoplastic polyimides. Part-I: Multi-walled carbon nano-tubes (MWNT)–polyimide composite films. International Journal of Adhesion and Adhesives. 2007;27:306-18.

Richeton J, Ahzi S, Vecchio K, Jiang F, Makradi A. Modeling and validation of the large deformation inelastic response of amorphous polymers over a wide range of temperatures and strain rates. International journal of solids and structures. 2007;44:7938-54.

Li J, Kim J-K. Percolation threshold of conducting polymer composites containing 3D randomly distributed graphite nanoplatelets. Composites Science and Technology. 2007;67:2114-20.

Goglio L, Peroni M, Rossetto M. Effect of the strain rate on the mechanical behaviour of epoxy adhesives. Key Engineering Materials. 2007;347:671-6.

ASTM D5054. Standard test methods for plane-strain fracture toughness and strain energy release rate of plastic material. West Conshohocken, PA: ASTM; 2007.

ASTM D257 Standard test method for DC resistance or conductance of insulating material. West Conshohocken, PA: ASTM International; 2007.

Yeh M-K, Tai N-H, Liu J-H. Mechanical behavior of phenolic-based composites reinforced with multi-walled carbon nanotubes. Carbon. 2006;44:1-9.

Wetzel B, Rosso P, Haupert F, Friedrich K. Epoxy nanocomposites – fracture and toughening mechanisms. Engineering Fracture Mechanics. 2006;73:2375-98.

Wang T, Lei CH, Dalton AB, Creton C, Lin Y, Fernando KAS, et al. Waterborne, Nanocomposite Pressure-Sensitive Adhesives with High Tack Energy, Optical Transparency, and Electrical Conductivity. Advanced Materials. 2006;18:2730-4.

Thostenson ET, Chou T-W. Processing-structure-multi-functional property relationship in carbon nanotube/epoxy composites. Carbon. 2006;44:3022-9.

Richeton J, Ahzi S, Vecchio K, Jiang F, Adharapurapu R. Influence of temperature and strain rate on the mechanical behavior of three amorphous polymers: Characterization and modeling of the compressive yield stress. International journal of solids and structures. 2006;43:2318-35.

Ramakrishna S, Lim TC, Inai R, Fujihara K. Modified Halpin-Tsai Equation for Clay-Reinforced Polymer Nanofiber. Mechanics of Advanced Materials and Structures. 2006;13:77-81.

Li J, Lumpp JK. Electrical and mechanical characterization of carbon nanotube filled conductive adhesive. Aerospace Conference, 2006 IEEE: IEEE; 2006. p. 6 pp.

Lanticse LJ, Tanabe Y, Matsui K, Kaburagi Y, Suda K, Hoteida M, et al. Shear-induced preferential alignment of carbon nanotubes resulted in anisotropic electrical conductivity of polymer composites. Carbon. 2006;44:3078-86.

Kang I, Heung YY, Kim JH, Lee JW, Gollapudi R, Subramaniam S, et al. Introduction to carbon nanotube and nanofiber smart materials. Composites Part B: Engineering. 2006;37:382-94.

Hedia HS, Allie L, Ganguli S, Aglan H. The influence of nanoadhesives on the tensile properties and Mode-I fracture toughness of bonded joints. Engineering Fracture Mechanics. 2006;73:1826-32.

Gojny FH, Wichmann MHG, Fiedler B, Kinloch IA, Bauhofer W, Windle AH, et al. Evaluation and identification of electrical and thermal conduction mechanisms in carbon nanotube/epoxy composites. Polymer. 2006;47:2036-45.

Ci L, Bai J. The reinforcement role of carbon nanotubes in epoxy composites with different matrix stiffness. Composites Science and Technology. 2006;66:599-603.

Cheng J, Taheri F. A smart single-lap adhesive joint integrated with partially distributed piezoelectric patches. International Journal of Solids and Structures. 2006;43:1079-92.

Brunner AJ, Necola A, Rees M, Gasser P, Kornmann X, Thomann R, et al. The influence of silicate-based nano-filler on the fracture toughness of epoxy resin. Engineering Fracture Mechanics. 2006;73:2336-45.

Viculis LM, Mack JJ, Mayer OM, Hahn HT, Kaner RB. Intercalation and exfoliation routes to graphite nanoplatelets. Journal of Materials Chemistry. 2005;15:974-8.

Lu C, Mai YW. Influence of aspect ratio on barrier properties of polymer-clay nanocomposites. Physical review letters. 2005;95:088303.

Jinquan C, Farid T. A novel smart adhesively bonded joint system. Smart Materials and Structures. 2005;14:971.

Cho D, Lee S, Yang G, Fukushima H, Drzal LT. Dynamic Mechanical and Thermal Properties of Phenylethynyl-Terminated Polyimide Composites Reinforced With Expanded Graphite Nanoplatelets. Macromolecular Materials and Engineering. 2005;290:179-87.

Anderson TL. Fracture Mechanics: Fundamentals and Applications, Third Edition: Taylor & Francis; 2005.

Shen L, Phang IY, Liu T, Zeng K. Nanoindentation and morphological studies on nylon 66/organoclay nanocomposites. II. Effect of strain rate. Polymer. 2004;45:8221-9.

Novoselov KS, Geim AK, Morozov SV, Jiang D, Zhang Y, Dubonos SV, et al. Electric Field Effect in Atomically Thin Carbon Films. Science. 2004;306:666-9.

Liu S, Chao YJ, Zhu X. Tensile-shear transition in mixed mode I/III fracture. International Journal of Solids and Structures. 2004;41:6147-72.

Jiang H, Liu B, Huang Y, Hwang KC. Thermal Expansion of Single Wall Carbon Nanotubes. Journal of Engineering Materials and Technology. 2004;126:265.

Jacob GC, Starbuck JM, Fellers JF, Simunovic S, Boeman RG. Strain rate effects on the mechanical properties of polymer composite materials. Journal of Applied Polymer Science. 2004;94:296-301.

Gojny FH, Wichmann MHG, Köpke U, Fiedler B, Schulte K. Carbon nanotube-reinforced epoxy-composites: enhanced stiffness and fracture toughness at low nanotube content. Composites Science and Technology. 2004;64:2363-71.

Bian L-C, Kim KS. The minimum plastic zone radius criterion for crack initiation direction applied to surface cracks and through-cracks under mixed mode loading. International Journal of Fatigue. 2004;26:1169-78.

ASTM D4496 Standard test method for D-C resistance or condutance of moderately conductive materials. West Conshoohoken, PA: ASTM International; 2004.

Yasmin A, Abot JL, Daniel IM. Processing of clay/epoxy nanocomposites by shear mixing. Scripta Materialia. 2003;49:81-6.

Wong M, Paramsothy M, Xu XJ, Ren Y, Li S, Liao K. Physical interactions at carbon nanotube-polymer interface. Polymer. 2003;44:7757-64.

Hsiao K-T, Alms J, Advani SG. Use of epoxy/multiwalled carbon nanotubes as adhesives to join graphite fibre reinforced polymer composites. Nanotechnology. 2003;14:791.

Davis GD. Durability of adhesive joints. Handbook of adhesive technology. 2003:273.

Tay TE, Shen F. Analysis of Delamination Growth in Laminated Composites with Consideration for Residual Thermal Stress Effects. Journal of Composite Materials. 2002;36:1299-320.

Schöllmann M, Richard H, Kullmer G, Fulland M. A new criterion for the prediction of crack development in multiaxially loaded structures. International Journal of Fracture. 2002;117:129-41.

Piggott MR. Load Bearing Fibre Composites: Kluwer Academic Publishers; 2002.

Pascault J-P, Sautereau H, Verdu J, Williams RJ. Thermosetting polymers: CRC Press; 2002.

Chiu PW, Duesberg GS, Dettlaff-Weglikowska U, Roth S. Interconnection of carbon nanotubes by chemical functionalization. Applied Physics Letters. 2002;80:3811-3.

Scott CD, Arepalli S, Nikolaev P, Smalley RE. Growth mechanisms for single-wall carbon nanotubes in a laser-ablation process. Appl Phys A. 2001;72:573-80.

Lazarus V, Leblond J-B, Mouchrif S-E. Crack front rotation and segmentation in mixed mode I+III or I+II+III. Part II: Comparison with experiments. Journal of the Mechanics and Physics of Solids. 2001;49:1421-43.

Bolotin VV. Mechanics of Delaminations in Laminate Composite Structures. Mechanics of Composite Materials. 2001;37:367-80.

Sukumar N, Moës N, Moran B, Belytschko T. Extended finite element method for three-dimensional crack modelling. International Journal for Numerical Methods in Engineering. 2000;48:1549-70.

Simpson GJ, Sedin DL, Rowlen KL. Surface Roughness by Contact versus Tapping Mode Atomic Force Microscopy. Langmuir. 1999;15:1429-34.

Crasto AS, Kim RY. Hygrothermal influence on the free-edge delamination of composites under compressive loading1997.

Chao Y, Liu S. On the failure of cracks under mixed-mode loads. International Journal of Fracture. 1997;87:201-23.

Deo RB. Composite materials: testing and design: ASTM; 1996.

Celzard A, McRae E, Deleuze C, Dufort M, Furdin G, Marêché JF. Critical concentration in percolating systems containing a high-aspect-ratio filler. Physical Review B. 1996;53:6209-14.

Bolotin VV. Delaminations in composite structures: Its origin, buckling, growth and stability. Composites Part B: Engineering. 1996;27:129-45.

Bagheri R, Pearson RA. Role of particle cavitation in rubber-toughened epoxies: 1. Microvoid toughening. Polymer. 1996;37:4529-38.

S. RR, D.C. L. Mechnaical and thermal properties of caron nanotubes. Carbon. 1995;33:6.

Xu G, Bower AF, Ortiz M. An analysis of non-planar crack growth under mixed mode loading. International Journal of Solids and Structures. 1994;31:2167-93.

A.M. K, J.P. H, R. H, X. F. A Suggested Test Procedure to Measure Mixed Mode I–III Fracture Toughness of Brittle Materials. Journal of Testing and Evaluation. 1994;23:327-34.

White SR, Hahn HT. Cure Cycle Optimization for the Reduction of Processing-Induced Residual Stresses in Composite Materials. Journal of Composite Materials. 1993;27:1352-78.

Lee SM. An edge crack torsion method for mode III delamination fracture test. Journal of Composites, Technology & Research. 1993;15:193-201.

Davenport JCW, Smith DJ. A STUDY OF SUPERIMPOSED FRACTURE MODES I, II AND III ON PMMA. Fatigue & Fracture of Engineering Materials & Structures. 1993;16:1125-33.

Ashbee KHG. Fundamental Principles of Fiber Reinforced Composites, Second Edition: Taylor & Francis; 1993.

Manoharan M, Lewandowski JJ. Combined Mode I-Mode III Fracture Toughness of a Particulate Reinforced Metal-Matrix Composite. Journal of Composite Materials. 1991;25:831-41.

Suresh S, Tschegg EK. Combined Mode I-Mode III Fracture of Fatigue-Precracked Alumina. Journal of the American Ceramic Society. 1987;70:726-33.

Bradley WL, Corleto CR, Goetz DP, A T, MECHANICS MUCS, CENTER. M. Fracture Physics of Delamination of Composite Materials: Defense Technical Information Center; 1987.

Kinloch AJ. Mechanics and mechanisms of fracture of thermosetting epoxy polymers. Epoxy Resins and Composites I: Springer Berlin Heidelberg; 1985. p. 45-67.

Johnson GR, Cook WH. Fracture characteristics of three metals subjected to various strains, strain rates, temperatures and pressures. Engineering Fracture Mechanics. 1985;21:31-48.

Faber KT, Evans AG. Crack deflection processes—II. Experiment. Acta Metallurgica. 1983;31:577-84.

Faber KT, Evans AG. Crack deflection processes—I. Theory. Acta Metallurgica. 1983;31:565-76.

Chow TS. The effect of Particles shape on the mechanical properties of filled polymer. Journal of Material Science. 1980;15:15.

Spitzig W, Richmond O. Effect of hydrostatic pressure on the deformation behavior of polyethylene and polycarbonate in tension and in compression. Polymer Engineering & Science. 1979;19:1129-39.

Green D, Nicholson P, Embury JD. Fracture of a brittle particulate composite. J Mater Sci. 1979;14:1413-20.

Bažant ZP, Estenssoro LF. Surface singularity and crack propagation. International Journal of Solids and Structures. 1979;15:405-26.

Chell GG, Girvan E. An experimental technique for fast fracture testing in mixed mode. International Journal of Fracture. 1978;14:R81-R3.

Bauwens J. Relation between the compression yield stress and the mechanical loss peak of bisphenol-A-polycarbonate in the β transition range. J Mater Sci. 1972;7:577-84.

Sommer E. Formation of fracture 'lances' in glass. Engineering Fracture Mechanics. 1969;1:539-46.

Cowper G, Symonds P. Strain hardening and effects in the impact loading of cantilever beams. Tech Rep Brown University Division of Applied Mathematics, Technical rept no 28. 1957.

Wicks SS, Wang W, Williams MR, Wardle BL. Multi-scale Interlaminar Fracture Mechanisms in Woven Composite Laminates Reinforced with Aligned Carbon Nanotubes. Composites Science and Technology.

Appendix A: Copyright permissions

This is a License Agreement between Babak Ahmadi Moghadam ("You") and Springer ("Springer") provided by Copyright Clearance Center ("CCC"). The license consists of your order details, the terms and conditions provided by Springer, and the payment terms and conditions.

All payments must be made in full to CCC. For payment instructions, please see information listed at the bottom of this form.

License Number	3490850794421
License date	Oct 16, 2014
Licensed content publisher	Springer
Licensed content publication	Journal of Materials Science (full set)
Licensed content title	Effect of processing parameters on the structure and multi-functional performance of epoxy/GNP-nanocomposites
Licensed content author	B. Ahmadi-Moghadam
Licensed content date	Jan 1, 2014
Volume number	49
Issue number	18
Type of Use	Thesis/Dissertation
Portion	Full text
Number of copies	2
Author of this Springer article	Yes and you are the sole author of the new work
Order reference number	None
Title of your thesis / dissertation	Development of a Highly Resilience Graphene Nanoplatelet Adhesive
Expected completion date	Dec 2014
Estimated size(pages)	200
Total	0.00 CAD

This is a License Agreement between Babak Ahmadi Moghadam ("You") and Elsevier ("Elsevier") provided by Copyright Clearance Center ("CCC"). The license consists of your order details, the terms and conditions provided by Elsevier, and the payment terms and conditions.

All payments must be made in full to CCC. For payment instructions, please see information listed at the bottom of this form.

Supplier	Elsevier Limited The Boulevard,Langford Lane Kidlington,Oxford,OX5 1GB,UK
Registered Company Number	1982084
Customer name	Babak Ahmadi Moghadam
Customer address	1360 Barrington Street, D304 Halifax, NS B3H 4R2
License number	3491311014209
License date	Oct 17, 2014
Licensed content publisher	Elsevier
Licensed content publication	Engineering Fracture Mechanics
Licensed content title	Fracture and toughening mechanisms of GNP-based nanocomposites in modes I and II fracture
Licensed content author	B. Ahmadi-Moghadam,F. Taheri
Licensed content date	Available online 3 September 2014
Licensed content volume number	n/a
Licensed content issue number	n/a
Number of pages	1
Start Page	None
End Page	None
Type of Use	reuse in a thesis/dissertation
Intended publisher of new work	other
Portion	full article
Format	both print and electronic

Dear

I am preparing my PhD thesis for submission to the Faculty of Graduate Studies at Dalhousie University, Halifax, Nova Scotia, Canada, I am seeking your permission to include a manuscript version of the following paper as a chapter in thesis:

B. Ahmadi-Moghadam and Farid Taheri " An Effective Means for Evaluating Mixed-mode I/III Stress Intensity Factor Using Single-Edge Notch Beam Specimen" Journal of Strain Analysis, Vol 48: 245-257, 2013.

would you please sign the attached form and send me back a copy of signed form,

Regards,

...

--
Babak Ahmadi Moghadam,

PhD candidate
Advanced Composites & Mechanics Research Center
Department of Civil & Resource Engineering
Dalhousie University,
1360 Barrington Street, PO BOX 15000
Halifax, Nova Scotia B3H 4R2, Canada
Phone: 1(902) 494-3821
Email: babak.ahmadi@dal.ca

Dear Babak Ahmadi Moghadam,

Thank you for your email.

Please consider this email as written permission to include the article 'An Effective Means for Evaluating Mixed-mode I/III Stress Intensity Factor Using Single-Edge Notch Beam Specimen' form our publication Journal of Strain Analysis as part of your forth coming PhD thesis / Dissertation.

Please note:
This permission does not cover any 3rd party material that may be found in the work.
The author(s) of this work must be informed of this reuse.
A full reference to the original SAGE published work must be given.

Best Wishes,

Ellie Hodge
Permissions Assistant
SAGE Publications Ltd
1 Oliver's Yard, 55 City Road
London, EC1Y 1SP
UK
www.sagepub.co.uk

This is a License Agreement between Babak Ahmadi Moghadam ("You") and Elsevier ("Elsevier") provided by Copyright Clearance Center ("CCC"). The license consists of your order details, the terms and conditions provided by Elsevier, and the payment terms and conditions.

All payments must be made in full to CCC. For payment instructions, please see information listed at the bottom of this form.

Supplier	Elsevier Limited The Boulevard,Langford Lane Kidlington,Oxford,OX5 1GB,UK
Registered Company Number	1982084
Customer name	Babak Ahmadi Moghadam
Customer address	1360 Barrington Street, D304 Halifax, NS B3H 4R2
License number	3502490482172
License date	Nov 05, 2014
Licensed content publisher	Elsevier
Licensed content publication	Materials & Design
Licensed content title	Effect of functionalization of graphene nanoplatelets on the mechanical response of graphene/ epoxy composites
Licensed content author	B. Ahmadi-Moghadam,M. Sharafimasooleh,S. Shadlou,F. Taheri
Licensed content date	Available online 24 October 2014
Licensed content volume number	n/a
Licensed content issue number	n/a
Number of pages	1
Start Page	None
End Page	None
Type of Use	reuse in a thesis/dissertation
Intended publisher of new work	other
Portion	full article

This is a License Agreement between Babak Ahmadi Moghadam ("You") and Elsevier ("Elsevier") provided by Copyright Clearance Center ("CCC"). The license consists of your order details, the terms and conditions provided by Elsevier, and the payment terms and conditions.

All payments must be made in full to CCC. For payment instructions, please see information listed at the bottom of this form.

Supplier	Elsevier Limited The Boulevard,Langford Lane Kidlington,Oxford,OX5 1GB,UK
Registered Company Number	1982084
Customer name	Babak Ahmadi Moghadam
Customer address	1360 Barrington Street, D304 Halifax, NS B3H 4R2
License number	3490851305946
License date	Oct 16, 2014
Licensed content publisher	Elsevier
Licensed content publication	Materials & Design
Licensed content title	The effect of strain-rate on the tensile and compressive behavior of graphene reinforced epoxy/nanocomposites
Licensed content author	Shahin Shadlou,Babak Ahmadi-Moghadam,Farid Taheri
Licensed content date	July 2014
Licensed content volume number	59
Licensed content issue number	n/a
Number of pages	9
Start Page	439
End Page	447
Type of Use	reuse in a thesis/dissertation
Intended publisher of new work	other
Portion	full article
Format	both print and electronic